𝛾

MASTER

Los Alamos Scientific Laboratory Summer School on

Nuclear Science

June 1978

University of California

LOS ALAMOS SCIENTIFIC LABORATORY

Los Alamos Scientific Laboratory Summer School on

Nuclear Science

June 1978
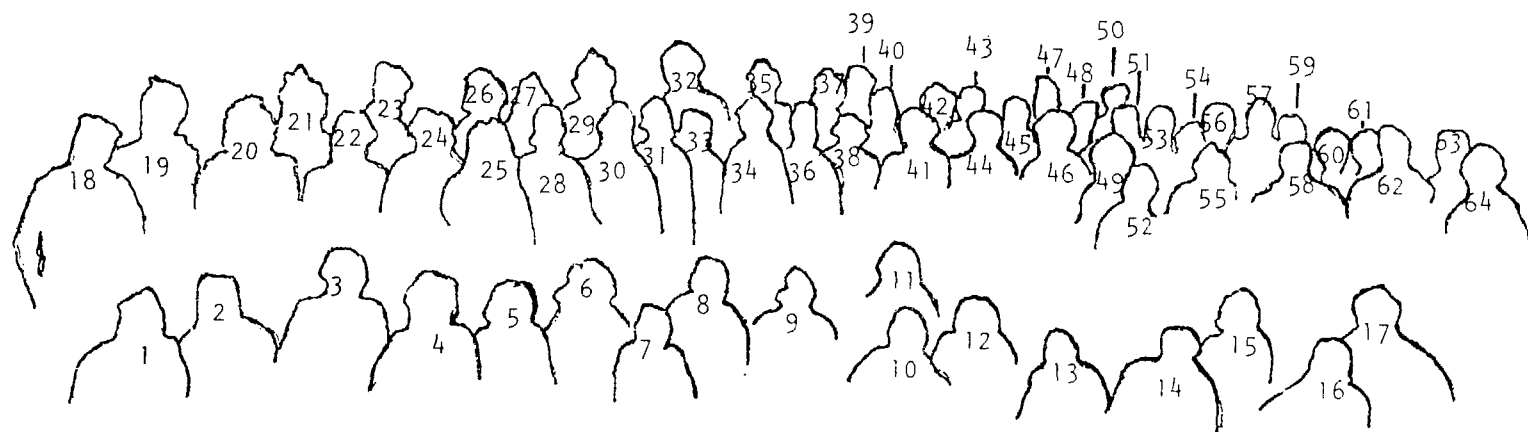
Compiled by

Martin Cooper
Robert Redwine*
Richard Mischke

*Massachusetts Institute of Technology, Cambridge, MA 02139.

1. R. Redwine	17. A. Shor
2. C. Hoffman	18. R. Mischke
3. J. McKibben	19. M. Cooper
4. T. Kary	20. S. Turpin
5. V. Yuan	21. S. Dam
6. M. A. Yates-Williams	22. L. Hopkins
7. K. Giovanetti	23. A. Wapstra
8. K. Aniol	24. B. Preedom
9. E. Cooper	25. R. Chaky
10. E. Adelberger	26. D. Hertzog
11. L. Antonuk	27. J. Lissanti
12. E. Mathie	28. N. Wright
13. S. Chakravarti	29. G. Pepin
14. K. Daneshvar	30. B. Peterson
15. J. Kim	31. K. Stricker
16. W. Henning	32. D. Peterson

33. A. Szyjewicz	49. B. Tsang
34. J. Vrba	50. Unidentified
35. B. Bassalleck	51. Unidentified
36. R. Ransome	52. A. Wang
37. Unidentified	53. R. Jeppeson
38. D. Dowell	54. M. Haji-Saeid
39. S. Greene	55. W. Sheers
49. R. Meyer	56. W. Lynch
41. Unidentified	57. S. Wissink
42. J. Becker	58. B. Tippins
43. D. Youngblood	59. J. Kapusta
44. Unidentified	60. T. Tombrello
45. D. Marlow	61. T. Renner
46. N. Colella	62. D. Vieira
47. J. Ullman	63. W. Briscoe
48. M. Hoehn	64. D. Bowman
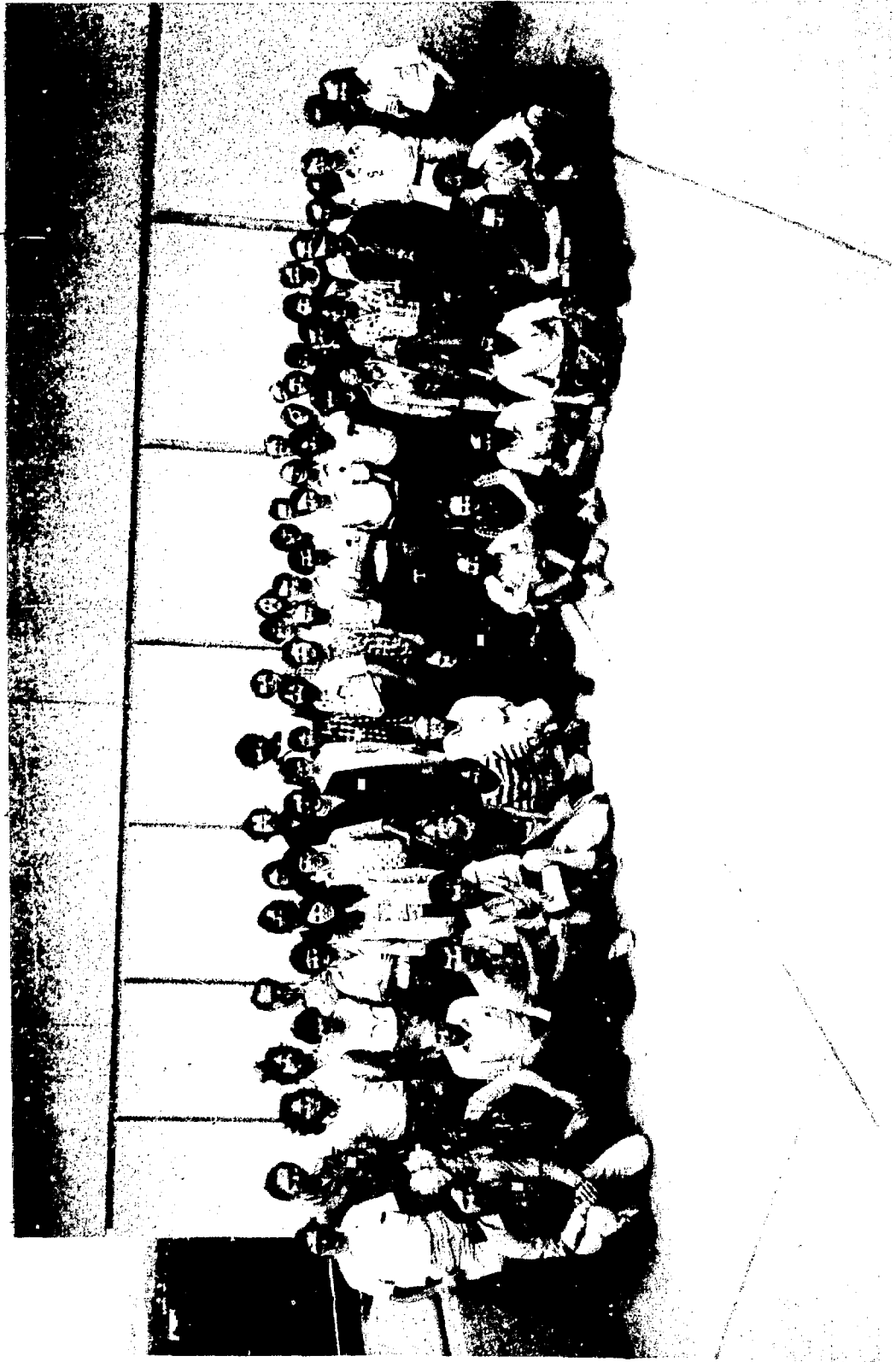
LIST OF LECTURES FOR THE 1978 LOS ALAMOS SUMMER SCHOOL

I. FUNDAMENTAL SYMMETRIES IN NUCLEI (5 lectures)
        E. Adelberger, Univ. of Washington, Lecturer

    1. How good is isospin symmetry in nuclei?
    2. Phenomenology of weak interactions (charged and neutral currents).
    3. Beta decay and μ capture (probes of charged current).
    4. Neutrino induced reactions (probe of neutral currents).
    5. Nuclear and atomic parity violations.

II. NUCLEAR SHAPES AND MATTER DISTRIBUTIONS (5 lectures)
        J. Friar, LASL, Lecturer

    1. Electron scattering and muonic atoms-basic theory.
    2. Meson exchange currents.
    3. "Model independent" analysis and results on radial shapes from elec-
        tron scattering and muonic atoms.
    4. Matter distributions using Hadronic probes.

III. HEAVY ION PHYSICS (5 lectures)
        W. Henning, Argonne National Laboratory, Lecturer

    1. Quasi-elastic collisions and direct reaction behavior.
    2. Fluctuations, intermediate structure, and resonances.
    3. Compound reactions and high angular momentum states.
    4. Fusion, fission and strongly damped collisions.
    5. Relativistic heavy ions.

IV. MESONIC EFFECTS IN NUCLEAR SYSTEMS (5 lectures)
        M. Johnson, LASL, Lecturer

    1. Mesons, nucleons and their interactions; Feynman diagrams.
    2. Basic nuclear matter theory: Feynman-Goldstone diagrams, Goldstone's
        theorem, Brueckner-Bethe method, variational method.
    3. Results of nuclear matter theory; ordinary nuclear matter; high
        density nuclear matter of neutron stars.
    4. Pions in nuclear matter: the pion Green's function, pion condensation.

V. IMPLICATIONS OF SOME PARTICLE PHYSICS IDEAS (5 lectures)
        G. Stephenson, LASL, Lecturer

    1. Are nucleon-nucleon forces similar to Van der Waals forces?
    2. Can we predict meson-nucleon couplings in the nuclear medium?
    3. Is nuclear PCAC applicable?
    4. Are there clean experimental tests of any of the above?

VI. APPLICATIONS OF NUCLEAR PHYSICS (5 lectures)
        T. Tombrello, California Institute of Technology, Lecturer

    1. Nuclear astrophysics
    2. Planetary science.
    4. Ion-solid interactions
    5. Materials analysis.

TABLE OF CONTENTS

for

MESONIC EFFECTS IN NUCLEAR PHYSICS

LOS ALAMOS SCIENTIFIC LABORATORY SUMMER SCHOOL ON
NUCLEAR SCIENCE

June 1978

Compiled by

Martin Cooper, Robert Redwine, and Richard Mischke

ABSTRACT

This volume contains written versions of lectures given by
Mikkel Johnson and Thomas Tombrello at the LASL Summer School
on Nuclear Science in 1978. The purpose was to present to an
audience of graduate students considering careers in nuclear
science, a series of lectures which would advance their under-
standing and would identify areas of challenge in nuclear science.
In addition to those in this volume, principal lectures were
presented by Eric Adelberger, James Friar, Walter Henning, and
Gerard Stephenson. Special lectures were presented by John
Schiffer, David Youngblood, Donald Sprung, and John Walecka.
David Youngblood and Donald Sprung also appear in this volume.
A second volume containing the written lectures of Walter
Henning is anticipated by the summer. There was also a session
of contributed papers.

MESONIC EFFECTS IN NUCLEAR PHYSICS

by

Mikkel Johnson
University of California
Los Alamos Scientific Laboratory

I.   INTRODUCTION

The theme of this series of five lectures will be the relationship between mesons and nucleons and the properties of nuclear matter, as we understand these things today. The lectures unfortunately cannot be comprehensive because of the limitations of time and the great body of literature falling within this general subject area. Although the topic is difficult because of the enormity of its scope, nuclear physics becomes simpler by virtue of the unification afforded by the description in terms of mesons. One thus naturally finds a few ideas dominating many different phenomena. For example, the Δ_{33} pion-nucleon resonance plays a prominent role not only in pion-nucleon scattering but also in the theoretical description of the nucleon-nucleon interaction; these two fundamental interactions in turn play a decisive role in all aspects of the physics of nuclear matter at low density, i.e., normal nuclei, and at high density, e.g., neutron stars. Likewise, there are a few mathematical tools which are useful throughout nuclear physics for developing physical intuition into definite predictions. The computer is one trivial example, familiar to everybody, but another which should be equally as familiar, but unfortunately isn't, is a knowledge of Feynman diagrams. In this series of lectures I shall try to emphasize the common ideas and methods rather than the diversity inherent in this topic.

I should begin by saying that the fundamental strongly interacting fields are believed to be quarks and gluons, described by the theory quantum chromodynamics, QCD.[1] Thus, I will not be discussing a truly fundamental theory. However, for low and intermediate energy physics the mesons and baryons are presumably more useful than quarks, because quarks like to lump together into the meson and nucleon "collective coordinates." The low-lying meson and baryon states of relevance to this set of lectures are shown in Table I, along with their spins

and parities. The MIT bag model[2] does a fairly good job in reproducing these results from the point of view of QCD, except the π meson. The working hypothesis is that the meson and baryon states observed in isolation are also the relevant coordinates inside nuclei and, thus, what nuclear physics needs in order to proceed is a table such as the one below of the properties of the mesons and baryons in isolation, and in addition a table showing how these mesons and baryons interact. A partial list of interactions is presented in Table II. The general form of the coupling for a given meson-baryon interaction may be deduced from the spin, isospin, and parity of the particles involved, the requirement being that the interaction be a scalar. Sometimes several types of coupling may be involved, for example, the vector mesons have a so-called vector and tensor coupling allowed, and two independent coupling constants must be specified. The theory of quarks provides a scheme[3] for relating the couplings of the mesons and baryons in terms of just a few numbers, and one uses this theory when the relevant experimental data are not available. Often it is necessary to introduce a form factor, or high momentum cutoff, into the theory in order to get finite answers; if one were able to work entirely within the framework of QCD this would be unnecessary, however, because QCD is renormalizable.

From the point of view of these lectures, we shall assume that mesons and nucleons are the fundamental degrees of freedom and that the interaction shown in Table II is the fundamental interaction. From the point of view of modern particle physics, mesons and nucleons span a model space in the full quantum mechanical Hilbert space, and their interaction expressed in Table II is an effective interaction (or at least a piece of the effective interaction) in this model space. One goal of theory is to make rigorous the connection between the description in terms of quarks and gluons on the one hand and mesons and baryons on the other, or at least to define the shortcomings of the latter description.

Traditional nuclear physics has not developed within the framework of meson physics; after all the pion wasn't discovered until 1947, many years after nuclear physics had become an established discipline. We find, rather, that nuclear physics has developed (rather successfully) from static, phenomenological potential models. The large measure of success of this approach is presumably due to the fact that the energy required to create a meson or heavy baryon is so much greater than typical nuclear excitation energies, that these particles have only

TABLE II

TABLE I

A PARTIAL LIST OF THE LIGHT MESONS AND BARYONS

A. Mesons	Mass (MeV)	Spin	Isospin	Parity
π^+,π^0,π^-	$\pi^{\pm}(140)\ \pi^0(135)$	0	1	-
η^0	549	0	0	-
ρ^+,ρ^0,ρ^-	773	1	1	-
ω^0	783	1	0	-
B. Baryons				
n,p	940	1/2	1/2	+
Λ	1116	1/2	0	+
$\Sigma^+,\Sigma^0,\Sigma^-$	1193	1/2	1	+
$\Delta^{++},\Delta^+,\Delta^0,\Delta^-$	1232	3/2	3/2	+

COUPLINGS OF MESONS AND NUCLEONS (NON-RELATIVISTIC)

Particles	Coupling form	Coupling Constant
	$\dfrac{f_\pi}{m_\pi}\,\sigma\cdot q\,\tau_q$	$\dfrac{f^2_{\pi NN}}{4\pi}=0.08$
	$\dfrac{f_\eta}{m_\eta}\,\sigma\cdot q$	$\dfrac{f^2_{\eta NN}}{4\pi}\ \dfrac{1}{14}\ \dfrac{f^2_{\pi NN}}{4\pi}$
	$\left(\dfrac{g_{\rho NN}}{m_\rho}\,q\cdot\varepsilon-\dfrac{f_{\rho NN}}{m_\rho}\,\sigma\cdot\varepsilon\times q\right)\tau_q$	$\dfrac{f^2_{\rho NN}}{4\pi}=3.7,\ \dfrac{g^2_{\rho NN}}{4\pi}=0.89$
	$\dfrac{g_\omega}{m_\omega}\,q\cdot\varepsilon$	$\dfrac{g^2_\omega}{4\pi}=6.36$

a short "virtual" existence in low energy nuclear physics. The time Δt that these objects exist is limited by the uncertainty principle. For example, if a meson of mass m is created by a nucleon in the nuclear ground state, it will stay around for a time

$$\Delta t \approx \frac{\hbar}{m} \tag{1}$$

which is exceedingly short. For a π-meson

$$\Delta t_\pi \approx \frac{\hbar}{m_\pi} = \frac{6.6 \times 10^{-22}\ \text{MeV-s}}{1.4 \times 10^2\ \text{MeV}} = 4.7 \times 10^{-24}\ \text{s} \tag{2}$$

The π-meson can't do much in this time; it may influence another nucleon within a distance

$$\Delta t \cdot c \approx 1.4\ \text{fm} \tag{3}$$

but this distance is not especially large considering that the average spacing between nucleons in the nucleus is

$$d = \left(\frac{1}{\rho_o}\right)^{1/3} = 1.8\ \text{fm} \tag{4}$$

The conclusion is that the space-time dependence of the meson fields is so restricted that these fields do not need to be given explicit roles in theories of nuclear structure. This observation gives support to the idea that potential theory is an adequate framework for describing low-energy nuclear physics. However, one should not be satisfied with a purely phenomenological approach through potentials; one should strive to build the potential theory as much as possible on the ideas of more fundamental approaches. Later in this first lecture I shall indicate how to build systematically a potential theory equivalent to a more

3

fundamental meson exchange description. In this sense, a potential theory will include not only two-body potentials but also three- and higher-body contributions

One hopes not only to learn how to explain the properties of complex nuclear systems in terms of fundamental theories but also to learn about fundamental theories from measurements on nuclei. However, the success of the potential description in nuclear physics means that it is hard to learn about meson-baryon interactions by studying low-energy nuclear physics. Nevertheless, this is an important and active area of nuclear physics today. The approach which one must take is the following (a) a good potential must be chosen; it must reproduce the properties of the deuteron and nucleon-nucleon scattering phase shifts up to an energy comparable to the meson production threshold; (b) the many-body theory of A interacting nucleons must be solved using this interaction; (c) discrepancies between theory and experiment must be sought. If a discrepancy is found it may be related to an inadequacy in the theory which can be remedied by more careful attention to the underlying meson-baryon interaction. This is the nature of much theoretical work today. Clearly, this procedure is most likely to pay dividends first in the two- and three-body systems where the nuclear many-body physics is essentially exactly solvable. Here there is an enormous accumulation of evidence, mostly dealing with exchange current corrections, i.e., corrections to transition operators for example, in the reaction

$$n + p \rightarrow d + \gamma \tag{5}$$

which can not be explained without the assumption of intermediate mesonic and heavy baryonic states. The situation here has been recently reviewed in Ref. 4.

Low energy properties of heavy nuclei will begin to teach about meson degrees of freedom when reliable many-body theories become available. In the study of large nuclear systems, the most important theoretical problem presently is to understand the interplay between the nucleon-nucleon interaction and the bulk properties of nuclear matter. The finite size of nuclei is actually a complication, and the most popular system to study is the idealization of nuclear matte.. Used in this context, nuclear matter is an infinite, uniform system of neutrons and protons of densities ρ_n and ρ_p which interact in some prescribed way. The Coulomb interaction must of course be turned off. The properties of such a system may be deduced from experiments on ordinary nuclei. Some of these properties are shown in Table III. The central density of nuclei can be determined

4

from electron scattering; as is well-known, nuclear matter saturates, i.e., the maximum density in a nucleus is roughly the same in all heavy nuclei. The binding energy per nucleon of 15.68 MeV may be deduced from the semi-empirical mass formula,[5]

$$
\begin{aligned}
E &= (M - ZM_p - NM_n)c^2 \\
&= -15.68A + 18.56A^{2/3} + 0.717\, Z^2 A^{-1/3}\,(1 - 1.69A^{-2/3}) \\
&\quad + 28.1\,(N - Z)^2\,A^{-1}\,(1 - 1.18A^{-1/3}) \\
&\quad + \text{paring} + \text{shell effects,}
\end{aligned} \tag{6}
$$

which separates the bulk properties of the nucleus from the surface, Coulomb, shell, and pairing effects. The symmetry energy of 28.1 MeV is also shown in the table; it is repulsive which means the lowest energy state contains equal numbers of neutrons and protons. If nuclear matter is subjected to pressure the energy per particle changes, giving a curve which presumably looks like Fig. 1. The properties shown in Table III are properties at the minimum of the curve. There is an additional important parameter of this minimum, namely the curvature, related to the incompressibility K,

$$
K = k_F^2\,\frac{d^2(E/A)}{dk_F^2} \qquad \left(\frac{3}{2}\,\pi^2\rho = k_F^3\right) \tag{7}
$$

The incompressibility is related to a collective mode of the nucleus, the so-called giant monopole "breathing mode," and recently, after years of searching, this mode has been seen experimentally.[6a] One deduces the value of 210 MeV from these experiments.[6b]

TABLE III

EMPIRICAL PROPERTIES OF NUCLEAR MATTER, $\rho_n = \rho_p$

Central Density	0.17 fm^{-3}	Electron Scattering
E/A	-15.68 MeV	Semi-empirical mass formula
Symmetry energy	28.1 MeV	
Incompressibility	210±30 MeV	Breathing mode
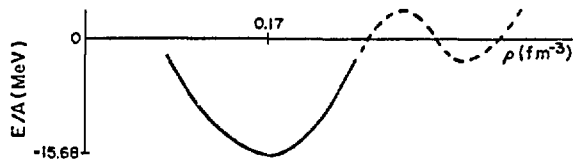
Fig. 1. Equation of state of nuclear matter, $\rho_n = \rho_p$. The equation of state at high density is not well understood and is therefore dashed.

5

There are two principal theories for studying the properties of nuclear matter: the Brueckner-Bethe method and the variational method. The Brueckner-Bethe theory has met with some successes and is presumably the best method of dealing with the properties of nuclear matter at and near normal nuclear density, but recently this position has been challenged by the proponents of the variational theory. The situation is in a state of flux today, and one may expect that before long improved methods and a deeper understanding of the interaction among nucleons embedded in a medium will emerge. I have great hopes that the resolution of the present mysteries will greatly enhance the appreciation of the role of mesonic degrees of freedom in nuclei. I will, therefore, devote several lectures to the current status of nuclear matter theory. A third approach should also be mentioned, the so-called exp S method.[7a] This method has so far been applied only to finite nuclei, but it is a powerful many-body method. I shall not discuss this in these lectures.

Beyond nuclear matter lies finite nuclei, and nuclear matter methods have been applied quite successfully to develop theories of the structure of finite nuclei in a semi-phenomenological manner.[7b] Predictions for finite nuclei would of course provide a much more stringent test of the underlying ideas than the predictions for infinite nuclear matter. This aspect of the physics will be covered by Don Sprung in his lectures. Nuclear matter methods have also been applied to determine nucleon-nucleus optical potentials,[8] with interesting results.

Another way to learn about the meson-baryon interactions is to study nuclear matter under unusual conditions. For example, neutron stars hold out the possibility for learning about nuclear matter at high density. Unfortunately, it is difficult to study the properties of neutron stars, but there is a slow accumulation of data and the emerging profile may be seen in Table IV. Heavy ion collisions also provide a means of studying nuclear matter under unusual conditions, high temperature and density. Theoretical studies of high density systems have led to the unexpected possibility of pion condensation[9] and the Lee-Wick abnormal state.[10] Some of the conjectured phases of high density nuclear matter are listed in Table V. I will have more to say about some aspects of high density matter in the last lecture.

TABLE IV
NEUTRON STARS

		System
Mass	1.3 ± 0.2 Solar Masses (⊙)	Her X-1, Vela
I	8.6×10^{44} gm-cm^2	Crab
R*	7.7 ± 2 km	Flares from variety of compact x-ray sources

*Gordon Baym, private communication.

TABLE V
PHASES OF NUCLEAR MATTER

Density (fm^{-3})	Phase	Constituents	System
$0.17 \equiv \rho_0$	liquid	neutrons, protons	isolated nuclei
$2\rho_0$	liquid	nucleons, π	neutron stars, heavy ions
$5\rho_0$	liquid (solid)	nucleons, Δ hyperons, π quark matter	neutron stars

There have been many attempts to study nuclear systems <u>directly</u> in terms of meson theory. This approach is notoriously difficult, but within the last few years there have been several moderately successful explanations of nucleon-nucleon scattering in terms of meson theory.[11,12] There have also been some attempts to describe large nuclear systems directly in terms of mesons and nucleons in the mean field approximation.[13,15] These theories have been remarkably successful in reproducing properties of nuclei and nuclear matter where the coupling constants and/or masses of the mesons are suitably adjusted. However, it is yet to be demonstrated that a meson theoretical model which reproduces the nuclear properties in the mean field approximation is also capable of reproducing nucleon-nucleon scattering. Experience with potentials has shown that the meson-nucleon couplings necessary to reproduce nucleon-nucleon scattering induce strong correlations among nucleons, which are neglected in the mean field approximation. It is my own feeling that a quantitative theory of nuclear structure would be too awkward formulated directly in terms of the meson and nucleon fields; practical considerations seem to force one to a potential theory description.

Meson factories clearly provide a rich source of information about the properties of meson degrees of freedom in nuclei. At these laboratories, energies and intensities of beams are sufficient to study in detail the production of pions and Δ resonances. As these channels open, the justification of treating the interaction between nucleons as potentials begins to break down, and the availability of this data will force theoretical descriptions which take the meson and baryon degrees of freedom more explicitly into account. Here we stand to learn an enormous amount about mesonic degrees of freedom in nuclear systems. The availability of pion beams provides the possibility of examining in detail how the pion interacts in a nuclear environment. There are a great deal of new and poorly understood effects which come into play in these experiments. These

reactions not only hold intrinsic interest, but an understanding of them will help pave the way for using pion beams as a tool to study the structure of a nuclei.

II. FEYNMAN DIAGRAMS

The most convenient language for expressing nuclear physics with mesons and nucleons is the language of Feynman diagrams. I will use this language throughout these lectures and it is therefore appropriate to review it. I don't want to derive rules because everybody here has seen this before, but rather to state the results which will be used time and again. An excellent introduction can be found in Ref. 16.

Let me begin by pointing out that a Feynman diagram is a term in the matrix element of the time-evolution operator[17] $U(t,t')$, which takes the solution of the time-dependent Schroedinger equation $|\psi(t)>$ from time t' to time t, i.e.,

$$|\psi(t)> = U(t,t') |\psi(t')> \tag{8}$$

where

$$i\hbar \frac{\partial}{\partial t} |\psi(t)> = H |\psi(t)> \tag{9}$$

We may be describing by H a particle interacting with a potential, a collection of nucleons interacting through nucleon-nucleon potentials, or a collection of nucleons emitting and absorbing mesons. In all these cases H will have a kinetic energy and interaction energy piece

$$H = T + H_I \tag{10}$$

It is convenient to express T and H_I in terms of creation and annihilation operators. A collection of nonrelativistic nucleons will have kinetic energy

$$T = \sum_{\underset{\sim}{k}} a_{\underset{\sim}{k}}^+ a_{\underset{\sim}{k}} \frac{k^2}{2m} \tag{11}$$

where a_k and a_k^+ respectively destroy and create nucleons of momentum k. The nucleon-nucleon potential is expressed as

$$H_I = \frac{1}{2} \sum_{\substack{k_1' k_2' \\ k_1 k_2}} a_{k_1'}^+ a_{k_2'}^+ < k_1' \, k_2' |V| k_1 k_2 > a_{k_2} a_{k_1} \tag{12}$$

where k's stand for a complete set of quantum numbers (momentum, spin, isospin). We may represent the matrix elements of potentials as pictures

$$\langle k'_1 k'_2 | V | k_1 k_2 \rangle = \quad\quad ; \quad\quad\quad (13)$$

potentials may be thought of as inducing a transition from state (k_1, k_2) to state (k'_1, k'_2). In a meson-nucleon system we have

$$H_I = \Sigma\, a^+_{k_1}\, a_{k_2}\, b_{k_3}\, \langle k_1 | \Lambda | k_2 k_3 \rangle \quad\quad\quad (14)$$

where now b^+ creates a meson. Here Λ may be represented as

$$\langle k_1 | \Lambda | k_2 k_3 \rangle = \quad\quad\quad\quad\quad (15)$$

Non-relativistic limits for the quantities Λ were given in Table II.

Now, the point is that the amplitude for a system to make a transition from state $|k_1, k_2 \ldots k_A\rangle$ at time t to state $|k'_1, k'_2 \ldots k'_A\rangle$ at time t', i.e.,

$$\langle k'_1, k'_2, \ldots, k'_A | U\,(t',t)\, | k_1, k_2, \ldots, k_A \rangle \quad\quad\quad (16)$$

is the coherent sum of all possible histories, where a history is illustrated in Fig. 2. Each nucleon gets its own line, with an arrow going up (the direction of flow of time) and a label to designate the single particle energy and quantum numbers. Each interaction is labeled by the time at which it occurs. This is a Feynman diagram; it represents an algebraic expression and is evaluated as follows:

    (1) each dashed line gets a matrix element of the potential, as   (17a)
         described above,

    (2) each solid line segment gets the value

$$\alpha\; = e^{-iE_\alpha \Delta t}\, \theta(t'-t) \quad\quad\quad (17b)$$

where E_α is the energy of a nucleon in state α and Δt is the time-difference at the ends of the line evaluated in the direction of the arrow. All possible diagrams consisting of A nucleon lines connected in all possible ways by potential interactions are allowed. Each distinct topology is counted once and only once. One then sums over intermediate energies and integrates over times with $(-i)$ dt. Since each propagator carries a θ-function to maintain proper time-ordering, the limit on the time-integrations is $+\infty$, $-\infty$.

The sum over all topologies gives the matrix element in Eq. (16). In addition, one must multiply by a factor $(-)^\Lambda$, where Λ is the number of exchanges necessary to bring the initial or final state to some standard order; this takes care of the antisymmetrization of the nuclear states. As long as the initial (or final) state is antisymmetrized, it is unnecessary to pay explicit attention to the Pauli principle in intermediate states.

One may easily check that diagrams which violate the exclusion principle cancel in pairs when the initial or final state is antisymmetrized. For example, suppose $k_2'' = k_4$ in Fig. 2. This term then violates the Pauli exclusion principle. To find the term which cancels it, simply "cross" the lines which carry the same label, as in Fig. 3. When the lines are straightened out it is clear that the result is a simple permutation of the initial state lines labeled k_2, k_3 and k_4; otherwise Fig. 3 has the same value as Fig. 2. Since 3 exchanges are necessary to bring the labels to standard order this diagram has a factor $- = (-)^3$ and cancels the Pauli violating piece of Fig. 3.

Essentially the same rules apply if the system consists of nucleons interacting with a meson field. (Let's not worry about anti-nucleons for now.) An example is shown in Fig. 4. In this description each meson is treated as a separate particle with a propagator of its own.

$$\frac{e^{-i\omega_k \Delta t}}{2\omega_k} \; \theta(t_2' - t_2) \tag{17c}$$

where the factor $(2\omega_k)^{-1}$ is a wave-function normalization for bosons and is convenient to include in the propagator. Now we have also to consider anti-

mesons and so each meson α also occurs with its line propagating backwards in time as well,

$$\text{[diagram]} \quad = \quad \frac{e^{-i(-\omega_k)\Delta t}}{2\omega_k} \quad \theta(t_2' - t_2) . \tag{17d}$$

Δt is still counted in the direction of the arrow, but now its energy in the propagator is $-\omega_k$: this is Feynman's interpretation of antiparticles as particles traveling backward in time with negative energy.

It is a simple exercise to show that these rules give the more usual expression for a Feynman propagator for a π meson. First note that

$$\frac{e^{-i\omega_k(t_2'-t_2)}}{2\omega_k} \; \theta(t_2'-t_2) = \frac{i}{2\omega_k} \int \frac{d\omega}{2\pi} \; \frac{e^{-i\omega(t_2'-t_2)}}{\omega - \omega_k + i\eta} \tag{18}$$

which may be verified by contour integration. Thus

$$\frac{e^{-i\omega_k(t_2'-t_2)}}{2\omega_k} \; \theta(t_2'-t_2) + \frac{e^{i\omega_k(t_2'-t_2)}}{2\omega_k} \; \theta(t_2-t_2')$$

$$= \frac{i}{2\pi} \int_{-\infty}^{\infty} d\omega \frac{e^{-i\omega(t_2'-t_2)}}{\omega^2 - q^2 - \mu^2 + i\eta} \tag{19}$$

The complete relativistic Feynman propagator for a π meson is, in more standard notation[18]

$$D_F(x) = \int \frac{d^4p}{(2\pi)^4} \; \frac{e^{ip\cdot\Delta x}}{p^2 - \mu^2 + i\eta} \tag{20}$$

where now p is a 4-momentum. In the rules described we have already integrated over the positions of the nucleons $\vec{x}$; this gave rise to the conservation of momentum delta functions which have been included explicitly in the expressions for

$$\text{[diagram]} \quad \text{and} \quad \text{[diagram]} . \tag{21}$$
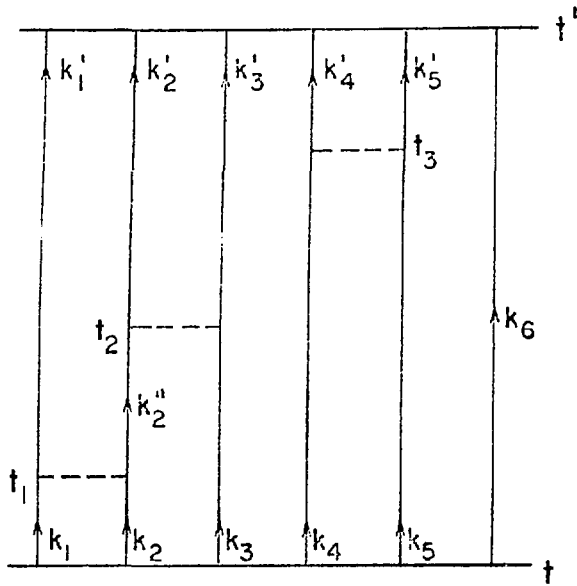
Fig. 2. A Feynman diagram for a six-particle system.
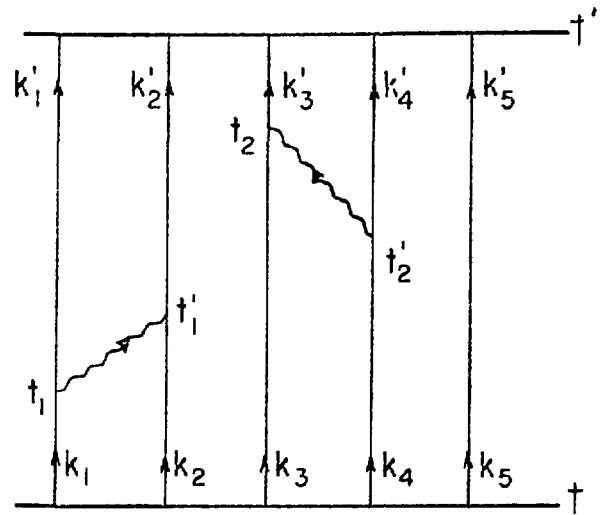
Fig. 4. Interacting mesons and nucleons.

=
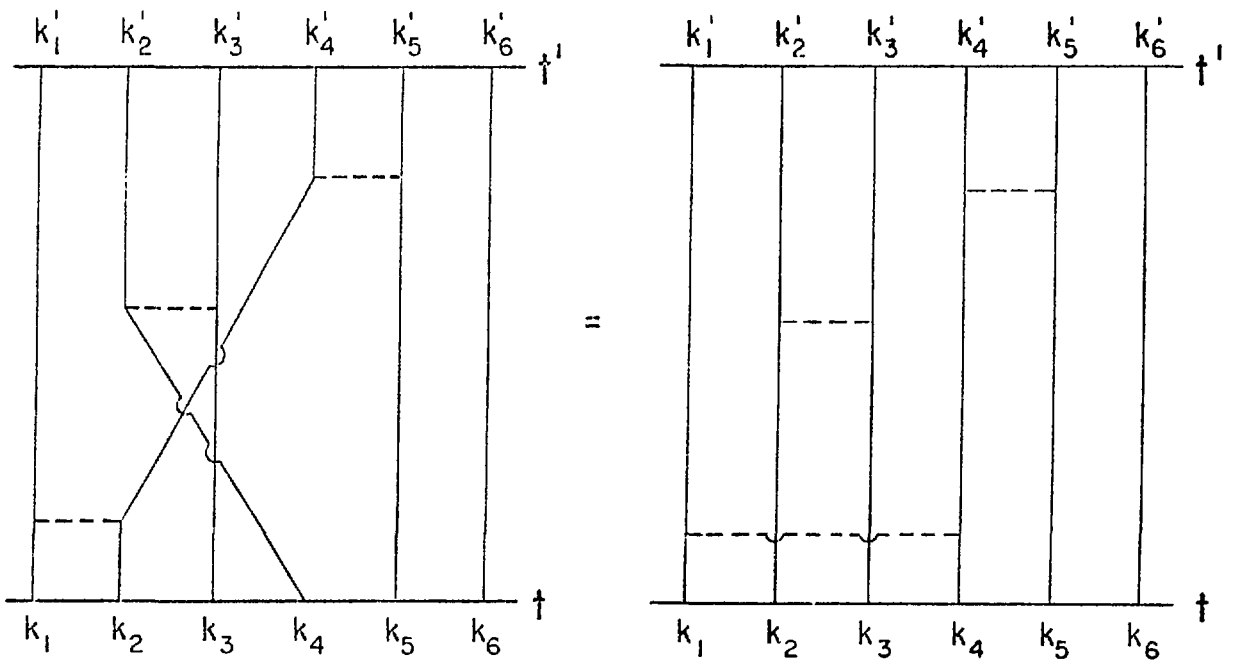
Fig. 3. Illustrating the Pauli exclusion principle for intermediate states. When $k_2'' = k_4$ in Fig. 2, the diagram shown here cancels against the diagram in Fig. 2.

12

Now a set of definite rules has been given for calculating the time-evolution operator $U(t,t')$. Of what value is this? As one example, the scattering amplitude of two particles is given by a matrix element of

$$< \phi_f(+\infty) \, | \, U(+\infty, -\infty) \, | \, \phi_i(-\infty) > \qquad (22)$$

where $|\phi(t)> = e^{-iH_ot}|k_1 \; k_2>$ is the initial and final unperturbed state of the system. Thus, scattering problems may be studied in this formulation. Also, ground state properties of nuclei and nuclear matter may be studied in terms of the time-evolution operator, as we shall see below in Chapter VI.

III. MESON THEORETICAL NUCLEON-NUCLEON INTERACTIONS

A.   What is a Potential?

As I have remarked, nuclear physics has been carried out traditionally in terms of potentials. One reason for this is that the language of potentials is very convenient for discussing nuclear systems. As I will use this language throughout these lectures, it is necessary to explain what a potential is, and to try to dispel any preconception you may have that the potential description is intrinsically incompatible with an underlying meson theory description.

A potential is an instantaneous interaction, meaning that it acts <u>at</u> a time t. In a time-independent description, this means that potentials do not depend on the total incident energy of the system. Furthermore, potentials are Hermitian operators if they are to describe elastic scattering below meson production threshold. Nonlocality is different from energy-dependence, and is acceptable for potentials; a nonlocal potential depends on both the coordinates <u>and</u> momenta of the interacting nucleons. If a potential theory is to be equivalent to a meson theory then the potential must necessarily have components of n-body character. Basic observables, such as r, p, etc., must also be modified. (Modifications of observables are often called exchange currents.)

Meson exchange interactions, on the other hand, are retarded interactions, because the mesons are exchanged over an extended interval of time. In Fig. 5 we see the meson being emitted at time t, and absorbed at a later time t_2. How can a quantity which occurs at one time possibly account for time-delayed meson exchanges? The answer is that if the mesons are emitted and absorbed over a sufficiently narrow interval of time, ΔT, then the potential may be reasonably equated to the <u>time-average over ΔT</u> of the meson exchange it is to represent.

13
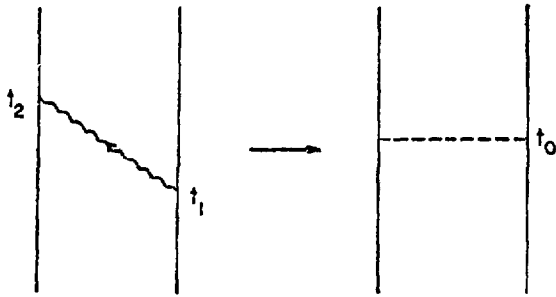
Fig. 5. Illustrating the difference between a potential and a meson exchange interaction.

If ΔT is sufficiently small, then the difference between the time-averaged interaction and the fully retarded interaction will be small and can be taken into account as a perturbation in higher order. A systematic way of replacing time-delayed interactions by instantaneous interactions was first worked out in the theory of effective interactions for bound states; it is known as the method of folded Feynman diagrams.[19]

I next want to show how the method of folded diagrams applies to the one-meson exchange contribution in the potential. The theory is worked out in detail for the two-meson exchange contribution and for corrections to other observables in Ref. 20. This application will serve two purposes. For one, it will illustrate an application of the Feynman diagram rules given in the preceeding discussion; secondly it will lay a solid foundation for the discussion of the nucleon-nucleon interaction which comes next.

Consider the meson exchanges shown in Fig. 6. The left-hand side shows a contribution to the scattering amplitude for two nucleons in a meson theory description. To sum together all the relevant contributions requires a solution of the Bethe-Salpeter equation,[21a] which is an exceedingly difficult task. The right hand side shows a contribution to the same process in a potential theory description. To sum together all relevant contributions in this theory requires a solution of the Schroedinger equation, which is, by comparison, a trivial task. When three nucleons interact, there is no known equation of which I am aware to account for the meson theory, but in potential theory there is the Faddeev approach, which is now standard. The point is that potentials are not only a convenient language for discussion, but are also of eminent practical value.

The discussion in Terms of Fig. 6 helps to motivate a definition for the contribution to the potential from the exchange of a single meson; we would like to define this contribution so that each diagram in the meson exchange description is equal to a term in the potential description, and vice versa. If such a procedure is to make sense, then it must not only be true for the entire diagram but also for the individual pieces. We thus isolate the pieces of Fig. 6 and

14

Fig. 6. A process contributing to the scattering of two nucleons, drawn in terms of meson theory and potential theory.

Fig. 7. Definition of contribution (i) to the one-meson exchange potential. The complete potential is a sum over all contributions (i). Each relative time difference t_1-t_2 is counted as a separate contribution.

equate the meson exchange and potential pieces, as in Fig. 7. To solve this equation for the potential, we have to come to grips with an ambiguity associated with when the equivalent potential is to act with respect to times t_1 and t_2. Let us leave this arbitrary for now and set

$$t_o(\lambda) \equiv \left(\frac{1+\lambda}{2}\right) t_1 + \left(\frac{1-\lambda}{2}\right) t_2 \qquad (23)$$

For example, when $\lambda=0$ the time t_o is located midway between the vertices and when $\lambda=\pm 1$ it passes through one or the other. We want now to remove the nucleon propagators from the right-hand side; what is left is the potential. To remove the nucleon propagator in the upper right-hand side, $e^{-iE_2'(t_1-t_o)}$, simply divide the right-hand side by this factor. To preserve the equality the left-hand side must also be divided by the same factor. But

$$1/e^{-iE_2'(t_1-t_o)} = e^{-iE_2'(t_o-t_1)} \qquad (24)$$

which may be represented diagrammatically as a line pointing from t_1 to t_0. All propagators may be treated in this fashion. Thus, the result of dividing out the nucleon propagators on the right-hand side may be represented diagrammatically as Fig. 8a. But this figure may be simplified, because equal length segments of lines with oppositely directed arrows and the same state labels cancel, e.g.,

15
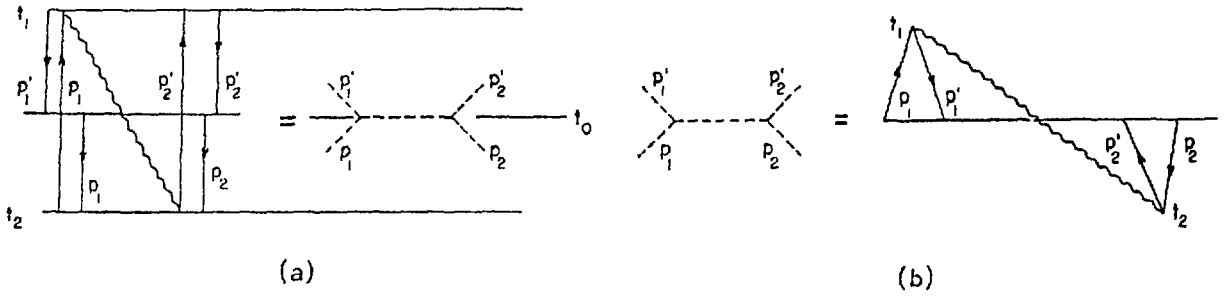
Fig. 8. The result of removing the nucleon propagators from the right-hand side of Fig. 7. When equal segments of lines are canceled as in (a) as discussed in the text, the result is (b).

$$\text{diagram} = e^{-iE_2'(t_\alpha - t_\beta)} \times e^{-iE_2'(t_\beta - t_\alpha)} = 1 \qquad (25)$$

The result is shown in Fig. 8b. This equation gives the potential corresponding to the meson exchange shown. However, for t_o (λ) given by Eq. (23), many different time extensions of duration T,

$$T \equiv t_1 - t_2 \qquad (26)$$

are possible, each of which may contribute to the potential. To get the complete potential we must sum over all contributions which means integrating over T.

Let us now evaluate Fig. 8b. For the moment we omit the contributions of the vertices. The propagators for the external legs contribute,

$$e^{-iE_1(t_1 - t_o)} \; e^{-iE_1'(t_o - t_1)} \; e^{-iE_2(t_2 - t_o)} \; e^{-iE_2'(t_o - t_2)} \qquad (27)$$

and the propagator for the meson contributes

$$\frac{i}{2\pi} \int_{-\infty}^{\infty} d\omega \; \frac{e^{-i\omega(t_1 - t_2)}}{\omega^2 - q^2 - \mu^2 + i\eta} \qquad (28)$$

Expressing the time-differences in terms of T we find

$$t_1 - t_o = (1-\lambda)T/2$$

$$t_2 - t_o = (1+\lambda)T/2 \qquad (29)$$

Furthermore, defining $\Delta E \equiv E_{out} - E_{in}$, so

$$\Delta E_1 = E_1' - E_1$$
$$\Delta E_2 = E_2' - E_2 \tag{30}$$

we find for the propagator contribution

$$\frac{i}{2\pi} \int_{-\infty}^{\infty} d\omega \; \frac{1}{\omega^2 - q^2 - \mu^2 + i\eta} \; e^{-iT[\omega - \Delta E_1(1-\lambda)/2 + \Delta E_2(1+\lambda)k]} \tag{31}$$

Now, integrating this by $-idT$ we clearly get a delta-function from

$$\int dT \; e^{-iTA} = 2\pi\delta(A) \tag{32}$$

which then permits the integral over ω to be done at once, to give

$$V \sim \frac{1}{[\Delta E_1(1-\lambda) - \Delta E_2(1+\lambda)]^2/4 - q^2 - \mu^2} \tag{33}$$

Now, we see that the potential depends explicitly on the parameter λ! What do we do? Well, the simplest thing is to average over λ, so

$$V \sim \int_{-1}^{1} d\lambda \; f(\lambda) \; \frac{1}{[\Delta E_1(1-\lambda) - \Delta E_2(1+\lambda)]^2/4 \cdot q^2 - \mu^2} \bigg/ \int_{-1}^{1} d\lambda \; f(\lambda) \tag{34}$$

How do we choose $f(\lambda)$? There is nothing to tell us how to choose $f(\lambda)$. The physics here should be clear from the way the problem was set up. The underlying interaction is time-delayed and therefore the potential, which is instantaneous, can be specified only up to an arbitrary average over the time-extension of the diagram. Clearly, we want V to be Hermitian, so in this case we merely require

$$f(\lambda) = f(-\lambda). \tag{35}$$

Different choices for $f(\lambda)$ correspond to performing a unitary transformation on the system. Although different choices of $f(\lambda)$ give quite different looking potentials in lowest order, Eq. (34), higher order terms in the expansion, which also depend on $f(\lambda)$, are needed in order to assure that the scattering phase shifts are independent of $f(\lambda)$. Likewise the corrections to observables (exchange current corrections) depend on the choice of $f(\lambda)$, and these are

17

also needed to assure the unitary equivalence of the various averaging procedures. It turns out that one choice of $f(\lambda)$ corresponds to a uniquely simple expansion in higher order; it corresponds to[20]

$$f(\lambda) = \delta(\lambda), \tag{36}$$

or

$$V \sim - \frac{1}{q^2 + \mu^2} \tag{37}$$

from Eq. (34). This is the familiar Yukawa potential which, in coordinate space leads to

$$V(r) \sim \frac{e^{-\mu r}}{r} \tag{38}$$

As a final remark, it should be pointed out that the description in terms of energy-independent potentials is not the only possible effective interaction description. Often one defines an effective energy-dependent interaction, one example of which is the Blankenbecker-Sugar method,[21b] which was applied by Partovi and Lomon.[21c] Also, methods based on dispersion theory lead to energy-dependent effective interaction. Generally, it is found that the energy-dependence is awkward for practical calculations and a transformation is applied which replaces the energy-dependence by a nonlocality. One cannot say that one approach is more fundamental than the other; the folded diagram approach is a generalization of Raleigh-Schroedinger perturbation theory.

B. One-Boson Exchange Potentials (OBEP)

1. Theory

Whether one conceives of the nucleon-nucleon interaction as being energy-dependent or energy-independent, the physical idea underlying the method of construction is that the range R of the interaction is, according to the uncertainty principle, proportional to the mass ΔM of the mesonic system exchanged.

$$R \sim \frac{\hbar c}{\Delta M} \tag{39}$$

This fact was first discussed by Wick[22] and later formalized into a systematic method of study of Taketani.[23] The longest range part of the interaction is thus expected to arise from one-pion exchange; the midrange interaction would then come from two-pion exchange, and the core from three- and more pion exchange.

In the one-boson exchange philosophy, the assumption is made that the n-pion exchanges are given predominently by the correlated piece of the n-pion exchange, i.e., the single exchange of the observed meson spectrum. In practice this philosophy has met with mixed success, because the attraction in the nucleon-nucleon potential requires a scalar isoscalar meson of mass $\approx$ 400-700 MeV (and in some cases a scalar isovector meson), the existence of which is and has been the subject of considerable debate. In the modern treatments the philosophy of nucleon-nucleon potentials improves on the one-boson exchange model in ways that I shall discuss.

Let me now develop the one-boson exchange model. This will bring together the ideas just discussed with the phenomenological aspects of the nucleon-nucleon interaction and will serve as a bridge to the more modern developments.

a. π-Meson

I want to begin with a discussion of the pion, which is the longest range and least ambiguous contribution to the nucleon-nucleon potential. The expression for the one-pion exchange potential is given diagramatically in Fig. 8b. Equation (37) gives the contribution of everything but the pion-nucleon vertices, which for the pion are (see Table II)

$$\text{(diagram)} = \langle p'k|\Lambda|p\rangle = \frac{f}{M_\pi} \langle \zeta'|\sigma|\zeta\rangle \cdot q \; \tau \cdot \phi_\pi$$

$$q = p - p' \tag{40}$$

where $|\zeta\rangle$ is a nuclear spinor, τ the nucleon isospin, ϕ the pion isospin wavefunction and k the pion momentum. The coupling constant is taken to be the renormalized value given in Table II.

Now, the complete contribution to the potential is

$$(2\pi)^3 \delta (\underline{P}'-\underline{P}) \; V_\pi(\underline{p}'-\underline{p}) = \text{(diagram)} \tag{41a}$$

$$V_\pi(\underline{p}'-\underline{p}) = \frac{f^2}{m_\pi^2} \frac{\sigma_1 \cdot q \; \sigma_2 \cdot q}{-q^2 - m_\pi^2} \sum_i \tau_1 \cdot \phi^*(i) \; \tau_2 \cdot \phi(i),$$

$$= \frac{f^2}{m_\pi^2} \frac{\sigma_1 \cdot q \; \sigma_2 \cdot q}{-q^2 - m_\pi^2} \tau_1 \cdot \tau_2 \tag{41b}$$

where $\underline{P}'$ and $\underline{P}$ are the final and initial total center-of-mass momenta and where p' and p are the final and initial relative momenta. We have used the prescription for the potential which associates the potential with the average time of emission and absorption of the corresponding meson exchange.

In order to express Eq. (41b) in terms of familiar operators write

$$\sigma_1 \cdot \underline{q} \; \sigma_2 \cdot \underline{q} = \frac{1}{3} S_{12}(q,\sigma_1,\sigma_2) + \frac{1}{3} \sigma_1 \cdot \sigma_2 q^2 \tag{42a}$$

where

$$S_{12}(q,\sigma_1,\sigma_2) \equiv 3\sigma_1 \cdot \underline{q} \; \sigma_2 \cdot \underline{q} - \sigma_1 \cdot \sigma_2 q^2 \tag{42b}$$

is the tensor operator expressed in coordinate space. Thus $V(\underline{p}'-\underline{p})$ becomes

$$V_\pi(\underline{p}'-\underline{p}) = \frac{f^2}{3m_\pi^2} \left\{ \frac{S_{12}(q,\sigma_1,\sigma_2)}{-q^2-m_\pi^2} + \frac{\sigma_1 \cdot \sigma_2 \; q^2}{-q^2-m_\pi^2} \right\} \; \tau_1 \cdot \tau_2 \tag{43}$$

To find the coordinate space potential, take the Fourier-transform of Eq. (43),

$$\delta(\underline{r}'-\underline{r})\,\delta(\underline{R}'-\underline{R})\,V_\pi(\underline{r}) = \int \frac{d^3P'}{(2\pi)^3} \int \frac{d^3p'}{(2\pi)^3} \int \frac{d^3P}{(2\pi)^3} \int \frac{d^3p}{(2\pi)^3} \; e^{-i\underline{P}'\cdot\underline{R}'} \; e^{-i\underline{p}'\cdot\underline{r}'}$$

$$\times \; (2\pi)^2 \delta(\underline{P}'-\underline{P}) V(\underline{p}'-\underline{p}) e^{i\underline{P}\cdot\underline{R}} \; e^{i\underline{p}\cdot\underline{r}} \tag{44a}$$

or

$$V_\pi(r) = \int \frac{d^3q}{(2\pi)^3} \; e^{-i\underline{q}\cdot\underline{r}} V(q) \tag{44b}$$

where $\underline{R}'$ and $\underline{R}$ are the initial and final center-of-mass variables and r and r' are the initial and final relative coordinate variables. The delta function $\delta(\underline{R}'-\underline{R})$ means simply that the center-of-mass is not changed by the interaction, and the $\delta(\underline{r}'-\underline{r})$ means that the relative variable is not changed by the interaction. The latter condition also means the potential is local, which is a consequence of V depending only on p'-p. Relativistic corrections to meson exchange potentials often depend in a more complicated way on p' and p and as a result the coordinate space potential will contain terms depending on the momentum operator $p = -i\nabla$.

To Fourier transform the second term in Eq. (43), note

$$\frac{-q^2}{q^2+M_\pi^2} = \frac{-m_\pi^2}{q^2+m_\pi^2} + 1 \tag{45}$$

and therefore

$$\int \frac{d^3q}{(2\pi)^3} e^{-i\underset{\sim}{q}\cdot\underset{\sim}{r}} \frac{q^2}{-q^2-m_\pi^2} = \delta(\underset{\sim}{r}) - m_\pi^2 \frac{e^{-m_\pi r}}{4\pi r} \tag{46}$$

The Fourier transform of the second term is given in Appendix A,

$$\int \frac{d^3q}{(2\pi)^3} \frac{e^{-i\underset{\sim}{q}\cdot\underset{\sim}{r}}}{q^2+m_\pi^2} S_{12}(\underset{\sim}{q},\sigma_1,\sigma_2) = \frac{-m_\pi^3}{4\pi} S_{12}(\underset{\sim}{r},\sigma_1,\sigma_2) \left(1 + \frac{3}{m_\pi r} + \frac{3}{m_\pi^2 r^2}\right) \frac{e^{-m_\pi r}}{m_\pi r} \tag{47a}$$

where

$$S_{12}(\underset{\sim}{r},\sigma_1,\sigma_2) = \frac{3\underset{\sim}{\sigma}_1\cdot\underset{\sim}{r}\ \underset{\sim}{\sigma}_2\cdot\underset{\sim}{r}}{r^2} - \underset{\sim}{\sigma}_1\cdot\underset{\sim}{\sigma}_2 \tag{47b}$$

Putting everything together, we find

$$V_\pi(r) = m_\pi \left(\frac{f^2}{4\pi}\right) \frac{\underset{\sim}{\tau}_1\cdot\underset{\sim}{\tau}_2}{3} \left[S_{12} \left(1 + \frac{3}{m_\pi r} + \frac{3}{m_\pi^2 r^2}\right) \frac{e^{-m_\pi r}}{m_\pi r} - \frac{\underset{\sim}{\sigma}_1\cdot\underset{\sim}{\sigma}_2}{m_\pi^3} \delta(\underset{\sim}{r}) \right.$$

$$\left. + \ \sigma_1\cdot\underset{\sim}{\sigma}_2 \frac{e^{-m_\pi r}}{m_\pi r} \right] \tag{48}$$

Equation 48 is the familiar one-pion exchange potential (OPEP). It consists of a tensor force $V_{\pi T}\ S_{12}\ \tau_1\cdot\tau_2$ and a spin-isospin dependent central force $V_{\pi c}\ \tau_1\cdot\tau_2\ \sigma_1\cdot\sigma_2$, where

$$V_{\pi T}(r) = \frac{m_\pi}{3} \left(\frac{f^2}{4\pi}\right) \left(1 + \frac{3}{m_\pi r} + \frac{3}{m_\pi^2 r^2}\right) \frac{e^{-m_\pi r}}{m_\pi r} \tag{49a}$$

and

$$V_c(r) = \frac{m_\pi}{3} \left(\frac{f^2}{4\pi}\right) [1-\delta(r)] \frac{e^{-m_\pi r}}{m_\pi r} \tag{49b}$$

Note that both pieces of the OPEP have singular behavior at the origin. This is a typical difficulty of meson mediated interactions and some mechanism is

necessary to regularize the interaction before Schroedinger's equation can be solved. Often a form factor or cutoff function is included as part of the pion-nucleon interaction; this smears out the singularities and allows a solution. However, in practice this problem may not be as bad as it seems. This is because there is a strong repulsion coming from other components in the nucleon-nucleon interaction which presumably does not allow the nucleons to come close enough together to experience the $\delta(r)$ in V_c. The second reason, which is in some sense accidental, is that the ρ-meson has a tensor interaction similar to that of the π-meson but of the opposite sign. Thus the ρ and π-meson exchange tensor forces tend to regulate each other and the difficulties are confined to very short distances.

Let me next make a few observations about the properties of the central and tensor forces. First, let me remind you that a state of two nucleons may be specified by an orbital angular momentum quantum number L (L = 0, 1, 2, . . .), a spin quantum number S (S = 0, 1) and an isospin quantum number T (T = 0, 1). Because nucleons are identical fermions the wave function must be antisymmetric upon exchange of particles. As you know, the orbital wave function behaves as $(-)^L$, and the spin and isospin wave functions as $(-)^{S+1}$ and $(-)^{T+1}$, respectively, under exchange of nucleon labels. Thus, L+S+T must be odd for a properly antisymmetrized wave function. Now, I shall leave it as an exercise to show that the operator $\sigma_1 \cdot \sigma_2 \, \tau_1 \cdot \tau_2$ has the values shown in Table VI, where the corresponding values of L even or odd are assigned according to the principle that the wave function must be antisymmetric. Thus, it is clear that the $\sigma_1 \cdot \sigma_2 \, \tau_1 \cdot \tau_2$ interaction in a given spin or isospin channel acts differently in even or odd partial waves. In the case of the neutron-neutron (or proton-proton) interaction the scattering is determined by the T = 1 component of the potential recalling

$$|NN> = |T = 1, M_T = -1>$$
$$|PP> = |T = 1, M_T = +1>$$
$$|NP> = \frac{1}{\sqrt{2}} \, (|T = 1, M_T = 0> -|T = 0, M_T = 0>) \tag{50}$$

Therefore the $\sigma_1 \cdot \sigma_2 \tau_1 \cdot \tau_2$ OPEP "exchange" interaction for two neutrons is attractive in even partial waves and repulsive in odd partial waves. Do we find a similar even-odd effect in the experimental data? The answer is yes. Consider for example, the T = 1 channel. Figure 9 shows the $^1S_0$ phase shifts (notation is

TABLE VI

	S = 0	S = 1
T = 0	9 (L = odd)	-3 (L = even)
T = 1	-3 (L = even)	1 (L = odd)
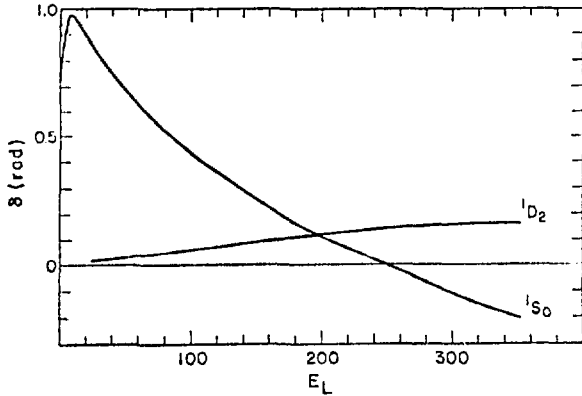
Fig. 9. Nucleon-nucleon phase shifts for the T=1 Reid potential, even L.

$2S+1 L_J$). You see that there is a strong attraction, almost giving rise to a bound state as evidenced by the phase shift approaching $\frac{\pi}{2}$ at zero energy. In Fig. 10 you see the ^3P phase shifts. These are split in J due to the tensor and spin-orbit components in the interaction. However, we may get an idea of the central interaction by averaging over J

$$\delta_{av} = \frac{1}{9} \Sigma (2J+1) \ \delta(^3P_J) \qquad (51)$$

the result of which is the dashed line. You see that there is very little net interaction in P-states. However, in the $^1D_2$ state we again find attraction, although less than in $^1S_0$. One finds an even-odd difference also in T = 0 states. This is shown in Fig. 11.

Qualitatively, at least, the spin-isospin dependence of the one pion exchange central interaction is consistent with the data; in both cases there is greater attraction in even states than odd states. Furthermore, the ^1P state shows more repulsion than the ^3P both experimentally and according to OPEP.

The tensor force has the structure of the interaction between two dipoles. In contrast to the central interaction, L is not a good quantum number. The tensor operator matrix element between states of S = 0 vanishes. For S = 1 its matrix elements are shown in Table VII. Note that for a given L the average of S_{12} over J as in Eq. (51) vanishes.

Is there evidence for a tensor force in the nucleon-nucleon interaction? It is well known that the deuteron has a quadrupole moment, and this is direct evidence for the tensor force. But the existence for a tensor force can also be seen by looking at the P-wave phase shifts. According to Table VII the matrix elements of S_{12} in $^3P_0$, $^3P_1$ and $^3P_2$ states are respectively -4, 2 and -2/5. The $^3P_1$ state has the least attraction experimentally, as it would if tensor force

Fig. 10. Nucleon-nucleon phase shifts
for the T=1 Reid potential,
odd L.
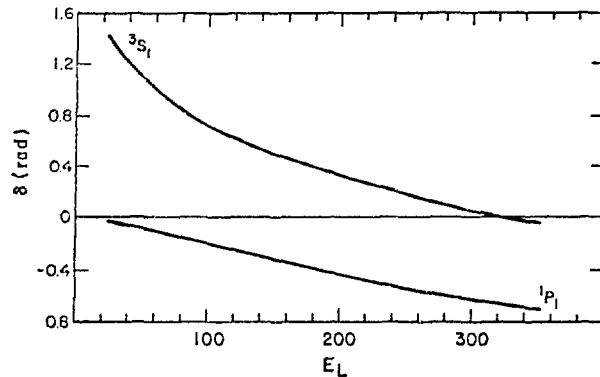
Fig. 11. Nucleon-nucleon phase shifts
for the T=0 Reid potential.

TABLE VII

MATRIX ELEMENTS OF THE TENSOR OPERATOR
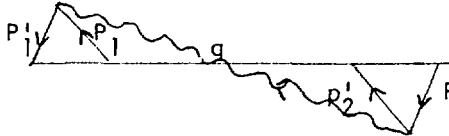
L	L'	$<JL|S_{12}|JL'>$
J-1	J-1	$-2L/(2L+3)$
J	J	2
J+1	J+1	$-2(L+1)/(2L-1)$
J-1	J+1	$6\sqrt{(L+1)(L+2)}/(2L+3)$

components were present. At low ener-
gy the $^3P_0$ is more attractive than the
$^3P_2$, as it should be also with the ten-
sor force.

So far, I haven't discussed hard
evidence for the one-pion exchange po-
tential. The one-pion exchange poten-
tial is now routinely used to constrain
phase shift analyses of the data; OPEP
is assumed generally for $L \geq L_{max} = 6$.
When $f^2_{\pi NN}$ is searched on as a variable
parameter, it assumes the value determined from pion nucleon scattering, and the
phase shifts approach the one-pion exchange contribution as L approaches L_{max}
from below. This is strong evidence for the correctness of the pionic contribu-
tion in the nucleon-nucleon potential. Furthermore, as discussed in the book by
Brink[24] the quadrupole moment of the deuteron is determined almost completely by
the one-pion exchange potential and is nearly independent of the interaction at
short distances.

b. The Vector Mesons, ρ and ω

The main difference between the ρ and ω mesons is that the ρ-meson is
an isovector meson and the ω isoscalar. The isospin comes in just as in the case
of the pion, i.e., $\tau_1 \cdot \tau_2$ for the isovector, 1 for the isoscalar. Ignoring iso-
spin, we have the following expression for the potential of a vector meson

$$\text{[diagram]} = (2\pi)^3 \delta(\underset{\sim}{P'}-\underset{\sim}{P}) V_v(\underset{\sim}{p'},\underset{\sim}{p}) \tag{52a}$$

$$V_v(\underset{\sim}{p'},\underset{\sim}{p}) = \frac{-1}{q^2+m_v^2} \sum_j \left(\frac{g}{m_v}\underset{\sim}{q} - \frac{f}{m_v}\underset{\sim}{q}\times\underset{\sim}{\sigma}_1\right)\cdot\underset{\sim}{\varepsilon}(j)\left(\frac{g}{m_v}\underset{\sim}{q} - \frac{f}{m_v}\underset{\sim}{q}\times\underset{\sim}{\sigma}_2\right)\cdot\underset{\sim}{\varepsilon}(j)$$

$$= \frac{-1}{q^2+m_v^2}\left(\frac{g}{m_v}\underset{\sim}{q} - \frac{f}{m_v}\underset{\sim}{q}\times\underset{\sim}{\sigma}_1\right)\cdot\left(\frac{g}{m_v} - \frac{f}{m_v}\underset{\sim}{q}\times\underset{\sim}{\sigma}_2\right)$$

$$= \frac{-q^2}{q^2 m_v^2}\left[\left(\frac{g}{m_v}\right)^2 + \left(\frac{f}{m_v}\right)^2\sigma_1\cdot\sigma_2\right] + \frac{1}{q^2+m_v^2}\left(\frac{f}{m_v}\right)^2 \underset{\sim}{\sigma}_1\cdot\underset{\sim}{q}\,\underset{\sim}{\sigma}_2\cdot\underset{\sim}{q} \tag{52b}$$

where $\underset{\sim}{\varepsilon}$ is the polarization of the vector meson. The second term of the last line in Eq. (52b) has the same form as OPEP, Eq. (41b), and it is therefore easily written down in coordinate space. The first term of the last line in Eq. (52b) may be Fourier transformed with the help of Eq. (46). Thus, the coordinate space interaction for the vector meson is

$$V_v(r) = m_v\frac{g^2}{4\pi}\left[\frac{-\delta(\underset{\sim}{r})}{m_v^3} + \frac{e^{-m_v r}}{m_v r}\right] - \left(\frac{f^2}{4\pi}\right)\frac{m_v}{3}\left[S_{12}\left(1+\frac{3}{m_v r}+\frac{3}{m_v^2 r^2}\right)\frac{e^{-m_v r}}{m_v r}\right.$$

$$\left. + \frac{2}{3}\frac{\underset{\sim}{\sigma}_1\cdot\underset{\sim}{\sigma}_2}{m_v^3}\delta(\underset{\sim}{r}) - \frac{2}{3}\underset{\sim}{\sigma}_1\cdot\underset{\sim}{\sigma}_2\frac{e^{-m_v r}}{m_v r}\right] \tag{53}$$

As in the case of the π meson, the delta functions must be either smeared out by form factors or dropped. Kisslinger[25] has recently argued that the delta functions cannot be dropped for the case of vector mesons.

In the case of the ω meson $f_\omega \approx 0$ and g_ω is large according to Table II. The omega exchange potential is therefore

$$V_\omega(r) \approx {}_\omega\left(\frac{g_\omega^2}{4\pi}\right)\frac{e^{-m_\omega r}}{m_\omega r} \tag{54}$$

Is there any evidence for a term of this form in the nucleon-nucleon potential? It is clear from the experimental phase shifts (Figs. 9 and 11) that the phase shifts change from attractive to repulsive at $E_L \approx 250\text{-}350$ MeV. This has been

taken to be evidence of a strong repulsive component in the nucleon-nucleon inter-
action, and the ω-meson is the most likely candidate for the effect.

The ρ meson is isovector, and f>g. The potential corresponding to this meson
is therefore

$$V_\rho(r) = m_\rho \left(\frac{g_\rho^2}{4\pi}\right) \tau_1 \cdot \tau_2 \frac{e^{-m_\rho r}}{m_\rho r} + \frac{2}{3} \frac{m_\rho}{3} \left(\frac{f_\rho^2}{4\pi}\right) \sigma_1 \cdot \sigma_2 \, \tau_1 \cdot \tau_2 \frac{e^{-m_\rho r}}{m_\rho r}$$
$$- \frac{m_\rho}{3} \left(\frac{f_\rho^2}{4\pi}\right) S_{12} \left(1 + \frac{3}{m_\rho r} + \frac{3}{m_\rho^2 r^2}\right) \frac{e^{-m_\rho r}}{m_\rho r} \tag{55}$$

Note that the sign of the central, spin-isospin dependent potential is the same
as that of the pion. However, the central force also consists of a purely iso-
spin-dependent contribution now. Referring to Table VI, we see that this term is
attractive for T=0 and repulsive for T=1. Note that the tensor force has the
opposite sign from the case of the π meson; this is the source of cancellation
between π and ρ tensor forces of which I spoke in the discussion of OPEP.

So far we have considered only one piece of the interaction due to vector
mesons. A more careful treatment of the non-relativistic reduction of the vector
meson coupling shows that in addition to the potentials discussed above there is
also a strong, short-ranged spin-orbit interaction[26]

$$V_{LS} \sim \underset{\sim}{L} \cdot \underset{\sim}{S} \frac{1}{m_v^2 r} \frac{d}{dr} \frac{e^{-m_v r}}{r} \tag{56a}$$

What is the evidence for vector mesons in the nucleon-nucleon interaction?
Evidence for the ω meson has been discussed already. Perhaps the strongest argu-
ment is the fact that a strong spin-orbit component is necessary to explain
the experimental phase shifts. First note that the L·S matrix elements have the
value

$$2 \langle JLS | \underset{\sim}{L} \cdot \underset{\sim}{S} | JLS \rangle = J(J+1) - L(L+1) - S(S+1) \tag{56b}$$

Thus, for a given L and S the splitting is in ascending (or descending) order in
J. Looking once more at Fig. 10 we see that the phases are tending to line up
in this order, with $^3P_2$ being the most repulsive. The fact that the $^3P_0$ and $^3P_1$
are reversed from what one expects from a pure spin-orbit force presumably means
that there is a tensor force competing with the spin-orbit force. In order to

26

explain this the ω meson contribution is needed, with a large coupling constant. It is an interesting historical fact that the necessity of a strong, short-range spin-orbit force was taken to be strong evidence for the existence of a neutral vector meson of about the correct mass before one was actually produced in a high energy experiment.[26]

c. Scalar Mesons

So far we have accounted for every major feature of the nucleon-nucleon interaction except for the attraction evident in the ^1S and ^3S phase shifts in Figs. 9 and 11. Scalar mesons are capable of providing a central, attractive interaction,

$$- \frac{g^2}{4\pi} \frac{e^{-m_s r}}{r} \tag{57}$$

This result follows immediately following arguments given already, noting that the coupling of a scalar meson to a nucleon is simply g in the non-relativisitc limit. Tables of particle properties list several scalar mesons as established resonances (Table XI).

d. Summary

A more complete derivation of OBE potentials including corrections to order $\frac{p^2}{m^2}$ has been made elsewhere.[27a] Table VIII summarizes the interaction Lagrangian and resulting OBE potentials. Note that the coupling constants required here are defined differently from those in Table II.

2. Results, OBEP

I have discussed the one-boson exchange potentials and given qualitative evidence for the existence of many of the effects they produce. There have been several attempts to fit these models to phase shift analyses of nucleon-nucleon scattering data, and I would now like to summarize these results.

The OBE models always include the well-established mesons π, η, ρ, and ω. The masses of these mesons are held fixed, and their coupling constants are regarded as free parameters. In addition to these mesons, two or three scalar mesons are included; the properties of these mesons are not well established, and the masses and coupling constants of these are almost always varied. The OBE models generally give surprisingly good fits of the phase shifts, but not perfect fits. Fits are usually made to $\delta(LSJ)$ for $J \leq 4$.

TABLE VIII

LAGRANGIAN AND CORRESPONDING OBEP

Meson	$\frac{INT}{\sqrt{4\pi}} = g\dots$
Pseudoscalar (PS)	$\sqrt{4\pi}\ g\bar{\psi}\gamma_5\psi\phi^{(PS)}$
Vector (V)	$\sqrt{4\pi}\ \bar{\psi}\left[g\gamma^\mu\phi_\mu^{(V)} + f/2M\ \sigma^{\mu\nu}\partial_\mu\phi_\nu^{(V)}\right]$
Scalar (S)	$\sqrt{4\pi}\ g\bar{\psi}\psi\phi^{(S)}$

(a) interaction Lagrangian

Meson	Central	Velocity Dep.	Tensor	Spin-Orbit
PS	$\frac{g^2}{12}\sigma_1\cdot\sigma_2$	---	$\frac{g^2}{12}$	---
V	$\frac{1}{2}(g^2+fg)+\frac{1}{6}(f+g)^2\sigma_1\cdot\sigma_2$	g^2	$-\frac{(f+g)^2}{12}$	$\frac{(3g^2+4fg)}{2}$
S	$\frac{1}{4}g^2$	g^2	---	$\frac{g^2}{2}$

(b) Composition of OBE

Potential	
Central	$\left(\frac{m}{M}\right)^2\left[\frac{e^{-mr}}{r} - \frac{4\pi\delta(r)}{m^2}\right]$
Velocity-Dep.	$\frac{e^{-mr}}{r} - \frac{1}{2M^2}\left(\nabla^2\frac{e^{-mr}}{r} + \frac{e^{-mr}}{r}\nabla^2\right)$
Tensor	$\left(\frac{m}{M}\right)^2\left(\frac{1}{m^2 r^2} + \frac{1}{mr} + \frac{1}{3}\right)\frac{e^{-mr}}{r}$
Spin-Orbit	$\frac{1}{M^2}\frac{1}{r}\frac{d}{dr}\frac{e^{-mr}}{r}$

TABLE IX

PSEUDOSCALAR AND VECTOR MESONS, OBE FITS

Meson	m(MeV)	PL[21]	UG[27b]	SRG[27c]	BS[27a]	URG[27d]
π	137.3	14.4	14.0	14.6	12.6	13.94
η	549	1.0	2.7	3.6	2.6	6.49
ρ,g²	765	0.53	0.78	1.20	1.81	0.357*
ρ,f²	765	7.09	17.5	32.0	2.3	20.02*
ω,g²	783	6.36	8.02	21.5	17.3	11.86
ω,fg	783	-0.38	0	0	0	0

*Distributed mass.

The masses and coupling constants of the π, η, ρ and ω are shown in Table IX. The column headed Partovi[21] gives the values of the couplings deduced from theoretical and experimental partical physics. The coupling constants are those which appear in the interaction Lagrangian in Table VIII. How reasonable are these results? The coupling constant for the pion comes out very close to the expected value. The η coupling constant is not well established and is not far from the guess based on SU(3). The coupling constant for the ρ meson was, until recently, considered as rather well-determined from experiment to be the values listed under the Partovi column. However, a recent analysis by Höhler and Pietarinen[28] give a slightly smaller vector coupling ($g^2 = 0.55$) and substantially larger tensor coupling ($f^2 = 24$). The ω coupling is not well established from particle physics; one characteristic feature of most potentials which fit the nucleon-nucleon phase shifts is that the repulsive core of the nucleon-nucleon interaction is stronger than can be explained by ω-meson exchange alone, with the value of g^2 which is determined by particle physics estimates. As Bethe points out in his review article,[34] the actual ω coupling constant obtained from OBE analysis is several times larger than the one shown, because of the way form factors are used to remove the singular behavior at small r. Results of various groups differ because different assumptions were made regarding the scalar mesons.

The masses and coupling constants of the scalar mesons are shown in Table X. Shown for purposes of comparison are the scalar mesons which appear in the table

TABLE X

SCALAR MESONS, OBE FITS

Isospin	BS[27a]	m(MeV)	g^2	UG[27b]	m(MeV)	g^2	SRG[27c]	m(MeV)	g^2	Γ(MeV)	URG[27d]	m(MeV)	g^2
1	σ_1	600	1.65	π_v	1016	4.11	δ	963	4.70	---	δ	963	2.51
0	σ_0	550	8.19	σ_c	416	1.19	ε	782	45.0	>300	$\pi\pi$	*	10.88
0	---	---	---	η_v	1070	4.44	---	---	---	---	---	---	---

*Distributed mass.

of particle properties.[29] The important point to notice is that there is not a very good correspondence. The BS and UG models show rather convincingly that the range of attraction in the nucleon-nucleon potential is longer than can be explained by the simple scalar meson exchange. The SRG model was an attempt to make more realistic choices of scalar meson masses and to incorporate the broad width of the ε meson. In order to get a fit, the ε needs an enormous coupling constant, but at the same time the ω-coupling constant takes on an enormous value; this seems to be an unsatisfactory situation. In Ref. 27d the model of Ref. 27c was improved by taking the interaction in the $\pi\pi$ $\ell = 0$ isoscalar channel directly from the experimental $\pi\pi$ s-wave phase shifts rather than matching just a mass and width in the vicinity of the ε meson. (A similar fit was made in Ref. 27d in the case of the $\pi\pi$ $\ell = 1$ isovector ρ-meson channel.) The theory seems to improve in the sense that the ω-meson coupling constant assumes a more reasonable value, but it is still too large in comparison to particle physics determinations. The model of Ref. 27d goes beyond the original OBE hypothesis and resembles more closely the philosophy embodied in the more modern approaches discussed below.

In summary, the OBE potentials are surprisingly successful in reproducing the qualitative behavior of the nucleon-nucleon phase shifts, but the quantitative results continue to have puzzling aspects. Unanswered questions concerning the source of the large central repulsion and attraction remain.

TABLE XI

SCALAR MESONS, PARTICLE PHYSICS

Meson	m(MeV)	Γ(MeV)	Isospin
δ	980	50±10	1
S^*	980	40±10	0
ε	1300	200-400	0

C. Semi-Phenomenological Nucleon-Nucleon Potentials

Although the one-boson exchange potentials fit the experimental nucleon-nucleon phase shift data well, the fits are not perfect. For purposes of doing nuclear calculations, better fits are required and a variety of purely phenomenological potentials have been constructed to fulfill the need. The potentials generally differ in some particular feature, i.e., some have infinite "hard" cores at a radius $\approx$ 0.4-0.5 fm (examples are the Hamada-Johnson[30] and Reid[31] hard core potentials) whereas others have soft cores, e.g., cores with Yukawa radial form (the Reid soft core). Other potentials emphasize velocity-dependence, such as that of Tabakin[32] and Rouben, Riihimäki and Zipse.[33] Bethe[34] discusses the various potentials in more detail.

It should be clear from the above remarks that potentials are not uniquely determined from the experimental data. One reason for this is that the nucleon-nucleon phase shifts are known only over a limited energy region and hence the potentials are guaranteed to fit the data only at low energy. There is presumably considerable ambiguity, particularly in the repulsive core region ($r \lesssim 0.5$fm), arising from the absence of these data. Even if the data did exist, it is not clear how one would construct a potential from it due to the existence of meson production channels, which begin to become important above $E_L \approx 400$ MeV.

However, there is another more fundamental ambiguity associated with the potentials, as emphasized by Coester.[35] He shows how to generate an entire class of potentials from a given one by performing a unitary transformation which, in coordinate space, only affects the potential for $r \leq$ potential range. Unitary transformations applied to the two-nucleon potential will not change the phase shifts, but the different two-body potentials will in general give different properties for many-nucleon systems. For this reason it is not a completely trivial problem to construct a potential which simultaneously reproduces the nucleon-nucleon phase shifts below meson production threshold and also serves as a suitable basis for nuclear structure physics. So far nobody has succeeded in finding a purely two-body interaction which succeeds in both problems.

Let me end the discussion of phenomenological potentials with a description of Reid's soft core potential. He takes the potential to be different in each state of given L, S, and J

$$v(LSJ,r) = \Sigma a_n \frac{e^{-n\mu r}}{r} \tag{58}$$

where μ is the reciprocal compton wave length of the pion and a_n are empirical constants, determined so as to fit the phase shifts. Only a_1 is fixed a priori; it is taken from the one-pion exchange potential, Eq. (48). For the tensor force Reid assumes a form

$$v_T(r) = -3.4876 \left[\frac{e^{-\mu r}}{r} \left(\frac{3}{\mu^2 r^2} + \frac{3}{\mu r} + 1 \right) - e^{-k\mu r} \left(\frac{3}{\mu^2 r^2} + \frac{3k}{\mu r} \right) \right] S_{12} \tau_1 \cdot \tau_2 \tag{59}$$
$$+ \sum_{n=2}^{\infty} b_n \frac{e^{-n\mu r}}{r}$$

The counter term with $k\mu r$ ensures that the tensor force diverges only as $\frac{1}{r}$ for small r. The _form_ chosen is clearly motivated by meson theory, but Reid made no attempt to choose the coefficients for different LSJ to be consistent with meson theory, except in the case of the pion.

Reid's potential fits the phase shifts of Arndt and MacGregor[36] generally within experimental error, except for the coupling between ^3S and $^3D_1$, which is very poorly known. Reid also gets the correct binding energy and quadrupole moment for the deuteron. It is interesting to note that the repulsion in the $^1S_0$ state is

$$6484 \text{ (MeV)} \frac{e^{-7\mu_\pi r}}{\mu_\pi r} \tag{60}$$

corresponding to an effective mass and coupling constant

$$m_\omega = 976 \text{ MeV} \qquad g_\omega^2 = 47 \tag{61}$$

The large value for g_ω^2 is yet another example of the difficulty of interpreting the repulsion as coming entirely from real ω-meson exchange.

D. Modern Models of Attraction in Nucleon-Nucleon Interaction

The phenomenological models show that the range of the intermediate attraction is ≈ 0.7-1.0 fm, suggesting that the attraction is associated with the exchange of two pions. There are numerous aspects of the physics of two-pion exchange, and next I want to consider several models which emphasize different aspects of this process.

1. Model of Partovi and Lomon[21]

Partovi and Lomon revived a model which was earlier investigated by many others. The idea is that the attraction comes from the simplest two-pion exchange mechanism, i.e., the perturbation correction of order g^4. The terms in this order are shown in Fig. 12. The method they used to convert these to potentials was the Blankenbecker-Sugar[21b] method, but the method of folded diagrams[20] provides a more systematic method of eliminating the energy-dependence than that employed by Partovi and Lomon.[21] In converting the terms of Fig. 12 to potentials, one must keep in mind that some piece of Fig. 12a is included already in an iteration of the one-meson exchange potential, and it is actually the difference between Fig. 12a and the iterated potential which should be considered. The method of folded diagrams shows that this difference may be represented as a diagram, evaluated according to the usual Feynman diagram rules.

Partovi and Lomon thus constructed their potential from exchanges of π, η, ρ and ω mesons and the two-pion exchange of Fig. 12. No scalar mesons were included. They showed that their final result closely resembles the radial dependence of Hamada-Johnston hard core phenomenological potential for $r \gtrsim 0.6$ fm. However, as Bethe[34] has pointed out, the Partovi and Lomon potential compares favorably to the Reid potential only for $r \gtrsim 1.3$ fm; at smaller distances there is too little repulsion. This is yet another example of meson theoretical potentials predicting less repulsion than that required by experimental nucleon-nucleon scattering.

The work of Partovi and Lomon is subject to criticism on the point of the nucleon-anti-nucleon pair terms (Fig. 12c, d). It is well known in π-nucleon scattering that these terms, evaluated with the NN Lagrangian given in Table VIIIa, give anomalously large S-wave scattering and therefore that some other effect is also present which cancels the pair terms. The scalar mesons are presumably these agents. In two later papers F. Partovi and Lomon[37] and later Lomon[38] investigated the corrections to the original H. Partovi and Lomon potential coming from the scalar meson, taking into account the width through disassociation into π-π intermediate states. In Ref. 38 it was shown that this effect resulted in a worsening of the comparison of the new potential to the Hamada-Johnston result. As might be expected, there resulted an excessive attraction in S-waves.

2. Isobars in the Nucleon-Nucleon Interaction

Before continuing the discussion on the nucleon-nucleon interaction, it is necessary to say a few words about isobars. These objects, although discovered more than twenty years ago, have only recently begun to play a prominent role in theoretical explanations of nuclear phenomena.

The isobars are excited states of nucleons which are prominent as bumps in π-nucleon total cross sections. Figure 13 shows the total cross section from $E_{cm} = 0.9$ to $E_{cm} = 2.5$ GeV. The most prominent is resonance of mass $M = 1232-57$ MeV (i.e., width of 115 MeV), called the Δ_{33} resonance. The designation 33 means 2T, 2J so the spin and isospin are each 3/2. Table XII lists the low mass non-strange isobars and their quantum numbers.[29] The numbers in parentheses are the masses of the resonances in MeV, and the angular momentum L is the πN partial wave in which the resonance is seen. The notation for a partial wave is $L_{2T,2J}$ so that the π-nucleon partial wave containing the Δ_{33} resonance is the P_{33} wave.

The behavior of the P_{33} partial wave for energies up to the position of the Δ_{33} resonance was first successfully described by the theory of Chew and Low.[39] They assumed that the interaction between a pion and a fixed, or infinitely heavy nucleon could be described by the Hamiltonian

$$H = a_k^+ a_k \omega_k + \Sigma V_k^{(0)} a_k + V_k^{(0)+} a_k^+, \quad V_k^{(0)} = if_{(r)}^{(0)} (\underset{\sim}{\sigma} \cdot \underset{\sim}{k}/\sqrt{2\omega_k}) \tau_k v(k) \tag{62}$$

where a_k is an annihilation operator for a meson, $\omega_k = \sqrt{k^2+m^2}$ is the pion energy, and where the interaction $V_k^{(0)}$ is the same as the interaction shown in Table II. The form factor $v(k)$ is the Fourier transform of the matter distribution of the nucleon which couples to the pion; it is generally believed that the rms radius of this distribution is comparable to or smaller than the radius of the charge distribution of a nucleon $r_{rms}^{ch} \simeq 0.8$ fm.

Chew and Low attempted to solve this theory for the P-wave pion-nucleon phase shifts. They found that the theory naturally predicted a resonance in the 3-3 state, whose position could be adjusted to coincide with the experimental result by picking the range of the form factor appropriately. The form factor was

$$v^2(p) = e^{-p^2/49} \tag{63}$$
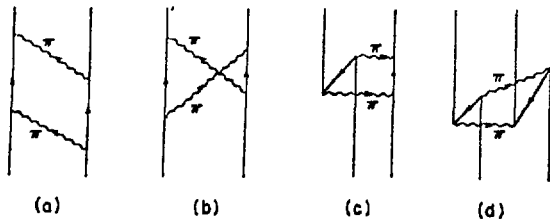
Fig. 12. Various possibilities for two mesons exchanged between two nucleons. The lines running backward in time in (c) and (d) are anti-nucleons.
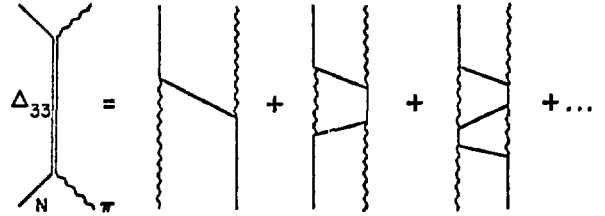
Fig. 14. The Chew-Low interpretation of the Δ_{33} as a resonance in the π-nucleon system.

TABLE XII

THE LOW MASS NON-STRANGE ISOBARS

Particle	I	J^P	L
$\Delta(1232)$	3/2	$3/2^+$	P
$\Delta(1650)$	3/2	$1/2^-$	S
$\Delta(1670)$	3/2	$3/2^-$	D
$N'(1470)$	1/2	$1/2^+$	P
$N'(1520)$	1/2	$3/2^-$	D
$N'(1535)$	1/2	$1/2^-$	S
$N'(1670)$	1/2	$5/2^-$	D
$N'(1688)$	1/2	$5/2^+$	F
$N'(1700)$	1/2	$1/2^-$	S
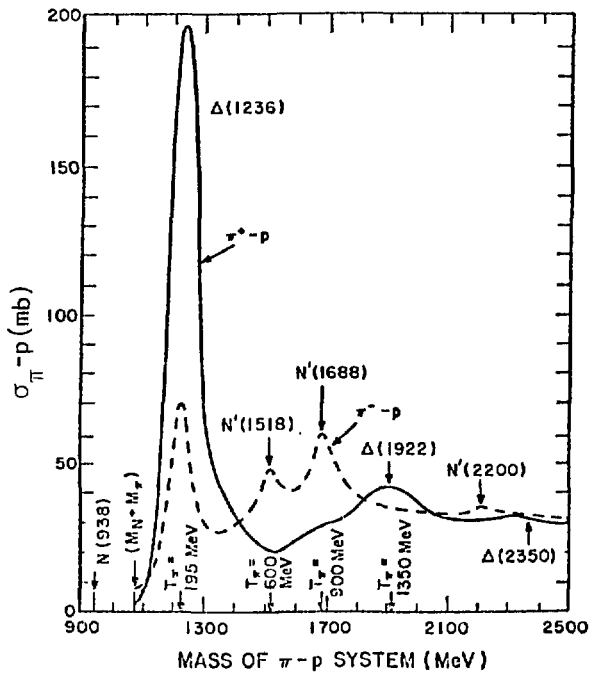
Fig. 13. Total cross sections for $\pi^+ p$ and $\pi^- p$ scattering.

However, the theory did not predict the phase shift accurately above resonance. Dave Ernst and M. Johnson[40] have recently shown that if the inelastic (multi-meson production) channels are taken into account, the Chew-Low theory reproduces accurately the phase shifts up to $p_{lab} = 1.2$ GeV/c with

$$v^2(p) = e^{-p^2/15} \tag{64}$$

The Chew-Low theory gives a diagrammatic interpretation of the Δ_{33} resonance, shown in Fig. 14; the main point here is that when a pion scatters from a nucleon the interaction is sufficiently strong that the pion will rescatter as much as it can; at and below resonance the most important intermediate states are those shown in Fig. 14. Because of this it is often said that the source of the attraction is nucleon exchange. Even at threshold, the rescattering accounts for half of the π-nucleon P_{33} scattering volume. These observations about the 3-3 resonance have led to the feeling that the resonance should play an important role in many aspects of low energy nuclear physics, even as a virtual state, and in most aspects of intermediate energy physics when energies are close to the energy required to excite the resonance. Part of my goal in the next lecture is to review some of the theoretical ideas surrounding the subject of Δ's in nuclei and some of the experiments that support these ideas. First, however, let me return to the subject being discussed, isobars in the nucleon-nucleon interaction.

Sugawara and Von Hipple[41] (SH) and later Riska and Brown[42] (RB) showed that intermediate Δ resonances deserve consideration as a possible source of the inter-mediate range attraction in the nucleon-nucleon interaction. Various possibilities contributing to the two pion exchange potential are shown in Fig. 15. In the calculations of Ref. 41 the processes in Figs. 15c and 15d were regarded as small corrections and neglected. The calculation was simplified by constructing a transition potential, defined in such a way so that certain time-orderings of Figs. 15a and b are reproduced for zero incident energy of the two nucleons. Figure 16 shows what the transition potentials look like graphically. When these authors evaluated the potential they assumed that terms of order $(M_\Delta - m)/(M_\Delta + m)$ could be neglected. When evaluating Figs. 15a and b, the intermediate Δ is assumed to behave like an elementary particle of mass M_Δ. No width was assumed for the Δ because Sugawara and Von Hipple were interested only in scattering below threshold for meson production. Both SH and RB made a closure approximation when

evaluating their respective theories of Fig. 15, i.e., they replaced certain intermediate state energies by averages.

It should now be clear that the contribution of Figs. 15a and b are attractive for energies less than threshold for producing real Δ or π, as these are second order processes and it is well known that such corrections are attractive. Incidentally, one advantage of having the transition potentials is that one can solve Schroedinger's equation, regarded now as determining a wave function

$$|\psi\rangle = |\psi_{NN}\rangle + |\psi_{n\Delta}\rangle + |\psi_{\Delta\Delta}\rangle \tag{65}$$

Such an equation was written down by Sugawara and Von Hipple. Since the writing of their paper, such procedures have become popular, and now is an appropriate time to examine the structure of this wave function in some detail.

Note that the $N\Delta$ and $\Delta\Delta$ states must be antisymmetric under interchange of particles.[43] The reason is that the nucleon-nucleon state is antisymmetric (Pauli principle) and because the interaction which induces $NN \to N\Delta$ or $NN \to \Delta\Delta$ is symmetric. This theorem may seem surprising at first, because nucleons and Δ are distinguishable particles. As we stated earlier, the symmetry of the two-particle wave function is

$$(-)^{L+S+T} \tag{66}$$

Now, $(-)^L$ must be the same for the NN and $N\Delta$ ($\Delta\Delta$) intermediate state because parity is preserved. T must be the same for both the initial and intermediate state, because isospin is conserved in the strong interactions (presumably!). Thus, by the theorem stated above $(-)^S$ must be the same for the NN and $N\Delta$ ($\Delta\Delta$) intermediate state. These considerations permit us to see how the most general transition potentials can couple states. The results for $NN \to N\Delta$ are shown in Table XIII, and for $NN \to \Delta\Delta$ in Table XIV. One point to be made here is that for a given value of J the isobar configurations can mix in many different orbital angular momentum states. The extent of mixing for a particular state depends of course on the details of the force, but the transition potentials have a strong tensorial character leading to appreciable mixtures of configurations with large ΔL. The case of $^1S_0$ (NN) is especially simple because there is only one $N\Delta$ and one $\Delta\Delta$ state to which it couples. Note that the deuteron ($^3S_1 - ^3D_1$) is complicated; not only is there no $N\Delta$ component but the $\Delta\Delta$ component may have L=2 or

(a)   (b)

(c)   (d)
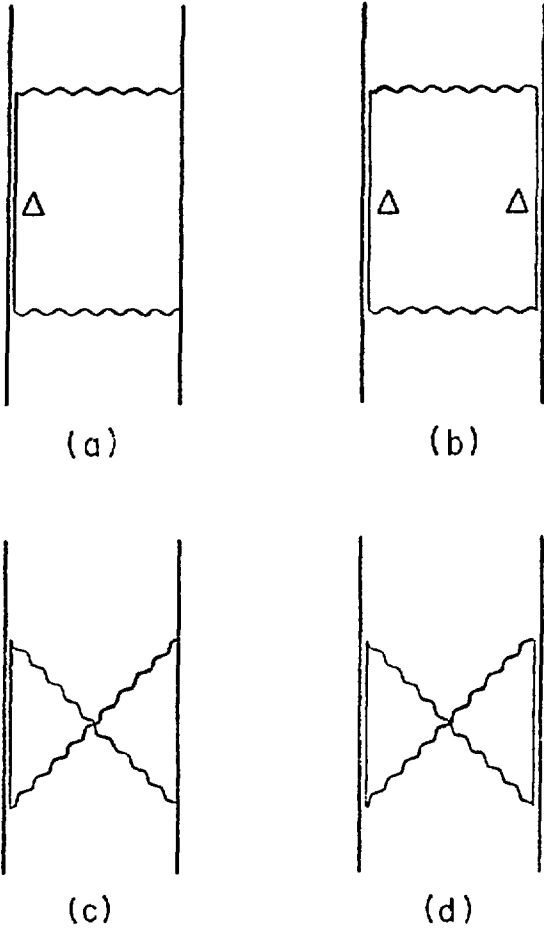
Fig. 15. Various ways that the Δ_{33} resonance may contribute to the two-pion exchange interaction.

(a)   (b)   (c)   (d)

(e)   (f)
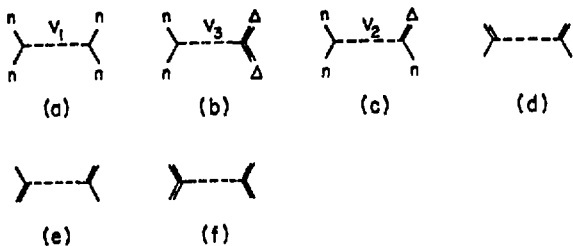
Fig. 16. Graphical representation of transition potentials.

TABLE XIII

NΔ STATES WHICH COUPLE TO GIVEN NN STATE

NN State (T=1 only)			NΔ States Which Couple		
S_{NN}	$J+L_{NN}$	Examples	$S_{N\Delta}$	$L_{N\Delta}$	Exceptions
0	even	$^1S_0, {}^1D_2$	2	$J+2, J, \lvert J-2\rvert$	$J=0 \to L_{N\Delta}=2$
1	even	$^3P_1, {}^3F_3$	1	J	
1	odd	$^3P_0, {}^3P_2, {}^3F_2, {}^3F_4$	1	$J+1, \lvert J-1\rvert$	

TABLE XIV

ΔΔ STATES WHICH COUPLE TO GIVEN NN STATE

NN State (T=1 or T=0)			ΔΔ States Which Couple		
S_{NN}	$J+L_{NN}$	Examples	$S_{\Delta\Delta}$	$L_{\Delta\Delta}$	Exceptions
0	even	$^1S_0, {}^1P_1, {}^1D_2$	2	$J+2, J, \lvert J-2\rvert$	$J=0 \to L_{\Delta\Delta}=2$
			0	J	
1	even	$^3P_1, {}^3D_2$	3	$J+2, J, \lvert J-2\rvert$	$J\neq0; J=1 \to L_{\Delta\Delta}=3$
			1	J	$J\neq0$
1	odd	$^3S_1, {}^3P_0, {}^3P_2, {}^3D_1, {}^3D_3$	3	$J+3, J+1, \lvert J-1\rvert, \lvert J-3\rvert$	$J=0 \to L_{\Delta\Delta}=3; J=1 \to L_{\Delta\Delta}=2,4$
			1	$J+1, \lvert J-1\rvert$	

$L=4$. The reason that NN couples to NΔ only in T=1 is that an N ($t_N=1/2$) and a Δ ($t_\Delta=3/2$) can add up to T=1 but not to T=0.

Sugawara and Von Hipple showed that the corrections of Figs. 15a and b simulated the exchange of scalar mesons. We have already shown from a simple argument that the contributions are attractive; Riska and Brown gave a simple argument to show what the corresponding mixture of isovector and isoscalar bosons would be. They noted that because Fig. 15a operates only in T=1 its isospin dependence must be

$$P_{T=1} = \frac{1}{4} (3 + \underset{\sim}{\tau}_1 \cdot \underset{\sim}{\tau}_2) \tag{67}$$

i.e., 3/4 isoscalar, 1/4 isovector.

37

Although Sugawara and Von Hipple and Riska and Brown were able to show the qualitative importance of Figs. 15a and b, they were unable to make a successful quantitative theory; Bethe pointed out[34] that the range of the attraction in the work of RB was too short and could be taken into account merely by reducing the coupling constant of the ω meson! Part of the problem is that these theories are very sensitive to cutoffs; essentially any answer could be obtained merely by changing the π-nucleon form factor.

a. Model of Green and Haapakoski[44]

Green and Haapakoski (GH) made two improvements in the work of Brown and Riska: (1) they avoided making the closure approximation in their evaluation of Fig. 15 and (2) they calculated the nucleon-nucleon phase shifts in the $^1S_0$ channel and showed that the theory gave sensible results.

GH avoided the closure approximation by introducing the Δ as an explicit degree of freedom in much the same way as advocated originally by SH before they made their series of approximations. This required solving a coupled equation [Eq. (70)]; the solution gave the separate nucleon and Δ components of the wave function. GH confined their attention to the $^1S_0(nn)$ state to simplify the numerical problem; this state is of course very interesting because it has $\ell=0$ and hence the attraction is a conspicuous feature of the partial wave. GH assumed, as did RB and SH, that the $\Delta\Delta$ intermediate state could be neglected; according to Table XIII this means that the states $^1S_0(nn)$ can couple only to $^5D_0(n\Delta)$.

The GH potential consisted of three components, V_1, V_2 and V_3 depicted in Figs. 16a, b and c. Because GH do not consider $\Delta\Delta$ intermediate states, Figs. 16d, f were not considered. Likewise, no exchange interaction (Fig. 16c) was considered. The potential V_1 consisted of π, η and ω exchange. The interaction V_2 is discussed in some detail below. Very little is known about the potential V_3, and GH simply set V_3 in the $^5D_0$ channel equal to V_1.

b. The Transition Potential

The concept of an instantaneous potential is meaningless for the transition interaction, Fig. 16c and the interactions in Figs. 16d, e. These interactions depend very strongly on the incident energy because the transition $\Delta \rightarrow n\pi$ is energetically allowed; consequently the method of folded diagrams may

38

not be used to calculate a potential for them. Instead, the transition interac-
tion must be evaluated as a true Feynman diagram and carry an explicit dependence
on the total energy of the system. The importance of the energy dependence has
been emphasized in the recent work of Ref. 45. However, the energy-dependence
of the NN → NN, $\Delta\Delta \rightarrow \Delta\Delta$ and NΔ → NΔ transitions is sufficiently smooth to allow
a description in terms of instantaneous potentials.

In the early work of SH, RB and GH the energy dependence of the effective
interaction was ignored; this was consistent with their taking the difference
$(M-M_\Delta)/(M+M_\Delta) = 0$. However, the importance of these early works lies not in the
details of the numerical work but in the demonstration of the relevance of the Δ
resonances in this problem. Consequently, I shall 'gnore the details of energy
dependence and $M-M_\Delta$ corrections and explain the theory as developed by GH. In
this case the transition potential consists of a propagator for the exchanged
meson (a π meson for GH)

$$\frac{-1}{q^2+m_\pi^2} \tag{68}$$

and vertex functions for N$\pi\Delta$,[41] with coupling constant f*. f* is determined from
the quark model or from the width of the 3-3 resonance, but in practice these two
methods lead to slightly different values for f*. The calculation is then paral-
lel to the derivation of the OPEP, Eq. (41).

$$\left(\text{diagram}\right) = (2\pi)^3 \delta(\underline{p}'-\underline{p})\ V_2(\underset{\sim}{p}'-\underset{\sim}{p}) \tag{69}$$

$$V_2 = \frac{ff*}{m_\pi^2}\ \frac{\underset{\sim}{\sigma}_1\cdot\underset{\sim}{q}\ \underset{\sim}{S}_2\cdot\underset{\sim}{q}}{-q^2-m_\pi^2}\ \tau_1\cdot T_2$$

A convenient representation of the transition spin and isospin operators S, T is
given in Ref. 41. Because these operators do not depend on momentum, a coordinate
space representation for V_2 may be found following the steps of Appendix A and B.

The projection of V_1, V_2 and V_3 onto the relevant states is given in Table
XV. It may be seen that GH chose to regularize the potential V_2 by a cutoff of
range B, a parameter to be varied. They also let the strength of the ω-meson
coupling be set by a free parameter, A.

To obtain the scattering, GH solve Schroedinger's equation,

$$(T + V)\psi = k^2\psi \tag{70}$$

where now ψ is a two component wave function having an nn and an nΔ component

$$\psi = \begin{pmatrix} u_{nn}(r) \\ w_{n\Delta}(r) \end{pmatrix} \tag{71}$$

and where T and V are matrices

$$T = \begin{pmatrix} -\dfrac{\hbar^2 d^2}{M\, dr^2} & 0 \\ 0 & -\dfrac{\hbar^2}{M}\left(\dfrac{d^2}{dr^2} + \dfrac{6}{r^2}\right) + (M_\Delta - M)c^2 \end{pmatrix} \tag{72}$$

$$V = \begin{pmatrix} V_1 & V_2 \\ V_2 & V_3 \end{pmatrix} \tag{73}$$

The term $\dfrac{6}{r^2}$ in the kinetic energy is the angular momentum barrier for the L=2 partial wave. The boundary conditions are that u have an incoming plane wave and an outgoing spherical wave in $\ell=0$, and that w have no component at $r = \infty$. (The Δ exists only virtually when the nucleons are close together.)

Green and Haapakoski chose three different values of A and then varied B to give the best fits to the ${}^1S_0$ phase shift for $E_1 \leq 350$ MeV. The results are shown in Table XVI. The calculated phase shifts are in qualitative agreement with experiment, but tend to be too attractive at high energy, the discrepancy being less for the larger values of A. Note that potential 1 gives a very satisfactory value of g_ω^2, to be compared to the value $g_\omega^2 = 6.36$ of Table IX.

Green and Haapakoski also give an interpretation of their cutoff B in Table XVI. They point out that the ρ meson may also excite the transition from $n \to \Delta$ and that just as in the nucleon-nucleon potential the π and ρ contributions to the exchange potential have opposite signs. They point out that although B appears to modify the potential at moderately large distances, the long range piece merely mocks up the ρ meson exchange and that with ρ and π exchange the transition potential is much less sensitive to the pion form factor.

Thus, for the first time, we have an example of a potential which gives reasonable repulsion (although perhaps still underestimating it somewhat) and sufficient attraction. The significance of the relatively small value for g_ω^2 was discussed by Durso, et al.[46] I will come back to this point later.

40

The successes of the GH approach are significant, but the specific calculation has met with some criticisms. Durso, et al[46] have criticized the neglect of $(M-M_\Delta)/(M+M_\Delta)$ corrections. They also point out that the crossed pion diagrams are important and, based on this observation, they question the utility of the coupled channel approach. Pandharipande and Smith[47] show that cancellations occur among the crossed box diagrams, so that the sum of crossed plus uncrossed box diagrams of Fig. 15 is closely approximated by the iteration of the transition potential. However, Durso, et al. point out that the extent of cancellation is model-dependent, e.g., depending upon whether the $f^*_{\pi n\Delta}$ coupling constant was determined by the quark model or from the width of the Δ. We have already remarked on the importance of the energy-dependence, as pointed out in Ref. 45. Much more careful theoretical work needs to be done before quantitative assessments of the importance of the Δ in the nuclear physics can be confidently made. Calculations within the coupled channel framework are continuing, and there is some hope that this method will prove to be a useful framework for including important physical effects both into the nucleon-nucleon interaction problem and other physically interesting problems as well. I shall return to this subject later to examine implications for other problems in nuclear physics.

3. Stony Brook and Paris Potentials

The situation that has emerged is that three models of the intermediate range attraction exist, each of which has been shown capable of supplying sufficient attraction: (1) scalar meson exchange, (2) uncorrelated two-pion exchange and (3) intermediate isobars. It should be clear that no theory can be correct which relies entirely on one or two of these effects. However, nobody has made a successful calculation by explicitly combining these effects.

The method of dispersion relations has provided some valuable insight into this problem and first demonstrated the extent to which an approach, which relies on these three two-pion exchange

TABLE XV

POTENTIALS OF GH

$$\langle {}^1s_0|v_1|{}^1s_0\rangle = -10.5\,\frac{e^{-0.7r}}{0.7r} - 43\,\frac{e^{-2.75r}}{2.75r} + A\,\frac{e^{-3.9r}}{3.9r}$$

$$\langle {}^1s_0|v_2|{}^5D_0(n\Delta)\rangle = 44\,\frac{e^{-0.7r}}{0.7r}\left[1 + \frac{3}{0.7r} + \frac{3}{(0.7r)^2}\right]\left(1-e^{-Br^2}\right)^2$$

$$\langle {}^5D_0(n\Delta)|v_3|{}^5D_0(n\Delta)\rangle = \langle {}^1s_0|v_1|{}^1s_0\rangle$$

TABLE XVI

RESULTS OF THE GH CALCULATION

Potential	A(MeV)	B(fm^{-2})	g^2_ω	a_s(fm)	r_s(fm)
1	2500	1.4	6.6	-6.0	2.4
2	5000	1.8	9.8	-6.3	2.4
3	10000	2.6	16.2	-5.5	2.5

mechanisms, may succeed. The essential points were discussed by Brown and Durso.[48] The two-pion exchange potential may be represented as in Fig. 17, where the blobs represent everything which connects the two pions to the nucleons; the antinucleon intermediate states, the Δ states and the interactions between the two pions which build up the scalar mesons and the ρ meson. Now, the point is that if the diagram is cut as shown in Fig. 17, each half represents the pion-nucleon scattering amplitude (evaluated possibly at some kinematically inaccessible point). Thus, there is an intimate connection between the two-pion exchange nucleon-nucleon amplitude and the pion-nucleon scattering amplitude. Dispersion relation theory is the mathematical relation for connecting these two quantities. A two-pion exchange potential can then be constructed provided one knows how to extrapolate off mass shell (this is mostly an art at the present time) and provided one subtracts out the iterated one-pion exchange potential, for reasons discussed in conjunction with Fig. 12.

Because the dispersion relations relate pion-nucleon and nucleon-nucleon scattering, this method makes possible a more stringent restriction on the terms which are included and therefore gives a greater chance that the various pieces are combined correctly. So far the approach has been largely phenomenological, i.e., the experimental πN amplitude has been fed in or else certain phenomenological constraints have been imposed, for example the soft pion condition that the pion-nucleon amplitude extrapolate smoothly off mass shell near zero energy. One hopes that eventually this approach will teach how to calculate more confidently with the individual terms that have been discussed and that are depicted in Fig. 18.

Two modern potentials have been constructed based on dispersion relations, often referred to as the Paris potential[12] and the Stony Brook potential.[11] In addition to this model of two-pion exchange, the potential consists of single π and single ω exchange. In Ref. 11 the cutoff form factors are calculated in a model. In the most recent work of Ref. 12 the short range part of the potential is parametrized and very reasonable fits to the data are obtained for nucleon-nucleon partial wave states of $J \leqslant 4$. These two potentials represent a departure from their predecessors in that they contain an explicit energy dependence; this is presumably a drawback for practical calculations and in Ref. 12 it is recommended that the energy dependence be replaced by a momentum dependence.
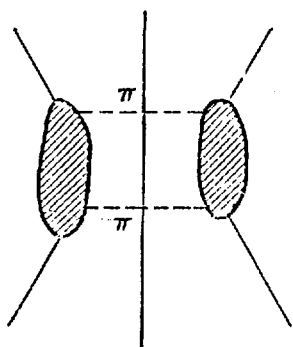
Fig. 17. Relationship between the 2π exchange NN potential and the π-nucleon scattering amplitude.
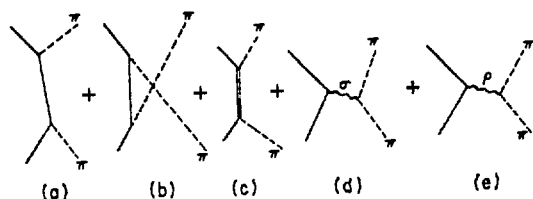
Fig. 18. Contributions to π-nucleon scattering. The diagram (a) and (b) are intended to include anti-nucleon as well as nucleon intermediate states.

TABLE XVII

COUPLING CONSTANTS FOR ω MESON IN PARIS

AND STONY BROOK POTENTIALS

Potential	g_ω^2
Paris	9.5
Stony Brook	7.0

The values of the ω coupling constants are shown in Table XVII. One should note that the couplings needed here are somewhat smaller than those appearing in Table IX, especially for the Stony Brook potential. This is presumably the result of the energy and momentum dependence in the potential, which is different from that appearing in the simple OBE models, but it is also due, at least in the Stony Brook potential, to imposing an artificial cutoff on intermediate momentum integrals appearing in the expression for Fig. 17 to take account of the omission of the 3π (e.g., simultaneous ρπ exchange shown in Fig. 19) exchange between the two nucleons. (Recall that the ρ-meson effect opposes the π-meson exchange.) The cutoff reduces the attraction and makes possible a smaller short range repulsion.

4. Three Pion Exchange

The fact that GH were able to reproduce the $^1S_0$ phases with a relatively small value for g_ω^2 suggests that their model contains a repulsive term which is normally not taken into account in one-boson exchange interactions. As I have repeatedly emphasized, the π and ρ exchanges have tensor components of opposite sign, so if we regard the attraction in the nucleon-nucleon interaction as coming from the two-pion exchange diagram in Fig. 15a, the exchange of a π and a ρ meson as shown in Fig. 19 must be repulsive and it is the candidate for the additional repulsion in the theory of GH.

Durso, et al.[46] examined this possibility in some detail and showed that the $\pi\rho$ exchange has the spin-isospin structure of the exchange of a vector, isovector meson, i.e., like the ω meson. Although the strength of this term depends sensitively on the form factor cutoff, Durso, et al. estimate the effect and find that the effect can be simulated by an increase of g_ω^2 from ≈ 6.4 (Table IX) to ≈ 12. This, they point out, may well explain why OBE models require ω mesons with coupling constants larger than those obtained from elementary particle considerations.

IV. MESONIC COMPONENTS IN NUCLEAR WAVE FUNCTIONS

We have seen that models of the nucleon-nucleon interaction have been constructed which are moderately successful and which rely on a description in terms of mesons, nucleons and nucleon resonances. One would like to find experiments other than elastic nucleon-nucleon scattering in which sensitivity to these elementary constituents is manifest.

The complete wave function for a two-nucleon system $|\psi\rangle$ would have a multitude of components:

$$|\psi_\alpha\rangle = \sum_i |i\rangle\langle i|\psi_\alpha\rangle \tag{74}$$

where $|i\rangle = \{|NN\rangle, |NN\pi\rangle, |NN\rho\rangle, \ldots, |NNN\bar{N}\rangle, \ldots\}$ and the sum extends over a complete set of the individual components. If it is possible to devise experiments sensitive to the individual terms, or different linear combinations of the terms than that which enters the nucleon-nucleon interaction, then one could be more confident of the mesonic models.

Unfortunately, it is very difficult to write down dynamical equations which can be solved explicitly for the various components in Eq. (74). However, as an

alternative to calculating the complete wave function, one might consider calculating observables, e.g., the magnetic moment, directly. The observable would be associated with an effective operator $\overline{0}_i$ which would have the property

$$< \overline{\psi}_\alpha \, | \overline{0}_i | \overline{\psi}_\beta > \equiv \, < \psi_\alpha \, | 0_i | \psi_\beta > \quad . \tag{75}$$

Here $| \overline{\psi}_\alpha >$ is a wave-function having only nucleon components, generated from some potential model Hamiltonian,

$$| \overline{\psi}_\alpha > \, = \Sigma \, | NN > \, < NN | \overline{\psi}_\alpha > \quad , \tag{76}$$

$| \psi_\alpha >$ is the exact wave function [Eq. (74)], and 0_i is the fundamental observable. The way to construct such operators $\overline{0}_i$ is the subject of effective interaction theory and the theory of exchange currents. The method of folded diagrams gives a method for calculating at energies below meson production threshold corrections corresponding to the instantaneous potentials (energy-independent interactions) discussed in the first lecture. In these methods, the operator $\overline{0}_i$ is expanded perturbatively to make corrections for the mesonic and $\overline{N}$ components in Eq. (74). These calculations are tractable and many have been done. Jim Friar will discuss exchange currents more extensively but I will show some results later as they bear on physics considerations already raised.

The method involving nucleon-nucleon potentials and exchange currents is generally believed to be satisfactory for examining mesonic effects at low energy. The dynamics, at least in the two-nucleon problem, is the solution of Schroedinger's equation, and exchange currents are calculated perturbatively. This simplicity is the attractive feature of this method. The drawback is that it is incapable of describing meson production channels which open at higher energies.

The actual wave function is presumably not either Eq. (74) or Eq. (75) but rather a wave function written in terms of quarks and gluons. Part of the task of theory is to show how all these descriptions are related and to provide rules according to which the same answer to physical questions will result, independent of the particular mode of description.

Let me begin by giving some examples of low energy properties of the deuteron.

A. Exchange Currents

1. Magnetic and Quadrupole Moment of the Deuteron

The magnetic moment of the deuteron is measured to have the value

$$\mu_{D, \text{expt}} = 0.8574 \text{ nuclear magnetrons} \tag{77}$$

If the deuteron were simply a neutron and proton, then $\mu(D)$ would be given by the expression

$$\mu(D) = \mu(p) + \mu(n) - \frac{3}{2}[\mu(p) + \mu(n) - \frac{1}{2}] \, P(D) \tag{78}$$

where $P(D)$ is the deuteron d-state probability. Most nucleon-nucleon potentials give $P(D)$ to lie in the range 0.04 to 0.065. If $P(D)$ were as small as 0.04 then Eqs. (77) and (78) would agree; however if $P(D)$ were 0.065 then Eq. (78) would underestimate the experimental value in Eq. (77).

In order to resolve this question, it is necessary to look at the calculation of the deuteron magnetic moment from a more fundamental point of view, i.e., from a meson exchange model point of view. As in all such studies one should consider potentials which are compatible with the effective magnetic moment operator $\overline{O}_m$, i.e., the wave function $\overline{\psi}$ and the operator $\overline{O}_m$ in Eq. (76) should be consistently derived from the same underlying meson theory.

Figure 20 shows some of the "meson exchange" contributions to O_α. It is important to point out that there is a folded diagram contribution to the meson exchange current[20] which should be used in place of Fig. 20c if the state $|\overline{\psi}_\alpha>$ is the eigenstate of an energy-independent Hamiltonian. Actually all calculations which have been made are based on energy-independent interactions and therefore there is some inconsistency regarding the treatment of this term. Sometimes heavy mesons are considered in Fig. 20a and b.

Figure 21 shows some of the isobar contributions to the exchange current $\overline{O}_\alpha$. In order to make use of Fig. 21c one needs to know the $\Delta\Delta$ and NN' components in the deuteron wave function (see below). Calculations are particularly uncertain due to the poorly known coupling constants and magnetic moments associated with the Δ and N'.

Results of some published calculations are shown in Table XVII. The calculation of Ref. 51 utilized an underlying one-boson exchange model; one would
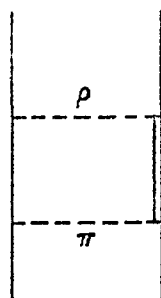
Fig. 19. A 3π exchange contribution. This contributes a dominently repulsive effect for reasons discussed in the text.
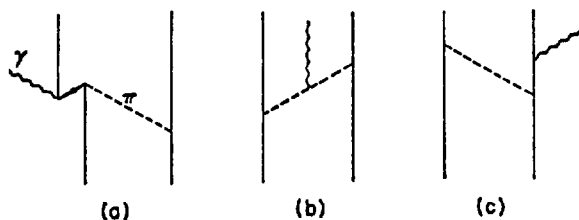
Fig. 20. Contributions to meson exchange currents. The wavy line represents the coupling to the electromagnetic field. Diagram (1) is called the pair term; (2) the mesonic term; (3) the recoil plus wave function renormalization term.
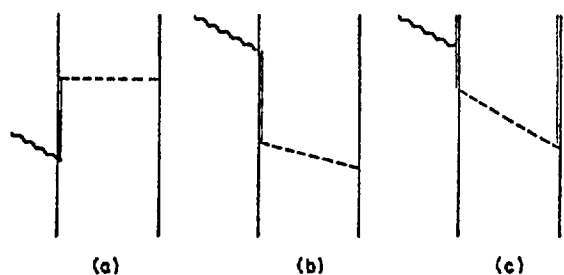
Fig. 21. Isobar contributions to the exchange current. The double solid line stands for N' or Δ.

TABLE XVIII

NUMERICAL RESULTS FOR CORRECTIONS TO

DEUTERON MAGNETIC MOMENT

Terms	$\Delta\mu(D)$ (%)	
NN'(1688) (2%)	+2	K[50a]
$\Delta\Delta$ (1%)	+5	FAM[50b]
$\sigma(\omega)$	+2 (+0.2)	HFY[51] (FAM[50b])
π	-5	JLR[52]
Relativity	+2	G[53]

like to see all exchange current calculations proceed consistently from a meson theory both in the underlying potential model and in the calculation of the exchange current. In addition to these results there is a recent calculation by Hadjimichael,[49a] in which the sensitivity of the deuteron magnetic moment and quadrupole exchange currents to various phenomenological potential models was considered. The results in the table indicate that the exchange current correction is $\Delta\mu(D)$ = + 6%. A P(D) of + 0.065 requires a + 2% correction, and so these results have the correct sign but overestimate the correction by a factor of 3. Hadjimichael has shown that the tendency to overestimate the magnetic moment is characteristic of many potential models having a range of values of P_D.

It is somewhat worrisome that all the corrections in Table XVIII are approximately the same size. One would

like to see a tendency for the corrections to get smaller in a systematic expansion procedure. It would be interesting to see what uncorrelated 2π exchange wou.d add to the magnetic moment. As it now stands, the exchange current corrections to the magnetic moment tend to be too large. This is not the only place that exchange current calculations tend to give too large results. Holstein, et al.[49b] have analyzed the reactions $\mu^- + {}^{16}O \to {}^{16}N^*(0^-) + \nu_\mu$ and ${}^{16}N^*(0^-) \to {}^{16}O + \bar{e} + \bar{\nu}_e$ and find that experiments do not require appreciable exchange current corrections contrary to the results of explicit theoretical calculations.

Hadjimichael[49a] has also considered exchange current corrections to the deuteron quadrupole moment in various potential models. The corrections to the quadrupole moment are smaller than the corrections to the magnetic moment, but the tendency is for the calculated corrections to be too large.

2. Radiative N-P Capture ($N+P \to D+\gamma$) of Thermal Neutrons

The experimental cross section is $\sigma = 334.2 \pm 0.5$ mb. Calculations without mesonic effects give $\sigma = 302.5 \pm 4$ mb; this is accurately known from knowledge of just the nucleon-nucleon phase shifts. The 10% discrepancy between these two numbers is in.eresting because it indicates that this reaction actually needs a substantial correction from mesonic effects. At low energy the transition is magnetic dipole, ${}^1S \to {}^3S$ and ${}^1S \to {}^3D$.

Again Figs. 20 and 21 show some of the terms that have been considered in trying to understand the discrepancy. The isobar terms are shown in Fig. 21. The piece in Fig. 21c appears to be quite small.[54]

Results of two calculations are shown in Table XIX. Note that the pair plus pion current contributes somewhat more than the Δ effect. The Δ terms have not been calculated with $\pi + \rho$ exchange nor have these calculations taken into account the effects of NN' and $\Delta\Delta$ components in the deuteron; the latter effect has an important _indirect_ effect, of affecting the deuteron wave function normalization, through Fig. 21c. Green[4] has pointed out that when these effects are taken into account the Δ effect will be significantly reduced.

The results seem to indicate a significant need for mesonic effects. Better calculations are needed before we can say what the actual balance between mesonic and non-mesonic effects is.

3. Other Experiments

There have also been calculations of the following reactions to investigate the contributions of the various mesonic effects.

$e+d \rightarrow e+d$

$\gamma+d \rightarrow n+p$

$e+d \rightarrow e'+n+p$

$\mu^-+d \rightarrow n+n+\nu$ (79)

$\pi^-+d \rightarrow n+n+\gamma$

These are discussed in the review arti-
cle by Green.[4]

The need for mesonic exchange current corrections is especially dramatic in
$e+d \rightarrow e'+n+p$;[55] a calculation is shown in Fig. 22. The dominant effect comes
from processes other than isobars.

B.   Isobars in Nuclei

An alternative approach to calculating mesonic effects in nuclear systems
is the coupled channel approach, discussed already in connection with the Green-
Haapakoski description of the nucleon-nucleon interaction. This description is
in some sense intermediate between those represented by Eqs. (74) and (76). In
this approach the wave function would be taken (for a two-nucleon system) as

$$|\bar{\bar{\psi}}\rangle = \sum_i |\bar{\bar{i}}\rangle \langle \bar{\bar{i}}|\bar{\bar{\psi}}\rangle \qquad (80a)$$

$$|\bar{\bar{i}}\rangle = \{|NN\rangle, |N\Delta\rangle, |NN'\rangle, \ldots\} \qquad (80b)$$

Since nucleons like to interact with mesons to form resonances, it is supposed
that a wave function of the form in Eq. (80a) is "closer" to the true wave func-
tion of Eq. (74) than is Eq. (76). Since more is being put into the wave func-
tion, one can expect simpler exchange current corrections. At higher energies,
the coupled equations take into account some of the inelastic channels, i.e.,
those that are fed through the N' and Δ states. Again one hopes that the wave-
function is sufficiently close to the actual wave function that the corrections
necessary for describing meson production will be small enough to handle in some
tractable fashion. However, so far nobody has carefully worked out the theory
of the equivalence between the descriptions in Eqs. (74) and (80), and it is
therefore too early to say for sure how quantative the coupled channel approach
can be.

1. Isobar Components in the Deuteron

This problem predates[56] the work of GH on the nucleon-nucleon interaction, but the theory is really just an extension of the ideas discussed earlier in that connection. Basically, the idea is to extend the number of coupled channels in Eqs. (70) to (73) to include more of the isobars shown in Table XII. In addition to the $\Delta(1232)$, the isobars which have been included in these calculations are shown in Table XX.

A description of the wave function containing the $\Delta(1232)$ and nucleon was described in detail earlier in conjunction with Table XIV; with the higher spin resonances of Table XII, the wave functions are even more complicated. One difference between the $T = 3/2$ and $T = 1/2$ resonances is that isospin considerations do not forbid $|NN'\rangle$ components in the deuteron, whereas $|N\Delta\rangle$ components cannot occur, as discussed earlier in conjunction with Table XIV. For this reason, the N' components will be as important as, or more important than, the Δ component even though the N' are more massive.

TABLE XX

SOME OF THE T=1/2 NUCLEON RESONANCES

Particle	j	Γ(MeV)	g^{*}
N'(1470)	1/2	66	3.4
N'(1520)	3/2	68.1	16.32
N'(1535)	1/2	12.5	0.36
N'(1670)	5/2	60.6	10.08
N'(1688)	5/2	74.7	26.88
N'(1700)	1/2	104.9	0.96

*g is the $\pi NN'$ coupling constant, determined from the resonance width (Ref. 43).

The description in terms of coupled channels introduces new theoretical quantities many of which are unknown in detail. One of these is the transition interaction NN → NN'. It is generally assumed that these transitions are induced by the pion and that the resonance width is determined by its decay into a pion and a nucleon. Under these circumstances a coupling of the appropriate tensorial character is written down and the known width of the resonance used to determine the coupling constant. See Ref. 43 for more details. Some couplings determined in this way are shown in Table XX. Diagonal matrix elements, e.g., $\langle N\Delta|V|N\Delta\rangle$ are also needed but virtually unknown; often these are equated to the diagonal matrix element for nucleons, or a quark model is used for an estimate.

Once the interactions are written down, the coupled equations are solved exactly or approximately to find the wave function components. One interesting

quantity which may then be calculated is the probability with which a certain isobar configuration occurs in the deuteron wave function. Some of the numerical results for $\Delta\Delta$ and NN' probabilities are shown in Table XXI.

At first, the calculation of the $\Delta\Delta$ component of the deuteron was very uncertain due to a strong cutoff dependence (analogous to the parameter B in Table XV) in the transition interaction $\langle NN|V|\Delta\Delta\rangle$, i.e., the $\Delta\Delta$ probability could change by a factor of 2 depending upon the cutoff at the $\pi N\Delta$ vertex. In the more recent calculations of Refs. 62 and 58 the transition potential includes the π plus ρ meson exchange and the sensitivity to cutoff is vastly reduced. The calculations A and HS of Table XXI both incorporate the ρ meson and the differences are indicative of other sources of uncertainty, e.g., A incorporates a diagonal interaction in the $\Delta\Delta$ channel whereas HS do not, and HS use a $\pi N\Delta$ coupling taken from the quark model whereas A takes his from the width of the $\Delta(1232)$. The errors on the HS result show the sensitivity to the very short range regularization of the transition potentials, i.e., the result of varying the hard core cutoff from 0.2 to 0.4 fm.

Table XXIb shows some of the other calculations of isobar components in the deuteron. We see that the total estimated probability is about 1.5%. Estimates for the $\Delta\Delta$ component range from 0.25 to 1%. Because these probabilities are small, the isobar components are going to be very difficult to detect. After all, the D-state probability of the deuteron has proved difficult to pin down to within 2%. However, as emphasized by Kisslinger, the isobar configurations are apt to dominate the momentum distribution of the deuteron for sufficiently high momentum. The large spin of some of these resonances implies that rather large orbital angular momentum will be found in the deuteron ground state. Because momentum distributions of orbital angular momentum L are expected to peak at Q

$$Q \approx L/R \tag{81}$$

where R is the deuteron radius, it is possible that the large momentum component will be more significant than the small overall probabilities. Similar considerations apply to larger nuclei. It has been hoped that this fact could be used to get an experimental handle on the Δ and N' probability but so far nothing has come from these attempts.

ESTIMATES FOR PROBABILITY OF $\Delta\Delta$

COMPONENT IN THE DEUTERON[*]

State ($\Delta\Delta$)	A[57]	HS[58]
$^3S_1$	0.17	0.16 $\pm$ 0.06
$^3D_1$	0.05	0.026 $^{+\ 0.003}_{-\ 0.005}$
$^7D_1$	0.51	0.25 $^{+\ 0.01}_{-\ 0.02}$
$^7G_1$	0.05	0.02
Sum	0.78	0.46 $\pm$ 0.07

[*]Probabilities are quoted in percent.
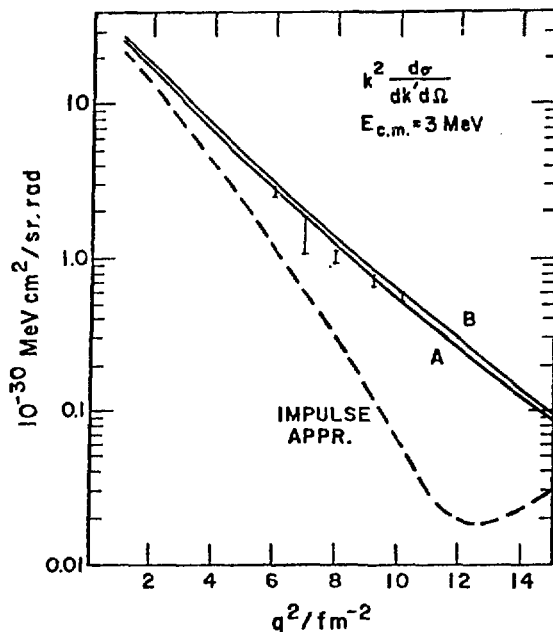
Fig. 22. Double differential cross section for the reaction $e+d \rightarrow e'+n+p$ for backward scattering at fixed neutron-proton energy $E_{CM} = 3$ MeV.[55] Solid and dashed curves are theoretical results with and without exchange currents, respectively; solid curve A contains only the OPEP currents, while curve B contains the isobar current.

TABLE XXIb

ESTIMATES FOR PROBABILITY (%) OF $\Delta\Delta$ AND NN' COMPONENTS IN THE DEUTERON

State	KK[56]	ADW[54a]	R[59]	FAM[60]	PS[47]	JK[61]
$\Delta\Delta$	---	1.	0.20		0.5-0.6	0.25
NN'(1470)	---	0.2	0.16			
NN'(1520)	---	---	0.26			
NN'(1670)	---	---	0.08			
NN'(1688)	1/2-1	---	0.43			
NN'(1700)	---	---	0.18			
Sum	---	1.2	1.3	1.5		

2. Tests of Isobar Components in the Deuteron

a. (P,D) Elastic Backward Scattering

The subject of isobar components in the deuteron was launched by the work of Kerman and Kisslinger (KK),[56] who were interested in explaining the backward peak in the P,D elastic differential cross section. KK emphasized that an exchange (transfer) mechanism such as that shown in Fig. 23a required less momentum transfer than a "bounce" mechanism shown in Fig. 23b, and hence would presumably dominate the transfer at high energy. However, the elementary nucleon transfer, depicted as a Feynman diagram in Fig. 23c, was too small to explain the backscattering peak; the deuteron wave function did not have a sufficiently large component for the momentum transfer involved. However, KK constructed a model in

(a) **(b)**

(c) **(d)**
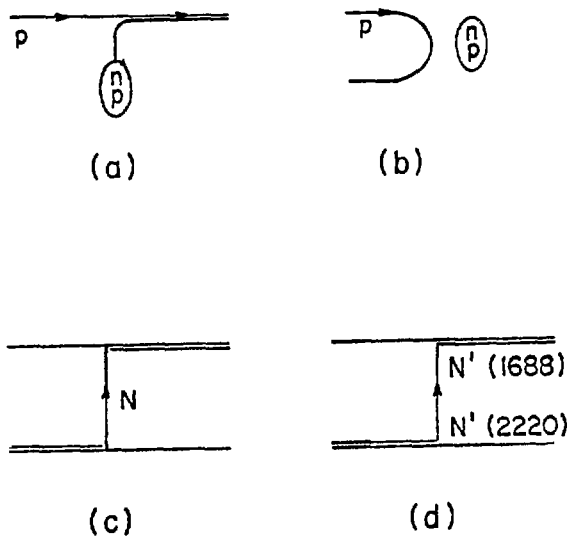
Fig. 23. Representations of (d,p)
backward scattering. (a) and
(b) are pictorial representa-
tions of transfer and bounce
scatterings, respectively,
in the lab frame. (c) and
(d) are Feynman diagrams for
the transfer of a nucleon or
t=1/2 isobar, respectively.

which the deuteron ground state con-
tained a sufficiently large admixture
of N' components that the exchange of
a resonance as in Fig. 23d could pro-
vide the needed momentum. They esti-
mated the amount of NN'(1688) in the
wave function to be from 1/2 to 1% and
showed that if the percentage were as
large as 1% then the backscattering
could be completely explained. Since
that time there have been a number of
other proposals for explaining the
backscattering, proposals which do not
rely on N' components. Incidentally,
the Δ must occur in pairs in the
deuteron.

b. <u>Δ Knock Out (p+d$\rightarrow$p+Δ^++Δ^0)</u>

In these experiments one
hopes to obtain directly evidence of Δ
components in the deuteron by quasi-
elastically scattering a Δ from the deuteron by a high energy pion or kaon. In
such a collision, when the incident meson strikes one of the Δ in the deuteron,
the spectator Δ can decay to give a number of πN events in the backward direction
in the laboratory. A backward peak was found and initially was interpreted as
evidence for Δ in the deuteron. Different experiments have been analyzed as
giving less than 0.4% for the percentage $\Delta\Delta$[63] and up to 3% for this probabil-
ity.[64] Recently A. Goldhaber[65] has made a critical study of the effects which
could impugn these analyses and has found many sources of ambiguity, including
final state interactions and the form factor for the virtual Δ-real Δ transition.
Some of the effects he considered could suppress the breakup by an order of
magnitude, and he concludes that the reported experiments did not have the nec-
essary sensitivity to detect $\Delta\Delta$ breakup.

3. Mesonic Degrees of Freedom in the Ground State of Large (A>2) Nuclei

a. Δ Components

This problem may be approached from the point of view of exchange currents or by explicit calculation of Δ and N' components just as in the case of the deuteron. However, for a large nucleus there is a new possibility, namely that a pion condensate might exist. I want to reserve the last lecture for a discussion of pion condensates.

Rather than discuss details of calculations of Δ and N' components and exchange currents in heavy nuclei, I want to mention two qualitative ideas, both due to Kisslinger and collaborators, on experimental consequences of isobars in the ground state of nuclei.

The first point is that in many cases the Δ and N' have large spin S. Thus, for a given single particle orbital of total angular momentum J these objects can occupy states of relatively large orbital angular momentum. For example, in a $J = 3/2$ state the $\Delta(1230)$ will occupy $L = \frac{3}{2} + \frac{3}{2} = 0,1,2,3$. Thus, in the absence of Δs the odd parity single particle orbital of $J = 3/2$ is

$$\psi^{(-)}_{3/2} = P_{3/2} \; (N) \tag{82a}$$

i.e., an $L = 1$ state. However, with both N and $\Delta(1232)$ components, this state is

$$\psi^{(-)}_{3/2} = \alpha \, P_{3/2} \; (N) + \beta \, P_{3/2} \; (\Delta) + \gamma \, F_{3/2} \; (\Delta) \tag{82b}$$

The hope is that the states of large L (in this case the $F_{7/2}$ or $L = 3$ state) would be a dominant source of large momentum components which could be easily detected in certain nuclear reactions. The (P,D) reaction (i.e., neutron pickup) on a light nucleus such as carbon was expected to be sensitive to these Δ components.[66]

Although the (P,D) reaction was initially quite attractive, the experimental results could be entirely explained without the Δ effect. Rost, et al.[67] showed that by taking into account the D state of the deuteron, all the necessary high momentum needed to explain the data could be found. Later calculations by Schaeffer, Kisslinger and Rost[68] showed that the Δ and N' components were not effective yet for 800 MeV protons.

The second proposal was one by Kisslinger and Miller,[69] the (P,π⁻) reaction on a nucleus. The process is illustrated in Fig. 24. A (P,π⁺) experiment on
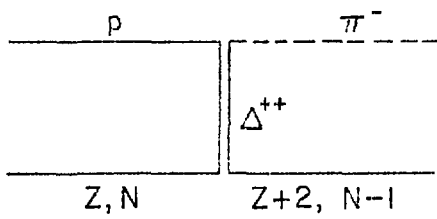
Fig. 24. The Δ^{++} mechanism for $p\pi^-$ reactions.

^{26}Mg at 180 MeV was reported in Ref. 70, but very poor agreement with theory was obtained. There is some worry, however, that the distorting optical potential was not sufficiently realistic in the theoretical estimates of Ref. 69, and the calculations should be redone investigating this point.

In any case we can say at this time there is no direct experimental evidence for Δ^{++} components in nuclei.

b. Mesons in Nuclei: Meson Propagator

Another very important subject is to know how a meson, once created in a nucleus, propagates. One might ask, for example, what the amplitude is to insert a pion of momentum k in a medium at time T and remove it at time T' ($T'>T$):

$$< \psi_0 | a_k^+ (T') \, a_k(T) | \psi_0 > \qquad (83)$$

where ψ_0 is the exact nuclear ground state wave function, $a_k(T) = e^{iHT} a_k e^{-iHT}$ and H is the full Hamiltonian including the pion. The matrix element shown in Eq. (83) is the pion Green's function, and is a fundamental quantity which specifies the way the pion propagates. It is essentially this matrix element which is examined in investigations of meson scattering, investigations of meson currents in the nuclear wave function, and pion condensation. This is an exceedingly important aspect to the work at the meson factories and to nuclear physics in general. I will not have time to talk about this in any generality, but I will illustrate the subject in my last lecture when I discuss pion condensation.

c. Mesons and Isobars in the Nuclear Ground State, Summary

There is a well-established "need" for mesonic effects in the ground state of nuclear systems, showing up especially in interactions with the electromagnetic field in exchange current corrections involving the deuteron. However, how much of this correction is due to the individual mechanisms shown in Figs. 20 and 21 is still not unambiguously answered by the experiments. Because the theoretical numbers depend on many terms with several sources of theoretical uncertainties, agreement between theory and any one experiment does not necessarily mean that the theory is completely correct.

55

Some of the outstanding theoretical questions include (1) How does one properly describe a Δ or N' embedded in a medium? Can one describe a virtual N' or Δ by a simple propagator characterized by its free mass? Does the coupling change at all for a virtual Δ or N',

(84)
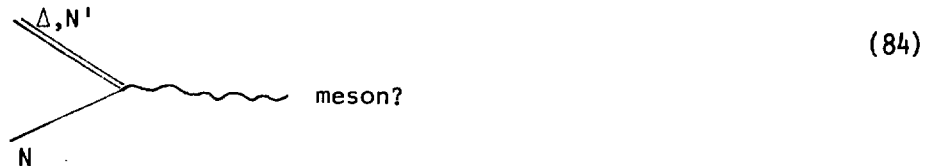
(2) What is the magnetic moment for N' and Δ?
(3) What are the diagonal couplings:

(85)

In addition to seeking answers to these questions, one should look closely at certain relativistic corrections to the exchange currents. One interesting term is the correction which arises from the use of instantaneous potentials in calculating the wave functions in the initial and final state. These corrections are calculable within the folded diagram framework.[20]

One of the difficulties of trying to learn about mesonic effects in the ground state of nuclei is that the mesons and resonances are not seen directly; their existence must be inferred by doing very accurate calculations with and without a conjectured mesonic effect and then looking for a systematic improvement with an experimental result.

In many respects the more satisfactory way to study mesonic effects is to raise the energy sufficient to produce the mesons. If the states of interest can be produced and studied directly, then many of the questions raised in these lectures may be subjected to a direct test. I therefore want to turn now to some of the questions that can be addressed by experiments above meson production threshold.

V. DIRECT OBSERVATION OF MESONIC COMPONENTS-NN SCATTERING ABOVE π PRODUCTION
THRESHOLD

The importance of pinning down the two-pion exchange interaction highlights
the importance of nucleon-nucleon scattering experiments above threshold for pion
production. Here there is an intimate connection between the two-pion exchange
interaction in elastic scattering and the reaction in which a pion is actually
produced as for example

$$P+P \rightarrow P+N+\pi^+ \tag{86a}$$

$$\rightarrow D+\pi^+ \tag{86b}$$

The point is that one of the pions in the two-pion exchange of Fig. 25a, rather
than attaching to the second nucleon, is actually produced as a free particle.
Thus the pionic piece of the black box, pieces of which are shown in Fig. 25b,
can be studied in some detail, for example, by varying the kinematics of the
final state.

It is important to learn the extent to which the Δ (and other resonances)
contribute to this process, because such would give an indication of the validity
of models which are used to estimate the NΔ and ΔΔ components in nuclear systems.

It is also important to measure the production channels to get an idea of
how the inelasticity is distributed among the various nucleon-nucleon partial
waves. This is an area of great importance, not only to learn about the nucleon-
nucleon potentials but to help arrive at unique nucleon-nucleon phase shift analy-
ses above meson production threshold. Usually it is assumed that the inelasticity
appears first in the $^1D_2$ nucleon-nucleon phase shift, but coupled channel calcu-
lations such as that of Green and Haapakoski[44] (see Green, et al.[71,72] who made
some modifications, e.g., including a width for the Δ(1232) above π production
threshold) give the results shown in Fig. 26. The point here is that in Ref. 73
it was assumed that the inelasticity occurred first in the $^1D_2$ channel because
here the NΔ may be in an S state. However, the detailed calculation shows an
appreciable imaginary phase shift in the $^1S_0$ states, casting doubt on the phase
shift analysis above threshold. Ambiguities such as this would be brought under
control by a direct measure of the inelastic channel.

Green and Niskanen[71] have also calculated the reaction in Eq. (86b). They
point out that this is dominated by the Δ_{33} and hence a sensitive test of the

coupled channel approach to calculating Δ components in nucleon-nucleon and nucleon-nucleus systems. They seem to be able to reproduce the broad resonance peak in the absorption cross section at a proton lab energy of about 600 MeV and they take this to be evidence of the qualitative correctness of their coupled channel theory.

Lastly, I should mention the polarized proton total cross section measurements recently carried out at Argonne around 1 GeV. Measurements of

$$\Delta\sigma_T \equiv \sigma(\uparrow\downarrow) - \sigma(\uparrow\uparrow) \tag{87}$$

for spin alignments transverse to the beam[74] and

$$\Delta\sigma_L = \sigma(\rightleftarrows) - \sigma(\rightrightarrows) \tag{88}$$

for longitudinal alignment[75] have been made. A dramatic variation in $\Delta\sigma_L$ was observed near $T_{LAB} = 750$ MeV, which appears to be a resonance in the $^3F_3$ (NN) partial wave.[76,77] From Table XIV we see that this would couple to the $^3F_3$ (NΔ) partial wave. Earle Lomon[78] has shown in a very schematic model that a sufficiently strong transition interaction NN $\rightarrow$ NΔ could give rise to a resonance close to the threshold for the production of the Δ. Kloet, et al.[79,80] have tried to make a more detailed calculation using a coupled channel approach which has three-body unitarity imposed. They do not reproduce the dramatic structure in $\Delta\sigma_L$, but this could be due to the fact that their model lacks realistic short ranged nucleon-nucleon forces. If Lomon's arguments turn out to be the correct explanation, there is some hope that extending the spin-dependent calculations to higher energy and a more detailed study of the reactions in the vicinity of the resonance could greatly help in understanding the same NΔ and NN' interactions at high energy needed for the low energy studies of N' and Δ components in nuclei.

Riska, et al.[81] have given some reason to believe that the cross section in Eq. (87) can teach about the role of the ρ meson in the nucleon-nucleon interaction.

VI. NUCLEAR MATTER THEORY

A. Brueckner-Bethe Method

Let me now skip from properties of few-body systems to large systems. Not as much can be said here because of the additional complexity of knowing how to

(a)

(b)
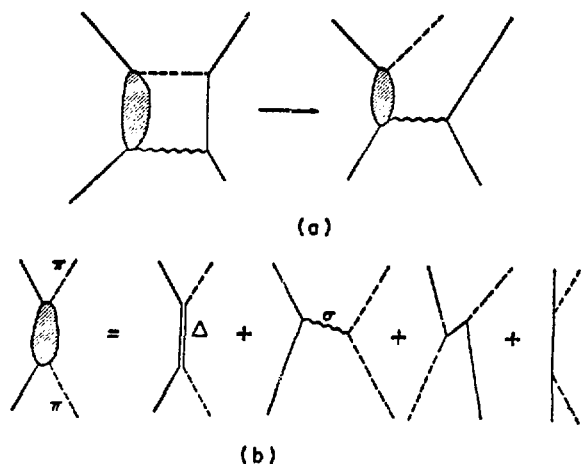
Fig. 25. A contribution to the two-pion exchange potential studied in pion production experiments.
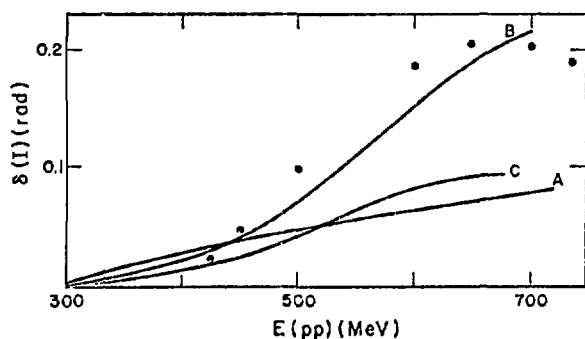
Fig. 26. Imaginary parts of the nucleon-nucleon phase shifts.[4] The solid curves are calculations of Ref. 71. A, for the $^1S_0$ channel; B for the $^1D_2$ channel with a small NN_ρ coupling constant; C, for the $^1D_2$ channel with a large NN_ρ coupling constant of Ref. 28. The points show the $^1D_2$ phase shifts from Ref. 73.

solve the many-body problem. Roughly half of the next two lectures will be devoted to developing aspects of many-body nuclear physics, and thus not directly dealing with the topic of mesons in nuclei. However, in order to appreciate the connection between the properties of a large part of the periodic table and the fundamental considerations we have just discussed, it is necessary to understand the theoretical methods being employed.

For the preparation of these lectures on the Brueckner-Bethe theory, I have relied heavily on the lectures by M. Baranger,[16] the review article by H. Bethe,[34] and the reviews by B. Day.[82,83] Reference 82 is an especially readable introduction to the methods.

The premise of the following discussion is that a collection of interacting nucleons can be described by a Hamiltonian

$$H = T + V \tag{89}$$

where T and V have representations given in Eqs. (11) and (12) in terms of creation and annihilation operators. We are thus supposing that the nuclear system can be described by a two-body potential. In the calculations that have been done, V is a nucleon-nucleon potential which fits the two-body data, i.e., the nucleon-nucleon phase shifts and the deuteron properties. Later we shall reinvestigate the validity of this representation from the point of view of meson theory (e.g., considering 3-body forces).

The system we shall try to describe is infinite nuclear matter. The reasons for studying this fictitious system were given in the first lecture.

1. Feynman-Goldstone Diagrams

We have already discussed the meaning of a Feynman diagram; our study of the properties of nuclear matter will strongly draw on this framework. However, the usual Feynman diagrams are not very convenient for the description of a large nuclear system because in this notation each nucleon must be represented by its own line: this would clearly be out of the question for a large system. Consequently, the Feynman-Goldstone notation for a Feynman diagram is commonly used. In this notation one draws the <u>difference</u> between the states in the Feynman diagram and some reference state, called the unperturbed ground state. This saves having to draw lots of unnecessary lines. The following discussion, through the description of Goldstone's theorem, comes from the lecture notes of M. Baranger.[16]

The reference state $|\phi_0>$ is taken to be an antisymmetrized product of orthogonal single-particle wave functions, which are plane waves for the case we are considering. All states of momentum $k < k_F \equiv$ Fermi momentum are occupied in $|\phi_0>$. We shall use capital letters A, B, C . . . to designate the single particle states which are occupied (i.e., A, B, . . denote the states $k < k_F$) and lower case letters a, b, . . . for those that are empty. For instance, Fig. 27a shows the propagation of the reference state, Fig. 27b is a Feynman diagram containing one interaction. The Feynman-Goldstone representation of Fig. 27b is shown in Fig. 27c; it has the same value as Fig. 27b but is drawn to give the <u>difference</u> between Figs. 27a and b The states that are missing from the reference state are given an arrow pointing downward and are called holes; those that are there in addition to the reference state are given an arrow pointing up and are called particles.

Now, it is convenient to define the basis states more carefully than we have already. Rather than use the kinetic energy in Eq. (89) it is convenient to add and subtract a potential energy term

$$H = H_0 + V - U \tag{90}$$

$$H_0 = T + U = \sum_A \left[\frac{k_A^2}{2m} + U(k_A) \right] a_A^+ a_A = \sum_A \epsilon(A_A) a_A^+ a_A \tag{91}$$

$$U = \sum_A U(k_A) a_A^+ a_A \tag{92}$$

60

and to use the energies $\varepsilon(k)$ as the unperturbed energies. Because the system is infinite we may take the eigenstates of H_0 still to be plane waves. The choice of U is to be made self-consistently later; for now we consider it to be arbitrary.

Let us now calculate the value of Fig. 27b or 27c. They both have the same value since they are different notations for the same physical process. Let

$$E_0 = \varepsilon(A) + \varepsilon(B) + . . + \varepsilon(Z) \tag{93}$$

Now, the value of Fig. 27b is, using the rules for Feynman diagrams discussed in the first lecture

$$\int_{-\infty}^{\infty} (-idt_0) \, e^{-i[\varepsilon(A)+\varepsilon(b)+\varepsilon(C)+\varepsilon(D)+...+\varepsilon(Z)](t'-t_0)}$$

$$<Ab|V|aB> \, e^{-i[\varepsilon(a)+\varepsilon(B)+\varepsilon(C)+...+\varepsilon(Z)] \, (t_0-t)}$$

$$\times \, \theta(t'-t_0)\theta(t_0-t) \tag{94a}$$

$$= \int_{-\infty}^{\infty} (-idt_0) \, e^{-i[E_0-\varepsilon(B)+ \varepsilon(b)] \, (t'-t_0)} <Ab|V|aB> \, e^{-i[E_0-\varepsilon(A)+\varepsilon(a)](t_0-t)}$$

$$\theta(t'-t_0)\theta(t_0-t) \tag{94b}$$

Now, let us define the zero of energy so that $E_0 = 0$. Then, Eq. (94b) becomes

$$\int_{-\infty}^{\infty} (-idt_0) \, e^{-i[\varepsilon(b)-\varepsilon(B)](t'-t_0)} <Ab|V|aB> \, e^{-i[\varepsilon(a)-\varepsilon(A)](t_0-t)}$$

$$\times \, \theta(t'-t_0)\theta(t_0-t). \tag{94c}$$

In order to decide what rules to assign the lines and vertices in the Feynman-Goldstone diagram, one has to return to the original Feynman diagram. Comparing Eq. (94c) to Fig. 27c we see that the matrix element of the potential enters always as, with the help of the arrows,

$$< \text{left out, right out} |V| \text{left in, right in} > \tag{95}$$

Furthermore, the propagator for a hole is

$$A \Bigg\downarrow \begin{matrix} t' \\ \\ \\ t \end{matrix} \quad = -e^{-i\varepsilon_A(t-t')}\theta(t'-t) \tag{96}$$

61

The overall minus sign is introduced for convenience later.

The transition from Feynman (F) to Feynman-Goldstone (FG) diagrams is not always unambiguous. There are two (and only two) types of F diagrams for which the FG equivalent is not obvious. They are shown in Fig. 28. Conversely, there are two types of FG diagrams which have no F equivalent. They are shown in Fig. 29. Diagrams of the type shown in Fig. 29, although they have no F equivalent, are convenient to retain. These terms always occur in pairs, one the exchange of the other, and signs are assigned to make these pairs cancel.

In the present lectures we are interested only in Feynman diagrams which begin and end with the unperturbed configuration. The reason for this will be clear shortly. In this case no FG diagrams have lines which extend from t or extend to t', e.g., they look as in Fig. 30. The rules for signs and coefficients are quite simple:

(1) All possible diagrams are drawn.

(2) Each distinct physical process should be counted once and only once.

(3) Each closed loop gets a (-) sign.

Otherwise the rules are as stated earlier. Diagrams which violate the Pauli principle can be shown to cancel.

2. Goldstone's Theorem

Goldstone's theorem for the energy of the ground state E is an expansion of this quantity in terms of $\varepsilon(k)$ and V. The theorem says

$$E - E_0 = \sum_L a_L \tag{97}$$

where the sum extends over all linked diagrams, i.e., over all diagrams which have no external lines and which are in one piece. To clarify the statement of the theorem, I shall indicate how it is derived.

To prove Goldstone's theorem, we must assume that the interaction V is turned on very slowly at negative times, so that the unperturbed wave function $|\phi_0\rangle$ evolves adiabatically into the exact ground state wave function $|\psi_0\rangle$ upon application of the time evolution operator U. We assume that the interaction has reached its full strength at time $t = 0$. The details of the turning on process are not important, but it must be sufficiently slow not to produce any transition to any exact state. The adiabatic theorem[16] states

$$|\psi_0\rangle = U(0, -\infty)|\phi_0\rangle \tag{98}$$

Now, if we let the system continue to evolve we get

$$|\psi_o(t)\rangle = U(t, -\infty)|\psi_o\rangle = e^{-i\Delta E t}|\psi_o\rangle \tag{99}$$

where

$$\Delta E = E - E_o \tag{100}$$

is the well-known time-dependence of an exact eigenfunction of H. Taking matrix elements of Eq. (99) we find

$$\langle\phi_o|U(t, -\infty)|\phi_o\rangle = e^{-i\Delta E t} \langle\phi_o|U(0, -\infty)|\phi_o\rangle \tag{101}$$

Each matrix element in this formula is equal to a sum of diagrams, each of which consists of a set of disconnected clusters. Schematically, we can write Eq. (101) as shown in Fig. 31 where every blob stands for a linked cluster. Now, to get the value of a diagram which consists of several individual linked clusters, we need only to multiply together the contributions `rom the individual clusters. This means that some time orderings of the separate clusters will violate the Pauli principle, but as we have said, Pauli violating terms always occur in pairs which cancel. Thus no harm is done. Thus the terms which contribute to the left-hand side of Eq. (101) factor into a piece which consists of all diagrams having their last interaction between times t=0 and t and a piece which is identical to the factor $\langle\phi_o|U(0,-\infty)|\phi_o\rangle$. We therefore write

$$e^{-i\Delta E t}=\Sigma \, \Pi \text{ [all possible clusters having their last interaction}$$
$$\text{in } (0,t)] \tag{102}$$

Now, to arrive at the theorem of Eq. (97) we must perform the operation $\Sigma\Pi$ in Eq. (102). First, consider n identical clusters. The top times t_{01}, t_{02}, . . ., t_{0n} of these clusters are in general all different. Then, if we let each t_{0i} vary from 0 to t, we are obviously including each history n! times, while according to our fundamental rule about counting it should be included only once. Therefore, we must divide by n! So, if a_c' is the contribution of a particular cluster c, $a_c' = \int_0^t (-i)dt_0 a_c = -ita_c$, the contribution of any number, including 0, of such clusters is

$$1 + a_c' + a_c'^2/2! + a_c'^3/3! +. . . = e^{a_c'} \tag{103}$$

There remains only to multiply together the quantities e^{a_c} arising from all possible different clusters, which gives

$$\prod_c e^{a'_c} = e^{\Sigma a'_c} \tag{104}$$

Thus, comparing Eqs. (102) and (104) we see

$$\Delta E = \sum_L a_L$$

thus proving the desired result.

Goldstone's theorem provides a systematic approximation scheme in which the energy per particle E may be calculated. Examples of linked clusters are shown in Fig. 32. Figures 32h and i give examples of terms which contain the interaction -U of Eq. (90), denoted by ----x.

I should end this section by illustrating how to calculate a cluster. Recall [Eq. (103)] that we have already integrated the last (topmost) time in a cluster. Therefore we have to integrate all except for the last time.

Figure 32a is the easiest. Since there is only one interaction, no time integrations remain to be done. The value of the term is

$$\frac{1}{2} \sum_A \sum_B \langle AB|V|AB \rangle \tag{105}$$

where the sums (actually integrals) over A and B run over single particle-hole states only, i.e., A, B $< \varepsilon(k_F)$. The factor of $\frac{1}{2}$ is needed according to rule 2 of this section to avoid counting the same contribution twice. The sign is + because the number of hole lines = number of closed loops.

Figure 32b requires one time integration. This term is redrawn in Fig. 33 with labels. The value of this diagram is

$$e^{-i(\varepsilon_a + \varepsilon_b - \varepsilon_A - \varepsilon_B)(t_0 - t_1)} \langle AB|V|ab \rangle \langle ab|V|AB \rangle \tag{106}$$

Integrating over time, $-i\int_{-\infty}^{t_0} dt_1$, summing over states and including the sign (again + because there are two hole lines and two closed loops).

$$\text{Fig. 32b} = \frac{1}{2} \sum_{\substack{AB \\ <\varepsilon(k_F)}} \sum_{\substack{ab \\ >\varepsilon(k_P)}} \langle AB|V|ab \rangle \frac{1}{\varepsilon_a + \varepsilon_b - \varepsilon_A - \varepsilon_B} \langle ab|V|AB \rangle \tag{107}$$
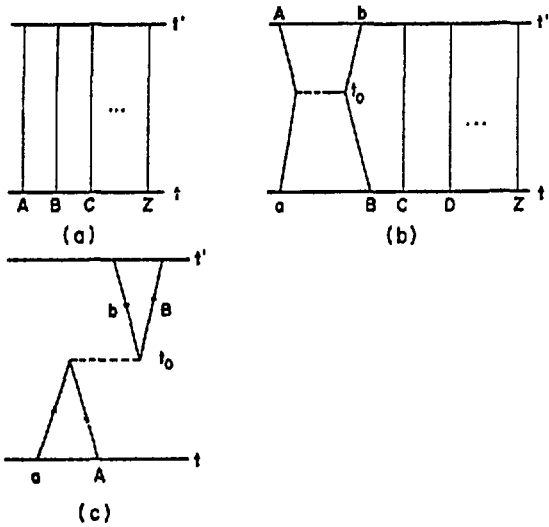
Fig. 27. Illustrating the difference between Feynman and Feynman-Goldstone diagrams.
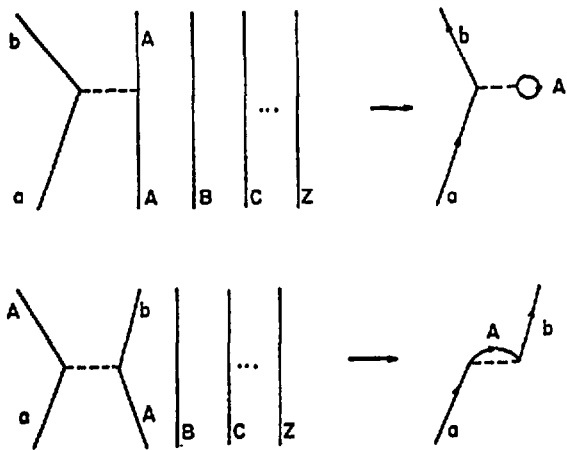
Fig. 28. Special cases of Feynman and corresponding Feynman-Gold-stone diagrams.
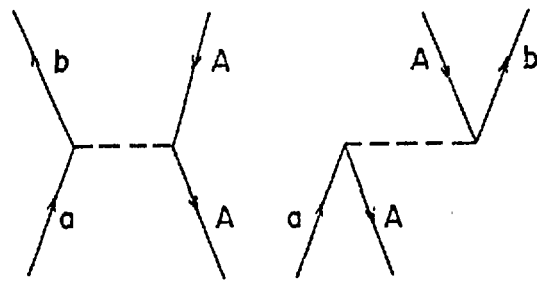
Fig. 29. Feynman-Goldstone diagrams with no Feynman equivalent.
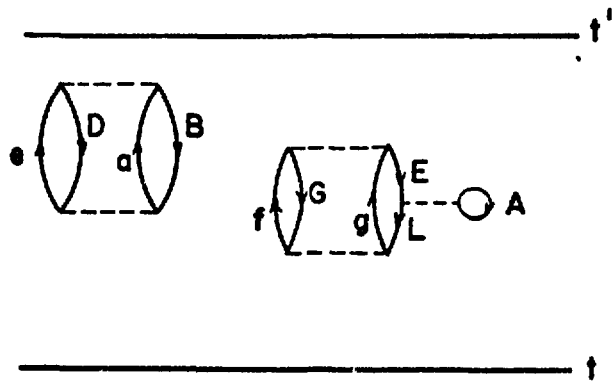
Fig. 30. A Feynman-Goldstone diagram which begins and ends in the unperturbed configuration.
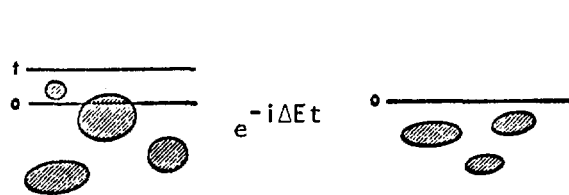
Fig. 31. A schematic representation of Eq. (101).
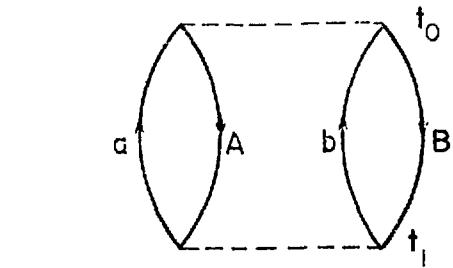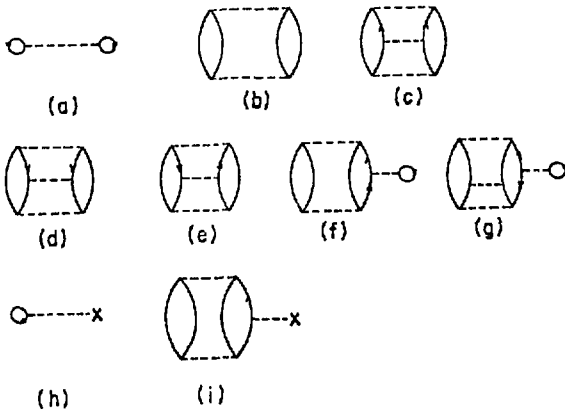
Fig. 33. Figure 32b redrawn with labels.

Fig. 32. Examples of linked clusters.

We may ignore the contribution from the limit $-\infty$ because the interaction was assumed to be slowly turned off at these times.

One result useful to note is that each time-ordering of a diagram (a time-ordering is a constraint which specifies the order in time in which the various interactions may occur. Figures 32a to f have only one possible time-ordering but Fig. 32g has two, depending upon the order in which the two intermediate interactions occur) can be written as a product of matrix elements of potentials and energy denominators

$$\text{Time-ordered diagram} = \langle |V| \rangle \frac{1}{\text{Energy Den.}} \langle |V| \rangle \frac{1}{\text{Energy Den.}} \cdots \langle |V| \rangle \qquad (108)$$

where

$$\text{Energy Den.} = -\sum_{\text{part.}} \epsilon_i + \sum_{\text{holes}} \epsilon_i \qquad (109)$$

The order of potentials in Eq. (108) *is the order in time as they occur in the* diagram, and the sums in Eq. (109) run over the particles and holes that exist during the time interval between the two interactions in Eq. (108). This result is easy to prove and one may consult Ref. 16 for details.

3. Energy of Nuclear Matter - Lowest Order

a. Theory-The Brueckner G-Matrix

Each of the linked clusters contains matrix elements of the potential V. But V has a very strong repulsion at short distances, as has been emphasized *in earlier lectures. Therefore we expect that the expansion in Eq.* (97) will not give meaningful results in its present form.

The idea of Brueckner was to sum together all similar diagrams so that instead of the matrix elements of V entering in each linked cluster, one would find the matrix element of a new object, the G-matrix. The sequence of terms that are to be summed together to form the G-matrix is shown in Fig. 34. From our discussion of how to evaluate diagrams, we see that this sequence has the value

$$G(\omega) = V + V \frac{Q}{\omega - h_o} V + V \frac{Q}{\omega - h_o} V \frac{Q}{\omega - h_o} V + \text{---}$$

$$= V + V \frac{Q}{\omega - h_o} G(\omega) \tag{110}$$

where the operator Q ensures that no intermediate states occur which are below the Fermi surface. The operator h_o is the single particle energy operator for the pair of nucleons that are interacting in Eq. (110). Because the sequence shown in Fig. 34 occurs within some larger cluster, the energy, ω, called the starting energy, may be determined from the other energies in the diagram in the same time interval.

The point is that the G matrix is a finite and well-behaved quantity even for an infinitely hard core potential V. Thus, the perturbation expansion for the energy is much better behaved when written in terms of G rather than V. The rearranged expansion in terms of G is often called the Goldstone expansion. The rules for it are very similar to the rules for the expansion in terms of V. The differences are: (1) the interactions are now G matrices everywhere instead of potentials (G-matrices are often denoted by wiggly lines, potentials by dashed lines); (2) to avoid double counting, two (or more) G matrices should never occur in succession between the same two particles.

It is generally believed that the single G matrix contribution to the energy, shown in Fig. 35 is the dominant contribution to the potential energy at normal nuclear matter density. To get the corrections to this it is necessary, however, to sum a large number of other terms according to a well-defined prescription, which I shall come back to later. Next I want to study in some detail the contribution of the terms in Fig. 35.

Let me begin by writing out the explicit expressions. Figure 35 specifies that the potential energy W is given approximately by

$$W = \frac{1}{2} \sum_{AB} \ <AB|G(\varepsilon_A + \varepsilon_B)|AB>$$

$$- \frac{1}{2} \sum_{AB} \ <AB|G(\varepsilon_A + \varepsilon_B)|BA>$$

$$- \sum_A <A|U|A> \tag{111}$$

The minus sign in the second term of Eq. (111) arises because the corresponding diagram has two hole lines and cne closed loop, hence receiving an overall factor $(-)^{2+1}$.

The discussion of the contribution of Fig. 35 is facilitated by working with wave functions rather than G-matrices. Consequently, we introduce the two-body wave function ψ defined as

$$\psi_{AB} \equiv \phi_{AB} + \frac{Q}{e} V\psi_{AB} \tag{112}$$

where ϕ is an unperturbed (plane wave) state

$$\phi_{AB}(\underset{\sim}{r}) = e^{i\underset{\sim}{k}_A \cdot \underset{\sim}{r}_A} e^{i\underset{\sim}{k}_B \cdot \underset{\sim}{r}_B} \tag{113}$$

e is the energy denominator in Eq. (110)

$$e = \omega - h_o \tag{114}$$

and G is the Brueckner G-matrix. ψ is useful because if we know ψ then we may calculate G according to the relationship

$$V\psi_{AB} = G\phi_{AB} \tag{115}$$

which follows from multiplying Eq. (112) by V and using the definition of G. Another useful definition is of the defect wave function ζ

$$\zeta_{AB} \equiv \phi_{AB} - \psi_{AB} = \frac{Q}{e} V\psi_{AB} \ . \tag{116a}$$

Several methods have been proposed for solving Eq. (112) for ψ. I want to mention only one, called the reference spectrum method. See Refs. 82 and 34 for more details.

To begin, I must discuss in some detail the energy denominator in Eq. (113), in particular the operator h_o. The eigenvalues of h_o are the energies $\varepsilon(k)$ defined in Eqs. (90) to (92).

68

$$\langle k_1' k_2' | G(\omega) | k_1 k_2 \rangle = \quad)---(\quad + \quad + \quad + \cdots$$
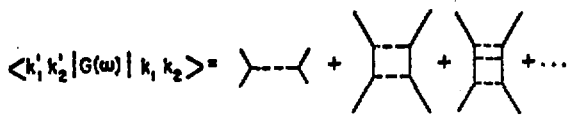
Fig. 34. The Brueckner G-matrix. All intermediate states are above the Fermi surface.

Fig. 35. Leading contributions to the potential energy term in the energy of nuclear matter. The wiggly lines are G-matrices; the dashed line ---x is the quantity -U of Eq. (90).

$$h_0 \, \phi_{ab} = [\varepsilon(k_a) + \varepsilon(k_b)] \, \phi_{ab} \tag{116b}$$

$$\varepsilon(k_a) = \frac{k_a^2}{2M} + U(k_a) \tag{117}$$

Because Eq.(112) contains the Pauli operator Q, h_0 will act only on states having no components below the Fermi sea, and therefore to solve Eq. (112) it is only necessary to specify $U(k)$ for $k > k_F$. The choice of energy for particles excited out of the Fermi sea is a moderately long story, about which I'll have more to say later. Suffice it to say here that setting the potential energy equal to zero for these states is believed to be at least an approximately correct procedure.

The energy variable ω in Eq. (114) assumes the values

$$\omega = \varepsilon_A + \varepsilon_B \tag{118}$$

according to Eq. (111). These are the energies of particles below the Fermi surface which are bound; hence, the potential energy for these states cannot be taken to be zero. (The potential felt by these particles must be chosen self-consistently.) Consequently, the energy denominator is

$$e \, \phi_{ab} = \left(\omega - \frac{\nabla_1^2}{2M} - \frac{\nabla_2^2}{2M} \right) \phi_{ab} = \left(\omega - \frac{k_a^2}{2M} - \frac{k_b^2}{2M} \right) \phi_{ab} \tag{119}$$

Note that $\omega - \frac{k_a^2}{2M} - \frac{k_b^2}{2M}$ is a negative number. It is convenient to rewrite e in terms of the relative and center of mass momenta, since the center-of-mass momentum $\underline{P}$ is conserved. Then we have

$$e_R = \omega - \frac{P^2}{4M} + \frac{\nabla^2}{M} \qquad (120)$$

where ∇^2 acts on the relative variable r. The second approximation of the reference spectrum method (the first was setting $U(k) = 0$ for particles) is to ignore the Pauli operator Q. This is not a bad approximation but it does require a correction, which is always made in realistic calculations.

Thus, the reference spectrum method approximation to the G-matrix consists of the following equations

$$< AB|G(\varepsilon_A + \varepsilon_B)|AB > = < AB|G_R(\varepsilon_A + \varepsilon_B)|AB > \qquad (121a)$$

where

$$< AB|G_R(\varepsilon_A + \varepsilon_B)|AB > = < \phi_{AB}|V|\psi_{AB}^R > \qquad (121b)$$

$$\psi_{AB}^R = \phi_{AB} + \frac{1}{e_R} V\psi_{AB}^R \qquad (121c)$$

It is easiest to solve Eq. (121c) by converting it to a differential equation. Multiplying through by e_R we get

$$(-\gamma^2 + \nabla^2) \zeta_{AB}^R(r) = - MV\psi_{AB}^R(r) \qquad (122a)$$

using Eq. (120) the definition in Eq. (116) and setting

$$- \frac{\gamma^2}{M} \equiv \omega - \frac{P^2}{4M} \qquad (122b)$$

We have already explained that $\omega - \frac{P^2}{4M}$ is a negative number. It is easiest to study Eq. (122) for S-waves. In this case we have

$$\left(\frac{d^2}{dr^2} - \gamma^2\right) \chi_0(r) = - MV(r) u_0(r) \qquad (123)$$

where χ_0 is the S-wave component of ρ_0 and u_0 the s-wave component of ψ. Now, because V vanishes for large r we have

$$\frac{d^2}{dr^2} \psi_0(r) = \gamma^2\chi_0(r) \qquad \text{large} \qquad (124)$$

70

or

$$\chi_0(r) \sim e^{-\gamma r} = u(r) - \phi_0(r) \qquad (125)$$

In other words, $u_0(r) \rightarrow \phi_0(r)$ at large r and the wave function ψ differs from a plane wave only when the two particles are close together. This is due to the fact that γ^2 is a positive number. If the scattering had occurred in free space then γ^2 would be negative and the wave function would be changed at large r. This "healing" of the wave function is a very important phenomenon. (The Pauli effect would give rise to healing also, because it does not allow particles to scatter into occupied states, but here the healing has occurred because of the spectrum of single particle energies.) It provides a physical explanation for why the shell model works so well, i.e., why nuclei are described so well by particles moving in well-defined single particle levels.

An important quantity is the defect integral K

$$K = \int |\overline{\rho_{AB}}|^2 d\tau \qquad (126)$$

where the bar indicates an average over states in the Fermi sea. This quantity may be thought of as a correlation volume, since as we have seen $\zeta \rightarrow 0$ for large separations of the two nucleons. One might expect intuitively that the Goldstone expansion would converge if this quantity were much smaller than the volume per particle, ρ^{-1}. One often defines a "smallness parameter" κ

$$\kappa \equiv K\rho \qquad (127)$$

and the condition for convergence is that $\kappa \ll 1$. Most calculations give $\kappa \simeq 0.14$ for densities near normal nuclear matter density. I shall return to the question of convergence later.

Let me end the discussion on the calculation of the G-matrix here. I have intended only to make you familiar with some of the ideas and you should refer to the reviews for further details. Now let me turn to a presentation of results of full calculations of nuclear matter energies with realistic potentials.

b. Results-Reid Potential

Results[84] for the Reid hard and soft core potentials are shown in Table XXII.[34] This table shows the contributions for the various partial waves to the potential energy and to the parameter κ at normal nuclear matter density ($\rho_0 = 0.17$ fm^{-3}). The table also shows the sum of the potential energy

contributions, the kinetic energy and finally the binding energy. Recall from the first lecture that the accepted experimental value is

$$E/A = -16 \text{ MeV at } k_F = 1.36 \text{ fm}^{-1} \tag{128}$$

One result to be learned from this table is that hard core interactions give less finding than soft cores; the soft core result seems to be giving a result closer to the experimental point than the hard core and this is taken as evidence strongly in favor of soft core potentials such as the Reid soft core over hard core potentials such as the Hamada-Johnston potential.

Table XXIII[34] shows the contributions to the binding energy as a function of density. Note that for $\rho \approx \rho_0$ the main contributions come from the S states; their sum is nearly equal to the total potential energy. The sum of the ^3P contributions is almost zero, which is closely related to the fact discussed earlier that there is essentially zero <u>central</u> interaction in the ^3P states. On the other hand, there is considerable repulsion in the ^1P state. The ^1D and sum of ^3D states are attractive. At the higher densities in this table the S states are no longer dominant; the attractive contribution of the D states begins to become important, but the sum of ^3P contributions remains small: as the density is increased, the average momentum of the particles becomes larger and hence the higher angular momentum states are more likely.

If the E/A vs k_F in Table XXIII is fit by a polynomial it is possible to perform the differentiations in Eq. (7) to find the incompressability K. One finds[34]

$$K = 134 \text{ MeV} \tag{129}$$

This is a bit low in comparison to the experimental value in Table III deduced from observations of the giant monopole resonances.

The contributions to κ from the various states are also shown in Table XXII. Note that the largest contribution comes from the ^3S state. This in turn is largely due to the strong tensor force rather than the repulsive core.

4. <u>Saturation of Nuclear Forces</u>

It is a well-known fact of nuclear physics that nuclear forces saturate, i.e., the energy as a function of density has a minimum. One manifestation of this is that the nuclear radius is proportional to $A^{1/3}$, showing that the average density in nuclei is roughly constant as a function of A. One of the requirements

of a successful theory of nuclear matter is that the saturation be predicted and be predicted to occur at the correct density.

If the nuclear force were purely central attractive nuclear forces, then the potential energy per particle would be proportional to the density. The contribution in S states would not increase as fast as ρ, but this would be compensated by increasing contributions coming from higher orbital angular momentum states. Figure 36[34] shows the contributions from the relative ^{1}S and ^{3}S states as a function of k_F. At small k_F the contribution of ^{3}S is numerically greater than that due to ^{1}S. This is to be expected because the attraction in ^{3}S leads to a bound state, the deuteron, while the ^{1}S state just fails to be bound. But at higher density, about $k_F = 1.3$ fm^{-1} the two curves cross, and beyond this ^{3}S is less bound than ^{1}S. This crossing is due to the tensor force, which contributes the major part of the binding in ^{3}S. Although the tensor force averages to zero for a pure ^{3}S state, if the tensor force is allowed to mix the ^{3}D and ^{3}S state together in a second order process shown in Fig. 36, then it can contribute to the energy. At low density the contribution is greater than at higher density because the Pauli exclusion principle forbids intermediate states in Fig. 36 for $k < k_F$; at higher density k_F is greater and more of the ^{3}D contribution is lost. A second effect for reducing the contribution in Fig. 37 is that the difference in potential energy between intermediate and initial states also increases with density. This effect is the most important cause for saturation.

The second cause for saturation is the partial exchange character of nuclear forces. Figure 38 gives the total contribution to the potential energy from S, P and D states. The S states have been discussed already. The P states give a repulsive contribution. This is made up mostly from the ^{1}P state as discussed earlier. If we had ordinary forces then the P curve would lie between the S and D curves. Because the central force in D states is less than in the ^{1}S state, the contribution of the D states is not as attractive as it would be for ordinary central forces. Note that the contributions from P and D states tend to cancel, leaving the dominant contribution in S states. Finally there is the short range repulsion. This is less important for saturation than the preceding effects near normal nuclear density.

5. Three- and Four-Body Clusters

So far we have considered only the lowest order term in the Goldstone expansion. The calculations with the Reid potential in this approximation show
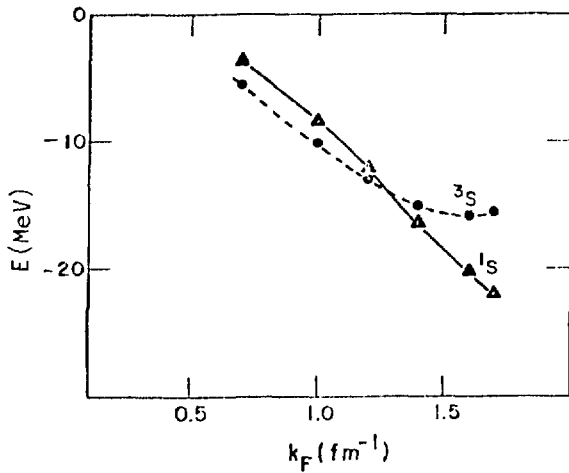
Fig. 36. Contribution to the binding energy of nuclear matter, of the ^1S and ^3S state, vs Fermi Fermi momentum k_F, according to the calculations of Sprung. The ^3S contribution saturates because of the important contribution of the tensor force.[34]
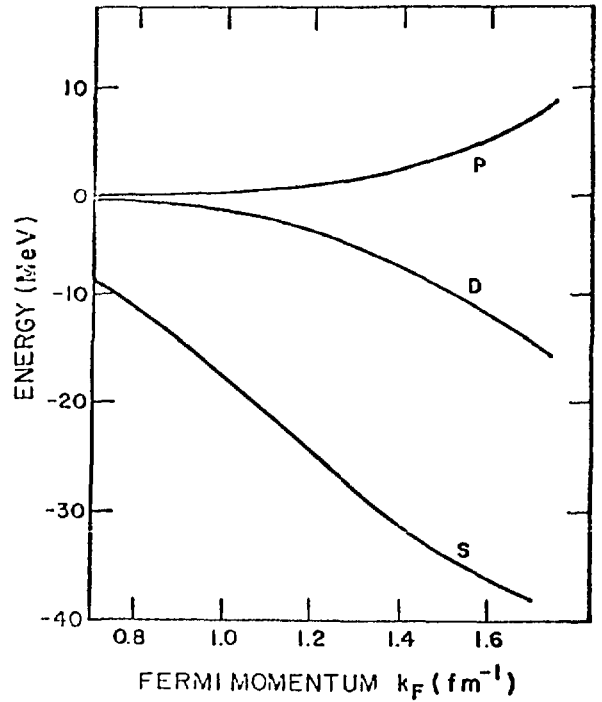
Fig. 38. Contribution of all S, P, and D states to the potential energy per particle.[34]
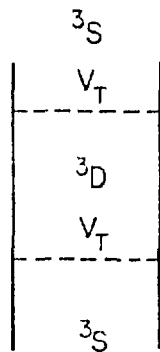
Fig. 37. A second order process occurring in G and involving the tensor force.
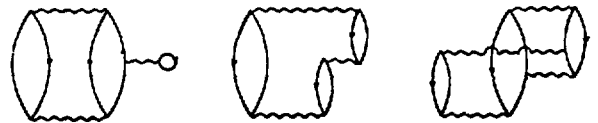
Fig. 39. Some contributions to the three hole line set.

TABLE XXII

PARTIAL WAVE CONTRIBUTIONS TO ENERGY

PER PARTICLE E/A AND PARAMETER κ [34]

State	Energy (MeV/Particle)			κ (percent)	
	Hard Core	Soft Core	Diff.	Hard	Soft
^1S	-14.66	-15.52	0.86	3.80	2.21
^1P	3.41	2.38	1.03	0.69	0.40
^1D	-2.75	-2.56	-0.19	0.02	0.02
^3S	-13.12	-14.99	1.87	13.54	9.78
$^3D_1$	1.47	1.46	0.01	0.01	0.02
$^3P_0$	-3.96	-3.31	-0.65	0.17	0.23
$^3P_1$	10.64	9.92	0.72	0.54	0.41
$^3P_2$	-6.82	-7.06	0.24	0.51	0.40
$^3D_2$	-4.54	-4.33	-0.21	0.04	0.04
$^3F_2$	-0.54	-0.56	0.02	0.00	0.00
J≥3	0.32	0.32	0	0	0
Sum	-30.55	-34.25	3.70	19.3	13.5
Kinetic	23.01	23.01			
Binding	7.54	11.24			

TABLE XXIII

CONTRIBUTIONS TO BINDING AT VARIOUS DENSITIES [34]

(MeV PER PARTICLE)

| k_F (fm^{-1})	0.7	1.0	1.2	1.4	1.6	1.7
ρ(fm^{-3})	0.023	0.068	0.117	0.185	0.276	0.332
^1S	-3.72	-8.36	-12.24	-16.35	-20.30	-22.10
^3S	-5.55	-10.15	-13.08	-15.19	-15.89	-15.67
^1P	0.13	0.55	1.30	2.76	5.34	7.17
$^3P_0$	-0.37	-1.34	-2.36	-3.56	-4.77	-6.54
$^3P_1$	0.72	3.02	6.15	11.08	18.30	22.90
$^3P_2$	-0.39	-1.93	-4.21	-7.91	-13.36	-16.84
^1D	-0.12	-0.65	-1.48	-2.69	-5.08	-6.54
$^3D_1$	0.07	0.40	0.87	1.62	2.67	3.31
$^3D_2$	-0.21	-1.17	-2.58	-4.85	-8.13	-10.19
$^3F_2$	-0.02	-0.11	-0.30	-0.64	-1.20	-1.58
J≥3	0.01	0.11	0.22	0.33	0.35	0.26
Sum	-9.45	-19.63	-27.71	-35.58	-42.05	-44.50
Kinetic	6.10	12.44	17.92	24.38	31.85	35.95
Binding	3.35	7.19	9.79	11.20	10.20	8.55

saturation at about the correct density but they do not come close to the experimental point. In order to understand whether this is a weakness of the interaction, one must evaluate higher order terms in the Goldstone expansion.

In order to calculate the next correction in the Goldstone expansion it is necessary to evaluate many terms together. The important terms are those that contain three independent hole lines; Rajaraman[85] showed that all these terms are of the same order of magnitude regardless of the number of interactions they contain, due to the hard core. Bethe[86] was able to sum the latter graphs using the method of Faddeev. Some of these contributions are shown in Fig. 39. The calculations are very difficult, but the initial work discussed in Ref. 34 gave a net attractive contribution of $\approx$ 1.8 MeV at k_F = 1.36 fm^{-1}. This result is very small compared to the two-body potential energy of about 33 MeV, in line with the expectations about convergence.

It is believed that the convergence of the Goldstone expansion is governed by the "small parameter" κ defined in Eq. (127). The two-body terms (two-hole line terms) contain one power of κ, the three-hole line terms two powers, four-hole line terms three powers, etc. It becomes progressively more difficult to

calculate the higher order contributions, but Day[87] has managed to estimate the four-hole line cluster and found them to be $\approx$ -0.24 MeV. In addition to the "true" four-hole line diagrams there are also other four-body correlations, which give a net contribution $\approx$ - 1.09 ± 0.5 MeV.

Day[83] has recently made more accurate calculations of the three- and four-hole line diagrams and finds the result shown in Fig. 40. The curve PWI is the latest variational calculation result Wiringa and Pandharipande[88] discussed in greater detail later. The remark worth making at this point is that the variational result lies <u>above</u> the Brueckner result which is consistent with the theoretical result that a variational calculation gives an upper bound on the energy. It is a bit disturbing, however, that the variational result saturates at such a larger density than the Brueckner result.

Further theoretical work is needed in order to firmly establish Brueckner-Bethe theory as a microscopic approach for studying nuclei. Day[83] has suggested tests for the consistency of Brueckner theory. Clearly, agreement with experiment is not a sufficient test of the many-body theory; a discrepancy could indicate either a breakdown of the many-body theory <u>or</u> a deficiency of the underlying interaction. Comparisons to results of alternative methods, e.g., the variational method discussed below, with the same interaction, is one way to assess the validity of the method, and such comparisons have stimulated improvements in Brueckner-Bethe theory calculations.

6. Calculations with Different Nucleon-Nucleon Interactions

Two-hole line results using a variety of potentials are shown in Fig. 41 as circles. Shown is the minimum in the energy vs. density curve for each interaction. The box is the experimental value and its associated uncertainty. Note that the circles define a band, called the Coester band. The band does not intersect the experimental box, however. In all cases where the potentials are carefully matched to the experimental nucleon-nucleon phase shifts the location of a point in this band depends upon the value of κ: potentials with smaller κ tend to saturate at higher density and with greater E/A. The dependence on κ is not unreasonable, based on the discussion of saturation: a larger κ means a stronger short range repulsion and/or a stronger tensor force, both of which enhance saturation.

One of the very interesting questions is: why does this band not include the experimental point? This failure is one of the most intriguing questions

in nuclear physics today. As we have said, there are two possible answers. One is that the Brueckner-Bethe theory has not been solved sufficiently well, and the other is that the underlying interaction is not correct. (A third possibility is that both the theory and interaction require improvements.)

The calculations in Fig. 41 are due to Wong and Sawada.[89] They also estimated the contributions of higher order terms in the Brueckner-Goldstone expansion. The arrows in Fig. 41 point to the two- plus three- plus four-hole line result. The result of Day discussed in connection with Fig. 40 is shown as the dashed line in Fig. 41. (The discrepancy between the WS and the Day results reflects recent progress in calculating the higher order terms.) Table XXIV shows the same results in tabular form along with the incompressibility coefficient K.

There are two interesting conclusions which can be drawn from Table XXIV and Fig. 41. The first is that for all the potentials, the higher order corrections are of about the same size and relatively small. The second conclusion is that different potentials which give roughly comparable reproductions of the nucleon-nucleon phase shifts may give substantially different results in nuclear matter. Much of this difference is related to the strength of the tensor force. These results should give some encouragement to the hope that a careful study of nuclear matter properties using the best many-body theories will eventually tell us about properties of the underlying nucleon-nucleon interaction which cannot be learned from the nucleon-nucleon phase shifts alone.

7. Meson Physics Corrections (Three-Body Forces, Etc.)

The energy per particle shown in Fig. 41 comes close to the experimental box but doesn't actually lie within it. Until very recently the calculation was not nearly as close to the experimental box and this has prompted searches for interaction-related effects which might move the theoretical saturation point.

The types of corrections to the potential which have been considered are generally of two types: (a) corrections to OBEP due to the nuclear matter background potential and (b) three-body force effects. The Bonn group[91] has considered the first type recently within an energy-dependent effective interaction formalism, and many groups have considered corrections of type (b). In both cases one needs an underlying meson exchange model in order to provide a theoretical basis for making the correction, i.e., a description purely in terms of phenomenological potentials would not permit such a question to be answered.

Let me first consider three-body forces. The need for three-body forces arises from the fact that some interactions cannot be described as the repeated action of a two-body potential. Figure 42 shows one such term. Figure 42a contains just the Λ intermediate state; Fig. 42b contains the entire pion-nucleon amplitude, which must be corrected because the nucleon pole piece, shown in Fig. 42c is included in part by the iterated one-pion exchange potential. As might be expected, the theory of folded diagrams[20] specifies how to express this correction diagrammatically.

The three-body force is a complicated operator which nobody has yet succeeded in using as an interaction in Schroedinger's equation. Instead, several levels of approximation have been involved. One important piece of the three-body force is the Λ contribution shown in Fig. 42a If lines 3 and 4 are the same states then the three-body force is the exchange diagram of the term shown in Fig. 43a. Both Fig. 43a and b violate the exclusion principle and the sign rule is such that they identically cancel. Hence in an actual calculation one should include both or neither. If one uses a two-body potential which reproduces the nucleon-nucleon scattering phase shifts, then the term in Fig. 43a is naturally included in V and the three-body force in Fig. 43b should be added in to cancel this piece of V. Alternatively, if one has a model of V with Fig. 43a given explicitly as a piece of it, then one may simply restrict the intermediate momenta so as to exclude the intermediate momenta[4] (see Fig. 43a) below the Fermi surface and omit the exchange term in Fig. 43b. A calculation of the latter type was done by Day and Coester (CD).[92] Actually these authors did their calculation in a coupled-channels framework with Δs and solved for the Brueckner G-matrix with the Pauli operator Q on all intermediate states. Their result was, not too surprisingly, that the exclusion of the intermediate states in Fig. 43a was a repulsive effect (it cuts out a piece of the ΔN intermediate state through which the nucleons obtain a large measure of their attraction) and grew more repulsive as the density increased. However, the curve E/A vs k_F in the lowest order approximation to the the Goldstone expansion still traced out the Coester band, i.e., the experimental point was still not reproduced!

TABLE XXIV

BINDING ENERGY, EQUILIBRIUM FERMI MOMENTUM k_F AND INCOMPRESSIBILITY K ACCORDING TO WONG AND SAWADA[89]

Potential	HJ[30]	ASC[31]	BKR[90]	UG1[27b]	BS[27a]	UG3[27b]
First order calculation (Two-body correlations only)						
B (MeV)	6.4	10.3	9.7	14.4	15.8	19.5
k_F (fm^{-1})	1.20	1.35	1.36	1.60	1.64	1.74
K (MeV)	65	120	110	170	330	240
Including higher order corrections						
B (MeV)	7.1	12.0	11.2	17.2	18.8	22.9
k_F (fm^{-1})	1.26	1.46	1.46	1.64	1.6·	1.81
K (MeV)	70	150	140	190	260	280

78
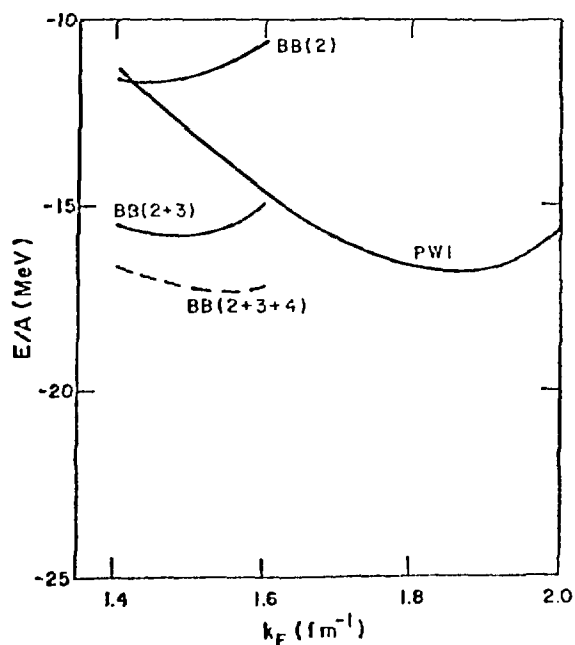
Fig. 40. Nuclear matter calculations according to Day.[83] The notation BB(2), BB(2+3) and BB (2+3+4) means Brueckner-Bethe calculations with 2-, 2- and 3-, and 2-, 3- and 4-hole line contributions, respectively.

Fig. 41. Results of two-hole line calculations with a variety of nucleon-nucleon potentials. The notation is the same as found in Table XXIV.

Fig. 42. Feynman diagrams which cannot be represented as an iteration of a two-body potential. The blob in (b) is the complete πN scattering amplitude, which must be corrected because it contains the nucleon pole, Fig. 42c.
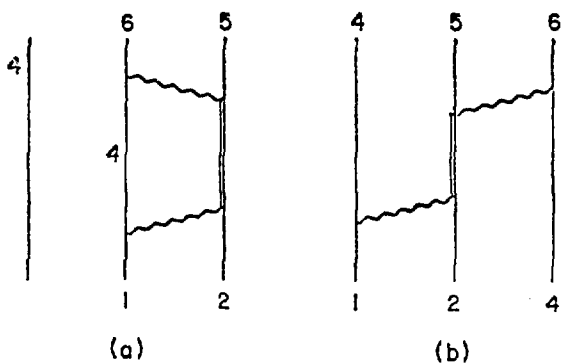
Fig. 43. Contributions to the 3-body force when state 3 = state 4 in Fig. 42a.

79

Day and Coester argued that if an additional attractive contribution with a dependence on $(k_F)^n$, $n < 4.2$ could be found, this in combination with their repulsive term which goes like $1.3\ k_F^{4.2}$ (MeV, if k_F is in fm^{-1}) could move the calculations off the Coester band. One should note that this piece of the interaction constitutes a saturation mechanism in addition to those discussed earlier. However, one should bear in mind that the extent of saturation depends upon the extent to which the Δs couple to nucleons, i.e., the magnitudes of the transition potentials for NN $\rightarrow$ NΔ, and that since the CD paper these potentials have been getting weaker. The matter is still not settled.

What about the remaining contributions to the three-body force? These calculations have a long history, but the modern calculations begin with Brown, Green and 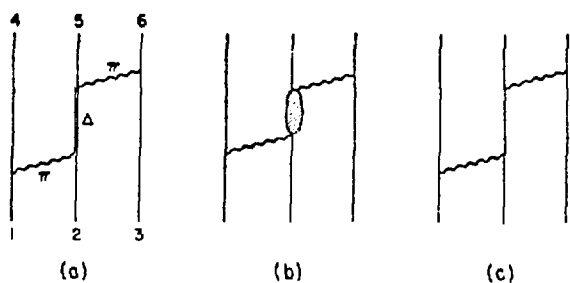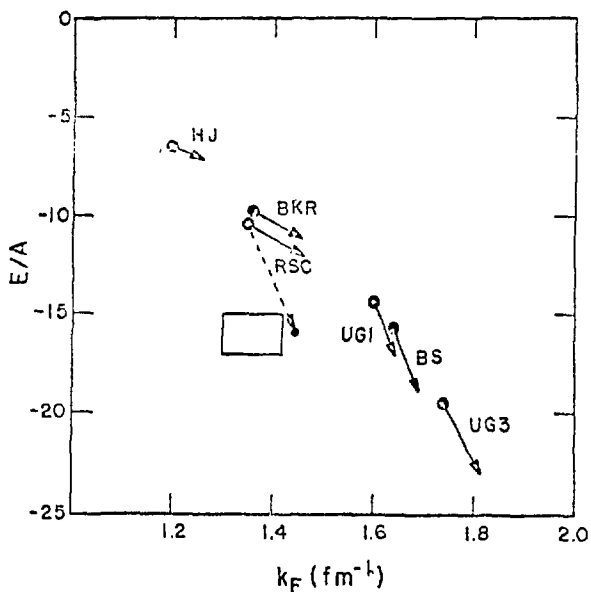Gerace.[93] The direct three-body force by itself, i.e., that of Fig. 42a with $1 = 4$, $2 = 5$ and $3 = 6$ is small, because there is no momentum transferred by the pion. However, the contribution becomes much larger, if the three-body force is followed by another interaction, as in Fig. 44. One of the most careful calculations of this term was done recently by Coon, et al.[94] They use the full three-body amplitude rather than just the Δ and make a correction for the iterated one-pion exchange. They find a contribution of the three-nucleon potential to the energy of symmetric nuclear matter to be -1.90 ± 0.2 MeV at normal density. They did not investigate the density-dependence.

Kouki, Smulter and Green[95] have recently considered three-body forces including exchange diagrams. They find an even smaller result, -1.1 MeV at $k_F = 1.4$ fm^{-1}, but they estimate some additional three-body forces including 3 Δs and find these terms large. More work needs to be done in order to settle the sizes of the three-body forces. KSG offer some hope that the three-body force in combination with the CD effect will be a mechanism to move results off the Coester band.

Finally, let me remark on the work of Anastasio, et at.[91] who use an energy-dependent OBE potential. They do a Brueckner calculation in a light finite nucleus and find that the energy dependence can improve the theory, but their effect is small in nuclear matter near normal density.

B. Variational Method

The variational principle says that if H is the Hamiltonian for a system and ψ a wave function, the energy E_{var},

$$E_{var} \equiv \frac{\langle \underline{\psi} | H | \underline{\psi} \rangle}{\langle \underline{\psi} | \underline{\psi} \rangle} \tag{130}$$

is an upper bound for the true ground state energy E_0, i.e.,

$$E_{var} > E_0 \tag{131}$$

By improving the choice of $\underline{\psi}$ one can come closer to estimating the actual ground state energy. In principle, the variational method is very easy to implement: one guesses $|\underline{\psi}\rangle$ and then one evaluates an integral, Eq. (130). However, for a realistic choice of $|\underline{\psi}\rangle$ a direct numerical integration is very difficult for a many-body system. Consequently, some systematic approximation scheme is needed, and the challenge of the theory is to invent such schemes for forces as complicated as the nucleon-nucleon interaction.

The simplest choice of wave function would be

$$\underline{\psi} = \Phi = A \prod_{p < p_F} \phi_p(r_p) \tag{132a}$$

where

$$\phi_p(r_p) = \frac{e^{i p \cdot r_p}}{\Omega^{1/2}} |s\rangle |t\rangle \tag{132b}$$

In this expression A antisymmetrizes the wave function, $|s\rangle$ and $|t\rangle$ are respectively spin and isospin wave functions. The wave functions are normalized in a box of volume Ω. However, this simple wave function would not be adequate for several reasons. The most serious difficulty is the strong, short-ranged repulsion present in realistic nucleon-nucleon interactions; with the wave function in Eq. (132) the repulsion would be allowed to dominate E_{var}.

To make a better estimate of the contribution of the repulsion, one could multiply Φ by a function $F(r_1, \ldots, r_A)$ which vanishes when any pair of nucleons come sufficiently close together. A simple function having this property is

$$F = \prod_{i < j} f(r_{ij}) \tag{133a}$$

where $f(r_{ij})$ might resemble the function in Fig. 45. With this prescription

$$\underline{\psi} = F\Phi . \tag{133b}$$

In order to make reliable estimates of the ground state energy of nuclear matter it is necessary that f be spin, isospin and momentum dependent. I will have more to say about this later.

Now, write

$$E_{var} = <T> + <V> \tag{134a}$$

$$<T> = \sum_i <\underline{\psi}, -\frac{\nabla_i^2}{2M} \underline{\psi}> / <\underline{\psi},\underline{\psi}> \tag{134b}$$

$$<V> = \frac{1}{2} \sum_{ij} <\underline{\psi}, V_{ij} \underline{\psi}> / <\underline{\psi},\underline{\psi}> \tag{134c}$$

The kinetic energy may be simplified by substituting Eq. (133b) into Eq. (134b) to get

$$<T> = \sum_i <\underline{\psi}, -\frac{1}{2M} [F \nabla_i^2 \Phi + 2\underset{\sim}{\nabla}_i \Phi \cdot \underset{\sim}{\nabla}_i F + \Phi \nabla_i^2 F] > / <\underline{\psi},\underline{\psi}> \tag{135a}$$

$$= \sum_i \frac{k_i^2}{2M} - \frac{1}{2M} \sum_i <\underline{\psi}, 2\underset{\sim}{\nabla}_i \Phi \cdot \underset{\sim}{\nabla}_i F + \Phi \nabla_i^2 F > / <\underline{\psi},\underline{\psi}> . \tag{135b}$$

1. What is a Cluster Expansion? Example: Interacting Boson Gas

In order to introduce the idea of the cluster expansion in many-body variational theory, let us consider a simpler problem than nuclear matter, namely the atomic system, liquid ^{4}He. This is a Bose system, and all atoms may therefore be assumed to occupy the lowest energy orbitals, plane waves with zero momentum. In this case the ground state wave function becomes

$$\underline{\psi} = \frac{1}{\Omega^{A/2}} F \tag{136}$$

The potential acting between two ^{4}He atoms has a strong short-ranged repulsion, and hence the factor F is needed as in the nuclear case. The only difference is that F is now of atomic rather than nuclear dimensions.

Because Φ is constant for bosons the first term of Eq. (135b) does not exist, and we write

$$<T> = \sum_i -\left(\frac{\hbar^2}{2M}\right) \int \frac{d^3 r_i}{\Omega} \ldots \int \frac{d^3 r_A}{\Omega} F\nabla_i^2 F / <\underline{\psi},\underline{\psi}> \tag{137a}$$

Here and in the remainder of the discussion we associate the normalization volume Ω with the volume elements d^3r_i. Each of the A particles has the same kinetic energy and hence Eq. (137a) may be written

$$T/A = - \frac{\hbar^2}{2M} \int \frac{d^3r_1}{\Omega} \ldots \int \frac{d^3r_A}{\Omega} \, F\nabla_1^2 F \; / <\underline{\psi},\underline{\psi}> \qquad (137b)$$

The potential energy $<V>$ of Eq. (134c) may be simplified, noting that each pair of particles (there are $A(A-1)/2$ pairs) contributes the same amount and hence

$$<V> = \frac{A(A-1)}{2} \int \frac{d^3r_1}{\Omega} \ldots \int \frac{d^3r_A}{\Omega} \, F^2 V_{12} \qquad (138)$$

This result is conveniently written in terms of the two-body distribution function g, defined by

$$g(r-r') \equiv \frac{1}{\rho^2} \sum_{i \neq j} <\delta(\underset{\sim}{r}-\underset{\sim}{r}_i)\delta(\underset{\sim}{r}'-\underset{\sim}{r}_j)> \qquad (139)$$

$$= \frac{A-1}{A} \int \frac{d^3r_3}{\Omega} \ldots \int \frac{d^3r_A}{\Omega} \, \prod_{i>j} f^2(r_{ij}) \; / <\underline{\psi},\underline{\psi}>$$

The physical interpretation of $g(r)$ is the probability of finding a particle in the volume element $d\tau$ at a distance r' from $r = 0$, given that there is a particle at $r = 0$. In terms of g, Eq. (138) becomes

$$V/A = \frac{1}{2} \rho \int d^3r \; V(r) \; g(r) \qquad (140)$$

2   Cluster Expansion for the Two-Body Distribution Function g(r)

The purpose of a cluster expansion is to give a systematic approximation scheme for evaluating the multi-dimensional integrals such as that appearing in Eq. (134c). As an example of the method, let me consider the cluster expansion for $g(r)$.

Because f differs from unity only when the two particles are close together, it makes sense to introduce the function $h(r)$

$$h(r) \equiv f^2(r) - 1,$$

which vanishes when $r > d$. The idea is now to express $g(r)$ as a power series in $h(r)$; if d is sufficiently small, then the series presumably converges rapidly since the likelihood that n particles will be close enough together for $h(r)$ to be non-zero gets smaller as n increases.

Consider first the normalization $< \psi | \psi >$

$$< \underline{\psi} | \psi > = \int \frac{d^3 r_i}{\Omega} \cdots \int \frac{d^3 r_A}{\Omega} \prod_{i>j} [h(r_{ij}) + 1] \qquad (142)$$

The power series in h is obtained by expanding the product

$$\prod_{i>j} [h(r_{ij}) + 1] = 1 + \sum_{i>j} h(r_{ij}) + \cdots \qquad (143)$$

It is convenient to express the various terms as diagrams. Imagine A points on the page, one for each atom. Then $h(r_{ij})$ is denoted by a line connecting points i and j. We may then state the general rule for a general term in Eq. (142): the points may be connected in any way as long as no more than one line connects any two points. Two examples are shown in Fig. 46. The value of Fig. 46a is

$$\frac{1}{2} \sum_{\substack{\ell,m \\ (\ell \neq m)}} \int \frac{d^3 r_\ell}{\Omega} \int \frac{d^3 r_m}{\Omega} h(r_{\ell m}) = \frac{A(A-1)}{2\Omega} \int dr\, h(r) \qquad (144)$$

There are also integrations over the points not shown explicitly, but these each contribute $\int \frac{d^3 r}{\Omega} = 1$. The factor of $\frac{1}{2}$ is necessary because of the particular symmetry of the diagram: if the line is rotated by 180° about its midpoint, the topology is unchanged. This means that the unrestricted summation in Eq. (144) counts each distinct diagram twice.

The value of Fig. 46b is

$$\left[\frac{1}{S_1} \sum_{\substack{p,q \\ R_1}} \int \frac{d^3 r_p}{\Omega} \int \frac{d^3 r_q}{\Omega} h(r_{pq}) \right] \left[\frac{1}{S_2} \sum_{\substack{\ell,m,n \\ R_2}} \int \frac{d^3 r_\ell}{\Omega} \int \frac{d^3 r_m}{\Omega} \int \frac{d^3 r_n}{\Omega} \right.$$

$$\left. h(r_{\ell m})\, h(r_{mn})\, h(r_{np}) \right] \qquad (145)$$

84

where R_1 and R_2 represent restrictions on the summation and S_1 and S_2 are factors necessary because of the symmetry of the individual terms. The restriction R_1 is that $p \neq (q, \ell, m, n)$, $q \neq (\ell, m, n)$; $S_1 = \frac{1}{2}$ as discussed in conjunction with Eq. (144). The restriction R_2 is that $\ell \neq (m, n, p, q)$, $m \neq (n, p, q)$, $n \neq (p, q)$; $S_2 = \frac{1}{3!}$ because there are $3! = 6$ orientations of a triangle on three points, so the unrestricted summation would count the same term six times. We may thus write the value of Fig. 44b as

$$\left[\frac{1}{2} \frac{(A-3)(A-4)}{\Omega} \int d^3 r_{pq} \, h(r_{pq}) \right]$$
$$\times \left[\frac{1}{6} \frac{(A-2)(A-3)(A-4)}{\Omega^2} \int d^3 r_{\ell m} \int d^3 r_{mn} \, h(r_{pm}) h(r_{mn}) h(r_{np}) \right] \qquad (146)$$

Note that the diagram factorizes into a number of terms equal to the number of <u>linked clusters</u> which constitute the diagram. Also note that when $A \to \infty$ the factors in front of the integrals become independent of the rest of the diagram, i.e., Eq. (146) becomes[*]

$$\left[\frac{1}{2} \rho A \int d^3 r \, h(r) \right] \left[\frac{1}{6} \rho^2 A \int d^3 r_{\ell m} \int d^3 r_{mn} \, h(r_{\ell m}) h(r_{mn}) h(r_{np}) \right] + O(A) \quad (147)$$

Generally, the value of a cluster in the limit $A \to \infty$ is

$$\text{Cluster} = \frac{A}{S} W_c \qquad (148)$$

where W_c is independent of A and contains a factor ρ^{n-1} where n is the number of points in the diagram.

There is only one other consideration. Suppose that a diagram has ν_Γ identical linked clusters Γ. Then the independent summation over coordinates will count the terms $\nu_\Gamma!$ too many times.

---

[*]Terms of $O(A)$ cannot actually be neglected. These are "factorizable terms" and are needed to cancel factorizable terms in $W_c(r_{12})$, Eq. (154). Our final result in Eq. (156) is correct because of the trick explained above Eq. (156).

Putting these ideas together, we have

$$< \underline{\psi} | \underline{\psi} > = \sum_D \quad \prod_{\substack{\text{Clusters } \Gamma \\ \text{in } D}} \frac{1}{\nu_\Gamma !} \left(\frac{A W_D}{S_D} \right)^{\nu_\Gamma} \tag{149}$$

For large A we may exchange the sum and product to get

$$< \underline{\psi} | \underline{\psi} > = e^{\sum_D \left(\frac{A W_D}{S_D} \right)} \tag{150}$$

Now consider the expansion for

$$\int \frac{d^3 r_3}{\Omega} \ldots \int \frac{d^3 r_A}{\Omega} F^2 (r_1, r_2, \ldots, r_A)$$

$$= f^2 (r_{12}) \int \frac{d^3 r_3}{\Omega} \ldots \int \frac{d^3 r_A}{\Omega} \prod_{\substack{i > j \\ \neq (1,2)}} [1 + h(r_{ij})] \tag{151}$$

Diagrams are again constructed as in the example of $< \underline{\psi} | \underline{\psi} >$. However, now there are two types of terms to be distinguished: those diagrams $W_c(r_{12})$ containing the points 1 and 2, which are not integrated, and those which do not contain the points 1 and 2. Some examples are shown in Fig. 47. In the limit $A \to \infty$ the value of any cluster is completely independent of the remainder of the diagram. Consider all diagrams containing the particular linked cluster $W_c(r_{12})$. This sum may be factorized in the $A \to \infty$ limit into the factor $W_c(r_{12})$ times the sum of all possible linked clusters. But we have just evaluated the sum over all possible linked clusters. It is

$$e^{\sum_D \left(\frac{A W_D}{S_D} \right)}, \tag{152}$$

i.e., just $< \underline{\psi} | \underline{\psi} >$. Therefore

$$\int \frac{d^3 r_3}{\Omega} \ldots \int \frac{d^3 r_A}{\Omega} \prod_{\substack{i > j \\ \neq (1,2)}} [1 + h(r_{ij})] = < \underline{\psi} | \underline{\psi} > f^2 (r_{12}) \sum_c W_c(r_{12}) \tag{153}$$

86
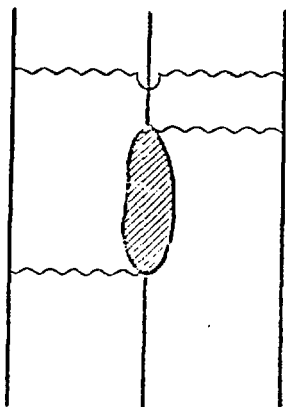
Fig. 44. A large contribution involving the 3-body force.

Fig. 45. A possible choice for f(r) in Eq. (133a). Beyond r=d f(r) = 1.

(a) **(b)**

Fig. 46. Examples of diagrams contributing to $< \underline{\psi} | \underline{\psi} >$. Points not connected by factors of h are not drawn.

(a) (b)
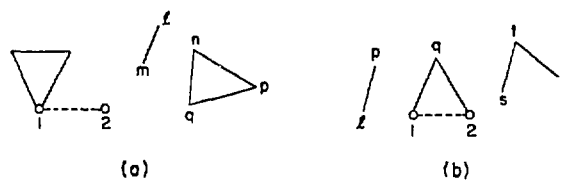
Fig. 47. Two contributions to Eq. (151). The dashed line represents $f^2(r_{12})$.

(a) (b) (c)
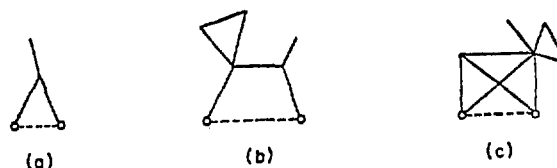
Fig. 48. Linked diagrams for $W_c(r_{12})$ having factorizable pieces.

from which we find $(A \to \infty)$

$$g(r_{12}) = f^2(r_{12}) \sum_c W_c(r_{12}) \tag{154}$$

The result is that g(r) is equal to $f^2(r_{12})$ times the sum of all linked diagrams connected to the points 1 and 2: all unlinked diagrams (i.e., linked clusters not connected to points 1 and 2) cancelled with the normalization $< \underline{\psi} | \underline{\psi} >$.

There is one further simplification before the final result. There are many diagrams in W_c which contain factorizable pieces, i.e., pieces which connect at a single point. Examples of factorizable diagrams are shown in Fig. 48. If

any diagram can be split into two or more completely separate pieces by cutting through a vertex on a diagram, the pieces which can be separated are factorizable, i.e., have values independent of the rest of the diagram.

Now, the further simplification is that <u>the diagrams which contribute to g(r) should not have any factorizable pieces</u>. The reason is, briefly, that the cluster expansion for the density ρ

$$\rho(r) = < \sum_j \delta(r-r_j)> / <\psi|\psi> \tag{155}$$

is the sum of all factorizable diagrams attached to a single point [this can be easily proved; it follows immediately after noting that the unlinked clusters in the numerator of Eq. (155) cancel, for the same reasons they cancelled in the calculation of g(r)]. Thus, it is entirely consistent to omit the factorizable pieces, provided the correct density factor is used at each vertex (when the f depend on spin and isospin the "factorizable" pieces may no longer be dropped).

The final result is

$$g(r_{12}) = f^2(r_{12}) \sum_c W'_c(r_{12}) \tag{156}$$

where W'_c is a diagram containing the points 1 and 2, containing no factorizable pieces.

The leading diagrams W'_c are shown in Fig. 49. The leading correction, Fig. 49a, is obtained by setting $g(r) = f^2(r)$. The first correction comes from the three-body term in Fig. 49b. To get an idea of its size, put $r = 0$ and find

$$C_3(0) = \rho \int (f^2(r) - 1)^2 \, d\tau \tag{157}$$

If this is small compared to 1, then the three-body term is small compared to the two-body term. We then expect terms involving four particles to be even smaller, and so on. This requires that $f(r)$ differ appreciably from 1 over a volume small compared to the volume per particle. Thus, the criterion for convergence of the cluster expansion is similar to that of Brueckner theory, $\kappa << 1$, [see Eq. (127)].

A great deal of effort has gone into calculating corrections to the simple approximations for bosons and Fermions, and the investigations for Fermions have seriously challenged the validity of the Brueckner-Bethe theory. If I have time I'll come back to this later.

C. Lowest Order Variational Theory for Fermions

Let me now jump to the problem of determining the equation of state of dense nuclear matter.[96,97,98] I will assume that the usual meson and baryon states are the relevent degrees of freedom and apply considerations developed in previous lectures. In this lecture I shall assume that real pions are not a constituent of dense nuclear matter, but will rather consider this possibility separately in the discussion of pion condensation.

The advantage of the variational method over the Brueckner theory is that in the former theory one has the possibility of keeping the correlation distance small and thereby increasing the chances that the lowest order variational result will give an accurate answer for the chosen correlation function. One pays for this simplification in that the trial wave function may not be optimal and hence the energy E_{var} may be too large by some amount.

Pandharipande[97] proposed a theory based on the lowest order variational result. He proposes that $f(r)$ be chosen so that

$$f(r) = 1 \quad r > d \tag{158}$$

and for $r < d$ he chooses f to minimize the lowest order cluster contributions to the energy of the system. d is defined as the radius of the volume which contains on the average just one particle. He calls this prescription LOVT (lowest order variational theory) and has shown that it is an accurate method for calculating the energy in liquid ^{3}He and ^{4}He. The method should also be reliable for calculating the equation of state of dense nuclear matter, for which the short-ranged repulsion dominates the remaining components of the interaction.

To begin we need an expression valid to lowest order in the functions $f(r_{ij}) = f_{ij}$ for the potential and the kinetic energy. An expression for the former follows immediately from Eq. (134c); in this expression the only correlations to be considered to lowest order are those between particles i and j. Therefore

$$< V> = \frac{1}{2} \sum_{ij} (\psi_{ij} |V_{ij} |\psi_{ij}),$$

$$\psi_{ij} = Af_{ij} \frac{e^{i\underset{\sim}{k}_i \cdot \underset{\sim}{r}_i}}{\sqrt{\Omega}} \frac{e^{i\underset{\sim}{k}_j \cdot \underset{\sim}{r}_j}}{\sqrt{\Omega}} |s_i>|t_i>|s_j>|t_j> \tag{159}$$

where the A antisymmetrizes the wave function ($A^2 = A$). The correlation function f_{ij} in Eq. (159) is to be state dependent.

The kinetic energy is given in Eq. (135b). The second piece of this may be rewritten as follows. First note

$$\Phi \sum_i \nabla_i^2 F = \sum_{ij} F \frac{\Phi}{f_{ij}} \nabla_i^2 f_{ij} + \sum_{ijk} \Phi F \frac{1}{f_{ij} f_{ik}} \nabla_i f_{ij} \cdot \nabla_i f_{ik} \tag{160}$$

The second term is of three-body character and will be dropped in accord with the philosophy of retaining terms involving only two nucleons. Now rewrite the first term as

$$\sum_{ij} F \frac{\Phi}{f_{ij}} \nabla_i^2 f_{ij} = \sum_{ij} \frac{\Phi F}{\phi_i \phi_j f_{ij}} \nabla_i^2 [f_{ij} \phi_i \phi_j]$$

$$- \sum_{ij} \frac{\Phi F}{\phi_i \phi_j f_{ij}} [f_{ij} \nabla_i^2 \phi_i \phi_j + 2 \nabla_i f_{ij} \cdot \nabla_i \phi_i \phi_j]$$

$$= \sum_{ij} \frac{\Phi F}{\phi_i \phi_j f_{ij}} \nabla_i^2 [f_{ij} \phi_i \phi_j] - \sum_{ij} F (-k_i^2) - 2 \sum_i \nabla_i \Phi \cdot \nabla_i F \tag{161}$$

Thus

$$< T > = \sum_i \frac{k_i^2}{2M} - \frac{1}{<\psi|\psi>} \sum_{ij} \int \frac{d^3 r_1}{\Omega} \cdots \frac{d^3 r_A}{\Omega} \frac{\psi^2}{\psi_{ij}} \left(\frac{k_i^2}{2M} + \frac{\nabla_i^2}{2M} \right) \psi_{ij} \tag{162}$$

To lowest order put all f's = 1 in ψ except f_{ij} to find

$$< T > = \sum_i \frac{k_i^2}{2M} + \frac{1}{2} \sum_{ij} \int \frac{d^3 r_i}{\Omega} \int \frac{d^3 r_j}{\Omega} \psi_{ij} \left[-\frac{\nabla_i^2}{2M} - \frac{\nabla_j^2}{2M} - \frac{k_i^2}{2M} - \frac{k_j^2}{2M} \right] \psi_{ij} \tag{163}$$

Combining Eqs. (159) and (163) we find[98]

$$W \simeq \sum_i \frac{k_i^2}{2M_i} + \frac{1}{2} \sum_{ij} \left(\psi_{ij}, \left[-\frac{\nabla_{ij}^2}{2\mu_{ij}} - \frac{k_{ij}^2}{2\mu_{ij}} + V_{ij} \right] \psi_{ij} \right) \tag{164}$$

where

$$\psi_{ij} = f_{ij}\phi_{ij}, \quad \phi_{ij} = e^{ik_{ij} \cdot r_{ij}} s_i s_j t_i t_j \qquad (165)$$

μ_{ij} = reduced mass for particles i,j

k_{ij} is the relative momentum for particles i,j.

In the present lecture we shall consider that the state of the neutron star matter is liquid. It is a possibility that the matter will crystallize due to the short-range repulsion. The repulsion is, however, now considered too weak to give rise to a lattice; see, however, the discussion in the next lecture.

Now, we want to choose f to minimize W. However, we want to restrict f to short enough distances so that the leading term in the cluster expansion suffices. Thus Pandharipande introduces a Lagrange parameter λ_{ij}, i.e.,

$$V_{ij} \rightarrow V_{ij} - \lambda_{ij} \qquad (166)$$

With this substitution W becomes W', and the idea is to minimize W' by varying λ_{ij} subject to the condition that f heals at a distance d. The condition that W' be minimum is that

$$\left(- \frac{\nabla^2}{2\mu_{ij}} - \frac{\hbar^2 k_{ij}^2}{2\mu_{ij}} + V_{ij} \right) \psi_{ij} \equiv h_2 \psi_{ij} = \lambda_{ij} \psi_{ij} \qquad (167a)$$

with

$$\left. \begin{array}{l} f_{ij} = 1 \\ f'_{ij} = 0 \end{array} \right\} \quad \text{at } r = d \qquad (167b)$$

[This may be derived by setting $\delta W' = 0$ upon varying $\psi_{ij} \rightarrow \psi_{ij} + \delta\psi_{ij}$. Insisting that $\delta W' = 0$ for arbitrary $\delta\psi_{ij}$ leads to Eq. (167).]

If ψ satisfies these conditions we have

$$h_2\psi_{ij} = V_{ij}\psi_{ij} \ r > d \qquad h_2\psi_{ij} = \lambda_{ij}\psi_{ij} \ r < d \qquad (167c)$$

It thus follows that the minimum in energy (W) is

$$W = \sum_i \frac{k_i^2}{2M_i} + \frac{1}{2} \sum_{ij} (\psi_{ij}, \lambda_{ij}, \psi_{ij})_{r < d} + \frac{1}{2} \sum_{ij} (\psi_{ij} V_{ij} \psi_{ij})_{r > d} \qquad (168)$$

1. Equation of State for Dense Nuclear Matter

Now, the idea is to apply this theory to dense nuclear matter. First, can we get some idea of the accuracy of the theory? Pandharipande has applied it to ^{3}He and ^{4}He and gets close to the experimental energies. Figure 50 shows some of his early results. We thus expect that the theory is able to make a sensible estimate for dense nuclear matter.

In order to make an estimate of the equation of state at high densities we must have an idea of the composition of dense matter. There is no a priori reason to expect matter to consist only of neutrons and protons; we must allow the possibility that all strongly interacting particles are constituents. To decide which are relevant it is necessary to minimize the energy with respect to the concentrations of the various species. So, to begin with, all hadrons and leptons are candidates.

Possibly at some very high density the observed particle spectrum becomes the wrong set of variables, and quarks and gluons become the correct variables; this possibility has been discussed in Ref. 100 where it is concluded that the phase transition will not occur for $\rho \lesssim (10\text{-}20)\rho_0$. We will, therefore, not consider this further.

Neutron star matter at low density consists of ordinary nuclei in a lattice. As the density is increased the nuclei grow larger and more neutron rich in order to minimize the energy of the electrons. The electrons become significant on the nuclear energy scale because of the high densities involved. For example, suppose neutron star matter at a total density $\rho \approx \rho_0$ consisted of equal numbers of neutrons and protons. Then the density of electrons would be

$$\rho_e = \rho_p = \rho_0/2 \approx 0.08 \text{ fm}^{-3} \tag{169}$$

Because electrons are Fermions they fill a Fermi sea up to momentum k_{Fe},

$$k_{Fe}^3 = 3\pi^2 \rho \tag{170}$$

$$\Rightarrow k_{Fe} = 1.33 \text{ fm}^{-1} \tag{171}$$

But an electron of this momentum has a kinetic energy

$$T_e = \sqrt{k_{Fe}^2 + m_e^2} - m_e \approx k_{Fe} = 263 \text{ MeV}, \tag{172}$$
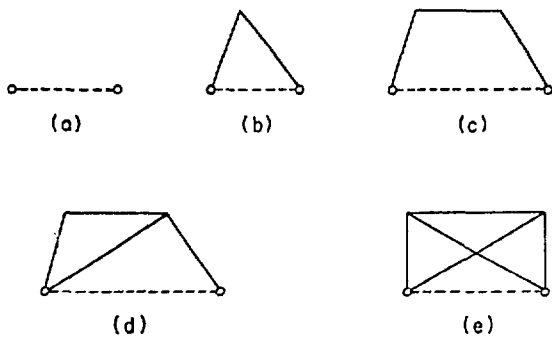
Fig. 49. Leading corrections to g(r).
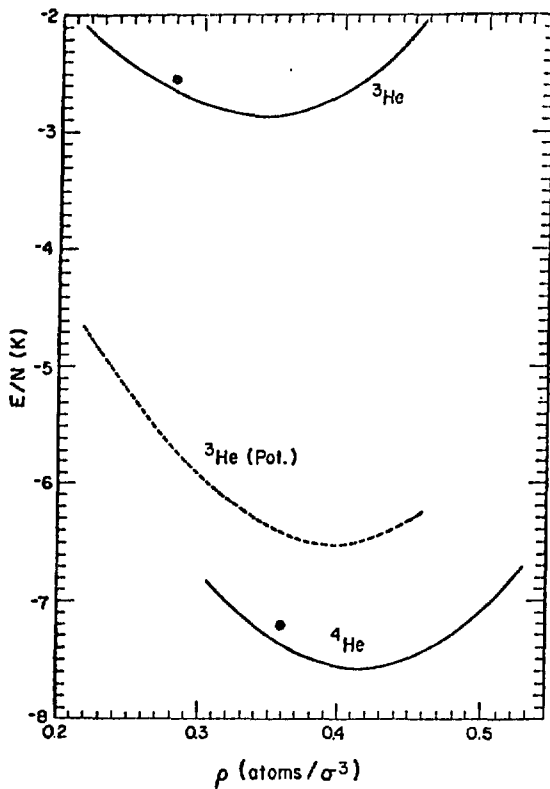
Fig. 50. Energy per particle vs density for the atomic systems ^{3}He and ^{4}He. The solid circles indicate the experimental equilibrium points.

In order to have coexisting neutron, proton and π^- phases in equilibrium it should not cost energy for the reaction

$$n \rightleftarrows p + \pi^-$$

which is very considerable. In order to minimize the electron kinetic energy, it pays for electrons and protons to combine to form neutrons as the density increases. The final balance of concentrations of N, P, and e is a compromise between minimizing the nucleon and electron energies. The mathematical condition for determining the concentrations in this state is

$$\mu_N = \mu_p + \mu_e \tag{173}$$

where the μ's are the chemical potentials of the particles, i.e., the energies required to add or remove a particle from its respective Fermi sea. Finally, at some density close to the density of normal nuclear matter, the nuclei have become so big that they touch, forming a uniform distribution of neutron matter with a small admixture of neutrons and protons.

Let us next consider the possibility of having pions in neutron star matter. The discussion I give now leads to the wrong conclusion for reasons discussed in the section on pion condensation, but the exercise is instructive. Suppose to begin with that the particles are non-interacting. The question is, is the pion more efficient than the electron at neutralizing the charge of the protons?

$$\tag{174}$$

to go. Because nucleons are Fermions, the energies to add and subtract nucleons are the energies at the top of the Fermi sea,

$$\frac{k_F^2}{2M} .$$

Because the pions are bosons, they may all be put into the same state; the lowest energy for a non-interacting pion is of course m_π. Balancing the energy gives the condition

$$\frac{k_{Fn}^2}{2M} = \frac{k_{Fp}^2}{2M} + m_\pi \tag{175}$$

Assuming that there is no admixture of protons to begin with $(k_{Fn} = 0)$, the threshold occurs where

$$k_{Fn} = \sqrt{2M\, m_\pi} \simeq 2.6 \text{ fm}^{-1} \tag{176a}$$

or

$$\rho_n = \frac{k_F^3}{3\pi^2} \simeq 3.71\ \rho_0 \qquad (\rho_0 = 0.16 \text{ fm}^{-3}) \tag{176b}$$

This is not an extremely high density for neutron stars; $\rho \simeq 10\ \rho_0$ is about the highest density one could expect before the star collapses. The conclusion is, therefore, that π^- could be a constituent of neutron star matter. This is not realistic, however, because the nuclear interactions have been ignored. Historically, the π^- was ruled out because the π^- neutron interaction is strongly repulsive in relative S states:

$$U_{\pi^-} \text{ (MeV)} \cong 217\ \rho_n \text{ (fm}^{-3}) \tag{177}$$

The addition of this term excludes π^- up to very high density as one may easily verify. However, the story changes when π-nucleon p-waves are considered; see next lecture.

In any case, I shall omit the π meson now. It is necessary to choose an interaction for the strongly interacting particles, calculate W and minimize this with respect to the concentrations of N, P, e^-, μ^-, Λ, Σ, Δ,...

The choice of a proper interaction can be made only on the basis of an educated guess. At high density the repulsive core is the dominant interaction, and we expect that the choice of core might make a difference in the equation of state. So, there are basically two questions

94

(1) how much latitude is permitted in the strength of the core in the nucleon-nucleon interaction if we insist that the interaction fit the nucleon-nucleon phase shifts?

(2) how much difference do these different potentials make in the description of the equation of state?

The idea[98] is to try to choose potentials which combine the best features of meson theory potentials and the phenomenological potential of Reid. The most serious shortcoming of Reid's[31] potential for our purposes is that he made no attempt to select the core to be the same in each partial wave state, as would be the case if the core were due to a ω-meson exchange. However, there may be some spin-isospin dependence of the core interaction; for example the ρ meson ($m_\rho \approx m_\omega$) was seen [cf. Eq. (55)] to give a central force $\sim \sigma_1 \cdot \sigma_2 \, \tau_1 \cdot \tau_2$. The sign is such as to make the core V_c satisfy the relationship

$$V_c(^1P) > V_c(^3P) > V_c(^1S) = V_c(^3S) \tag{178}$$

We fit the potential with the weaker requirement

$$V_c(^1P) > V_c(^3P) \geqslant V_c(^1S) \geqslant V_c(^3S) \tag{179}$$

The conditions on the interaction are

(1) It must have a repulsive core in all states.

(2) The core strength must satisfy the inequality in Eq. (179).

(3) The nucleon-nucleon interaction must give the correct experimental phase shifts for energies up to 350 MeV, and the correct binding energy and quadrupole moment of the deuteron, like Ried's.

(4) The nucleon-nucleon interaction must saturate nuclear matter at a reasonable density and energy.

(5) Hyperonic interactions must be consistent with the experimental measurements, especially those on hypernuclei. These indicate that the hyperon-nucleon interaction is less attractive than the nucleon-nucleon interaction, but not by much.

(6) It is desirable, but not necessary, that the repulsive core have the same range in all states.

(7) It is desirable that the repulsive core have a range corresponding to the exchange of an ω-meson. It is possible to find a family of interactions

consistent with these criteria and one purpose of the calculation in Ref. 98 was to see whether there was much variation among the different models.

In the calculation, the tensor force coupling between states of different L was ignored. There are two reasons for this: (a) the density of protons is relatively small and (b) the high density means that the tensor force coupling will be largely saturated. (See discussion of tensor force saturation in previous lecture.) In the actual calculation the details of the interactions were retained only for $L \leq 1$. For higher partial waves an average was used in all even states and an (different) average force in odd states. Five interaction models were considered, consistent with the above criteria. For the interaction between hyperons and nucleons, Δ and nucleons, and among the hyperons and Δ we took an exchange interaction which is the same as the NN $^1D_2$ in even states and the spin-isospin average of the NN P wave potentials in odd states.

The problem is now to solve for all pairs of particles the Eqs. (167a) and (167b), determining λ for a given potential model. In practice it is only necessary to solve the eigenvalue equation for the lowest two partial waves because the centrifugal barrier cuts out the contribution of higher partial waves to W for the small values of d used. Next W is determined from Eq. (168). It can be shown[98] that minimizing W with respect to the concentrations of the various species is equivalent to solving the following set of non-linear equations.

$$\mu_\alpha + m_\alpha = \mu_n + m_n - q_\alpha \mu_e \tag{180a}$$

$$\sum_i q_i c_i = 0 \quad \text{(charge neutrality)} \tag{180b}$$

$$\sum_\alpha c_\alpha = 1 \quad \text{(baryon conservation)} \tag{180c}$$

where

$$\mu_\alpha = \frac{\partial}{\partial c_\alpha} (E/A - \sum c_\alpha m_\alpha) \tag{180d}$$

where $c_\alpha = \rho_\alpha / \rho$ is the concentration of a given species. Typical results for the composition of the dense matter are shown in Fig. 51. The heavy baryons are energetically favored at high density for two reasons: (1) the energy per particle becomes very large at high density for a single species (such as neutrons), for essentially the same reasons discussed in the case of the electron. It

therefore pays energetically at some point to take neutrons off the top of the neutron Fermi sea and begin filling a Fermi sea of a different species. (2) The pairs involving the more massive particles have a greater reduced mass and hence can afford to avoid each other's repulsive cores more easily than two nucleons. The point is that when the correlation function bends more rapidly, which is necessary to keep particles apart, there is less kinetic energy associated with the bend for the heavier pairs.

The energy per particle vs. density is shown in Fig. 52. This result is parametrized to give

$$E = 236 \, \rho^{1.54} + m_n \quad \text{MeV/particle, } \rho \text{ in fm}^{-3} \tag{181}$$

Since

$$P = \rho^2 dE/d\rho \tag{182}$$

we find

$$P = 364 \, \rho^{2.54} \quad \text{MeV/fm}^3 \tag{183}$$

In order to find the properties of neutron stars one must solve the equations of hydrostatic equilibrium (for example, Ref. 101), which requires $P(\varepsilon)$ where

$$\varepsilon = \rho E \tag{184}$$

One point to note is that the appearance of many species has the effect of keeping the Fermi momenta of the individual species non-relativistic. Thus, dense matter is not a relativistic problem, anyway not much more than is nuclear physics at ordinary nuclear matter densities. Often, simplified approaches are taken in which the possibility of many species is not considered. This neglect leads to the artificial difficulty of creating a relativistic problem out of one which really isn't. (See, e.g., Ref. 15.)

2. Results: Structure of Neutron Stars

The five potential models were used to calculate the mass M_G, radius R, moment of inertia I and other quantities characterizing the neutron star.[101] If $P(\varepsilon)$ is given, then the equations of hydrostatic equilibrium may be integrated to give these profiles of the neutron star. Because of the intense gravitational field, general relativity must be considered, and the equations modified for this effect are known as the Tolman, Oppenheimer, Volkeff equations. Results for the gravitational mass, radius and moment of inertia are shown in Figs. 53, 54, and

55. The properties of the neutron star at its maximum mass is shown in Table XXV. In Figs. 53 to 55 and Table XXV, the notation for the various models is the same as that given in Ref. 101.

The neutron stars predicted by these models look all rather similar; varying the parameters of the potential within limits consistent with the criteria (1) to (7) really does not give rise to a very large variation in neutron star properties. Pandharipande calculated the equation of state based on the Reid potential, which is not consistent with these criteria, as discussed, and subsequent calculations gave maximum mass neutron stars for hyperonic and neutron matter, respectively, $1.41\odot$ and $1.66\odot$. Thus, using a consistent repulsion throughout the partial wave contributions to the nucleon-nucleon potential gives more massive neutron stars by as much as 30%. This is important, as we see from Table IV, because the experimental determination of neutron star masses is put at $1.3 \pm 0 2 \odot$. At least one model has been decisively ruled out. The theory of Leung and Wang[102] predicted the maximum mass of a neutron star before collapse due to gravitational instability to be $0.5\odot$, well below the masses of observed pulsars in Table IV. One puzzling feature of the results in Table IV is that the maximum masses and moments of inertia are comfortably below those corresponding to the maximum values (Figs. 53 and 55), whereas the observed radii correspond to the most massive neutron stars allowed. These data are not necessarily inconsistent because they correspond to measurements on different stars, but it is puzzling that some of the stars observed have a radius smaller than the minimum allowed by these calculations before gravitational collapse occurs.

VII. PION CONDENSATION

In the remainder of the talk I want to address the interesting subject of pion condensation. I shall take the point of view of nuclear physics, in which many questions discussed already in these lecutres can be brought to bear on the problem. There exists another approach which emphasizes some models popular in particle physics (the sigma model), which Gerry Stephenson will discuss.

A. Model of Sawyer and Scalapino for π^- Condensation

Let me now discuss more carefully the question of whether there can be a pion phase present in the ground state of nuclear matter. I briefly touched on this subject during the preceding lecture and concluded that no pion phase should exist in neutron matter such that all pions occupy the state of minimum
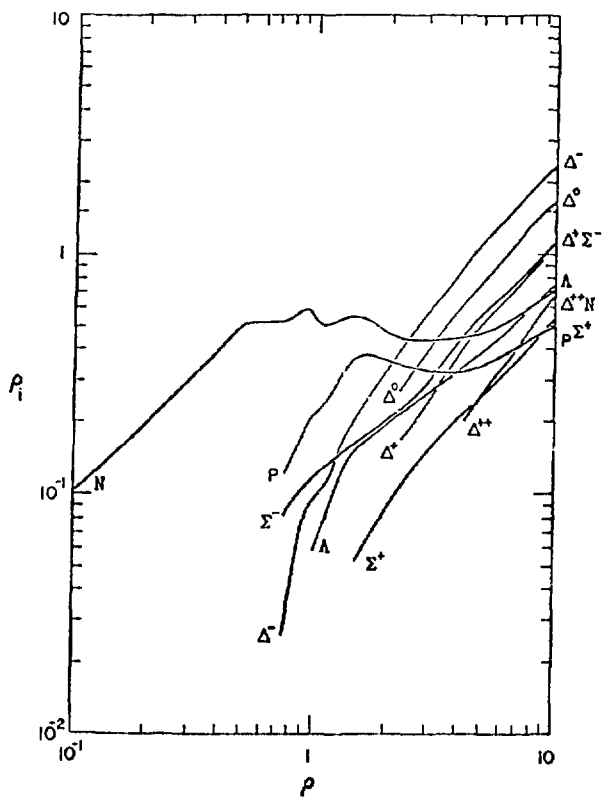
Fig. 51. Typical behavior of partial densities vs total baryon density.
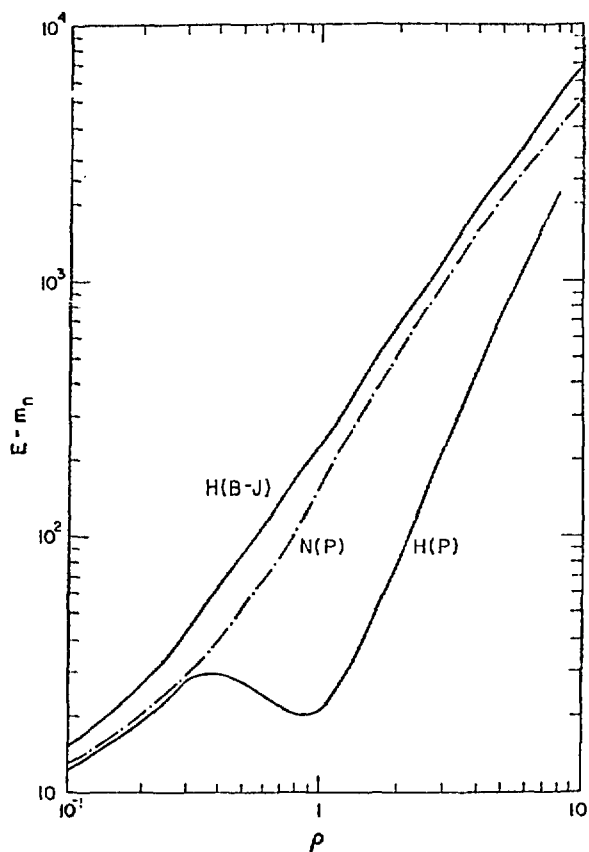
Fig. 52. Energy per particle (MeV) vs density (fm^{-3}) for Model I of Bethe and Johnson[98] (B-J). Shown for comparison are results of Pandharipande[97] (P) based on the (unmodified) Reid interaction. H stands for hyperonic matter, N for pure neutron matter.

TABLE XXV

PROPERTIES OF THE MAXIMUM MASS NEUTRON STAR MODELS

Model	g_ω^{2*}	r_{core}/μ*	$M_{g,max}/M_\odot$**	ρ_c/ρ_0	$R(Km)$+	$I(gm\text{-}cm^2)$++
I H	47	7	1.85	9.5	9.73	1.51×10^{45}
III H	47	7	1.73	11.2	8.88	1.20×10^{45}
V H	22	5.5	1.65	10.2	9.38	1.19×10^{45}
V N	22	5.5	1.76	10.4	9.18	1.29×10^{45}

---

*These columns give the strength and range of the repulsive core in the interaction models.

**The maximum gravitational mass of a stable neutron star.

+The radius.

++The moment of inertia.

momentum, $p_\pi = 0$. This conclusion was
forced because the interaction between
π^- and neutrons is repulsive in relative
πN S-states. The subject of π conden-
sation becomes interesting when the
interaction between pions and nucleons
in relative πN states of $\ell = 1$ is con-
sidered.

The subject of pion condensation
was invented independently by Migdal,[103]
Sawyer and Scalapino,[104] and Kogut and
Manassah.[105] By way of introduction, I
want to consider the model of Sawyer
and Scalapino in some detail. It

Fig. 54. Neutron star radius R, vs cen-
tral baryon density ρ_c. See
Fig. 53 for curve designations.

Fig. 53. Gravitational mass M_G vs cen-
tral baryon density $\rho_c = m_n$
$n_{B,c}$, where m_n is the neutron
rest mass and n_B is the bary-
on number density, for Model
I H (─ ·─ ─), Model III H (──
──), Model V H (──────), and
Model VN (─ ─ ─).
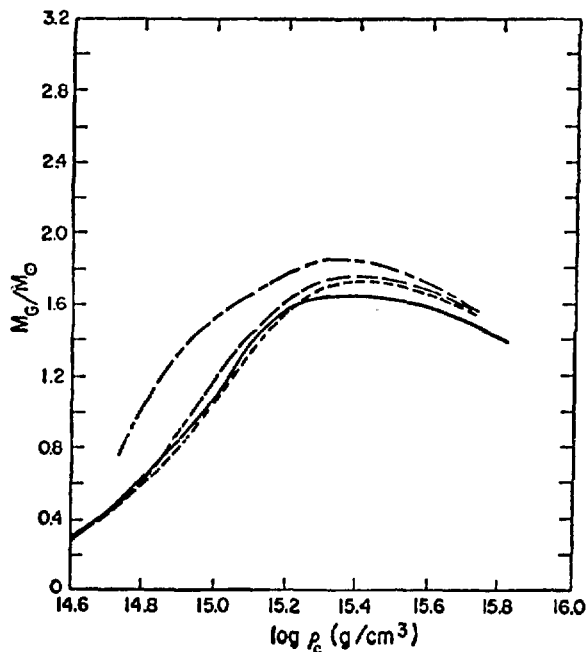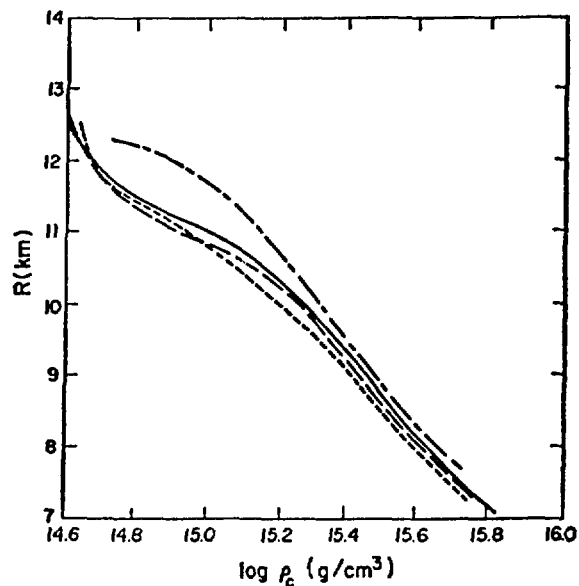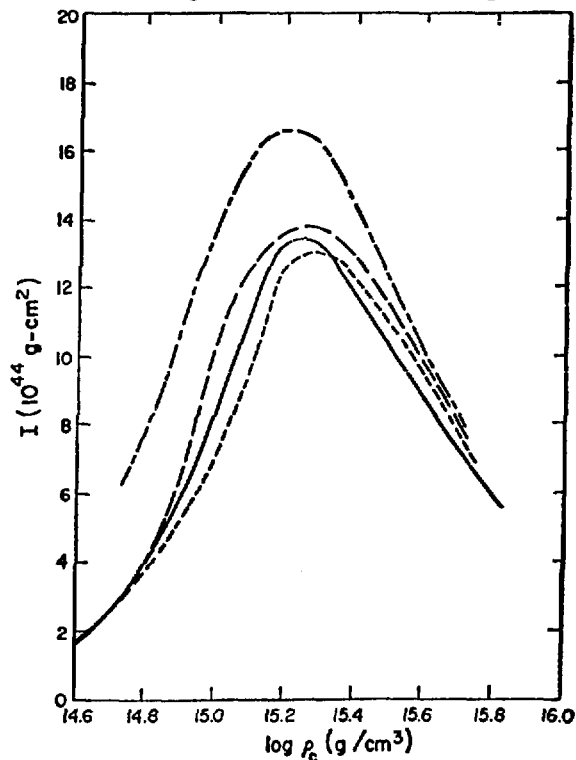
Fig. 55. Moment of inertia, I, vs cen-
tral baryon density ρ_c. See
Fig. 53 for curve designations.

contains the essential physics of pion condensation; several types of corrections to their model have been considered, and I shall discuss some of these later in detail. In the model to be discussed now I consider only π^- condensation, but in a more complete model there will appear an admixture of π^+ as well.

In this model the coupling of a pion to a nucleon is taken to be the non-relativistic coupling shown in Table II, i.e.,

$$\sim f \, \bar{\psi}_p \, \underset{\sim}{\sigma} \cdot \underset{\sim}{k} \, \tau_k \, \psi_N \, \phi_k \tag{185}$$

Here ψ is the nucleon and ϕ the pion field. It is important to note that the interaction increases in strength as the pion momentum k is increased. Thus, if the pionic phase consists of pions occupying a non-zero-momentum mode it may be possible to overcome the repulsive S-wave interaction and find pions in the ground state of nuclear matter.

So we now consider matter consisting of neutrons, protons and π^- with the π^- all put into a state of momentum $\underset{\sim}{k}$ (in Z direction) and we ask what are the conditions under which the ground state energy is minimized. Because we anticipate a state containing many pions it is permissible to treat the pion field as a classical field and replace

$$\phi_k \rightarrow \sqrt{N_\pi} \tag{186}$$

in Eq. (185) where $N_\pi \equiv$ number of π^- in the field. Now the Hamiltonian may be written

$$= \sum_{p\sigma} \frac{p^2}{2M} \, \psi_N^+ (p,\sigma) \, \psi_N(p,\sigma) + \sum_{p\sigma} \frac{p^2}{2M} \, \psi_P^+ (p,\sigma) \, \psi_P(p,\sigma)$$

$$- \sum_{p\sigma} \left[i M_k \, \psi_N^+(p,\sigma) \, \sigma_3 \, \psi_P (p-k,\sigma) \, \sqrt{N_\pi} + h\cdot c + \right] \omega_k N_\pi \tag{187}$$

where $\sigma = \pm 1$ is the value of σ_z,

$$M_k = \frac{fk}{m_\pi \sqrt{\Omega \omega_k}} \, , \tag{188}$$

and Ω is the volume of the system. Because we have omitted electrons, charge neutrality requires

$$N_\pi = N_p \tag{189a}$$

Define x so that if N is the total baryon density

$$N_p = xN = N_\pi \tag{189b}$$

$$N_N = (1-x)N \tag{189c}$$

The idea now is to diagonalize the Hamiltonian in Eq. (187) to find the energy and eigenstates. The important point is that Eq. (187) is quadratic in the nucleon fields. Thus, it may be diagonalized by changing variables from the fields ψ_N, ψ_P to u, v, defined by the canonical transformation

$$U_{p\sigma} = \sqrt{1-\theta^2}\,\psi_N(p,\sigma) + i\,\theta\,\sigma\,\psi_P(p-k,\sigma)$$

$$V_{p\sigma} = i\,\theta\sigma\psi_N(p,\sigma) + \sqrt{1-\theta^2}\,\psi_P(p-k,\sigma) \tag{190a}$$

Solving Eq. (190) for ψ_N and ψ_P we find

$$\psi_N(p,\sigma) = \sqrt{1-\theta^2}\,U_{p\sigma} - i\,\theta\,\sigma\,V_{p\sigma}$$
$$\psi_P(p-k,\sigma) = i\,\theta\,\sigma\,U_{p\sigma} - \sqrt{1-\theta^2}\,V_{p\sigma} \tag{190b}$$

Substituting Eq. (190b) into Eq. (187) yields, after some algebra

$$H = \sum_{p\sigma} U^+_{p\sigma} U_{p\sigma}\left[\varepsilon_N(1-\theta^2) + \theta^2\varepsilon_p - 2M_k\theta\sqrt{1-\theta^2}\sqrt{Nx}\right] + \sum_{p\sigma} V^+_{p\sigma}V_{p\sigma}$$

$$\times \left[\varepsilon_p(1-\theta^2) + \theta^2\varepsilon_n + 2M_k\theta\sqrt{1-\theta^2}\sqrt{Nx}\right] + \sum_{p\sigma} (V^+_{p\sigma}U_{p\sigma} - U^+_{p\sigma}V_{p\sigma})$$

$$\times \left[(\varepsilon_N-\varepsilon_p)\,i\sigma\theta\sqrt{1-\theta^2} + i\sigma\,M_k\sqrt{Nx}\,(1-2\theta^2)\right] + Nx\omega_k \tag{191}$$

102

where

$$\varepsilon_N = \frac{p^2}{2M} \ , \ \varepsilon_P = \frac{(p-k)^2}{2M} \tag{192}$$

H is diagonalized provided the coefficient of $v^+u - u^+v$ is set $= 0$, or

$$\frac{M_k \sqrt{xN}}{\varepsilon_P - \varepsilon_N} = \frac{\theta_p \sqrt{1-\theta_p^2}}{1-2\theta_p^2} \tag{193}$$

It is clear from inspecting Eq. (191) that the system can profit energetically by filling the N lowest U states. Hence, the ground state is

$$|\psi_0> \ = \ \prod_{p < p_F} U^+_{p\sigma}|vac> \tag{194}$$

where the state $|vac>$ contains the coherent state of π^-. The relationship between θ and x can be seen by taking the expectation values

$$<\psi_0|\psi^+_N (p\sigma) \ \psi_N(p\sigma) \ |\psi_0> \ = 1 - \theta_p^2 \qquad P \leqslant P_F \tag{195a}$$

$$= 0 \qquad p > P_F$$

$$<\psi_0|\psi^+_P(p,\sigma) \ \psi_P(p,\sigma)| \ \psi_0> \ = \theta_p^2 \qquad |\underset{\sim}{p} + \underset{\sim}{k}| \leqslant P_F \tag{195b}$$

$$= 0 \qquad |\underset{\sim}{p} + \underset{\sim}{k}| > P_F$$

The ground state energy E may be found from

$$E = <\psi_0| \ H \ |\psi_0> \tag{196}$$

$$= \sum_{p\sigma} <\psi_0| \ U^+_{p\sigma}U_{p\sigma}|\psi_0> \left[\varepsilon_N(1-\theta^2) + \theta^2 \ \varepsilon_P \ - 2M_k\theta \ \sqrt{1-\theta^2} \ \sqrt{xN} \right]$$

$$+ \ \omega_k \ Nx$$

Simpler expressions are obtained if recoil is neglected, i.e.,

$$\varepsilon_P - \varepsilon_N = \frac{(p+k)^2}{2M} - \frac{p^2}{2M} = \frac{k^2}{2M} - \frac{p \cdot k}{M} \sim \frac{k^2}{2M} \tag{197}$$

Baym[106] has emphasized that in the exact ground state the currents associated with conserved quantities (charge and baryon currents in this case) must vanish locally. Making the approximation in Eq. (197) we find [from Eq. (189b) and (195b)]

$$N_p = \theta^2 N = xN \tag{198a}$$

or

$$x = \theta^2 \tag{198b}$$

Now Eq. (196) may be rewritten

$$E = (1-\theta^2)\, T_N + \theta^2 T_p - 2M_k\, \theta \sqrt{1-\theta^2}\, \sqrt{xN}\, N + Nx\, \omega_k \tag{199}$$

where

$$T_N = \sum_{p\sigma} < \psi_o |U_{p\sigma}^+ U_{p\sigma}| \psi_o > \frac{p^2}{2M} = 2\Omega \int_{p<p_F} \frac{d^3 p}{(2\pi)^3} \frac{p^2}{2M} = \frac{3}{5} \frac{p_F^2}{2M} N \tag{200a}$$

$$T_p = \sum_{p\sigma} < \psi_o |U_{p\sigma}^+ U_\sigma| \psi_o > \frac{(p-k)^2}{2M} = \left(\frac{3}{5} \frac{p_F^2}{2M} + \frac{k^2}{2M} \right) N \tag{200b}$$

Hence

$$E/N = \frac{3}{5} \frac{p_F^2}{2M} - \frac{2fk}{m_\pi} x \sqrt{1-x} \sqrt{\frac{\rho}{\omega_k}} + x\omega_k + \frac{k^2}{2M} x \tag{201}$$

Equation (201) is an important result. The first term is just the energy of a Fermi sea of free nucleons filled to $p = p_F$. The remaining terms are corrections due to the presence of the pions: the second term in Eq. (201) is the (negative) interaction energy, the third is the rest plus kinetic energy of the pions and the fourth term is additional kinetic energy of the nucleons acquired through scattering from the pion field. It is clear from Eq. (201) that there is some density ρ at which the second term will dominate the remaining two terms and hence a density above which the energy will be lowered by the presence of the condensate.

The model may be worked out more fully than I intend to work it out here, but let me mention how it can be done. Minimizing E/N in Eq. (201) at a given density ρ gives a constraint between k, the pion momentum and x, the fraction of neutrons which have become converted to protons by the condensate. The other

condition needed in order that k and x be individually determined is Eq. (193), which may be written explicitly as

$$\frac{f}{m_\pi} \frac{2M}{k} \sqrt{\frac{\rho}{\omega_k}} = \sqrt{\frac{1-x}{1-2x}} \qquad (202)$$

using Eqs. (188) and (198b). The minimum density ρ for which these equations have a solution is the threshold for pion condensation. It occurs approximately for

$$k \simeq 1.26 \ m_\pi \qquad (203)$$

$$\rho \simeq 0.25 \ fm^{-3}$$

The model of Sawyer and Scalapino just described leaves out a number of physical effects which give rise to quantitatively different predictions (see below). However, the description of the π^- condensed state is the same in essentially all theories. The nucleon states which diagonalize the Hamiltonian are not the individual neutron and proton states but are rather linear combinations of a neutron hole and a proton particle state. The energy of this collective state is lowered by the interaction of the pion with the nucleons; likewise the energy of the pion is lowered by the interaction with the nucleons. Condensation occurs when equilibrium is established and the excitation energy $\varepsilon(PN^{-1})$ of the "particle-hole" state, which carries the quantum numbers of the π^+, becomes equal to the energy of the π^-. Such a characterization of the threshold condition is quite general and permits a formulation of the threshold condition in terms of the pion Green's function, which I'll have more to say about later.

B. π^o Condensation

In π^o condensation, equilibrium is established as

$$N \rightleftarrows \pi^o + N \qquad (204)$$

$$P \rightleftarrows \pi^o + P$$

and we require that the energy of the π^o be equal to the energy $\varepsilon(nn^{-1})$ of a neutron (NN^{-1}) and proton (PP^{-1}) particle-hole excitation. Migdal has shown that this occurs when the pion energy $\omega_\pi = 0$ (but of course, $k_\pi \neq 0$) in contrast to

the case of π condensation where ω_π may be closer to m_π. Because $\omega_\pi = 0$, the pion condensate will correspond to a static field and may be recognized from the structure of the nuclear particle-hole excitation which accompanies it. Because the π^0 couples to the density $\psi\sigma_z\tau_z\psi$ [Eq. (185)], the collective nuclear state will be a state of non-vanishing spin-isospin density.

An interesting model of π^0 condensation was given by Pandharipande and Smith.[107] They considered neutron star matter and found that the state of lowest energy consisted of a simultaneous neutron lattice and π^0 condensate. They observe that because the potential interaction between two neutrons due to π^0 exchange is tensor in character [Eq. (43)], an arrangement of neutrons on a lattice is energetically most favorable. They place the neutrons in the lattice so that in planes perpendicular to the Z-axis the spins all point in the same direction. However, the spin direction alternates from one plane to the next (Fig. 56a). The tensor force is such that the interaction between a given lattice point and its eighteen nearest neighbors is attractive. The next fourteen nearest neighbors have zero interaction with the given site and more distant neighbors give small contributions of varying signs. This describes the collective state. The pion field can be determined from the π^0 field equation

$$(\nabla^2 - \mu^2)\phi_\pi = -\frac{f}{m_\pi}\nabla \cdot \psi\sigma_z\psi \qquad (205)$$

which, when solved with the neutrons as classical point sources at locations R_i arranged as described above gives

$$\phi_\rho(r) = \frac{f}{4\pi m_\pi} \sum_i \sigma_i \cdot \nabla \left(\frac{e^{-\mu|\underset{\sim}{r}-\underset{\sim}{R}_i|}}{|\underset{\sim}{r}-\underset{\sim}{R}_i|} \right) \qquad (206)$$

At low density the π^0 field is essentially that due only to the nearest neutron. At high density the fields overlap significantly, and the ϕ_π is essentially a standing wave with nodes at the lattice points (Fig. 56b). In other words, there is a static π^0 condensate field with a wavelength of twice the lattice constant with momentum in the Z direction. To make the lattice stable, Pandharipande and Smith found it necessary to calculate the nuclear energy with explicit Δ_{33} components in the nuclear wave function using a coupled channel form of the variational theory.

C. Improved Estimate of π^- Condensation Threshold: The Green's Function

I next want to show how the estimate of Sawyer and Scalapino may be improved. For this purpose we shall examine the pion Green's function, defined already in Eq. (83). The importance of the Green's function is threefold: (1) the Green's function may be calculated, bringing together experience from nuclear matter many-body theory and meson physics, (2) the poles of the Green's function give directly the threshold condition for π condensation, (3) the Green's function is directly related to pion scattering, and therefore provides a method for unifying these two areas of physics.

Let me begin by showing the relevance of the Green's function to the determination of the threshold of π condensation. Actually, we want to consider a slightly more general operator than that defined in Eq. (83).

$$G_{\underset{\sim}{k}';\underset{\sim}{k}}(T'-T) = <\psi_0| \ a_{k'}(T') \ a_k^+(T) \ |\psi_0> \ \theta(T'-T) \tag{207}$$

$$<\psi_0| \ a_k^+ \ (T) \ a_{k'}(T')|\psi_0> \ \theta(T-T')$$

where a_k^+ creates a π^-. Substituting the definitions of $a_k^+(T)$, etc., defined below, Eq. (83), we see

$$G_{\underset{\sim}{k}';\underset{\sim}{k}}(T'-T) = \sum_n <\psi_0| \ a_{k'}|\psi_n^{(-)}> \ e^{-i(E_n^{(-)}-E_0)(T'-T)} \ \theta(T'-T) <\psi_n^{(-)}|a_k^+|\psi_0>$$

$$+ \sum_n <\psi_0|a_k^+|\psi_n^{(+)}> \ e^{-i(E_n^{(+)}-E_0)(T-T')} \ \theta(T-T') \ <\psi_n^{(+)}|a_{k'}|\psi_0> \tag{208}$$

where we have inserted a complete set of eigenstates of the complete Hamiltonian into the Green's function and where E_0 is the energy of the state ψ_0. The superscripts (+) and (-) refer to states of same baryon number but of charge +1 and -1 relative to ψ_0. If we now Fourier transform $G(T-T')$, using the Fourier transforms

$$\frac{i}{2\pi} \int_{-\infty}^{\infty} \frac{d\omega \ e^{-i\omega T}}{\omega-E+i\eta} = e^{-iET} \ \theta(T) \tag{209a}$$

$$\frac{-i}{2\pi} \int_{-\infty}^{\infty} \frac{d\omega \ e^{-i\omega T}}{\omega+E-i\eta} = e^{+iET} \ \theta(-T) \tag{209b}$$

we find

$$G_{k';k}(\omega) = \sum_n <\psi_0|a_{k'}|\psi_n^{(-)}> \frac{1}{\omega-(E_n^{(-)}-E_0)+i\eta} <\psi_n^{(-)}|a_k^+|\psi_0> \qquad (210)$$

$$- \sum_n <\psi_0|a_k^+|\psi_n^{(+)}> \frac{1}{\omega+(E_n^{(+)}-E_0)-i\eta} <\psi_n^{(+)}|a_{k'}|\psi_0>$$

In infinite nuclear matter $\underset{\sim}{k}' = \underset{\sim}{k}$ and I now want to consider this special case only. The Green's function may be calculated in terms of Feynman diagrams; refer to Ref. 109 for a derivation of these rules. The general diagram is completely connected and consists of everything which begins and ends with a pion propagator, as in Fig. 57. Generally we may organize diagrams as shown in Fig. 58. If the diagram can be broken into two pieces by cutting a pion line then this line is shown explicitly in Fig. 58. Thus, by definition, the blobs do not contain pieces which break into two pieces if one pion line inside the blob is cut. The blobs are called the "proper self energy" or "proper polarization" part, and denoted by Π (k,ω). It is easy to show that when Fourier transformed from time to energy, each diagram becomes a product of the propagator and proper self energy parts. For example, the third diagram on the right-hand side of Fig. 58 is

$$\left(\frac{1}{\omega^2-q^2-\mu^2+i\eta}\right)^3 \Pi^2(k,\omega) \qquad (211)$$

Thus, the entire sum is a geometric series, and

$$G(\omega) = \frac{1}{\omega^2-q^2-\mu^2-\Pi(k,\omega)+i\eta} \qquad (212)$$

Referring to Eq. (210), we note that the singularities of $G(\omega)$ which lie below the real axis are equal to $\Delta E_n^{(-)} \equiv E_n^{(-)}-E_0$, i.e., the energy which it costs to create a state with the quantum numbers of the π^-. The singularities above the axis are equal to $\Delta E_n^{(+)} \equiv -(E_n^{(+)}-E_0)$, i.e., the negative of the energy which

it costs to create a state of the quantum numbers of the π^+. The analytic structure is depicted in Fig. 59. When $\Delta E_{n1}^{(+)} - \Delta E_{n2}^{(-)} = 0$ then it costs no energy for the ground state of the system to spontaneously develop a π^-- and a π^+-like component; this is the phenomenon of π^- condensation. The point is that this condition can be determined if the Green's function is known. A practical method of determining the threshold condition for π condensation is to first calculate the Green's function and determine its singularities. For a given k, ω, one then searches for the density at which the leftmost singularity below the real axis just meets the rightmost singularity above the real axis. One then searches for the values of k, ω which give the lowest density; the values of k, ω and ρ at this minimum define the threshold of π condensation. In Ref. 110 it was shown that when the two singularities of the Green's function touch, the expectation value of the pion number operator diverges in an infinite system.

The various terms which contribute to $\Pi(\omega)$ in a realistic calculation are shown in Table XXVI.

The pion-nucleon S-wave part (Table XXVIB) is calculated from the free pion-nucleon S-wave scattering lengths; it is large and repulsive, as discussed earlier. Recently[111] the effect of going off the energy shell in the πN amplitude has been investigated and this extrapolation appears to be the source of additional repulsion.

The piece $\Pi^{(o)}$ corresponds to a particle-hole excitation, and if the energy of the nucleons is ignored relative to the energy of the pions the result can be shown to be the Sawyer-Scalapino model, already discussed. The bubble in Table XXVIB reminds that the interaction of the neutron and proton with the nuclear matter background must be included; such potentials may be calculated from Brueckner-Bethe theory or estimated from the variational theory discussed in the

TABLE XXVI

TERMS WHICH ENTER INTO $\pi(k,\omega)$ IN A REALISTIC

CALCULATION OF THRESHOLD OF π^- CONDENSATION

A. $\Pi_{S\pi} = 2\omega \times 217$ (MeV) ρ

B. $\Pi^{(o)} = P \left(\text{diagram} \right) N + \left(\text{diagram} \right) + \ldots \equiv 2f^2 k^2 G^{(o)}$

C. $\Pi_\Delta = N \left(\text{diagram} \right) \Delta^+ + \left(\text{diagram} \right) \Delta^-$

D. $\Pi^{RPA} = \left(\text{diagram} \right) + \left(\text{diagram} \right) + \left(\text{diagram} \right) + \ldots$

$\rangle\!-\!-\!\langle \equiv$ All meson exchanges __except__ π exchange

$= V_{NN} - V_{OPE} \equiv V_{corr}$

$\Pi^{RPA} = 2f^2 k^2 G^{(o)} (1 - V_{corr} G_0)^{-1}$

E. $\Pi_{N\Delta} = 2f^2 k^2 \left(G^{(o)} + \frac{4}{3} G^\Delta \right) \left[1 - V_{corr} \left(G_0 + \frac{4}{3} G^\Delta \right) \right]^{-1}$

109

preceding discussion of neutron star matter.

The Δ contribution is shown in Table XXVIC. One would like to include effects due to the interaction of the Δ with the nuclear matter background, but so far no calculations of these effects have been attempted.

The Π^{RPA} effect ($\Pi^{(o)}$ is the lowest order approximation to Π^{RPA} and therefore these two terms should not <u>both</u> be included) takes account of the possibility that the excited particles may interact with each other; the dashed lines are effective interactions V_{NN}, i.e., g-matrix elements. However, in the calculation, these were evaluated in the spirit of the lowest order variational theory [Eq. (168)]

$$
\begin{aligned}
V_<(r) &= \lambda f^2(r) \quad r < d \\
V_>(r) &= V(r) \qquad r > d
\end{aligned}
\tag{213}
$$

where f^2 is the square of the correlation function and λ the healing constraint. This is approximately equal to[112]

$$
V(r) = v(r) \, f(r)
\tag{214}
$$

However, because the pions are taken into account <u>explicitly</u> in the equation for the Green's function (Fig. 58) we must subtract the one pion exchange potential from V_{NN}, calling the result V_{corr}

$$
V_{corr} = V_{NN} - V_{OPE}
\tag{215}
$$

Subtracting V_{OPE} is exceedingly important. Mathematically, it simply avoids double counting, but physically it accounts for the fact that the short range nucleon-nucleon repulsion prevents two nucleons from coming close enough together to experience the δ function in the one-pion exchange potential seen in Eq. (48). Including the RPA sum takes this physical effect into account in a well-motivated formalism; if the RPA series were not summed, i.e., only the $\Pi^{(o)}$ piece of Π^{RPA} were included as in the Sawyer-Scalapino theory, then the δ-function piece of the one-pion exchange connecting the blobs in Fig. 58 acts and contributes a substantial amount of the attraction which tends to lower the threshold for pion condensation. The importance of taking the short-range correlations into account was emphasized by Barshay and Brown[113] in their discussion of π^0 condensation in nuclei. (In pion scattering this effect is known as the Lorentz-Lorenz effect.)

110

NEUTRON SOLID

(a)

(b)
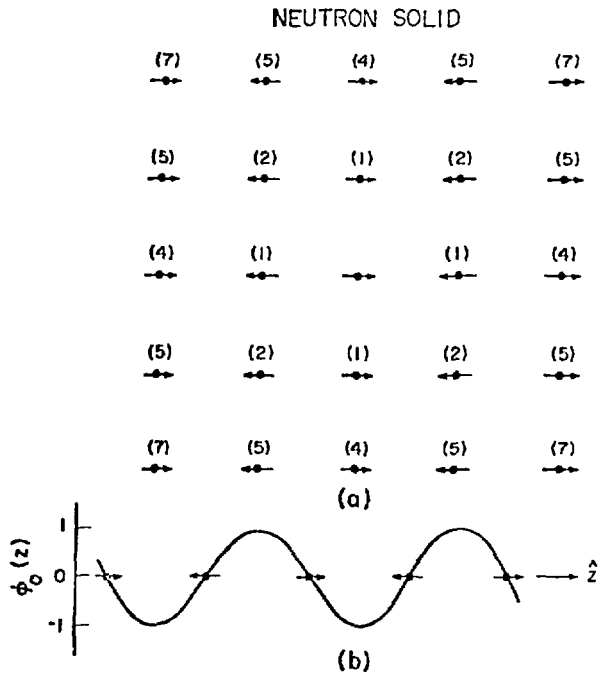
Fig. 56. The neutron solid proposed
by Pandharipande and Smith.
The arrows indicate the spin
direction of the neutrons.

(a)   (b)   (c)
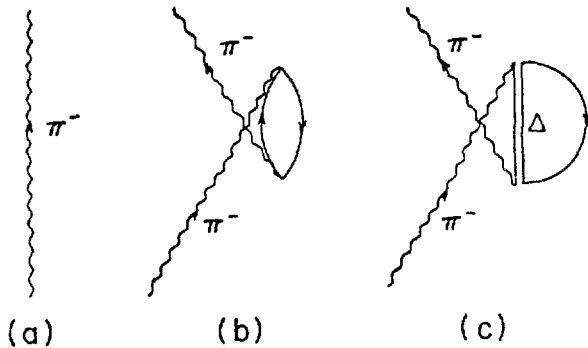
Fig. 57. Examples of Feynman-Gold-
stone diagrams in the expan-
sion of the pion Green's
function.
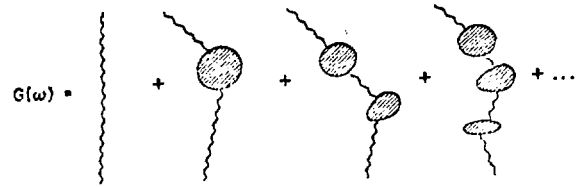
Fig. 58. General form of Green's func-
tion.
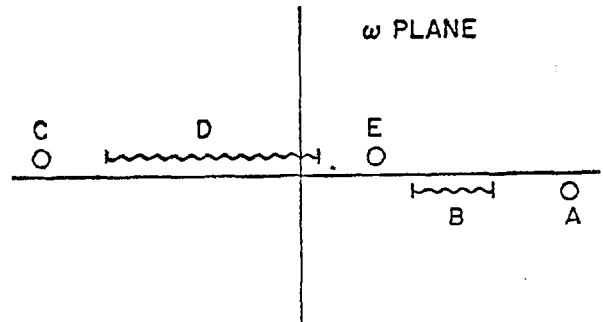
Fig. 59. Singularities of the pion
Green's function. A is the
π^- pole; B is the NP^{-1} cut,
not present in pure neutron
matter; C is the π^+ pole; D
is the PN^{-1} cut, and E is a
collective PN^{-1} state.
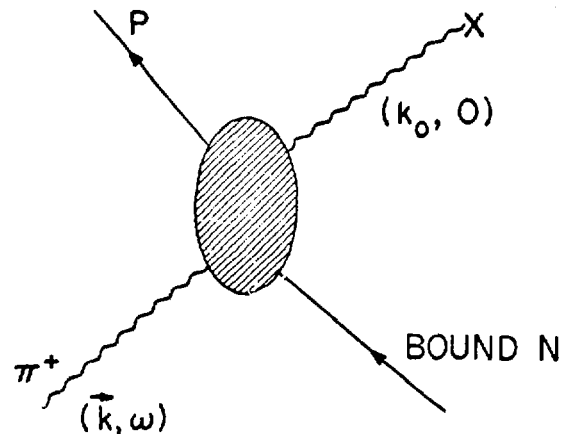
Fig. 60. The (π, P) reaction. In this
process the incident pion is
scattered into a pion-con-
densed mode (denoted by ∿∿x),
which helps satisfy an other-
wise large momentum mismatch.

111

Actually Π^{RPA} should be extended to include Δ as well as nucleons; after all, the nucleons and Δs presumably interact through one-pion exchange and a repulsive core, and the delta functions of OPEP in this channel also must be treated carefully. The interaction between the nucleon and Δ was assumed in the calculation[108] to be proportional to the interaction between two nucleons; such is true for the pion and ρ-meson exchange pieces of the interaction in the quark model.

The results are shown in Table XXVII. As I have stated, $\Pi^{(o)}$ gives the Sawyer-Scalapino result with the minor difference that in our model π^+ and π^- condensation is allowed by virtue of using the relativistic pion propagator in Eq. (1). (The difference is discussed in Ref. 114.) The RPA theory pushes the threshold up, showing explicitly the repulsive nature of the nucleon-nucleon correlations. RPA plus second order tensor refers to a prescription for including potential·energy on the nucleon states in the particle-hole excitation.[108] If πN S-waves are added, then the condensation threshold is pushed up to very high density; if the $\Delta$ is added without correlations then condensation again becomes possible. The last row gives the most realistic calculation, including correlations among N and Λ. Depending on our choice of nucleon-nucleon interaction, threshold occurred at $\rho = 0.225$ fm^{-3}, or at exceedingly high density. The lower density corresponds to a modified Reid potential, taken from the calculations of dense baryon matter discussed earlier,[98] and the higher density corresponds to a nucleon-nucleon potential developed at Michigan State for describing nuclei, i.e., low density nuclear matter. The most we can say is that pion condensation may occur in dense systems, but a detailed prediction depends on details of nuclear physics which are somewhat beyond our ability to calculate at the present time. It would be nice to have an experimental result to give some indication; some possible experiments are discussed next.

D. Experimental Implications

Migdal[103] has suggested that π^0 condensation might occur in finite nuclei. Barshay and Brown,[113] however, pointed out that if the coupling of the pion to spin-isospin modes in the

TABLE XXVII

THRESHOLD OF π^- CONDENSATION IN NEUTRON MATTER*

Model	ρ_{crit} (fm^{-3})	ω_π (MeV)	K_π (fm^{-1})
Simple [$\Pi^{(o)}$]	0.17	140	1.0
Π^{RPA}	0.22	152	1.2
$\Pi^{RPA} + \Pi_{S\pi}$	>> 0.8	---	---
$\Pi^{RPA} + \Pi_{S\pi} + \Pi_\Delta$	0.085	130	1.44
$\Pi_{N\Delta}$ $\Pi_{S\pi}$	> 0.225	119	1.50

*See Ref. 108.

nucleus were anywhere near the strength to produce pion condensation in nuclear matter, then there would be strong effects in nuclear spectra, which are not seen. In particular, there exists a $T = 1$ 0^- state in ^{16}O at $E(\text{expt}) = 12.78$ MeV. In a shell model calculation this lies at an unperturbed energy of 12.42 MeV. If there were a pion condensate this mode, which has the same quantum numbers as the π^0, would move down in energy, not up. Barshay and Brown then criticize Migdal's calculation, pointing out that he omitted correlations among nucleons, which, as we have seen, greatly reduces the attraction.

Pirner[115] has tried to put a limit on the amplitude for a π field by analyzing (π, P) reactions. He points out that such reactions need a large momentum transfer; if there exists a pion condensed mode in the nucleus then the momentum transfer is easier to achieve because the incident pion can scatter into the condensed mode, which has a momentum ≈ 1 to 1.5 fm^{-1}. (See Table XXVII.) The scattering process is indicated in Fig. 60. The experiment involved measuring the radioactive decay of ^{11}Be after π^- absorption by ^{12}C. He deduced an exceedingly small amplitude, corresponding to a pion density of 1/500 of nuclear density. It would be interesting to see a similar comparison for a heavy nucleus, such as lead. Use of a spectrometer such as the High Resolution Spectrometer (HRS) at LAMPF might be able to see this reaction [or rather the closely related (P, π) reaction].

Ericson and Wilkin[116] have proposed measuring the π field in a nucleus by observing reactions $\pi^- + \pi^+ \to 2\gamma$ or $\to e^+ e^-$, where the incident π^- annihilates on a virtual π^+ field in the nucleus. Experiments are now under way, with interesting but so far inconclusive results.

If there is no actual π condensed field in a nucleus it is still of interest to measure the propagation characteristics of a pion in a nucleus. The poles of the pion Green's function in Eq. (212) determines the pion energy ω as a function of its momentum k in infinite nuclear matter. In the same model[108] that gave π condensation in neutron matter the pion dispersion equation was calculated for symmetric nuclear matter and parametrized to give

$$\omega^2 = \mu^2 + \alpha k^2 \tag{216}$$

The parameter α was found to be 0.35 at normal nuclear density for $k < 0.5$ fm^{-1}. This gives a moderately high density of states which may be observable in reactions such as pion photoproduction or (P, π) reactions.

At energies above threshold $(\omega > \mu)$ the operator Π in Eq. (212) may be identified with the pion optical potential for elastic scattering. For the scattering problem k is complex, the imaginary part of which gives the attenuation of the pion wave function due to the competing reaction channels. Thus, low energy elastic pion scattering is another way to test theories of the pion propagator, and such experiments will hopefully provide some clues as to whether the physics is being correctly incorporated. Low energy is important because the nucleus is more transparent to pions than at higher energy and hence pions are more able to penetrate into the high density central portion of the nucleus.

Next, I want to mention an interesting proposal made by Sawyer and Soni.[117] They have suggested using neutrino reactions

$$\nu + \text{Nucleus} \rightarrow \ell^+ + \text{anything} \tag{217}$$

to measure the pion dispersion relation in the medium. The reaction goes through the process shown in Fig. 61. The point they make is that in symmetric nuclear matter, $(\rho \approx \rho_0)$, the pion dispersion relation $\omega = \omega(k)$ is such that the pion four-momentum (k,ω) may become space-like (i.e., $k > \omega$). They pick a simple model of the dispersion relation and show that this happens for $1 \leqslant \frac{k}{\mu} \leqslant 2.8$. If the four-momentum becomes spacelike, then the incident neutrino can actually decay in the medium into a lepton and a pion. (This is forbidden in free space.) This gives a distinctive signature in the cross section for the produced lepton. Their result for the case of $\bar{\nu}_\mu + \text{Nucleus} \rightarrow \mu^+ + \text{anything}$ is shown in Fig. 62 for $E_\nu = 420$ MeV. The quantity V is

$$V = \frac{1}{A} \frac{d^2}{dp_\mu d\cos\theta_\mu} \ , \ A = 4 \times 10^{-41} \ \text{cm}^2.$$

The numbers on the curves refer to $\cos\theta_\mu$. Sawyer and Soni point out that these cross sections are larger than what one would get by considering $\bar{\nu}+N \rightarrow N+\pi^-+\mu^+$ on the individual nucleons, with this cross section taken from the free space scattering. They also estimate background from the quasi-elastic process $\nu \rightarrow \mu^+$ + proton hole + neutron. They show that the quasi-elastic peak and the peak from the mechanism they propose are separated in momentum by more than 100 MeV/c, so that the background may be isolated from the signal if the neutrino energy spread in the beam is less than 100 MeV/c. The measurement of the location of the peak gives a direct point-by-point measurement of the pion dispersion

relation, and this is the attractive and very valuable feature of their idea. Sawyer and Soni made estimates using nuclear matter arguments, but it should be feasible to do the calculation for a finite nucleus.

Finally, I would like to mention the possibility of learning about pion condensation in a neutron star by measuring the cooling rate following a supernova explosion. Maxwell, et al.[118] have considered the effect of a pion condensate on the cooling rate and found that the rate can increase enormously, due to the β decay of the thermally excited "U particles" [Eq. (190a)]. In a subsequent paper[119] Maxwell considers the cooling in more detail and concludes that the present temperature limit on the crab pulsar does not rule out any model of cooling and in particular doesn't indicate a need for a pion condensate.
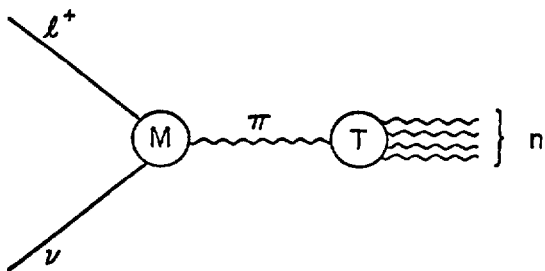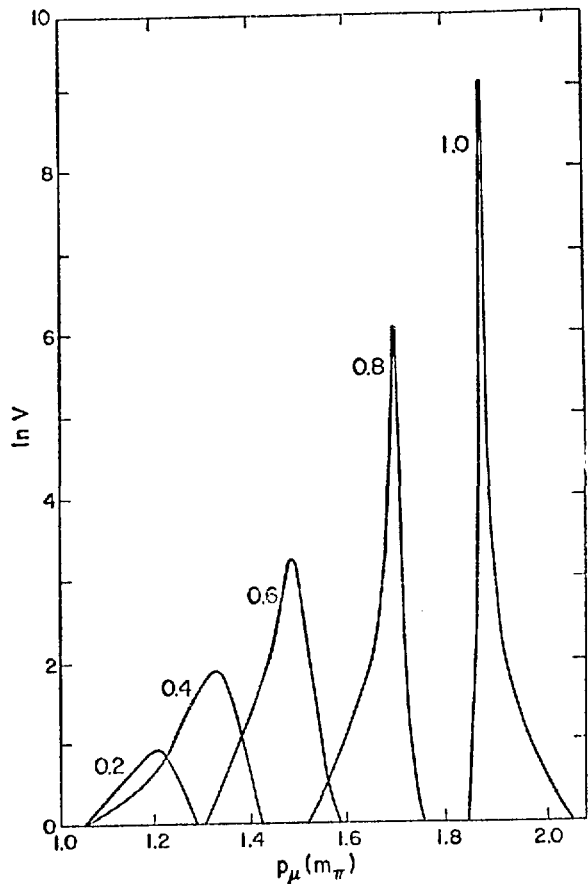
Fig. 62. The cross section for the reaction $\bar{\nu}_\mu$ + Nucleus $\rightarrow \mu^+$ + anything, according to Sawyer and Soni, Ref. 117.

Fig. 61. The reaction neutrino + Nucleus $\rightarrow$ lepton + anything.

APPENDIX A

Proof of Eq. (47)

In this appendix we want to show that

$$\int \frac{d^3q}{(2\pi)^3} \frac{e^{i\underline{q}\cdot\underline{r}}}{q^2+\mu^2} \left[3\underline{\sigma}_1\cdot\underline{q}\,\underline{\sigma}_2\cdot\underline{q} - \underline{\sigma}_1\cdot\underline{\sigma}_2 q^2\right] = -S_{12}\left(1+\frac{3}{\mu r}+\frac{3}{\mu^2 r^2}\right)\frac{e^{-\mu r}}{\mu r}\cdot\frac{\mu^3}{4\pi} \quad (A.1)$$

where S_{12} is defined in Eq. (47b). The proof goes as follows. Using the addition theorem for spherical harmonics we have

$$\underline{\sigma}_1\cdot\underline{q} = \frac{4\pi}{3}q \sum_m Y^*_{1m}(\underline{\sigma}_1) Y_{1m}(\underline{q}), \quad (A.2)$$

and hence

$$\underline{\sigma}_1\cdot\underline{q}\,\underline{\sigma}_2\cdot\underline{q} = \left(\frac{4\pi}{3}\right)^2 q^2 \sum_{mm'} Y^*_{1m}(\underline{\sigma}_1) Y_{1m}(\underline{q}) Y_{1m'}(\underline{\sigma}_2) Y^*_{1m'}(\underline{q}) \quad (A.3)$$

Substituting Eq. (A.3) into Eq. (A.1) we find

$$\int \frac{d^3q}{(2\pi)^3} \frac{e^{i\underline{q}\cdot\underline{r}}}{q^2+\mu^2} \left[3\underline{\sigma}_1\cdot\underline{q}\,\underline{\sigma}_2\cdot\underline{q} - \underline{\sigma}_1\cdot\underline{\sigma}_2 q^2\right] = \left(\frac{4\pi}{3}\right)^3 \sum_{\substack{m_1 m'_1 m_2 m'_2 \\ \ell m}} Y^*_{1m_1}(\underline{\sigma}_1) Y_{1m'_1}(\underline{\sigma}_2) Y^*_{\ell m}(\hat{r})(2\ell+1) i^\ell$$

$$\times \int \frac{d^3q}{(2\pi)^3} \frac{q^2 j_\ell(qr)}{q^2+\mu^2} Y_{1m_2}(\underline{q}) Y^*_{1m'_2}(\underline{q}) Y_{\ell m}(\underline{q}) [3\delta(m_1 m_2)\delta(m'_1 m'_2) - \delta(m_1 m'_1)\delta(m_2 m'_2)] \quad (A.4)$$

This expression may be simplified by noting that the only ℓ-value contributing is $\ell = 2$. To see this, note[120]

$$\sqrt{\frac{4\pi}{2\ell+1}}\left(\frac{4\pi}{3}\right)\int d\underline{q} Y_{1m_2}(\underline{q}) Y^*_{1m'_2}(\underline{q}) Y_{\ell m}(\underline{q}) = 4\pi \begin{pmatrix} 1 & 1 & \ell \\ m_2 & -m'_2 & m \end{pmatrix}\begin{pmatrix} 1 & 1 & \ell \\ 0 & 0 & 0 \end{pmatrix}(-)^{m'_2} \quad (A.5)$$

From Eq. (A.5) and the properties of 3-j symbols, we see that $m = 0$ and hence $m_2 = m'_2$. Thus we write the $\ell = 0$ term of Eq. (A.5) as

$$\int \frac{d^3q}{(2\pi)^3} \frac{e^{i\underline{q}\cdot\underline{r}}}{q^2+\mu^2} \left[3\underline{\sigma}_1\cdot\underline{q}\,\underline{\sigma}_2\cdot\underline{q} - \underline{\sigma}_1\cdot\underline{\sigma}_2 q^2\right] \Bigg|_{\ell=0}$$

$$= \left(\frac{4\pi}{3}\right)^2 \sum_{\substack{m_1 m_1' \\ m_2 m_2'}} \delta(m_1 m_1') \delta(m_2 m_2') Y^*_{1m_1}(\underset{\sim}{\sigma}_1) Y_{1m_1'}(\underset{\sim}{\sigma}_2) \left[3\delta_{m_1 m_2} - 1\right] \frac{1}{3\sqrt{4\pi}} \int \frac{q^2 dq}{(2\pi)^2} \frac{j_0(qr)}{q^2+\mu^2} \cdot$$

$$(A.6)$$

But

$$\sum_{m_1 m_2} Y^*_{1m_1}(\underset{\sim}{\sigma}_1) Y_{1m_1}(\underset{\sim}{\sigma}_2) \left[3\delta_{m_1 m_2} - 1\right] = 0 \tag{A.7}$$

and hence the left-hand side of Eq. (A.6) vanishes as conjectured. But all terms of $\ell > 2$ also vanish in Eq. (A.4), as can be seen from the property of the 3-j symbol in Eq. (A.6). We take advantage of this by setting $i^\ell j_\ell(qr) = -j_2(qr)$ in Eq. (A.5), with the result

$$\int \frac{d^3 q}{(2\pi)^3} \cdot \frac{e^{i\underset{\sim}{q}\cdot\underset{\sim}{r}}}{q^2+\mu^2} \left[3\underset{\sim}{\sigma}_1\cdot\underset{\sim}{q}\,\underset{\sim}{\sigma}_2\cdot\underset{\sim}{q} - \underset{\sim}{\sigma}_1\cdot\underset{\sim}{\sigma}_2 q^2\right] = -\left(\frac{4}{3}\right)^2 \frac{4}{8\pi^3} \int_0^\infty \frac{q^4 dq j_2(qr)}{q^2+\mu^2}$$

$$\times \sum_{\substack{m_1 m_1' \\ m_2 m_2'}} (-)^{m_2'} \sum_{\ell m} (2\ell+1) Y^*_{\ell m}(\underset{\sim}{r}) \begin{pmatrix} 1 & 1 & \ell \\ m_2 & -m_2' & m \end{pmatrix} \begin{pmatrix} 1 & 1 & \ell \\ 0 & 0 & 0 \end{pmatrix} \sqrt{\frac{2\ell+1}{4\pi}} \tag{A.8}$$

$$\times Y^*_{1m_1}(\underset{\sim}{\sigma}_1) Y_{1m_1'}(\underset{\sim}{\sigma}_2) \times \left[3\delta(m_1,m_2)\delta(m_1',m_2') - \delta(m_1 m_1')\delta(m_2 m_2')\right]$$

But note that

$$\sqrt{4} \sum_{\ell m} (2\ell+1)^{1/2} Y^*_{\ell m}(\underset{\sim}{r}) \begin{pmatrix} 1 & 1 & \ell \\ m_2 & -m_2' & m \end{pmatrix} \begin{pmatrix} 1 & 1 & \ell \\ 0 & 0 & 0 \end{pmatrix}$$

$$= \sqrt{4} \sum_m (-)^m \sum_\ell (2\ell+1)^{1/2} Y_{\ell m}(\underset{\sim}{r}) \begin{pmatrix} 1 & 1 & \ell \\ m_2 & -m_2' & -m \end{pmatrix} \begin{pmatrix} 1 & 1 & \ell \\ 0 & 0 & 0 \end{pmatrix} \tag{A.9}$$

117

$$= \sum_m \cdot \sqrt{\frac{4}{3}} \sqrt{\frac{4}{3}} \; Y_{1m_2}(\hat{r}) \; Y_{1-m_2'}(\hat{r}) \; \delta(m_2-m_2' = m)$$

where the last step utilizes an identity in Appendix IV of Ref. 120. Substitu-ting Eq. (A.9) into Eq. (A.8) we find

$$\int \frac{d^3q}{(2\pi)^3} \; \frac{e^{i\underset{\sim}{q}\cdot\underset{\sim}{r}}}{q^2+\mu^2} \; \left[3\underset{\sim}{\sigma}_1\cdot\underset{\sim}{q} \; \underset{\sim}{\sigma}_2\cdot\underset{\sim}{q} - \underset{\sim}{\sigma}_1\cdot\underset{\sim}{\sigma}_2 q^2 \right]$$

$$= - \left(\frac{4}{3}\right)^3 \frac{1}{2\pi^2} \; \frac{3}{4\pi} \int_0^\infty \frac{q^4 dq \; j_2(qr)}{q^2+\mu^2} \sum_{m_1 m_1'} \sum_{m_2 m_2'} Y_{1m_2}(\hat{r}) Y^*_{1m_2'}(\hat{r}) Y^*_{1m_1}(\underset{\sim}{\sigma}_1) Y_{1m_1'}(\underset{\sim}{\sigma}_2)$$

$$\times \left[3 \; \delta(m_1 m_2)\delta(m_1' m_2') - \delta(m_1 m_1')\delta(m_2 m_2') \right]$$

$$= - \frac{1}{2\pi^2} \int_0^\infty \frac{q^4 dq \; j_2(qr)}{q^2+\mu^2} \; \left[3\underset{\sim}{\sigma}_1\cdot\hat{\underset{\sim}{r}} \; \underset{\sim}{\sigma}_2\cdot\hat{\underset{\sim}{r}} - \underset{\sim}{\sigma}_1\cdot\underset{\sim}{\sigma}_2 \right] \tag{A.10}$$

The integral over q is done in Appendix B and we find

$$\int \frac{d^3q}{(2\pi)^3} \frac{e^{i\underset{\sim}{q}\cdot\underset{\sim}{r}}}{q^2+\mu^2} \left[3\underset{\sim}{\sigma}_1\cdot\underset{\sim}{q}\,\underset{\sim}{\sigma}_2\cdot\underset{\sim}{q} - \underset{\sim}{\sigma}_1\cdot\underset{\sim}{\sigma}_2 q^2 \right] = \frac{-\mu^3}{4} S_{12} \left[\frac{3}{(\mu r)^3} + \frac{3}{(\mu r)^2} + 1 \right] e^{-\mu r}$$

$$= - \frac{\mu^3}{4} S_{12} \left[\frac{3}{(\mu r)^3} + \frac{3}{(\mu r)^2} + \frac{1}{\mu r} \right] e^{-\mu r}$$

In this appendix we want to evaluate the integral

$$\int_0^\infty \frac{q^4 dq}{q^2+\mu^2} \, j_2(qr) \tag{B.1}$$

Use the differential equation satisfied by the spherical Bessel function $j_2(qr)$

$$\left(-\frac{1}{r^2} \frac{d}{dr} r^2 \frac{d}{dr} + \frac{6}{r^2} \right) j_2(kr) = k^2 j_2(kr) \tag{B.2}$$

to write

$$\int_0^\infty \frac{q^4 dq \, j_2(qr)}{q^2+\mu^2} = \left(-\frac{1}{r^2} \frac{d}{dr} r^2 \frac{d}{dr} + \frac{6}{r^2} \right) \int_0^\infty \frac{q^2 dq \, j_2(qr)}{q^2+\mu^2}$$

$$= \left(-\frac{1}{r^2} \frac{d}{dr} r^2 \frac{d}{dr} + \frac{6}{r^2} \right)^2 \int_0^\infty \frac{dq \, j_2(qr)}{q^2+\mu^2} \tag{B.3}$$

But

$$\int_0^\infty \frac{dq \, j_2(qr)}{q^2+\mu^2} = \frac{1}{2} \int_{-\infty}^\infty \frac{dq \, j_2(qr)}{q^2+\mu^2} = \frac{1}{4} \int_{-\infty}^\infty \frac{dq \, h_2^{(+)}(qr)}{q^2+\mu^2} + \frac{1}{4} \int_{-\infty}^\infty \frac{dq \, h_2^{(-)}(qr)}{q^2+\mu^2} \tag{B.4}$$

where $h_2^{(\pm)}$ are spherical Hankel functions. Also, now write

$$\frac{1}{q^2+\mu^2} = \frac{1}{q+i\mu} \cdot \frac{1}{q-i\mu} = \frac{1}{q-i\mu} \cdot \frac{1}{2i\mu} - \frac{1}{q+i\mu} \frac{1}{2i\mu}$$

Close the contour for the integral involving $h_2^{(+)}$ in upper 1/2, and that for $h_2^{(-)}$ in lower 1/2 plane. This gives

$$\int_0^\infty \frac{dq \, j_2(qr)}{q^2+\mu^2} = \frac{1}{4} \cdot \frac{2\pi i}{2i\mu} h_2^{(+)}(i\mu r) - \frac{1}{4} \frac{1}{2i\mu} (-2\pi i) \, h_2^{(-)}(-i\mu r)$$

$$= \frac{1}{2} \frac{\pi}{\mu} h_2^{(+)}(i\mu r) \tag{B.5}$$

Noting that the spherical Bessel and Hankel functions satisfy the same differential equation, use of Eq. (B.3) gives

$$\int_0^\infty \frac{q^4 dq\ j_2(qr)}{q^2+\mu^2} = (i\mu)^4\ \frac{\pi}{2\mu}\ h_2^{(+)}(i\mu r) = \frac{\mu^3}{2}\left[\frac{3}{(\mu r)^3} + \frac{3}{(\mu r)^2} + \frac{1}{\mu r}\right] e^{-\mu r} \qquad (B.6)$$

REFERENCES

1. W. Marciano and H. Pagels, Phys. Reports 36C (1978).

2. A. Chodos, R. L. Jaffe, K. Johnson, C. B. Thorn, and V. F. Weisskopf, Phys. Rev. D9, 3471 (1974); A. Chodos, R. L. Jaffe, K. Johnson, C. B. Thorn, Phys. Rev. D10, 2599 (1974); T. DeGrand, R. L. Jaffe, K. Johnson, and J. Kiskis, Phys. Rev. D12, 2060 (1975).

3. S. Gasiorowicz, Elementary Particle Physics (Wiley, 1967).

4. A. M. Green, Repts. in Prog. Phys. 39, 1109 (1976).

5. W. D. Meyers and W. J. Swiatecki, Nucl. Phys. 81, 1 (1966).

6a. S. Fukuda and Y. Torizuka, Phys. Lett. 62B, 146 (1976); M. N. Harakeh, K. Van der Borg, T. Ishimatsu, H. P. Morsch, A. Van der Woude, and F. E. Bertrand, Phys. Rev. Lett. 38, 676 (1977); N. Marty, M. Morlet, A. Willis, V. Comparat, and R. Frascaria, in Proc. Int. Symp. on Highly Excited States in Nuclei, Jülich, Germany, 1975, Kernforschungsanlage Jülich Report Jül-Conf-16 (1975), Vol. 1, p. 17; N. Marty, M. Morlet, A. Willis, V. Comparat, and R. Frascaria, Institut de Physique Nucléaire d'Orsay Report IPNO-PhN-76-03 (1976); N. Marty, M. Morlet, A. Willis, V. Comparat, R. Frascaria, and J. Kallne, Institut de Physique Nucléaire d'Orsay Report IPNO-PhN-75-11 (1975); C. M. Rozsa, D. R. Brown, J. M. Moss, and D. H. Youngblood, Bull. Am. Phys. Soc. 22, 1023 (1977); D. H. Youngblood, C. M. Rozsa, J. D. Bronson, D. R. Brown and J. M. Moss, in Proc. Int. Conf. on Nuclear Structure, Tokyo, Japan, 1977, Organizing Committee (1977), Contributed Papers, p. 375.

6b. J. P. Blaizot, et al., Nucl. Phys. A265, 315 (1976).

7a. See, e.g., F. Coester, Lectures in Theoretical Physics, Vol. XIB (Gordon and Breach, NY, 1969).

7b. J. W. Negele, Phys. Rev. C1, 1260 (1970).

8. J. P. Jeukenne, A. Lejeune and C. Mahaux, Phys. Reports 25, 83 (1976).

9. R. F. Sawyer, Phys. Rev. Lett. 29, 382 (1972); D. J. Scalapino, Phys. Rev. Lett. 29, 386 (1972); A. B. Migdal, Phys. Rev. Lett. 31, 257 (1973), Zh. Eksp. Teor. Fiz. 61 2209 (1971) [Sov. Phys. JETP 34, 1184 (1972)]; Usp. Fiz. Nauk 105, 781 (1971) [Sov. Phys. Usp. 14 813 (1972)].

10. T. D. Lee and G. C. Wick, Phys. Rev. D9, 2291 (1974).

11. A. D. Jackson, D. O. Riska and B. Vervest, Nucl. Phys. A249, 397 (1975).

12. R. Vinh Mau, J. M. Richard, B. Loiseau, M. Lacombe, and W. N. Cottingham, Phys. Lett. 44B, 1 (1973); M. Lacombe, B. Loiseau, J. M. Richard, and R. Vinh Mau, Phys. Rev. D12, 1495 (1975); W. N. Cottingham, M. Lacombe, B. Loiseau, J. M. Richard, and R. Vinh Mau, Phys. Rev. D8, 800 (1973).

13. L. D. Miller and A. E. S. Green, Phys. Rev. C5, 241 (1972).

14. M. Bolsterli, Ann. of Phys. 62, 569 (1971).

15. J. D. Walecka, Ann. of Phys. 83, 491 (1974); S. A. Chin and J. D. Walecka, Phys. Lett. 52, 24 (1974).

16. M. Baranger in "Physique Nucleaire," Proc. of the 1968 Les Houches Summer School (C. deWitt and V. Gillet, Eds.), Gordon and Breach, New York, 1969; Recent progress in the understanding of finite nuclei, in "Proc. Int. School of Physics Enrico Fermi," Course 40, Varenna 1967 (M. Jean, director), Academic Press, New York, 1969.

17. See, e.g., A. Messiah, Quantum Mechanics, Vol. II (North Holland, 1961).

18. J. D. Bjorken and S. D. Drell, Relativistic Quantum Mechanics (McGraw-Hill, 1964).

19. M. B. Johnson and M. Baranger, Ann. of Phys. 62, 172 (1971).

20. M. B. Johnson, Ann. of Phys. 97, 400 (1976).

21a. E. E. Salpeter and H. A. Bethe, Phys. Rev. 84, 1232 (1951).

21b. R. Blankenbecker and R. Sugar, Phys. Rev. 142, 1051 (1966).

21. H. Partovi and E. L. Lomon, Phys. Rev. D2, 1999 (1970).

22. G. C. Wick, Nature 142, 994 (1938).

23. M. Taketani, S. Machida and S. Ohnuma, Prog. Theor. Phys. 7, 45 (1952).

24. D. M. Brink, Nuclear Forces (Pergamon Press, Oxford), 1965.

25. L. S. Kisslinger, preprint.

26. G. Breit, Proc. Nat. Acad. Sci. 46, 746 (1960).

27a. R. Bryan and B. L. Scott, Phys. Rev. 177, 1435 (1969).

27b. T. Ueda and A. E. S. Green, Phys. Rev. 174, 1304 (1968).

27c. R. W. Stagat, F. Riewe, and A. E. S. Green, Phys. Rev. Lett. 24, 631 (1970).

27d. T. Ueda, F. E. Riewe, and A. E. S. Green, Phys. Rev. C17, 1763 (1978).

28. G. Höhler and E. Pietarinen, Nucl. Phys. B95, 210 (1975).

29. N. Barash-Schmidt, Phys. Lett. 75B, 1 (1978).

30. T. Hamada and I. D. Johnston, Nucl. Phys. 34, 382 (1962).

31. R. V. Reid, Ann. Phys. 50, 411 (1968).

32. F. Tabakin, Phys. Rev. 174, 1208 (1968).

33. B. Rouben, PhD Thesis, MIT (1969); J. Zipse, MS Thesis, MIT (1970); E. Riihimaki, PhD Thesis, MIT (1970).

34. H. A. Bethe, Ann. Rev. Nucl. Sci. 21, 93 (1971).

35. F. Coester, S. Cohen, B. Day, C. M. Vincent, Phys. Rev. C1, 769 (1970).

36. R. A. Arndt and M. H. MacGregor, Phys. Rev. 141, 873 (1966).

37. F. Partovi and E. L. Lomon, Phys. Rev. D5, 1192 (1972).

38. E. L. Lomon, Phys. Rev. D14, 2402 (1976).

39. G. Chew and F. E. Low, Phys. Rev. 110, 1570 (1956).

40. D. J. Ernst and M. B. Johnson, Phys. Rev. C17, 247 (1978).

41. H. Sugawara and F. Von Hippel, Phys. Rev. 172, 1764 (1968).

42. D. O. Riska and G. E. Brown, Nucl. Phys. A 153, 153 (1970).

43. L. S. Kisslinger, "Experimental Tests of Isobar Components in Nuclei," preprint.

44. A. M. Green and P. Haapakoski, Nucl. Phys. A221, 429 (1974).

45. K. Holinde, R. Machleidt, M. R. Anastasio, A. Faessler, and H. Müther, preprint.

46. J. W. Durso, M. Saarela, G. E. Brown and A. D. Jackson, Nucl. Phys. A278, 445 (1977).

47. V. R. Pandharipande and R. A. Smith, Nucl. Phys. A237, 507 (1975).

48. G. E. Brown and J. W. Durso, Phys. Lett. 35B, 120 (1971).

49a. E. Hadjimichael, preprint.

49b. B. R. Holstein and C. W. Kini, preprint.

50a. L. Kisslinger, Phys. Lett. 29B, 211 (1969).

50b. W. Fabian, H. Arenhövel, and H. G. Miller, Z. Phys. 271, 93 (1974).

51. Y. Horikawa, T. Fujita and K. Yazaki, Phys. Lett. 42B, 173 (1972).

52. A. D. Jackson, A. Lande, and D. O. Riska, Phys. Lett. 55B, 23 (1975).

53. F. Gross, Proc. Int. Conf. on Few Body Problems in Nuclear and Particle Physics, Laval 1974, pp. 780-8.

54a. H. Arenhövel, M. Danos, and H. T. Williams, Nucl. Phys. A162, 12 (1971).

54b. M. Gari and A. H. Huffman, Phys. Rev. C7, 994 (1973).

54c. D. O. Riska and G. E. Brown, Phys. Lett. 38B, 193 (1972).

55. E. J. Moniz, Comments Nucl. Part. Phys. 7, 131 (1977).

56. A. Kerman and L. Kisslinger, Phys. Rev. 180, 1483 (1969).

57. H. Arenhövel, Z. Phys. A275, 189 (1975).

58. P. Haapakoski and M. Saarela, Phys. Lett. 53B, 333 (1974).

59. E. Rost, Nucl. Phys. A249, 510 (1975).

60. W. Fabian, H. Arenhövel, H. G. Miller, Z. Phys. 271, 93 (1974).

61. S. Jena and L. S. Kisslinger, Ann. Phys. 85, 251 (1974).

62. H. Arenhövel, Phys. Lett 53B, 224 (1974).

63. R. Beurtey, et al., Phys. Lett. 61B, 409 (1976).

64. R. Beurtey, Proc. Int. Conf. on High-Energy Physics and Nuclear Structure, Los Alamos, 1975 pp. 653-65.

65. A. S. Goldhaber, Nucl. Phys. A294, 293 (1978).

66. L. S. Kisslinger in High-Energy Collisions Involving Nuclei (G. Bellini, L. Bertocchi, P. G. Rancoita, Ed.), Editorice Composition, 1975.

67. E. Rost and J. R. Shepard, Phys. Lett. 59B, 413 (1975).

68. R. Schaeffer, L. S. Kisslinger, and E. Rost, to be published.

69. L. S. Kisslinger and G. A. Miller, Nucl. Phys. A254, 493 (1975).

70. B. Höistad, T. Johansson and O. Jonsson, Phys. Lett. 73B, 123 (1978).

71. A. M. Green and J. A. Niskanen, Nucl. Phys. A271, 503 (1976).

72. A. M. Green, J. A. Niskanen, and M. E. Sainio, to appear in J. of Phys. G.

73. M. H. MacGregor, R. A. Arndt and R. M. Wright, Phys. Rev. 169, 1149 (1968).

74. W. de Boer, et al., Phys. Rev. Lett. 34, 558 (1975).

75. I. P. Auer, et al., Phys. Lett 67B, 113 (1977).

76. N. Hoshizaki, Prog. Theor. Phys. 58, 716 (1977).

77. H. Hidaka, et al., Phys. Lett. 70F, 479 (1977).

124

78. E. L. Lomon, private communication.

79. W. M. Kloet, R. R. Silbar, R. Aaron, and R. D. Amado, Phys. Rev. Lett. $\underline{39}$, 1643 (1977).

80. W. M. Kloet and R. R. Silbar, private communication.

81. G. N. Epstein and D. O. Riska, Z. Phys. A$\underline{283}$, 193 (1977).

82. B. D. Day, Rev. Mod. Phys. $\underline{39}$, 719 (1967).

83. B. D. Day, Rev. Mod. Phys. $\underline{50}$, 495 (1978).

84. A. Kallio and B. Day, Nucl. Phys. A$\underline{124}$, 177 (1969).

85. R. Rajaraman, Phys. Rev. $\underline{129}$, 265 (1963).

86. H. A. Bethe, Phys. Rev. B $\underline{138}$, 804 (1965).

87. B. E. Day, Phys. Rev. $\underline{151}$, 826 (1966).

88. R. B. Wiringa and V. R. Pandharipande, Nucl. Phys. A$\underline{299}$, 1 (1978).

89. C. W. Wong and T. Sawada, Ann. Phys. $\underline{72}$, 107 (1972).

90. C. N. Bressel, A. K. Kerman, and B. Rouben, Nucl. Phys. A$\underline{124}$, 624 (1969).

91. M. R. Anastasio, A. Faessler, H. Müther, K. Holinde, and R. Machleidt, preprint.

92. B. D. Day and F. Coester, Phys. Rev. C$\underline{13}$, 1720 (1976).

93. G. E. Brown, A. M. Green, and W. J. Gerace, Nucl. Phys. $\underline{115}$, 435 (1968).

94. S. A. Coon, M. D. Scadron, P. C. McNamee, B. R. Barrett, D. W. E. Blatt, and B. H. J. McKellar, preprint.

95. T. Kouki, L. E. W. Smulter, and A. M. Green, Nucl. Phys. A290, 381 (1977).

96. P. J. Siemens and V. R. Pandharipande, Nucl. Phys. A$\underline{173}$, 561 (1971).

97. V. R. Pandharipande, Nucl. Phys. A$\underline{178}$, 123 (1971).

98. H. A. Bethe and M. B. Johnson, Nucl. Phys. A$\underline{230}$, 1 (1974).

99. V. R. Pandharipande, private communication.

100. S. Chin and J. D. Walecka, Phys. Lett. $\underline{52B}$, 24 (1974); B. Keister and L. Kisslinger, Phys. Lett. $\underline{64B}$, 117 (1976); G. Baym and S. Chin, Phys. Lett. $\underline{62B}$, 241 (1976); G. Chapline and M. Nauenberg, Nature $\underline{259}$, 377 (1976).

101. R. C. Malone, M. B. Johnson, and H. A. Bethe, Astrophys. J. $\underline{199}$, 471 (1975).

102. Y. C. Leung and C. G. Wang, Astrophys. J. $\underline{170}$, 499 (1971).

103. A. B. Migdal, Phys. Rev. Lett. $\underline{31}$, 257 (1973); Zh. Eksp. Teor. Fiz. $\underline{61}$, 2209 (1971) [Sov. Phys. JETP $\underline{34}$, 1184 (1972)]; Usp. Fiz. Nauk $\underline{105}$, 781 (1971) [Sov. Phys. Usp. $\underline{14}$, 813 (1972)].

104. R. F. Sawyer, Phys. Rev. Lett. $\underline{29}$, 382 (1972); D. J. Scalapino, Phys. Rev. Lett. $\underline{29}$, 386 (1972).

105. J. Kogut and J. T. Manassah, Phys. Lett. $\underline{41A}$, 129 (1972).

106. G. Baym, Phys. Rev. Lett. 30, 1340 (1973).

107. V. R. Pandharipande and R. A. Smith, Nucl. Phys. A$\underline{237}$, 507 (1975).

108. G. Bertsch and M. B. Johnson, Phys. Rev. D$\underline{8}$, 2230 (1975).

109. A. L. Fetter and J. D. Walecka, Quantum Theory of Many-Particle Systems, McGraw-Hill, 1971; B. R. Easlea, Lectures on the Many-Body Problem and Its Relation to Nuclear Physics, University of Pittsburgh, 1963.

110. G. Bertsch and M. B. Johnson, Phys. Lett. $\underline{48B}$, 397 (1974).

111. B. H. Wilde, S. A. Coon, and M. D. Scadron, Phys. Rev. D$\underline{18}$, 4489 (1978).

112. V. R. Pandharipande, Nucl. Phys. A$\underline{174}$, 641 (1971); A$\underline{178}$, 123 (1971); A$\underline{181}$, 33 (1972).

113. S. Barshay and G. E. Brown, Phys. Lett. $\underline{47B}$, 107 (1973).

114. R. F. Sawyer and A. C. Yao, Phys. Rev. D$\underline{7}$, 1579 (1973).

115. H. J. Pirner, Phys. Lett. $\underline{69B}$, 170 (1977).

116. T. E. O. Ericson and C. Wilkin, Phys. Lett. $\underline{57B}$, 345 (1975).

117. R. F. Sawyer and A. Soni, Phys. Rev. Lett. $\underline{38}$, 1383 (1977); R. F. Sawyer and A. Soni, Phys. Rev. C$\underline{18}$, 898 (1978).

118. O. Maxwell, G. E. Brown, D. K. Campbell, R. F. Dashen and J. T. Manassah, Astrophys. J. $\underline{216}$, 77 (1977).

119. O. Maxwell, preprint.

120. D. M. Brink and G. R. Satchler, Angular Momentum (Clarendon Press, 1968).

THE APPLICATION OF NUCLEAR PHYSICS TO OTHER SCIENTIFIC FIELDS[*]

by

T. A. Tombrello

California Institute of Technology

ABSTRACT

Knowledge of the structure of nuclei, their systematic
properties, and the mechanisms by which they interact pro-
vides us with a powerful tool that may be applied to under-
standing a variety of phenomena. In these five lectures I
shall give a few specific examples that have arisen in the
fields of astrophysics, planetary science, geophysics, and
materials science. Although some of the nuclear physics in-
volved was well known to Rutherford, we shall find that it
continues to generate new ideas for application.

INTRODUCTORY REMARKS

In addition to the serious topics in nuclear physics covered by the other
speakers I was chosen to provide a bit of comic relief. Because my subjects
tend to come from outside the field, the coverage will be relatively more superficial and thereby more in the nature of entertainment. In 1972 I gave a lecture at a summer school for the Indiana Cyclotron; I began that talk with the
classification of my material as a kind of Kama Sutra for their developing research program -- it would take considerable flexibility to apply my ideas, but
at the very least what I said might whet their appetites. In the same sense I
hope that I can stimulate you into thinking of nuclear physics in a broader context, one in which it is not a separate discipline but one that is well integrated with all of science.

From the beginning, I want to dispel the notion that applications consist mainly in using the techniques of nuclear physics to manufacture better mouse-traps. That is certainly a part of the picture, but it is perhaps the least exciting aspect of applying nuclear physics. To briefly state a suitable philos-ophy for an applied nuclear physicist it would be that whenever you hear of a new problem or discovery anywhere in science or society, you should ask yourself if there is anything you know that is related to that problem or discovery. Most of us are in science because it's fun -- and it's even more fun if you can use what specialized knowledge you have in a variety of diverse ways. Though all of us tend to bear the label "nuclear physicist," we should think of ourselves first as scientists who like Faust are dedicated "to understanding the world in its innermost part."

I. NUCLEAR PHYSICS AND TESTS OF THE EQUIVALENCE PRINCIPLE

Legend has it that Galileo performed the first test of the equivalence prin-ciple by dropping iron and wooden balls from the leaning tower of Pisa. Whether this is true or not, he certainly believed that the acceleration of a body by gravity was independent of the material from which the body was made. This idea of the equivalence of gravitational and inertial mass was absorbed without ques-tion into the mechanics formulated by Newton; though there was, of course, no obvious reason why it should be strictly true. (One should, however, note that Newton performed experiments that established the equivalence to 10^{-3}.)

Before we continue with this historical progression, let us first be more specific about what we mean by the Principle of Equivalence:

(1) In its "weak" form the Equivalence Principle involves only the equiva-lence of inertial and gravitational mass for a local observer -- it does not say that the proportionality of these two masses will be the same everywhere in a gravitational field.

(2) Einstein used "equivalence" in a much stronger sense when he set forth the postulates on which his theory of general relativity rests. This "strong" Equivalence Principle states that all the laws of physics are independent of the location in a gravitational field. This means that to a local observer in a freely falling, non-rotating, electromagnetically-shielded laboratory there is no change in the results of _any_ experiment due to gravity. _Obviously, we exclude tidal effects_, i.e., variations of the gravitational potential (ϕ) within the

laboratory. Thus, all particle masses and the coupling constants of all fields cannot depend on ϕ.

In this strong form the equivalence principle puts enormous constraints on the theory of gravity and there are some interesting consequences of this postulate. Let us first consider one of the most spectacular of them. A slight rewording of the equivalence principle is that mass and all forms of energy are strictly equivalent. Thus, energy "falls" just like matter and all forms of matter or energy attract one another. Imagine squeezing a mass so that its volume decreases; eventually the body will be so small that the internal gravitational force will cause it to contract by itself. Ah, but what about repulsive forces (nuclear, electromagnetic, . .)? It doesn't matter because once gravity takes over, the energy in even the repulsive forces adds to the mass and contributes to the collapse. The gravitational field around the mass is so strong that even photons are gravitationally bound and no light can escape -- a black hole. The strong equivalence principle makes this collapse unavoidable once it starts.

How does this bear on ideas of elementary particle or nuclear physics? One finds that once matter has gone into a black hole external measurements can detect only its mass, charge, and angular momentum. Thus, we lose contact with many other quantum numbers we hold dear -- like baryon number. Penrose calls this "cosmic censorship,"[1] but it was at first thought to be no problem because though the information is not readily available, it is all still there inside the singularity. The situation turns out to be somewhat worse than that, however, and I will make a slight digression to show you why. This digression has a moral, which I will tell you in advance: take seemingly paradoxical results seriously.

About nine years ago Roger Penrose made an amusing discovery which was called the Penrose Paradox.[1] He found theoretically that if one scattered a particle from the gravitational field of a black hole, for a small range of impact parameters the particle gained energy in the collision. We all had a great laugh at that. We even joked that if we had a black hole all our problems would be solved at once; you could not only dump waste into it without fear of pollution but you could also extract energy from it. (Who needs either reactors or solar energy?) Well, we were all dumb because when you extract all the energy, the black hole and the singularity are gone and you've really lost the censored

quantum numbers. But what about quantum mechanics; will it change the outcome? A graduate student named Steve Hawking was much smarter than the rest of us; he realized that if we could devise ways of extracting energy from a black hole, nature could also manage to do it. He proposed the following process: virtual particle-antiparticle pair formation just outside the Schwartzschild radius. One particle has to get captured into the black hole in a negative energy state, the other gets enough positive energy to escape to infinity. He showed that the emission spectrum is that of a black body, with higher temperatures and shorter lifetimes for smaller mass black holes.[2] This causes deep philosophical trouble for the theorists because summing over all the unobserved quantum numbers of the captured particle of the pair is equivalent to a loss of information. In the standard jargon: "an S-matrix can't be defined for the process." Hawking puts it another way: "Einstein attacked the uncertainty principle by saying that God does not play dice; well, not only does he play dice but sometimes he throws them where they can't be seen."[3]

Before ending this digression I want to remind you of the moral. We all laughed at the Penrose Paradox, but Hawking won the Heineman Prize and the Vatican Medal and has certainly had the last laugh.

Returning to the equivalence principle we see that one of its consequences is black holes. And if they exist, then we get some interesting connections to the fundamental structure of quantum mechanics. Now that I've tried to convince you that it's important to determine to what extent the strong equivalence principle is valid, I want to first deal with tests of its weak form -- the equivalence of gravitational and inertial mass.

Over 80 years ago Baron Roland von Eötvös began a series of torsion pendulum measurements to look for differences in the gravitational and inertial masses for different materials, a fancier version of the Galileo legend. He used balls of metal, glass, snakewood -- all kinds of exotic materials, Ultimately he showed that all the materials behaved the same way to a level of 3×10^{-9}.[4] Using modern techniques this same torsion pendulum approach was employed by Roll, et al., for gold and aluminum to get a limit of $1.3 \pm 1.0 \times 10^{-11}$.[5] Braginsky and Panov picked up another order of magnitude for platinum and aluminum and got $-0.3 \pm 0.9 \times 10^{-12}$.[6]

The Braginsky experiment represents an incredibly sensitive test that platinum and aluminum behave the same way when their gravitational and inertial

masses are compared, but what does the result mean at a more fundamental level? If the aluminum and platinum atoms were made of exactly the same stuff (nucleons, quarks, cottage cheese, . .) then it would be no real surprise that they "fell" the same way. We must, therefore, look at the problem in greater detail.

Consider first the atomic properties: the electrostatic potential of the nucleus seen by the atomic electrons is very much larger for platinum or gold than for aluminum. Thus, if we consider the virtual positron-electron pairs created in this field, there are many more pairs for the high-Z elements. Schiff has shown that if the positrons "fell up" there would be an anomalous contribution to the weight of the atom that would be quite different for the two materials. For aluminum and platinum there would be a difference of $\sim 3 \times 10^{-7}$; i.e., the Braginsky-Eötvös experiment confirms that matter and antimatter have the same sign for the mass to a precision of 3×10^{-5}.[7]

What about differences in the nuclei? Platinum and aluminum have different ratios of neutrons to protons,

$$(N/Z)_{Pt} - (N/Z)_{Al} \simeq 1/5.$$

So we see the neutrons and protons fall the same way to $\sim 5 \times 10^{-12}$.[8] But since neutrons and protons are composed of the same constituents this is not too surprising. If we assume that neutrons and protons are collections of reasonably heavy quarks, one must ascribe the whole n-p mass difference to differences in the strong and electromagnetic binding of the quarks. The difference is, however, only about 1 MeV (out of ~ 1 GeV), so we lose a factor of 10^{-3}. Thus, we have only verified the equivalence to

$$\sim 5 \times 10^{-12} \times 10^3 \simeq 5 \times 10^{-9}$$

What about the differences in the binding energies of the neutrons and protons in the two nuclei? We can crudely estimate the differences in electrostatic binding energy:

$$E_{em} (MeV) \simeq \frac{1.44 \ Z(Z-1)}{R}$$

$$\simeq \frac{1.44 \ Z(Z-1)}{1.2A^{1/3}} = \frac{1.2 \ Z(Z-1)}{A^{1/3}}$$

$$\frac{E_{em}}{unit\ mass} \simeq \frac{E_{em}}{A} = \frac{1.2\ Z(Z-1)}{A^{4/3}} \left(\frac{MeV}{amu}\right)$$

$$\left(\frac{E_{em}}{A}\right)_{Al} \sim 2\ MeV/amu$$

$$\left(\frac{E_{em}}{A}\right)_{Pt} \sim 6\ MeV/amu$$

$$\Delta\left(\frac{E_{em}}{A}\right) \sim 4\ \frac{MeV}{amu}\ or \sim 4 \times 10^{-3}$$

Thus, we have checked the equivalence of electromagnetic energy and mass to

$$\sim \frac{10^{-12}}{4 \times 10^{-3}} \simeq 2 \times 10^{-10}\ .$$

What about the strong interaction? If we look at the binding energy per nucleon curve we find that these two nuclei differ by only about 200 keV/amu; thus, we have checked the equivalence of total binding energy and mass to only

$$\frac{10^{-12}}{2 \times 10^{-4}} \simeq 5 \times 10^{-9}\ .$$

However, this is misleading because the two nuclei have different amounts of nuclear and electromagnetic binding energy. A way to approximately decompose the contributions is with the semi-empirical mass formula. Almost any version gives comparable results, but since I'm at LASL I'll use an old form given by Phil Seeger:[9]

$$\frac{Mass\ excess}{A}\ \frac{MeV}{amu} = \overbrace{8.3674\ \frac{N}{A}}^{(1)} + \overbrace{7.5848\ \frac{Z}{A}}^{(2)} - \overbrace{16.11}^{(3)}$$

$$+ \overbrace{\left(20.65 - \frac{48.00}{A^{1/3}}\right)\left(\frac{(N-Z)^2 + 2|N-Z|}{A^2}\right)}^{(4)}$$

$$+ \overbrace{\frac{20.21}{A^{1/3}}}^{(5)} + \overbrace{0.8076 \; \frac{Z^2}{A^{4/3}} \left(1 - \frac{0.7636}{Z^{2/3}} - \frac{2.29}{A^{2/3}} \right)}^{(6)}.$$

Binding Energy

(MeV/amu)

	(1) Neutrons	(2) Protons	(3) Volume	(4) Asymmetry	(5) Surface	(6) ~ Coulomb
Al	4.338	3.652	-16.11	0.0191	6.737	0.7090
Pt	5.020	3.034	-16.11	0.5202	3.485	3.2727
Pt-Al	0.682	-0.618	0	0.5011	-3.252	2.564

Thus, though the strong and electromagnetic interactions differ a great deal in overall strength, since the difference is all that is tested by the Eötvös experiment we check each interaction separately to about

$$\frac{10^{-12}}{3 \times 10^{-3}} \sim 3 \times 10^{-10} \quad .$$

So far we've managed to look at the strong and electromagnetic interactions as well as possible differences between matter and antimatter. Can we say anything about the other interactions? We know that the weak interaction doesn't conserve parity; perhaps it also violates the equivalence principle. For many years it was thought that the weak contribution to nuclear binding was too small to be tested even by the Braginsky experiment. This isn't really true; nearly everyone made the same mistake, considering only the parity-non-conserving part of the weak interaction. Thus, the weak binding would go as the square of the coupling constant, i.e., one power to mix in the opposite parity and one power to connect back to the original state.

$$\sum_n \; < 0 | G' | n > \quad < n | G' | 10 >$$

(G' is the parity-non-conserving part of the potential.)

This was stupid, because the weak interaction is half parity conserving and half parity non-conserving. There is, therefore, a contribution to the

binding energy that goes as the first power of the coupling constant. Haugen and Will have calculated the volume part of the weak binding energy.[10] Though they used a current-current form for the interaction, one could equally well consider the exchange of intermediate vector bosons. Very schematically:

charged current

neutral current

$$\frac{energy}{nucleon} \sim \frac{NZ}{A^2} \qquad\qquad \frac{N^2}{A^2} \ , \ \frac{Z^2}{A^2} \ \cdots$$
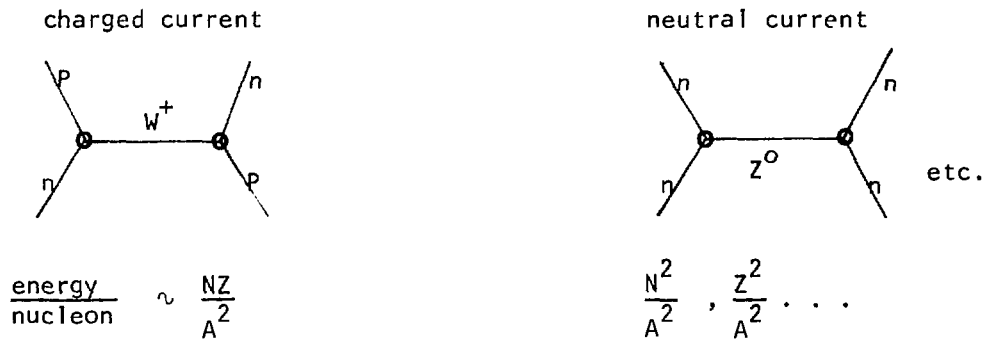
It's easy to see where the N, Z, A dependence comes from. The interaction is $\sim$ zero range so it depends on the local nucleon densities. For the charged current case:

$$\frac{1}{A}\left(\frac{N}{Vol.} \times \frac{Z}{Vol.} \times Vol.\right)$$

but volume $\widetilde{\propto} A$

$$\Rightarrow \frac{NZ}{A^2} \ .$$

The contributions of the charged and neutral currents are roughly comparable but the charged current piece is somewhat larger.

$$\left(\frac{E_{weak}}{A}\right) \sim 2 \times 10^{-8} \frac{NZ}{A^2}$$

	NZ/A^2
Al	0.25
Pt	0.24
Pt-Al	$\sim 10^{-2}$

Thus,

$$\delta \left(\frac{E_{weak}}{A} \right) \sim 2 \times 10^{-10} \quad .$$

This implies that the weak interaction obeys the "weak" equivalence principle to $\sim 10^{-2}$. If one corrects for the difference in the surface energy from the weak interaction we can get a difference that is perhaps as much as ten times larger, which would make the test good to $\sim 10^{-3}$.

Very recently I received a copy of a paper by J. P. Hsu that is soon to appear in Physical Review.[11] He computes the self energy of the nucleons in the nucleus due to the weak interaction and gets

$$\left(\frac{E_{self}^{weak}}{A} \right) \sim 10^{-5}, \text{ an enormous effect!}$$

I haven't had the time to go through the calculation in detail. As you know, self-energy contributions contain divergences and the results can be quite sensitive to the cut-off parameters used. I have to admit that I'm suspicious, and I'll have to do some work on it before I'm convinced.

Now I want to discuss an interesting idea to test the validity of the strong equivalence principle for the weak interaction. The Eötvös experiments have basically been done at constant ϕ so they really don't apply; what we need is an appreciable change in ϕ. Obviously, one can consider doing the Braginsky experiment on a space mission, but that is probably not possible for a while. The idea I'll discuss came from P. D. Parker at Yale;[12] although it doesn't work quite well enough yet, it's so clever that I'll tell you anyway.

In the decay chain for thorium (Fig. 1) there is an ambivalent nucleus, ^{212}Bi. It can decay either by ordinary beta decay or by alpha emission. The strength of the beta decay depends on the weak interaction coupling constant; the strength of the alpha decay depends in some complicated way on the strong and electromagnetic interactions which are pretty well tested by the Eötvös experiments.

One can thus consider a measurement of the branching ratio as a function of ϕ on a space mission as a way of comparing the weak coupling constant to the

strong and electromagnetic interactions as a function of ϕ. What makes the experiment so clever is that one doesn't have to observe the β's because the daughter nucleus after the β-decay decays only by alpha emission. You just measure the relative strengths of two alpha lines using a ^{228}Th source (Fig. 2) and a solid-state detector. What could be simpler?

Before we go on we should look at another possible complication -- the β-decay and α-decay are strongly affected by the mass of the decaying nucleus. If a violation of the equivalence principle changes that mass, will it help or partially cancel the effect to be observed?

For α-decay:

$$\ln \lambda_{\substack{decay \\ const.}} \simeq -3.92\ Z/\sqrt{E} + \sim const$$

So,

$$\lambda \overset{\sim}{\propto} E^{66.4} \quad ,$$

or

$$\frac{d\lambda}{\lambda} \sim 66.4\ \frac{dE}{E} \quad .$$

For β-decay:

$$F \overset{\sim}{\propto} E^5 \quad .$$

For $ft \sim const.$,

$$t \overset{\sim}{\propto} E^{-5} \text{ or } \lambda \overset{\sim}{\propto} E^5$$

Thus, the branching ratio (R) changes as

$$\frac{\Delta R}{R} \sim 61\ \frac{\Delta m}{m}$$

This is a reasonable amplification, but since the contribution to m from the weak interaction is already so small, the change in R due to this change in mass can be neglected. Thus, we need only consider the direct change in the branching ratio due to changes in the weak coupling constant with ϕ.[13]

The experiment has been checked by Parker in the laboratory. With some improvements one could probably make measurements of the branching ratio to 10^{-6} in a very compact experiment.

Where is the trouble? The change in the gravitational potential in going from the earth's orbit (1 A.U.) to four solar radii (4 R⊙) is approximately 6×10^{14} ergs/gm, i.e., an $\sim 10^2$ increase. (This mission is being planned now by JPL but is not funded. It will require either new technology in the form of an ion engine or solar sail or for a longer mission a gravitational assist by Jupiter.)

We don't really have much of an idea how a coupling constant might depend on $\Delta\phi$, but one might expect that it will mainly be affected by the change in the metric (like the gravitational red shift experiment).[14]

$$g \sim 1 + \frac{\phi}{c^2} \quad ,$$

So

$$\frac{\Delta g}{g} \sim 10^{-6} \quad .$$

Thus, the weak interaction would either have to have a much stronger dependence on g or the experiment will have to be made more sensitive. It looks difficult to just increase the source strength, because the detector suffers too much radiation damage.

So there's plenty of room for clever ideas to test the strong form of the equivalence principle, and I expect that a nuclear technique is just what's needed.
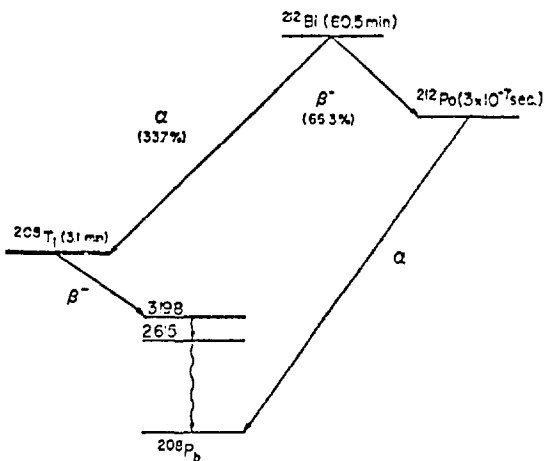
Fig. 1. The decay scheme for ^{212}Bi and its daughters, ^{208}Tl and ^{212}Po.
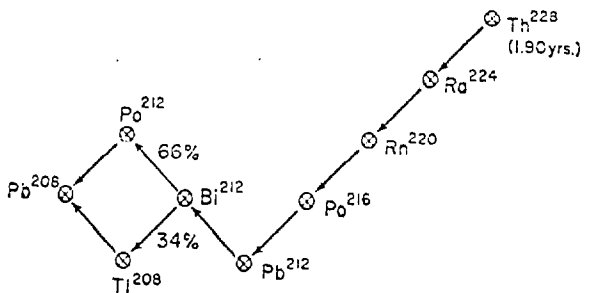
Fig. 2. The portion of the thorium decay chain from ^{228}Th to ^{208}Pb.

REFERENCES

1. R. Penrose, Nuovo Cimento 1, special number, 252 (1969).

2. S. W. Hawking, Nature 248, 30 (1974).

3. S. W. Hawking, Phys. Rev. D14, 2460 (1976).

4. R. von Eötvös, Ann. Phys. Chem. 59, 354 (1896).

5. P. G. Roll, R. Krotkov, and R. H. Dicke, Ann. Phys. (N.Y.) 26, 442 (1964).

6. V. B. Braginsky and V. I. Panov, Sov. Phys. JETP 34, 563 (1971).

7. L. I. Schiff, Proc. Nat. Acad. Sci. U.S. 45, 69 (1959).

8. A. H. Wapstra and G. J. Nijgh, Physica 21, 796 (1955).

9. P. A. Seeger, Nucl. Phys. 25, 1 (1961).

10. M. P. Haugen and C. M. Will, Phys. Rev. Lett. 37, 1 (1976).

11. J. P. Hsu, Phys. Rev. (in press) (1978).

12. P. D. Parker, Proposal for participation on the Out-of-Ecliptic mission (1977).

13. P. D. Parker, private communication.

14. C. W. Misner, K. S. Thorne, and J. A. Wheeler, Gravitation, (W. H. Freeman, San Francisco, 1973).

II. $^{12}C(\alpha,\gamma)^{16}O$ AND STELLAR HELIUM BURNING

When the hydrogen is exhausted in the core of a main sequence star, the star gradually contracts, which increases the temperature sufficiently that hydrogen begins to burn in a shell just outside the core of helium. The increased heat flux from this source causes a large expansion of the outer regions of the star; thus, although the total luminosity has increased, the surface of the star becomes cooler -- a red giant. When the inward pressure on the core helium finally exceeds the outward pressure from the highly degenerate electrons, the helium must begin to burn to resist the inward pressure. At this point the core density is $\sim 10^4$ gm/cm^3 at a temperature of 1-2 x 10^8 °K. (This is to be compared with our sun's central density of ~ 100 gm/cm^3 and a temperature of ~ 15 x 10^6 °K.)[1,2]

The helium burning reactions that can take place are complicated by the fact that ^{8}Be is unbound with respect to decay into two alpha particles. Thus, it is only when 3 alphas can react to form ^{12}C that a nuclear energy source becomes available. In Fig. 1 we see the level diagrams for ^{8}Be and ^{12}C. It is an interesting coincidence that at about the same energy where two alphas can form the ^{8}Be ground state, a third alpha can scatter from this short-lived state at an energy corresponding to the 0^+ second excited state of ^{12}C. The occasional radiative or pair decay of this state produces ^{12}C. Whether one can add additional alpha particles to the ^{12}C nuclei depends in a very sensitive fashion on the level structures of the alpha particle nuclei, ^{16}O, ^{20}Ne, . . . There are also minor (but interesting) effects due to the presence of small amounts of ^{14}N left over from the hydrogen burning CNO cycle, but that story will have to wait for another time.[2]

The level structure of ^{16}O is shown in Fig. 2. Determination of the rate of the $^{12}C(\alpha,\gamma)^{16}O$ reaction under stellar conditions is non-trivial because at the energy involved (0.3 MeV) the cross section is probably dominated by the tail of the bound 7.12 MeV, 1^- state. A direct measurement of the cross section (10^{-8} nb) at this energy is not now feasible. At higher energies the broad 1^- state at 9.6 MeV reaches a maximum capture cross section of about 40 nb; it is the interference of these two 1^- states that provides the opportunity to probe the structure of the 7.12 MeV state. The interpretation of such data is, of course, complicated by the possible presence of other unresolved, broad states at higher energies that also contribute a coherent background.

The only pieces of information that are needed to determine the stellar reaction rate are the probability to form the 7.12 MeV state (proportional to its alpha decay width, Γ_α) and the probability of its radiative decay (proportional to its radiative width, Γ_γ). The latter can be determined independently by resonance fluorescence measurements -- inelastic photon scattering from ^{16}O (g.s.) to its 7.12 MeV state.[3] Thus, we need only one additional parameter, Γ_α. Before going on with our discussion, I shall make a short detour to remind you of some of the details of the resonance theory of nuclear reactions. Since I don't plan to get bogged down in theoretical details, I'll present an abbreviated account for the simplest case: spinless particles (ok for $\alpha + ^{12}C$) and one channel open (elastic scattering only; the radiative capture is very small and we can add it later). I shall leave out most of the algebra, but you can find all the details in Preston[4] or Lane and Thomas.[5]

We shall assume that the nuclear potential has a sufficiently short range that beyond $r = a$ it can be entirely neglected. Thus, for $r \geq a$ we can write the wave function in terms of ingoing and outgoing Coulomb waves:

$$\psi = \sum_{\ell=0}^{\infty} i^\ell \sqrt{\pi(2\ell+1)}\; e^{i\sigma_\ell}\, \frac{1}{kr} \left\{ I_\ell(r) + e^{2i\delta_\ell} O_\ell(r) \right\} Y_\ell^0(\theta,\phi)$$

where $I_\ell = F_\ell + iG_\ell$, $O_\ell = F_\ell = iG_\ell$, σ_ℓ is the Coulomb phase shift, δ_ℓ is the nuclear phase shift, and the F_ℓ and G_ℓ are the Coulomb functions that are regular and irregular at the origin, respectively.

Inside the range of the potential ($r \leq a$) we'll write the wave function as:

$$\psi = \sum_\ell \frac{U_\ell(r)}{r}\; Y_\ell^0(\theta,\phi)$$

We may evaluate the nuclear phase shift (δ) by matching the inner and outer solutions at $r = a$. We find it useful to define the log derivative, $1/R_\ell$:

$$U_\ell(a) = R_\ell a \left(\frac{dU_\ell}{dr} \right)_{r=a} .$$

In a multi-channel case R becomes a matrix -- the R matrix. After about a page of algebra we obtain:

$$\delta_\ell = \tan^{-1}\left(\frac{R_\ell P_\ell}{1-R_\ell S_\ell}\right)_{r=a} - \phi_\ell(a) \quad ,$$

where

$$\phi_\ell(a) = \tan^{-1}\left(\frac{F_\ell}{G_\ell}\right)_{r=a} \quad ,$$

$$P_\ell = \left(\frac{kr}{F_\ell^2+G_\ell^2}\right)_{r=a} \quad \text{(the penetrability),}$$

and

$$S_\ell = \left[\frac{\left(F_\ell\dfrac{dF_\ell}{dr} + G_\ell\dfrac{dG_\ell}{dr}\right)r}{F_\ell^2+G_\ell^2}\right]_{r=a} \quad \text{(the shift function).}$$

At this point we've merely traded our lack of knowledge of δ_ℓ for a lack of knowledge of R_ℓ. The only assumption made is that there exists a value of a, outside of which we may neglect the nuclear potential.

Let us now introduce for each ℓ a complete set of solutions to the nuclear Hamiltonian in the region $r \lesssim a$. These solutions differ from the correct solutions in that we shall choose them to satisfy a more convenient (but arbitrary) boundary condition at $r = a$. We shall denote these functions by a subscript λ which refers to each discrete eigenfunction $U_{\ell\lambda}$ with eigenvalue $E_{\ell\lambda}$. At $r = a$,

$$\frac{a\left(\dfrac{dU_{\ell,\lambda}}{dr}\right)_{r=a}}{U_{\ell\lambda}(a)} = B \text{ (a constant).}$$

Since these are eigenfunctions of a real Hamiltonian, they are orthogonal and we shall normalize them so that

$$\int_0^a U_{\ell,\lambda} \, U_{\ell,\lambda'} \, dr = \delta_{\lambda,\lambda'} \quad .$$

Expanding the actual solution at energy E in terms of the $U_{\ell,\alpha}$:

$$U_{(E)\ell}(r) = \sum_\lambda A_\lambda U_{\ell,\lambda}(r)$$

and using Green's theorem (and more algebra) we can evaluate the R_ℓ in terms of the $U_{\ell,\alpha}(a)$.

$$R = \frac{\displaystyle\sum_\lambda \frac{\gamma_{\ell\lambda}^2}{E_{\ell,\lambda}-E}}{1 + B \displaystyle\sum_\lambda \frac{\gamma_{\ell\lambda}^2}{E_{\ell,\lambda}-E}} \quad , \text{ where}$$

$$\gamma_{\ell,\lambda}^2 = \frac{\hbar^2}{2\mu a} U_{\ell,\lambda}^2(a) \quad . \quad (\mu \text{ is the reduced mass})$$

The form of the function suggests that resonances may occur in the scattering as a function of the energy. In many cases we may be able to consider a range of E sufficiently close to one of the E_λ's that we can neglect all the other terms in the summation.

$$R_{\ell,\lambda} \simeq \frac{\gamma_{\ell\lambda}^2}{E_{\ell,\lambda}-E} \bigg/ \left(1 + \frac{\gamma_{\ell,\lambda}^2 B}{E_{\ell,\lambda}-E}\right)$$

$$= \frac{\gamma_{\ell,\lambda}^2}{E_{\ell,\lambda}-E + \gamma_\lambda^2 B}$$

or

$$\delta_{\ell,\lambda}+\phi_\ell = \tan^{-1}\left\{\frac{P_\ell \gamma_{\ell\lambda}^2}{E_{\ell,\lambda}-E -\gamma_{\ell,\lambda}^2 (S_\ell-B)}\right\}_{r=a}$$

This is the Breit-Wigner <u>single</u> level formula.

In this expression, $\gamma_{\ell\lambda}^2$ and $E_{\ell\lambda}$ are independent of the energy, E, P_ℓ and S_ℓ are energy dependent and are determined from the Coulomb functions. For a narrow resonance,

$$\Gamma_{\ell\lambda} = 2 \gamma_{\ell\lambda}^2 P_\ell$$

142

gives the resonance width in terms of $\gamma_{\ell\lambda}^2$. In the case we're considering $(\alpha + {}^{12}C)$ we have $\ell = 1$ for the 9.6 and 7.12 MeV levels. We thus get the following expressions for the scattering phase shift and the E-1 capture cross section:

$$\delta_1 = \left[-\phi, + \tan^{-1}\left(\frac{R_{\alpha\alpha}P_1}{1-R_{\alpha\alpha}S_1} \right) \right]$$

and

$$\sigma_{\alpha\gamma}(E-1) = \frac{6\pi}{k^2} \left| \frac{R_{\alpha\gamma}}{1-(S_1+iP_1)R_{\alpha\alpha}} \right|^2 \quad .$$

There have been several attempts to parametrize the $\ell = 1$ scattering phase shift for ${}^{12}C(\alpha,\alpha){}^{12}C$ and the E-1 cross section for ${}^{12}C(\alpha,\gamma){}^{16}O$ in terms of the γ_λ^2 and E_λ's so that a reliable extrapolation to stellar energies could be made. These have all had difficulties, which I will discuss later.[6]

There have also been attempts to extract information on $U_{\alpha;7.12}^2(a)$ (and hence $\Gamma_{\alpha,7.12}$) from direct reaction alpha transfer analyses of reactions like ${}^{12}C({}^7Li,t){}^{16}O$.[7,8] The results obtained have considerable scatter, which in some cases is known to be due to an appreciable compound nucleus contribution to the reaction cross section. Later, I shall summarize these results along with those from the analysis of ${}^{12}C(\alpha,\gamma){}^{16}O$.

I shall tend to restrict my remarks to the direct measurements of ${}^{12}C(\alpha,\gamma){}^{16}O$ because it now appears that these data have led to a successful extrapolation of the cross section. The key to this success is entirely due to a beautiful experiment done by Peggy Dyer and Charles Barnes that I shall describe briefly.[9]

The main difficulties in performing the measurements were the very small cross section for the ${}^{12}C(\alpha,\gamma){}^{16}O$ reaction (down to $\sim 1/4$ nb) and the very large cross section for ${}^{13}C(\alpha,n){}^{16}O$. The first experimental improvement they made was to separate the neutrons and γ rays by time of flight. Though this is an obvious step, it had to be done efficiently because one loses solid angle for the NaI detectors as the flight path is increased, and beam intensity is lost in order to provide a pulsed beam for the timing. Figure 3 shows the time-of-flight spectrum. The data points shown as crosses are for a natural carbon target ($\sim 1\%$ ${}^{13}C$). Also shown are the data points using a target that was greatly depleted (by $\sim 10^2$) in ${}^{13}C$; this was the second improvement that made this experiment possible.

143

Though most of the capture cross section is from E-1 capture ($\ell = 1$ partial wave), there is enough non-resonant E-2 ($\ell = 2$) contribution to complicate the analysis. However, measurements of the angular distributions of the γ rays allow the E-2 part to be subtracted. Figure 4 shows the angular distributions. The E-1 gives a pure $\sin^2\theta$ pattern, so it's obvious that there is some E-2 present. The derived ratio of the E-2 to the E-1 is shown in Fig. 5. The solid line is theoretical, a direct capture calculation for the E-2 that I made for Peggy. (The reason for the dip in the curve is not that the E-2 varies, but rather that the E-1 resonates at 2.4 MeV -- the 9.6 MeV state.)

Figure 6 shows the total E-1 cross section obtained. I'll also define a new quantity, S(E).

$$\sigma_{\alpha\gamma} = \frac{S_{\alpha\gamma}(E)}{E} \; e^{-2\pi\eta}$$

where $\qquad \eta = \dfrac{Z_\alpha Z_c e^2 \mu}{\hbar^2 k}$ and E is the center-of-mass energy.

The $\dfrac{e^{-2\pi\eta}}{E}$ is the Gamov factor; thus, S is the cross section with the effect of the Coulomb barrier crudely removed. This gives us a curve that doesn't fall quite so fast with decreasing energy (Fig. 7).

The curves shown are the best fits available using the R-matrix parametrization.

(a) The dashed curve leaves out the effect of the 7.12 MeV state.

(b) The solid curve is the best fit.

(c) The dotted curve is the largest contribution from the 7.12 state that is not totally excluded by the data.

In terms of the value of S at 0.3 MeV, they get:

$$S(E = 0.3 \text{ MeV}) = 0.14 \; ^{+\,0.14}_{-\,0.12} \text{ MeV b.}$$

A slightly different resonance formalism employed by Humblet, Dyer and Zimmerman[10] (the K-matrix) gives $S(0.3) = 0.08 \; ^{+\,0.14}_{-\,0.07}$ MeV b. The reason that the uncertainty is so large is that many parameters must be determined from the data, and the greatest unknown concerns the possible presence of broad, unresolved states at higher energies.

About the same time that Dyer and Barnes were getting their data (1972), Steve Koonin and I had a new idea about this problem. It is well known that one runs into trouble if you try to describe the broad resonances of a simple potential (e.g., a square well) in terms of the single level formula. What happens is that the convergence of the R-matrix expansion is very slow in such cases and one must keep quite a few terms. We realized that the 9.6 MeV resonance was just this sort of resonance and that all the previous R-matrix analyses had tried to treat this level in terms of one (or at most two) terms in the expansion. Rather than just add terms, and thereby add more free parameters, we figured out a way to combine the R-matrix formalism with ordinary scattering from a potential -- a "hybrid" analysis.[11] I won't go through this in detail; it would take a lot of time and would appeal only to the experts. What I will do is show how it goes for just the elastic scattering; the extension to the case of $^{12}C(\alpha,\gamma)$ is in our paper.[11]

Suppose we describe the 9.6 MeV level by scattering from a potential $V(r)$; this is just the first approximation, but we have to start somewhere. We choose the depth of the potential to get the right energy for the resonance, we pick a radius appropriate to the scattering of an alpha particle from ^{12}C, and we adjust the surface thickness (diffuseness) of the potential to fit the width of the resonance. What about the 7.12 MeV state? There's no reason to assume that it should be an eigenstate of $V(r)$ -- how do we include it?

Prescription:

1. Use $V(r)$ to calculate $\delta^0(E)$.

2. Invert the expression that connects δ and R to get $R^0(E)$

3. Remember the $R^0(E)$ is just a sum of poles and that the 7.12 state is just another pole.

4. Add in the pole for the 7.12 state -- having chosen $E_{7.12}$ to put it at the correct energy.

$$R(E) = \frac{\gamma^2_{7.12}}{E_{7.12}-E} + R^0(E)$$

5. Now we can consider $\delta(E)$ as a fn of $R(E)$. We vary $\gamma^2_{7.12}$ and the parameters of $V(r)$ to get the best fit to δ_{exp}.

You must remember that this is just an example, because δ turns out to be insensitive to $\gamma^2_{7.12}$. Thus, we can approximately fix the parameters of $V(r)$ in fitting δ, then use the $\sigma_{\alpha,\gamma}$ data to determine $\gamma^2_{7.12}$.

The results are summarized in Figs. 8 and 9. In Fig. 8 $\sigma_{\alpha\gamma}$ is given with the solid curve representing the best fit and the dashed curve leaving out the effect of the 7.12 MeV level. The same curves are shown for S(E) in Fig. 9.

The "final" result for the hybrid analysis gives:

$$S(0.3) = 0.08 \, {}^{+\,0.05}_{-\,0.04} \text{ MeV b}$$

Recently Brad Flanders and I have done a bit more work on the problem to investigate some of the approximations that underlie the hybrid model. The up-shot of the new work is

$$S(0.3) = 0.09 \, {}^{+\,0.05}_{-\,0.04} \text{ MeV b}$$

and we're feeling much more secure that the problem is really solved.

I promised a comparison with the direct reaction analyses. In these I've given the ratio of $\gamma^2_{\alpha,7.12}$ to $\gamma^2_{\alpha,9.59}$. I have also changed one of the conventions used by Koonin to make all the numbers directly comparable. (This basically has to do with a uniform way of choosing the boundary condition, B.)

Method	$\left(\dfrac{\gamma_{\alpha,7.12}}{\gamma_{\alpha,9.59}} \right)^2$	Reference
Theory	0.09 ± 0.05	13
$^6\text{Li}(^{12}\text{C},d)^{16}\text{O}$	$0.07 \rightarrow 0.16$	8
$^{12}\text{C}(^7\text{Li},t)^{16}\text{O}$	0.03	7
Hybrid analysis	0.03 ± 0.015	11
Hybrid analysis	0.1 ± 0.05	12

Before closing I want to return to a brief discussion of the astrophysics. Based on the results of the "hybrid" analysis, we obtain the following ^{12}C mass fractions at the end of helium burning.[9] (Note that since $^{16}\text{O}(\alpha,\gamma)^{20}\text{Ne}$ is non-resonant at these temperatures, helium burning yields predominantly ^{12}C and ^{16}O.)

Core Mass/$M_\odot$	^{12}C Mass Fraction
2	$0.72 \begin{smallmatrix} +0.20 \\ -0.14 \end{smallmatrix}$
5	$0.62 \begin{smallmatrix} +0.20 \\ -0.14 \end{smallmatrix}$
10	$0.54 \begin{smallmatrix} +0.20 \\ -0.14 \end{smallmatrix}$
20	$0.46 \begin{smallmatrix} +0.20 \\ -0.14 \end{smallmatrix}$

So, one ends up with roughly equal amounts of carbon and oxygen. One should realize that if $\gamma^2_{\alpha,7.12}$ were much larger then one would end up with almost pure ^{16}O, which would have made it much more difficult to produce a life form based on carbon.
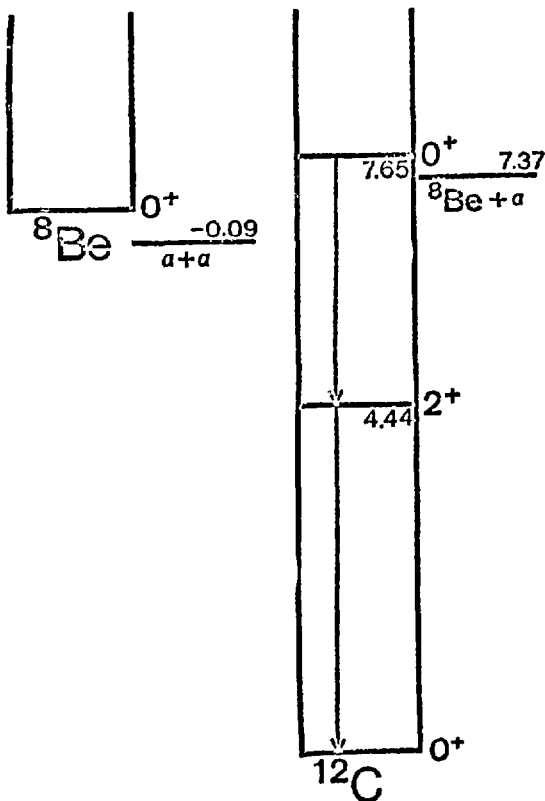
Fig. 1. Abbreviated energy level diagrams for ^8Be and ^{12}C that show the states that are important in stellar helium burning.
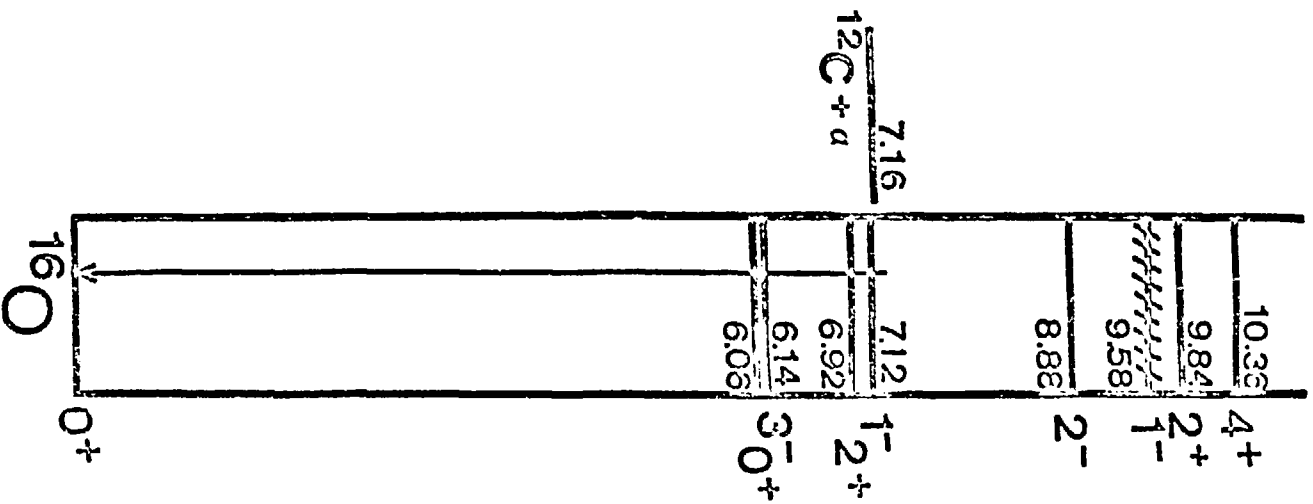
Fig. 2. The level structure of the low lying states of ^{16}O.

$^{12}C + \alpha$

7.16

^{16}O

10.36 4^+
9.84 2^+
9.58 1^-
8.88 2^-

7.12 1^-
6.92 2^+
6.14 3^-
6.05 0^+

0^+

COUNTS / CHANNEL

$E_\alpha(c.m.) = 1.96$ MeV

CHANNEL NUMBER

I NANOSECOND

COUNTS / CHANNEL

$E_\alpha(c.m.) = 2.42$ MeV

CHANNEL NUMBER

I NANOSECOND

COUNTS/CHANNEL

$E_\alpha(c.m.) = 2.86$ MeV

CHANNEL NUMBER

I NANOSECOND
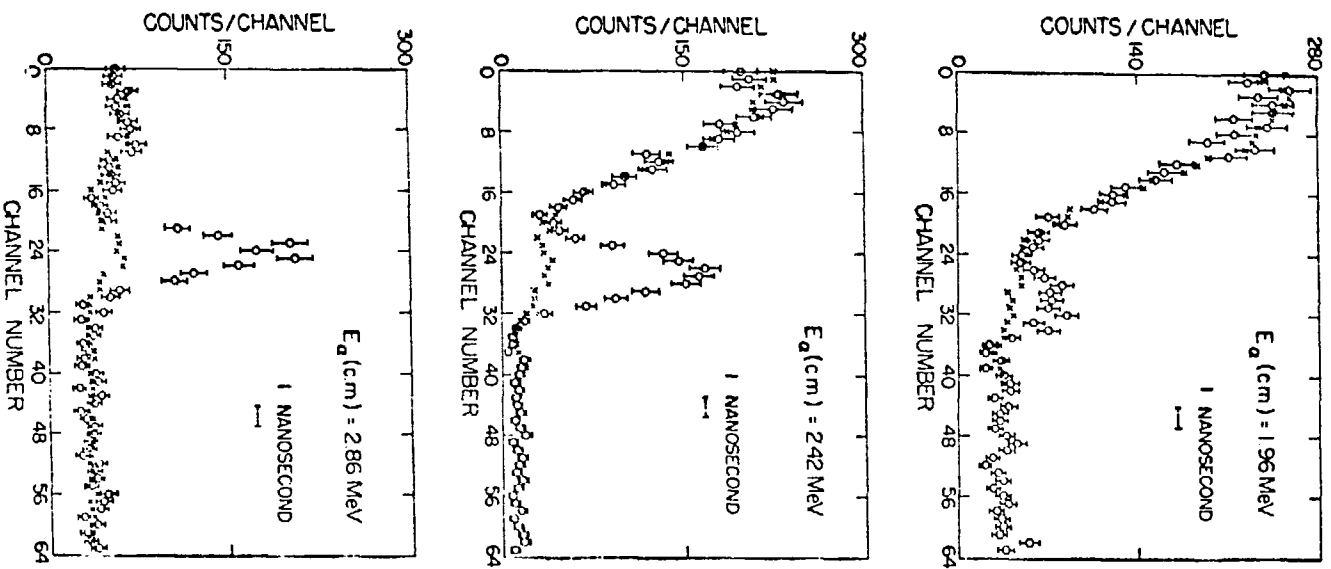
Fig. 3. The time-of-flight spectrum for an NaI detector used for an alpha particle beam on a natural carbon target (crosses) and on a target depleted in ^{13}C (open circles).
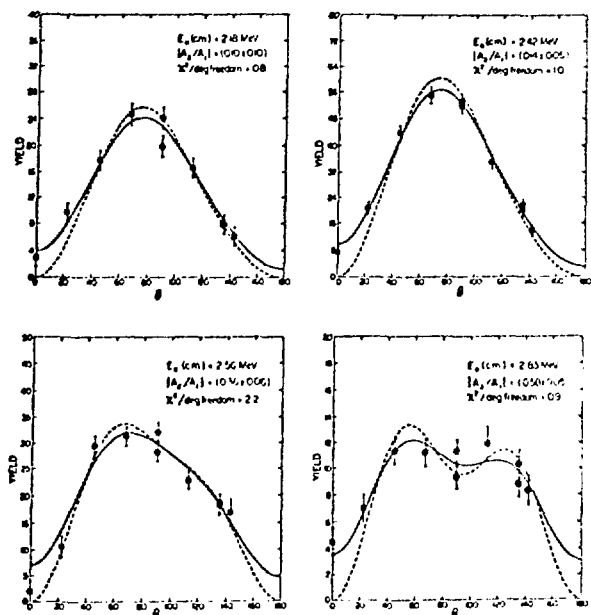
Fig. 4. The angular distributions for $^{12}C(\alpha,\gamma)^{16}O$. The dashed curves are the same distributions as they would be measured by a point detector.

Fig. 6. The E-1 cross section for $^{12}C(\alpha,\gamma)^{16}O$. The solid curve is the best R-matrix fit. The dashed curve leaves out the 7.12 MeV level.

Fig. 5. The ratio of E-2 to E-1 capture. The solid curve is a theoretical calculation normalized to the data shown.
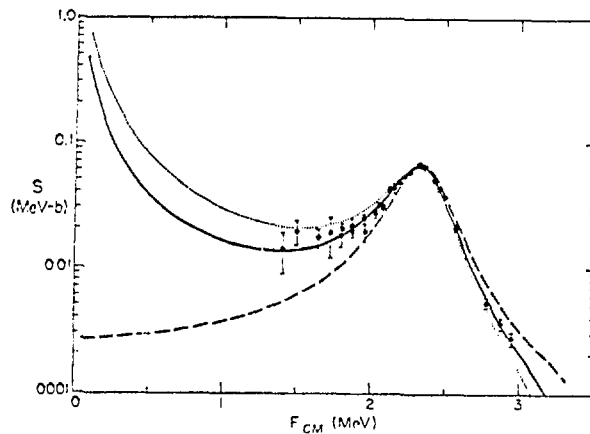
Fig. 7. The S-factor for the E-1 part of $^{12}C(\alpha,\gamma)^{16}O$. The solid an and dashed curves have the same meanings as in Fig. 6. The dotted curve is the maximum contribution from the 7.12-MeV state that is consistent with the data.
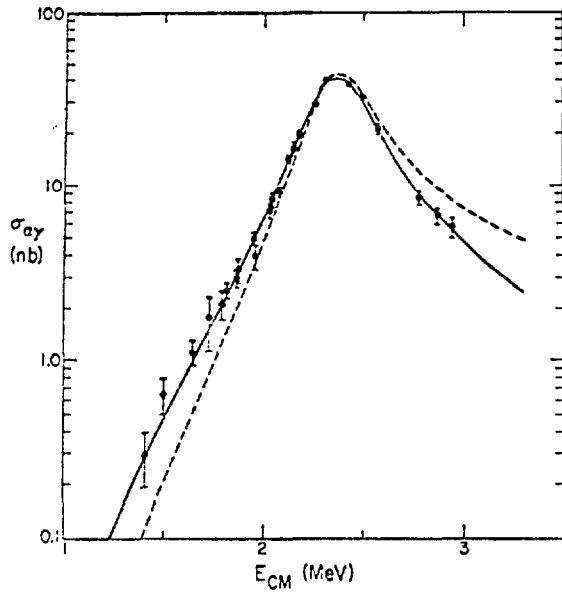
Fig. 8.   The hybrid model fit to the E-1
           part of the $^{12}C(\alpha,\gamma)^{16}O$ cross
           section is given by the solid
           curve.   The dashed curve leaves
           out the effect of the 7.12-MeV
           level.
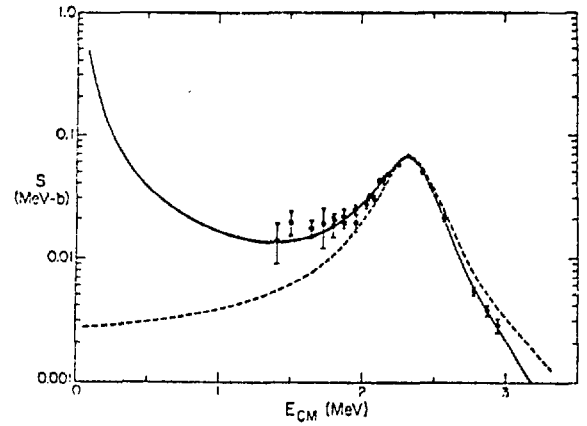
Fig. 9.   The hybrid model fit to the
           S-factor for the E-1 part of
           $^{12}C(\alpha,\gamma)^{16}O$.   The curves have
           the same meanings as in Fig.
           8.

REFERENCES

1. D. D. Clayton, _Principles of Stellar Evolution and Nucleo-synthesis_, McGraw-Hill, New York, 1968.

2. C. A. Barnes, Adv. in Nucl. Phys., Vol. 4, Ed. M. Baranger and E. Vogt, Plenum Press, New York, p. 133 (1971).

3. C. P. Swann, Nucl. Phys. A150, 300 (1970).

4. M. A. Preston, _Physics of the Nucleus_, Addison-Wesley, Palo Alto, pp. 481-496 (1962).

5. A. M. Lane and R. G. Thomas, Rev. Mod. Phys. 30, 257 (1958).

6. D. C. Weisser, J. F. Morgan, and D. R. Thompson, Nucl. Phys. A235, 460 (1974).

7. F. Pühlhofer, H. G. Ritter, R. Bock, G. Brommundt, H. Schmidt, and K. Bethge, Nucl. Phys. A147, 258 (1970).

8. H. M. Loebenstein, D. W. Mingay, H. Winkler, and C. S. Zaidins, Nucl. Phys. A91, 481 (1967).

9. P. Dyer and C. A. Barnes, Nucl. Phys. A233, 495 (1974).

10. J. Humblet, P. Dyer, and B. A. Zimmerman, Nucl. Phys. A271, 210 (1976).

11. S. E. Koonin, T. A. Tombrello, and G. Fox, Nucl. Phys. A220, 221 (1974).

12. B. Flanders and T. A. Tombrello, to be published.

13. G. J. Stephenson, Astrophys. J. 146, 950 (1966).

III. RADON MONITORING AND EARTHQUAKE PREDICTION

During the past fifteen years unusual crustal uplifts and downwarping have been occurring along the San Andreas fault from Cajon to Maricopa and eastward into the Mojave Desert and along the base of the San Gabriel mountains. During 1976 and 1977 anomalous swarms of small earthquakes were noted on a section of the San Andreas fault near Palmdale that had exhibited little seismicity during the past four decades.[1] At present there is controversy over the interpretation of these observations. Among the varying interpretations, one finds the following possibilities: (1) this is part of the normal mountain building process and is likely to proceed without significant seismic events, (2) the uplift is related to strain accumulation along the locked southern portion of the San Andreas fault, or (3) the uplift is associated with thrust-type movement on the north dipping thrust faults along the Transverse Range. There appears to be little agreement as to whether or not the geodetic and seismic data can be considered premonitory to an impending major seismic event.

Regardless of the interpretation, it is quite clear that Southern California is a heavily populated region of high seismic risk. Damaging earthquakes have occurred in the past in this area, and they certainly will occur in the future. The presence of the uplift on a part of the San Andreas fault that has been accumulating strain since the Fort Tejon earthquake of 1857 only underlines the need for a credible earthquake prediction capability for this region.

The proximity of the uplift region to the heavily populated areas of Southern California makes imperative the need for upgraded monitoring of those geophysical and geological parameters that could provide a prediction of an impending major seismic event. At present, the specific models that would lead to a fundamental understanding of the earthquake risk in the uplift zone need much additional work. Nevertheless, a growing body of empirical evidence suggests that a number of geological and geophysical parameters undergo fairly marked changes before an earthquake.[2-6,7-13,14] These parameters include seismicity, acoustical velocity, uplift, tilt, strain, local gravity, resistivity, ground water levels, radon content of ground water, and radon and thoron emanation. In addition, before some major earthquakes there have been reports of strange animal behavior and anomalous atmospheric electrical discharges (earthquake lights and lightning).[2,14,15] While it is unlikely that any one parameter can be used to provide definitive predictions of impending earthquakes, it is likely that

correlated changes in a number of parameters will provide reasonably reliable predictions.

Radon and Thoron Monitoring and Earthquake Activity

Uranium and thorium are two of the most ubiquitous elements in the earth's crust. Their daughters, radon and thoron, are radioactive noble gases with half-lives of 3.83 days and 55 seconds, respectively. These gases migrate through the earth's crust and emanate into the atmosphere and ground water. Radon, together with its principal daughter products ^{214}Pb ($T_{\frac{1}{2}}$ = 26.8 min), ^{214}Bi ($T_{\frac{1}{2}}$ = 19.7 min), and ^{210}Pb ($T_{\frac{1}{2}}$ = 22 yr), and thoron together with its principal daughter product ^{212}Pb ($T_{\frac{1}{2}}$ = 10.8 hr), long have been used as geophysical tracers of hydrological and atmospheric processes. (See Table I.)

TABLE I

RADON AND THORON DECAY SERIES

Isotope	Half-Life	Principal Decay Modes
^{222}Rn (radon)	3.824 d	α (5.49 MeV, ~100%)
^{218}Po	3.05 m	α (6.00 MeV, 100%)
^{214}Pb	26.8 m	β (1.04 MeV, 7%; 0.75 MeV, 43%; 0.69 MeV, 46%; others)
		γ many
^{214}Bi	19.8 m	β (3.28 MeV, 19%; 1.90 MeV, 8.6%; 1.43 MeV, 8.7%; many others)
		γ many
^{214}Po	162 μs	α (7.69 MeV, 100%)
^{210}Pb	21.3 y	β (0.06 MeV, 20%; 0.015 MeV, 80%)
^{220}Rn (thoron)	55.3 s	α (6.28 MeV, 100%)
^{216}Po	0.15 s	α (6.78 MeV, 100%)
^{212}Pb	10.64 h	β (0.57 MeV, 19%; 0.33 MeV, 77%; 0.15 MeV, 4.9%)
		γ many
^{212}Bi	60.6 m	α (5.61-6.09 MeV, 35.9%) β (2.25 MeV, 54.8%; 1.52 MeV, 5.0%; others)
		γ many
^{212}Po	0.3 μs	α (8.79 MeV, 64.07%)
^{208}Tl	3.07 m	β (1.80 MeV, 18.7%; 1.52 MeV, 8.2%; 1.29 MeV, 8.5%; 1.03 MeV, 1.0%)
		γ many

Geological processes prior to earthquakes that result in a change of pore volume or a change in the state of local stress fields are expected to result in anomalous values for subsurface radon concentrations. The dilatancy-diffusion model makes specific qualitative predictions for the behavior of this radon anomaly prior to an earthquake.[16] For at least some of the observed anomalies there appears to be agreement with the model.[3,4]

Increased radon in well water was observed prior to the major 1966 Tashkent earthquake,[4] the major Liaotung Peninsula earthquake,[5,6] and the major Haicheng earthquake, as well as a number of small earthquakes.[9,11-13] Earthquake lights or lightning which may be due to the increased ionization of the lower atmosphere resulting from increased radon and thoron emanation[14] was also observed in several cases.[14,15]

Several of the possible radon anomalies preceding small and moderate earthquakes have been observed on the San Jacinto fault in Southern California,[10] and

at Lake Jocasse in South Carolina.[9] In most of these cases <u>reductions in the</u> <u>radon levels</u> were noted prior to the events.

Several techniques have been used to monitor radon. In this country, radon levels are measured in discrete, small samples of well water,[7,8] <u>in situ</u> in water from continuously flowing wells and springs,[8,9] in soil gas using track detectors,[10,11] and with continuous and near continuous air monitoring systems.[11,12] Radon concentrations are measured by monitoring the alpha activity of the radon itself[7,10,11] and by monitoring the gamma activity[8] or beta activity[12] of the radon decay products. Examination of the available radon data provides the following information:

(1) Radon anomalies frequently, but not always, precede earthquakes.[2-12] The proximity to the epicenter does not always correlate with the size of the precursory signal.[2] Sensitivity appears to be greatest for those events located on the same fault or fault system as the monitor.

(2) Precursory radon signals may be either increases or decreases from "normal" levels. One Chinese study[13] suggests that monitors located in zones of compressional strain record anomalous increases, while those located in dilatant zones record anomalous decreases.

(3) Data from continuous or almost continuous radon monitors frequently show diurnal variations.[8,12,17] Some investigators are of the opinion that these diurnal variations are related to the lunar tides,[8] while in other cases temperature variations are believed responsible.

(4) Monitors which sample soil gas or groundwater radon close to the surface frequently exhibit a rapid response to short term atmospheric variations and to rainfall.[11,12]

(5) When the effects listed in (3) and (4) are removed from the data, long term variations in the radon levels often remain.[11,12] Some of these signals appear to be correlated with local earthquakes, while others appear to be seasonal variations.

(6) Some radon anomalies have been observed only hours before earthquakes.[2] Therefore, a complete radon monitoring system must include the capability for continuous or near continuous monitoring.

The Caltech Monitor

Sub-surface radon and thoron are formed by the decay of uranium and thorium which are ubiquitous in the earth's crust. Once formed, these radioactive gases

diffuse to some extent into the pore spaces within rock and into soil voids where they can become dissolved in pore fluids and soil gases. In order to measure these sub-surface radon concentrations, the instrument is sited in a tunnel or mineshaft, or over a borehole.

The radon and thoron within the air space of the tunnel, mineshaft, or bore-hole decay with half-lives of 3.8 d and 55 s, respectively. The principal decay products of ^{222}Rn (radon) are ^{214}Pb and ^{214}Bi with half-lives of 26.8 and 19.8 min respectively, while the principal decay product of ^{220}Rn (thoron) is ^{212}Pb with a 10.6 hr half-life (Table I). These decay products are formed as small charged ions which are highly reactive. In the free atmosphere they quickly agglomerate on much larger aerosol particulates. Typical times for agglomeration in clean air at sea level are of the order of a minute or two.[18] If adequate aerosol counts are maintained, similar agglomeration times obtain within the more confined space of the tunnel or borehole. Once agglomeration has taken place, the charged aerosol thus formed will carry the radioactive atom for several minutes (until decay occurs). Some collisions with surfaces can take place during this time. With each collision there is a small probability that the charged aerosol will attach to the wall and be lost from the sample volume. We have found that these wall effects depend linearly on temperature, and thus can be corrected for without difficulty.

To obtain a measurement of the radon and thoron daughter activity, the instrument draws a measured amount of air from the borehole or tunnel through Whatman Grade 4 chromatography filter paper. This concentrates the aerosols in a 1.27 cm diameter spot on the filter paper. The β activity of the aerosols is determined with a small pancake type GM tube (Technical Associates P1210).

In order to determine background and distinguish between radon daughter and thoron daughter activity, the following sampling sequence is carried out for each measurement. First, a fresh segment of the continuous filter paper strip is positioned over the air intake port and a 60-minute background count is taken. Aerosol is then injected into the air volume if necessary, and one-half hour is allowed for agglomeration. Next, the GM tube is moved away from the air intake location and air is drawn through the filter paper for a short period of time (typically 4 min at approximately 0.1 m^3/min). The GM tube is repositioned over the aerosol spot on the filter paper and a 20-min count is taken. This second count includes contributions from both radon and thoron daughters. The sample

is allowed to decay for 220 min, and then a 60-min count is taken. Because of the short half-lives for the radon daughters, ^{214}Pb and ^{214}Bi, the excess above background in this third count is due almost entirely to the thoron daughter ^{212}Pb.

The Caltech instruments are controlled by inexpensive on-board microcomputers which are able to handle up to eight additional digital or analog inputs besides the basic monitor operation. These additional input channels will be used to monitor temperature probes at each site in order to gather data on thermoelastic strains in the vicinity of each unit. Each of the field units is capable of communicating its data to a central location in response to a telephone call from a central computer. (At present, a microcomputer with an automatic dialing system is used to communicate with the field monitors.) This allows the use of ordinary voice quality telephone lines, thus reducing telemetry costs.

In addition to the collection of scientific data, each on-board microcomputer monitors the status of all key electronic and mechanical components of the device. The information also is telemetered to the central computer. This feature greatly reduces the need for service trips to remotely sited units. Although the Caltech radon-thoron monitor is a highly sophisticated device, its initial cost is lower than most competitive real-time radon monitoring systems. Indeed, over the long run the total cost of installation and operation is competitive even with passive monitoring techniques (radon cups and discrete water samples) owing to the elimination of the need for frequent costly trips to the field.

The first prototype Caltech radon-thoron monitor has been in field operation at the Kresge Seismological Laboratory in Pasadena for over one year. During that time it has proven exceptionally reliable. There have been no failures of the computer or ancillary electronics, and only a few minor mechanical problems that were easily diagnosed with data from the on-board microcomputer. This experience resulted in design changes for succeeding units.

Before I talk about our results, I want to give a bit of background on the use of radon cups in radon monitoring in the USA.

Radon cups employ solid track detectors to measure alpha-particle radioactivity from soil-gas radon in the vicinity of the cup. Because they are low in cost and easy to deploy, they have been widely used in radon monitoring

156

programs in California. Typically, they are sited about 1 m below the surface and are collected at weekly intervals. The track detectors are etched and counted under a microscope.

The major drawbacks of the radon cup method are the lack of sensitivity owing to the small and unconcentrated nature of the sample, and the non-real time data collection. At the Kresge site we typically find that a radon cup deployed for a two-week period will yield under 100 tracks, while a single cycle of the Caltech instrument at the same location yields close to 1000 counts (5 min air sample from borehole -- 20 min count). However, since these cups are in widespread use as in situ monitors we employ them at each of the instrument locations for comparison purposes.

At the Kresge site radon and thoron data are obtained from a 24.38 m deep borehole which is cased through the overburden. The lower 15.24 m of the borehole is in solid rock. Water fills the hole to within 4.55 m of the surface. Exhaust air from the positive displacement air pump in the radon-thoron monitor is bubbled through the water in the borehole in order to strip radon and thoron into the airspace above. The instrument vault housing of the monitor is mounted directly over the borehole and is sealed from the ambient air.

Initially, strong diurnal variations in the data from borehole operation were noted. These were found to correlate with the external ambient air temperature, with morning values of radon levels low and afternoon values high. This effect was determined to be a result of condensation in the instrument vault at low temperatures which removes radon daughters from the instrument vault air space. Insulation of the instrument vault and the installation of a small thermostatically controlled heater eliminated almost all of the diurnal variations in the data. Small remaining short term temperature-related variations in the data were found to be nearly a linear function of temperature, so that corrections are easily made.

Figure 1 suggests an annual cycle in the Kresge monitor data. To test this hypothesis, we have fitted the data with a curve of the form

$$R(t) = R_{ave} \left[1 + A \cos \left(\frac{2\pi}{52} t - \theta \right) \right] \quad .$$

Here t is time (in weeks) taking t = 0 to represent the week of maximum average ambient air temperature, and θ is a phase delay representing the amount of time

required for the radon levels to respond to the input temperature wave. Although only data extending over a period of two or more years can fully establish the existence of an annual cycle, the reasonably good fits to Fig. 1 strongly suggest that the long term variations observed in the data are a response to the annual thermal cycle. Good fits are obtained with A = -0.4 and θ = 20° indicating both strong and rapid coupling of the radon levels to changing thermoelastic strains in the rock in the vicinity of the borehole. In this respect, this particular site appears to be excellent for testing models of radon transport.

During the period of operation since location of the Kresge instrument over the 24.38 m borehole and thermal insulation of its vault, there has been only one felt earthquake within 25 km of the instrument. This was a 3.1-M event near downtown Los Angeles on December 22, 1977. A positive anomaly of approximately two weeks duration was noted prior to the event (Fig. 2). The anomaly associated with this event was a 40% increase in radon level lasting for about 9 days and terminating about 6 days before the event. The 40% increase is referred to the data level expected from the annual variation. As can be seen from Fig. 1, the anomaly is discernable in both the raw data and the data to which the short term temperature correction has been applied.

The second Caltech instrument recently was installed in a 27.43 m-long sealed, horizontal tunnel at Big Dalton Canyon Dam. This site is near the Sierra Madre fault line, and approximately 25-km east of the Kresge instrument. The tunnel is located quite close to the flood control dam, and should provide some very interesting comparisons with the Kresge instrument since at this location one can expect some strain from reservoir loading in addition to the thermoelastic strains. The amount of water impounded behind the flood control dam is accurately recorded. Reasonably accurate estimates of the mass loading will therefore be possible.

Depending upon the availability of project funds, we intend to extend the network of Caltech monitors (with accompanying radon cups and thermal sensors) along the foothills of the San Gabriel mountains at approximately 10-km intervals. This will allow intercomparison of data from a series of instruments on interconnected faults.

Recently we received USGS funding for this project and by fall will have another four units in the field.
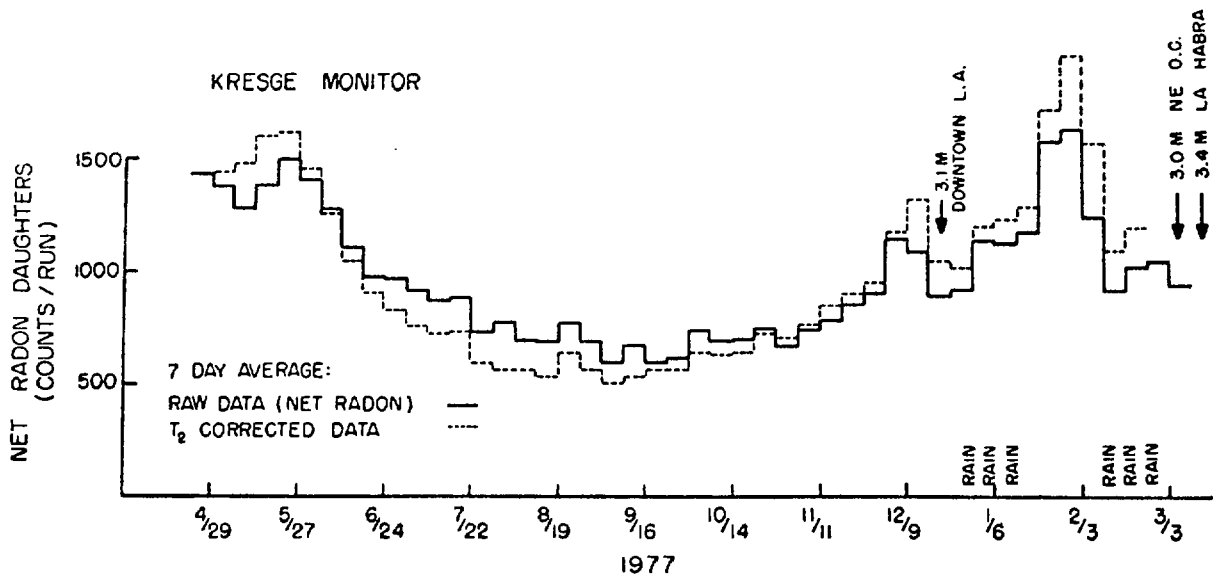
Fig. 1. Seven-day averages of raw data and temperature corrected data from the Caltech radon-thoron monitor at Kresge Laboratory, Pasadena.
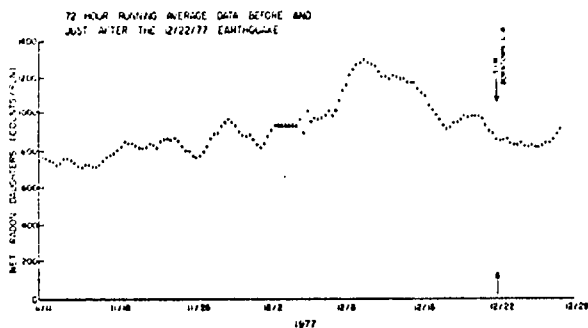

Fig. 2. Three-day running averages of the raw data from Kresge during the period before and just after the December 22, 1977 Los Angeles earthquake. This earthquake was the only earthquake felt within 25 km of Pasadena during the period of data accumulation. A 72-h running average is plotted for each 8-h cycle of the monitor. A change in radon level of ∿ 40% on a time scale much shorter than the seasonal variation is observable between 15 and 6 days before the earthquake.

159

REFERENCES

1. McNally, K., and H. Kanamori, paper G28, E⊕S, <u>58</u>, 1120 (1977).

2. Haicheng Earthquake Study Delegation, E⊕S, <u>58</u>, 236 (1977).

3. Ulomov, V. I., <u>Zemya i Vselennaya</u>, <u>3</u>, 23 (1968).

4. Kisslinger, C., Phys. Today, 36 (March 1974).

5. Anon., Request for Proposal RFP 287W - Attachment C, USGS, Menlo Park, CA (1976).

6. Press, F., E⊕S, 57, 435 (1976).

7. Craig, H., J. E. Lupton, Y. Chung, and R. M. Horowitz, "Investigation of Radon and Helium as Possible Fluid Phase Precursors to Earthquakes," Scripps Institute of Oceanography Rpt 75-15, UCSD, La Jolla, CA (1975).

8. Smith, A. R., H. R. Bowman, D. F. Mosier, F. Asaro, H. A. Wollenberg, and C. Y. King, "Investigations of Radon 222 in Subsurface Waters as an Earthquake Predictor," LBL Rpt 4445, Lawrence Berkeley Laboratory, Berkeley, CA (Nov. 1975); A. R. Smith, H. A. Wollenberg and D. F. Mosier, paper S69, E⊕S, <u>57</u>, 957 (1976 and paper S103, E⊕S, .<u>58</u> 1196 (1977); private communications (1977).

9. Talwani, P., L. Tathey, J. H. Chiang, and W. S. Moore, papers S22-24, E⊕S, <u>58</u>, 434 (1977).

10. Birchard, G. F., and W. F. Libby, paper S71, E⊕S, <u>57</u>, 957 (1976) and paper S102, E⊕S, <u>58</u>, 1195 (1977).

11. King, C. Y., paper S70, E⊕S, <u>57</u>, 957 (1976) and paper S25, E⊕S, <u>58</u>, 434 (1977); C. Y. King, "Radon Emanation on San Andreas Fault," USGS, Menlo Park, CA (1977), to be published; private communication concerning the placement of solid state detectors in radon cups (1977).

12. Shapiro, M. H., J. D. Melvin, T. A. Tombrello, and J. H. Whitcomb, paper S26, E⊕S, <u>58</u>, 434 (1977); J. D. Melvin, M. H. Shapiro, and N. A. Copping, "An Automated Radon-Thoron Monitor for Earthquake Prediction Research," Caltech, Pasadena, CA (1977), Nucl. Instr. and Methods, in press (included as Appendix A of this proposal).

13. Li, Liu Po, Wan Di Kun, and Wan Tsen Min, Acta Geophysica Sinica, <u>18</u>, 279 (1975).

14. Pierce, E. T., Geophys. Res. Lett., <u>3</u>, 185 (1976) and references therein.

15. Malcolm, H., <u>New York Times</u>, p. 1 (Late City Ed., June 2, 1977).

16. Scholz, C. H., L. R. Sykes, and Y. P. Aggarwal, Science, <u>181</u>, 803 (1973).

17. Noguchi, M., and H. Wakita, J. Geophys. Res., <u>82</u>, 1353 (1977).

18. C. Junge, <u>Air Chemistry and Radioactivity</u> (Academic Press, New York, 1963) Ch. 3.

IV. NUCLEAR TECHNIQUES IN PLANETARY SCIENCE

For those of us who are interested in stellar phenomena, the abundances of the chemical elements and their isotopes provide many clues about the environments in which they were created. Figure 1 shows what we think is an approximate picture of the relative universal abundances of the elements. These data come mainly from two sources: spectroscopic analyses of the atomic transition lines from stars and chemical analyses of samples from carbonaceous chondritic meteorites.[1] For the most part terrestrial samples have been so fractionated chemically by aeons of geological processing that they are of limited value in determining universal abundances. The carbonaceous chondrites are thought to be the first condensates from the evolving solar nebula and thus are expected to be an accurate representation of the abundances of the non-volatile elements at the time of solar system formation. It has been demonstrated for many elements that the correspondence is excellent between the elemental concentration in these meteorites and in the solar photosphere.

In this talk I shall consider three examples of how nuclear analysis techniques can be used in the determination of elemental abundances in meteorites and how the extension of these techniques to planetary samples can give us new perspectives about typical planetary processes.

You should notice in Fig. 1 that there are three elements that lie far below the curve established by the other elements, lithium, beryllium and boron. Because these elements have very large (p,α) cross sections, they are easily destroyed in stars. Thus, we find that they must have been created in non-stellar, astrophysical processes. We now think that ^{7}Li was produced in the Big Bang;[2] and the others (^{6}Li, ^{9}Be, ^{10,11}B) were made by proton and alpha particle spallation reactions from cosmic rays striking material in the interstellar medium.[3]

The abundances of the lithium and beryllium are reasonably well known, but boron analyses have continued to cause trouble. A few years ago we set out to correct this situation by developing a technique to measure ^{10}B and ^{11}B concentrations at levels down to $\sim$ 0.1 ppm.[4] Until recently I thought that everything was finally in good shape, but some preliminary data from Curtis and Gladney here at LASL is giving somewhat lower boron concentrations on one meteorite, which will probably send us all back to the laboratory for a new round of experiments.

The ^{11}B analyses serve as an excellent example of how bits of old-fashioned nuclear physics can be used in a completely new context. The ^{11}B(d,p)^{12}B reaction has a large cross section ($\sim \frac{1}{2}$b) and an easily distinguished final product (20 ms half life, 13 MeV end point energy for the β^-'s). Nevertheless, the fact that we must detect the boron in the presence of a million times more other stuff in the sample, keeps it from being a trivial exercise. Figure 2 indicates how simple the apparatus is -- a plastic scintillator and some SCA's. Figure 3 shows the bombardment and counting sequence, and an example of the raw and subtracted data. We have a signal to noise of only $\sim$ 1/20 at 1 ppm -- most of the background coming from the decay of the ^{16}N produced in the reaction ^{18}O(d,α)^{16}N. This reaction has a small cross section, but since the meteoritic material is $\sim$ 50% oxygen, the ^{16}N becomes a problem. Fortunately, the ^{16}N lifetime (7.2 s) is so different from that of ^{12}B, we can easily separate the two decay contributions.

Table I shows some of our results for six meteorites, which gives what we think is a good average value for the boron abundance in the solar system. But, as I indicated earlier, it's not clear that our work is finished on this problem.

Another element whose abundance was ill-determined was ^{19}F. Though fluorine is probably made in stars, its high (p,α) cross section causes its abundance to be particularly sensitive to the detailed bookkeeping on its production and destruction.

Again we have used a nuclear reaction that is well known to all of us with low-energy accelerators, ^{19}F(p,$\alpha\gamma$)^{16}O. At the narrow 872 keV resonance the reaction cross section is 540 mb, and the 6 and 7 MeV γ rays are easily observed with high efficiency.

The fact that the resonance is isolated and sharp, allows us information on the depth distribution as well. Figure 4 shows this schematically.[5] Obviously one would need to fold in the effects of the resonance width and the proton straggling in any real situation. (At the surface of the target the resolution is limited by the resonance width, which is equivalent to $\sim$ 500 Å.) Our first use of this technique was to look at the concentration

TABLE I

AVERAGE BORON CONCENTRATIONS IN CARBONACEOUS CHONDRITES

Type	Meteorite	No. Samples Analyzed	Average B ppm	Atomic B/Si (10^{-6})
C1	Ivuna	1	3.0	77
	Orgueil	1	1.6	40
C2	Murray	6	1.4	29
	Murchison	12	1.7	35
C3-4	Allende	9	1.8	23
	Lance	2	1.5	19

163

of ^{19}F in meteoritic samples. The depth sensitivity was used to check for the presence of contaminant fluorine on the sample surfaces. Our results are given in Table II. The half day's work given in this table is the only accurate determination of solar system fluorine which clearly shows the power (and selectivity) of a nuclear technique.[6]

The success of the meteorite work convinced us that we should try to apply the fluorine analysis to other planetary problems. The most obvious application involved a controversy about the moon's history; in addition to the obvious effects of meteorite impact, was there any clear-cut evidence of lunar vulcanism?

Lunar samples are special in many ways, but the lure that has drawn many of us into their analysis is that the record of over 3 billion years of solar and solar system history is held in them. With neither atmosphere nor magnetic field to deflect the solar wind or flare ions, we have the hope that with sufficient cleverness we can unravel that tangled recording. In the process of studying the solar wind implanted hydrogen (using $^1H(^{19}F,\alpha\gamma)^{16}O$, naturally), we

TABLE II

FLUORINE CONCENTRATION DATA FOR CARBONACEOUS CHONDRITE METEORITES[#]

	Solid Samples			Crushed Samples	
		F concentration			F concentration
Sample	ppmF	atoms F/10⁶ atoms Si	Sample	ppmF	atoms F/10⁶ atoms Si
Murchison[*]	80	910	Murchison 5[*]	75	853
Murchison 7b[*]	72	819	Murchison 6[*]	60	682
Murchison 7c[*]	73	830	Murchison 10[*]	66	751
Murchison 7d[*]	80	910	Murchison 11[*]	59	671
Murchison 7e[*]	53	603	Mighei[*]	66	751
Murchison 7f[*]	93	1058	Essebi[*]	80	910
Allendé Z1-14[†]	165	1562	Haripura[*]	59	671
Allendé Z1-15[†]	94	890	Ivuna[ε]	70	981
			Orgueil[ε]	74	1037
Murchison Ave.	75.2	855	Allendé[†]	59	559
Allende Ave.	129.5	1226			
			Murchison Ave.	65	739
			Type II Ave.	67	762
			Type I Ave.	72	1009
			All Crushed Ave.	67	787

[#]Since no samples exhibited surface peaks, concentrations quoted are taken from net average yields over the resonance. Typical analytic precision is ± 8%. Carbonaceous chondrite type is also indicated.

[ε]Carbonaceous chondrite Type I.

[*]Carbonaceous chondrite Type II.

[†]Carbonaceous chondrite Type III.

came up with what we thought was an unambiguous way to look for evidence of lunar vulcanism. ^{19}F is virtually non-existent in the solar wind, and the bulk concentration of ^{19}F in lunar rocks is quite low. We knew, however, that the halogens are frequently a component of terrestrial volcanic gases; thus, we would look for fluorine surface films on lunar samples.

The data in Fig. 5 was one of our first tries, an embarassment of riches.[7] There was an enormous amount of fluorine on the outside of several samples, but only a relatively small amount in the interior. One must, however, be suspicious in this business, so we finally got around to a control experiment. We prepared several quartz disks, keeping some at home and sending some to Houston to be treated as if they were lunar samples. Figure 6 shows what happened.[7] It's clear that the sample that went to Houston, and came back in a teflon bag had picked up some fluorine. This led us to a more detailed investigation and we discovered that virtually all the lunar samples came home from the moon in teflon bags.[8]

Now, the hard work started, we tried to get samples that were never exposed to fluorine by their handling. We first set out to get SESC samples, the contingency sample that was collected in a small stainless steel can just after the landing. Unfortunately, most of these were collected under the LM, where its exhaust had contaminated the surface. After almost a year of negotiation with NASA we got two small samples from the SESC from Apollo 15.[8] The dark points in Fig. 7 show data for the glass sides of the two small pieces of glass-welded breccia. The distribution of fluorine was uniform; no teflon, but no volcanoes. Not leaving well enough alone, we turned them over and got the open points, which created visions of new and even more subtle forms of fluorine contamination. Then, we took a look at these surfaces under a microscope, and saw collections of small green glass spheres. The spheres are ∿ 100 μm in diameter; it's an absolutely unique material; there is nothing like it on the earth. Figure 8 shows a picked sample, done with tweezers, a binocular microscope, and a strong-eyed graduate student. There is lots of fluorine in a thin layer on the surface. A fraction of brown glass from the same "soil" clod shows no effect and provides a control against contamination. (Other investigators have found that the surfaces are covered with other volatile materials: zinc, gallium, sulphur, chlorine, etc.) The orange soil from Apollo 17 is similar and has the same sort of surface film.[8]

Nothing like the green or orange glass occurs on the earth. We think that it's clear that they were made in a volcanic process ∿ 3 billion years ago. Figure 9 shows one guess concerning the mechanism, a lava fountain. The absence of water and an atmosphere makes lunar volcanoes quite different from those on the earth. It is very likely that these small glass balls represent the most unusual material that came back from the moon, and we expect to be busy trying to understand their origin for a long time.

In our concern with lunar volcanoes and the magmas that resulted from the large impact craters, we tried to identify the gases that produced all the vesiculation (bubbles) in lunar rocks. We became convinced that the major contribution came from carbon monoxide, which led us into the problem of understanding the lunar abundance of carbon.

The basic difficulty is that there isn't enough carbon on the moon; there are three sources (the solar wind, meteoritic impacts, and indigenous), each of which could easily have supplied more than is now there. We needed a way of separating these contributions, so we turned again to a depth-sensitive nuclear reaction, $^{12}C(d,p)^{13}C$.

Figure 10 shows the excitation curve for the reaction, and Fig. 11 gives a schematic description of the technique. We observe the proton spectrum; protons that originate near the surface have higher energies than those from inside due to the energy loss of the incident deuterons and the protons.

We immediately found that all the samples had carbon on them. (It wasn't obviously from our vacuum system. It runs at 10^{-10} torr and has no hydrocarbons.) To make a long story (2 years worth) much shorter, it turns out the carbon monoxide loves to sit on surfaces, and small amounts of carbon monoxide are present in even very clean ^2N (the way all these samples were handled) and in our super vacuum system.

How do you get the carbon monoxide off without disturbing the stuff that was there originally? Blind luck and black magic; we discovered that it could be removed by heavy ion (∿ 2 MeV) induced desorption. (We are still trying to understand how it works because it may be important in molecular formation processes on interstellar grains.) Figure 12 shows how it works in cleaning the carbon monoxide from a radiation damaged quartz sample, and the following figure shows how we can remove carbon monoxide from various lunar samples. After the carbon monoxide is removed, nothing else changes. (To check this we let the

carbon monoxide "grow" back and then do it again.)[9]

Lately we've been studying breccias,[10] soil particles welded together by glass from meteoritic impacts. Figure 13 shows a typical proton spectrum from such a sample and the contribution of other elements in the region of the carbon peak. Because the samples are quite rough at a microscopic level, the spectrum shape is somewhat different from that from a smooth target. Figure 14 shows a typical decomposition (using the standard line shapes from the previous slide) into "surface" and volume components.

We are just now beginning to sort out some of the systematics; Fig. 15 shows the surface concentration vs. volume concentration for a variety of samples. It seems that the surface exposure (probably implanted solar wind carbon) is pretty much the same, but the volume component is highly variable. What this may mean is that solar wind (and perhaps meteoritic carbon) are gradually converted into volume carbon as the soil "matures;" the approximately constant surface value representing an equilibrium that is quickly established ($\sim 10^4$ yrs).

We have decided that soils are also interesting and have bombarded one soil sample. Obviously, there are problems when you try to use a very fine powder as the target for a charged particle beam. Our first spectrum is shown in Fig. 16; it doesn't look much like that from a breccia. The curve shown is just the surface component form taken from a breccia. It doesn't fit very well and we have lots more work to do.
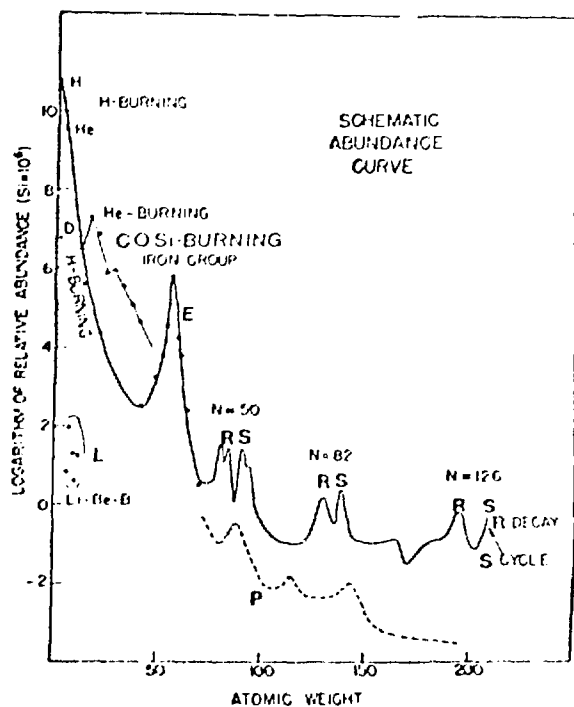
Fig. 1.   Nuclear abundances. The proc-
esses believed to be mainly
responsible for the synthesis
of nuclei are as follows: hy-
drogen burning, helium burning,
carbon burning, oxygen burning,
silicon burning, the equilib-
rium process (e), neutron cap-
ture on a rapid (r) or slow
(s) time scale, the p-process
for the low abundance proton-
rich heavy nuclides, and the ℓ-
process for the low-abundance
highly-reactive light elements
lithium, beryllium, and boron.
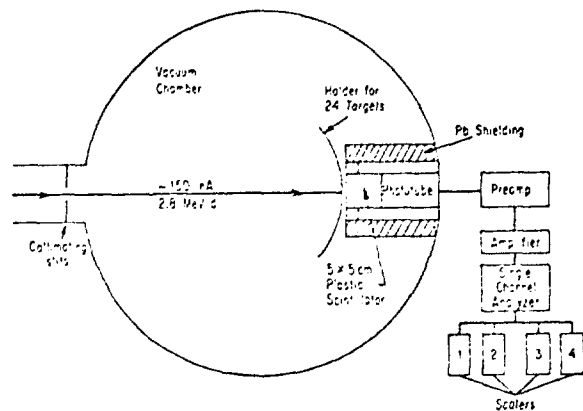
Fig. 2.   Schematic experimental arrange-
ment for ^{12}B activation mea-
surement. To maximize count-
ing efficiency the target hold-
er is mounted off-center and
the plastic scintillator is
mounted on a re-entrant, Pb-
shielded tube in the scattering
chamber. To minimize back-
ground only the higher energy
portion of the beta spectrum
is allowed to pass the single
channel analyzer. The beam is
pulsed and counts measured
sequentially in each of the
four scalers according to the
counting cycle shown in Fig. 3.

$$^{11}B(d,p)^{12}B \quad \text{Counting Cycle}$$

(a)

All scalers blocked

beam on target

sequence timer
signal for beam on — delay — | scaler 1 on | scaler 2 on | scaler 3 on | scaler 4 on

$Y_1 \quad Y_2 \quad Y_3 \quad Y_4$

t (msec)

(b)

$\ell n \, A$

(c)

$\ell n \, A_{corr}$

$t_{1/2} = 20 \, msec$

(t − 45), msec
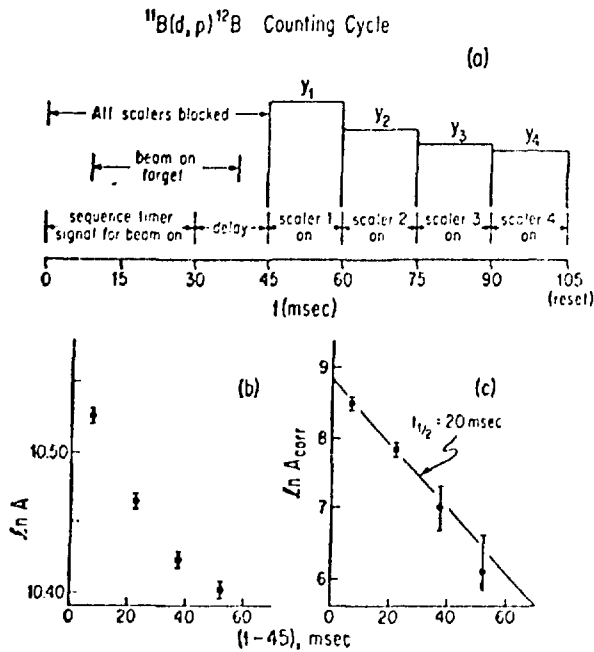
Fig. 3. (a) Counting cycle for ^{12}B pulsed beam activation measurement. The delays between 0-6 and 30-45 ms are to insure that the beam is totally deflected. The Y values indicate the number of counts in the four successive counting intervals after beam deflection. The decrease from Y_1 to Y_4 schematically indicates the ^{12}B decay. (b) Example of an uncorrected decay curve for a meteorite (Ivuna) sample. Decay time is measured after the start of interval Y_1. (c) Background corrected decay curve of data from Fig. 3b. The corrected activity follows the 20 ms decay of ^{12}B.

p beam

E_0

Meteorite Sample

$^{19}F(p,\alpha\gamma)^{16}O$

x
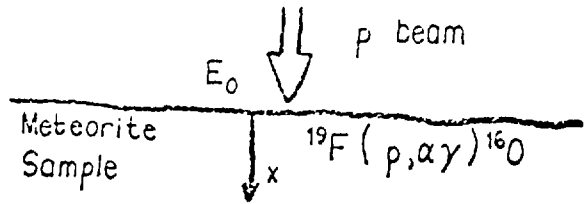
$$E(x) = E_0 - x(dE/dx)$$

$$\text{Counting rate} \propto H(x_R)$$

where x_R = depth where $E(x) = E_R$

$$\Delta x = \Delta E_R/(dE/dx) = 500 \, \text{Å}$$

Fig. 4. Schematic diagram showing the relation between the proton beam energy and the ^{19}F concentration versus depth.
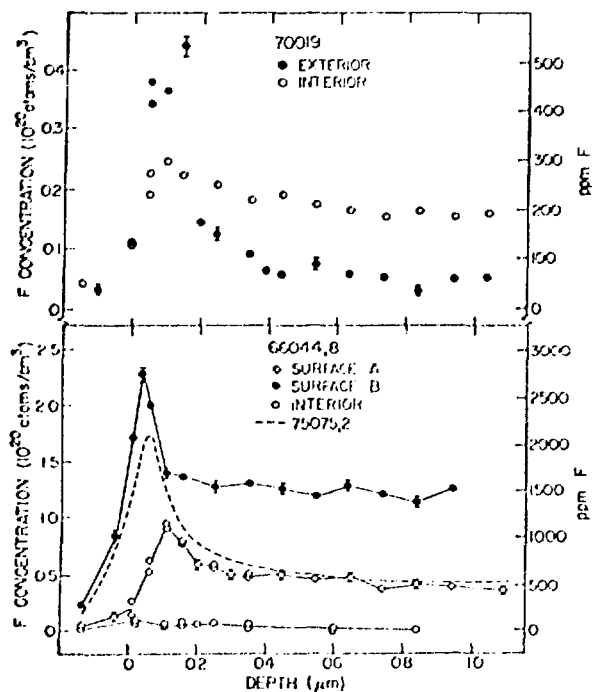
Fig. 5. Top: Fluorine concentration
versus depth for sample 70019,
17, a sealed rock box sample.
Exterior points are from meas-
urements of an interior soil
breccia surface, freshly ex-
posed in our laboratory.
Bottom: Fluorine concentration
versus depth for anorthosite
coarse fine 66044,8, and pat-
inated breccia 75075,2, both
sealed rock box samples.
Shown are data from two sur-
faces of 66044,8 and from an
interior surface freshly ex-
posed in our laboratory. The
smooth dashed curve is drawn
through the data points of
75075,2 for clarity in the
figure.
    The depth scale has not
been corrected for electro-
static charging of the samples
but the profiles shown are
consistent with surface F
peaks on all samples.
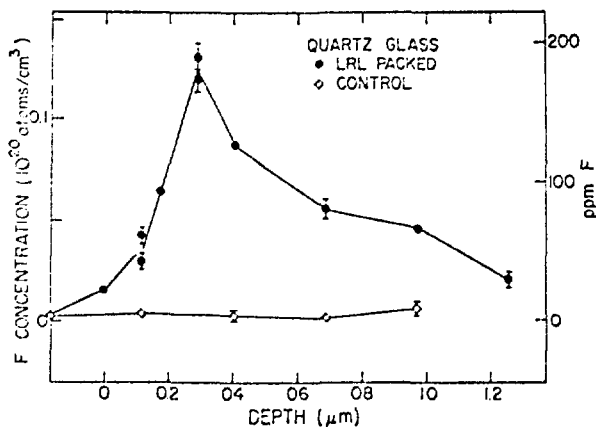
Fig. 6. Fluorine concentration versus
depth for quartz glass discs.
Solid points correspond to a
disc packaged in Teflon by the
Lunar Curatorial Facility;
open points are data from a
disc serving as a control.
The depth of the peak location
of F concentration is probably
caused by electrostatic charg-
ing of the sample during pro-
ton beam bombardment.
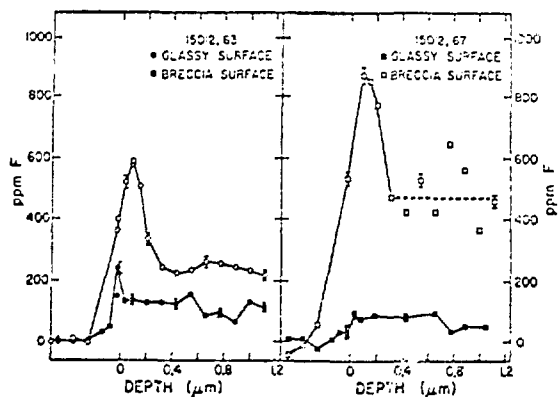
Fig. 7. Depth profiles of fluorine con-
centration for two glass-
coated soil breccia chips from
sample 15012, an Apollo 15
Sealed Environment Surface
container (SESC) sample. The
brown "glassy" surfaces (indi-
cated by solid points) show a
uniform distribution of fluo-
rine consistent with bulk val-
ues of lunar fluorine concen-
trations. The significant sur-
face peaks and distribution of
fluorine with depth for the
soil "breccia" surfaces are
due to the presence of surface
coatings on green glass spheres
which are present in the brec-
cia surface. The dashed line
for the 15012,67 breccia sur-
face profile is an average of
interior data point values.
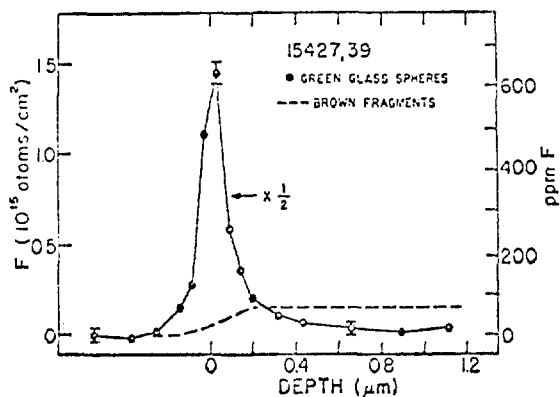
Fig. 8a. Fluorine depth profiles for
samples from 15427,39. The
circles are plotted on half
scale so that the interior
fluorine in the "brown frag-
ments" (about 60 ppm) is more
easily seen.
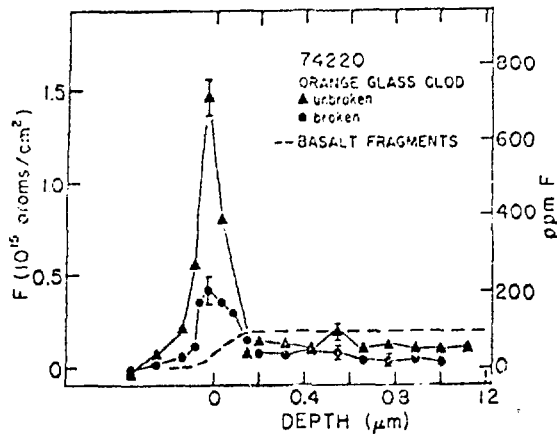
Fig. 8b. Fluorine depth profiles for samples from 74220. The lines shown merely connect the points; for clarity the data points corresponding to the dashed line (basalt fragments) have not been shown. The surface- and volume-correlated concentrations of f fluroine are clearly resolved. The lest-hand scale (atoms/cm^2) was obtained by integration over a depth range corresponding to the width of the surface peak (see text). The absence of a surface peak for the basalt fragments insures the absence of Teflon contamination in the 74220 samples. Interior F in basalt fragments is about 100 ppm.
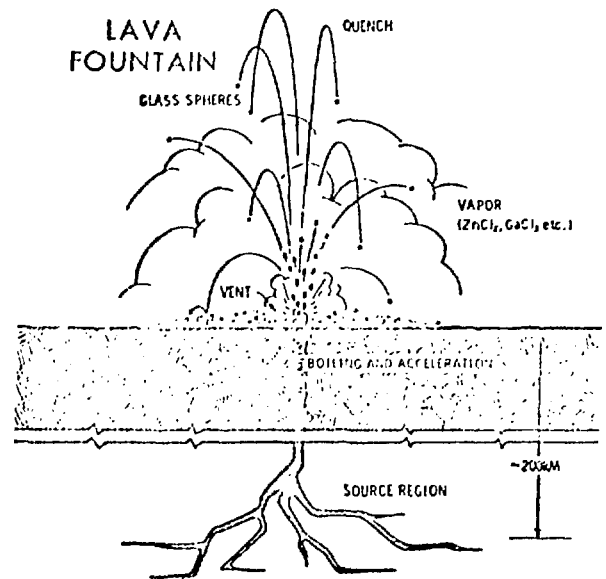
Fig. 9. One proposed volcanic process for producing lunar green and orange glasses, a lava fountain.
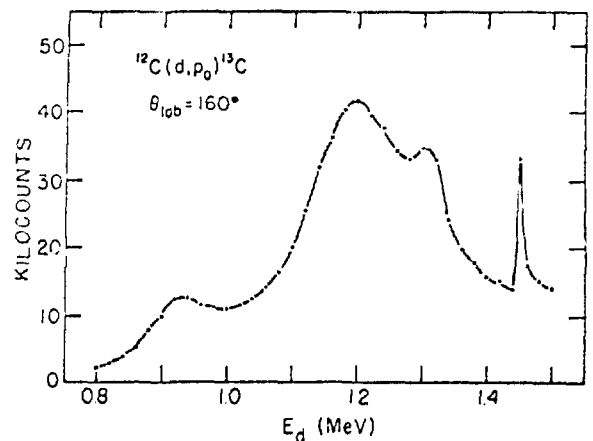
Fig. 10. Excitation function for the reaction [12]C(d,p$_0$)[13]C at θ_{lab}= 160°. Data points are taken from integrals of thin carbon target (11.2 µg/cm^2) yields for 20 microcoulombs integrated deuteron beam.

$^{12}C(d,p_0)$

to detector
($\theta_{lab}=160°$)

d beam

$E_{p_{max}}$

$E = E_{p_{max}} + 0.6(E_d - E_{d_0}) + \Delta x \sec 20°(dE/dx)_p$

E_{d_0}

Δx

$E_d = E_{d_0} + \Delta x(dE/dx)_d$
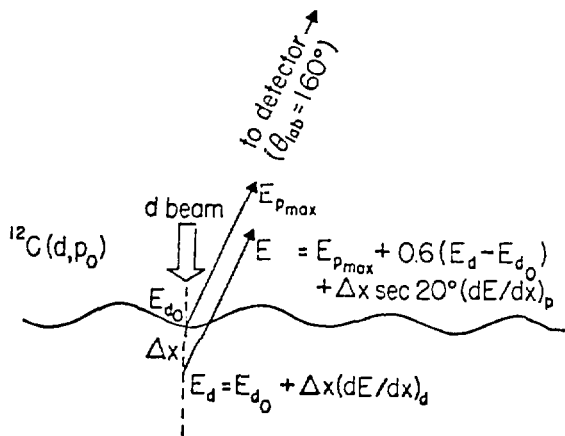
Fig. 11. Schematic drawing of energy dependence of detected protons at $\theta_{lab}=160°$ for the reaction $^{12}C(d,p_0)^{13}C$. Proton energy is shown to depend on deuteron energy loss, proton energy loss, and kinematic factors.
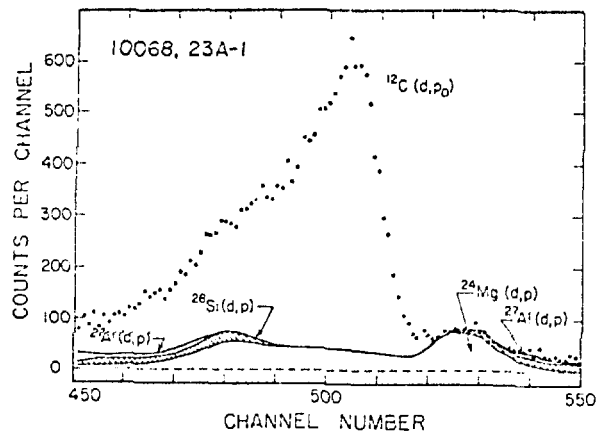
Fig. 13. The raw proton spectrum obtained for sample 10068. The smooth curves shown are the proton spectra obtained for pure targets of ^{24}Mg, ^{27}Al, and ^{28}Si that have been normalized to features characteristic of these nuclides in the spectrum for 10068. The remaining counts are from the ^{12}C in the sample.
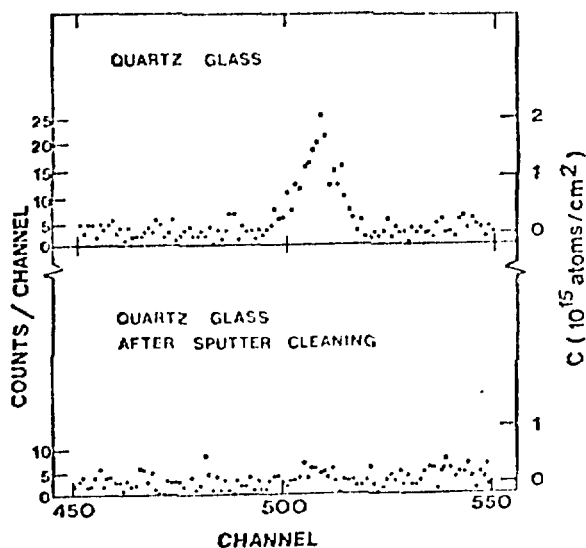
Fig. 12. Upper: Proton pulse height spectrum for quartz glass showing a contamination carbon surface peak corresponding to CO or CO_2. Lower: Same sample after sputter-cleaning with $\sim 10^{16}/cm^2$ of 2 MeV F ions.

173
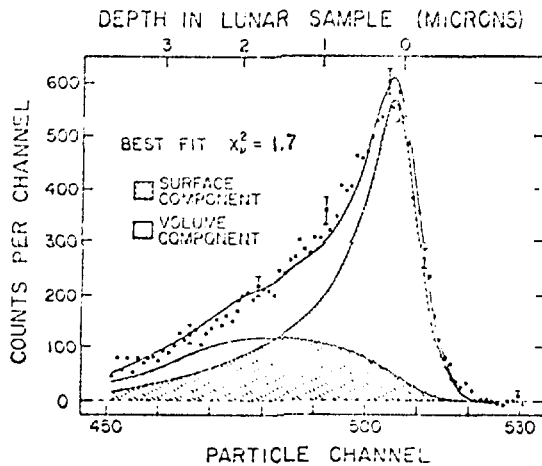
Fig. 14. The points shown correspond to the background-corrected (Fig. 13) proton spectrum from carbon for sample 10068, 23. The two cross-hatched regions show how this spectrum has been decomposed into surface and uniform volume components, each of which has the distorted shape that is a consequence of surface roughness. The solid curve through the data is the sum of the two contributions and has $\chi^2 = 1.7$.
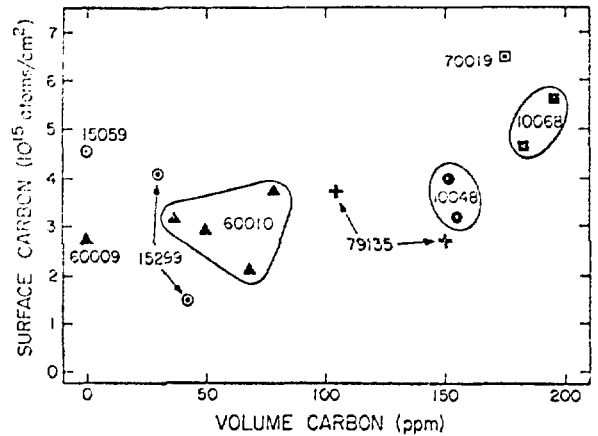
Fig. 15. The measured surface and volume concentrations for carbon for each sample are compared. It is clear that there is no strong correlation between surface concentration and volume concentration for these samples.
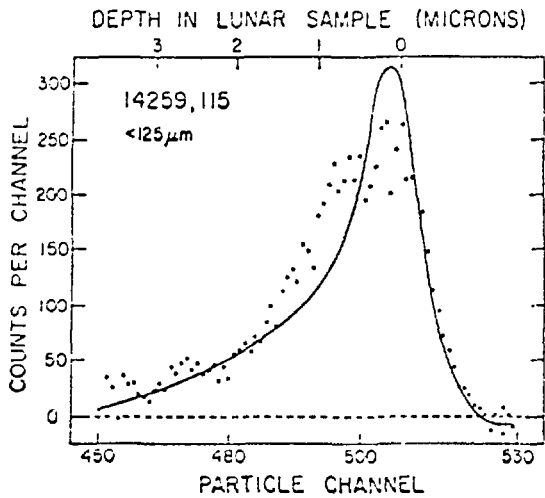
Fig. 16. The proton spectrum from carbon is the soil sample, 14259,115. The solid curve is the best fit possible in terms of the surface plus uniform volume components described in the text and shown in detail in Fig. 5. The best fit corresponds to a surface concentration of 6×10^5 C atoms/cm^2 and a volume concentration less than 20 ppm. The relatively poor fit indicates that the actual distribution of carbon in the soil grains is more complicated than provided for by the model.

REFERENCES

1. A. G. W. Cameron, in Origin and Distribution of the Elements, L. H. Ahrens, ed., Pergamon Press, London and New York (1968).

2. R. V. Wagoner, W. A. Fowler, and F. Hoyle, Astrophys. J. 148, 3 (1967).

3. W. A. Fowler, G. R. Burbidge, and E. M. Burbidge, Astrophys. J. Suppl., No. 17, 2, 167 (1955).

4. M. R. Weller, M. Furst, T. A. Tombrello and D. S. Burnett, Astrophys. J. 214, L39 (1977).

5. D. A. Leich and T. A. Tombrello, Nucl. Instr. and Meth. 108, 67 (1973).

6. R. H. Goldberg, D. S. Burnett, T. A. Tombrello and M. Furst, Meteoritics 9, 347 (1974).

7. D. A. Leich, R. H. Goldberg, D. S. Burnett, and T. A. Tombrello, Proc. of the 5th Lunar Science Conf., Pergamon Press, 1869 (1974).

8. R. H. Goldberg, D. S. Burnett and T. A. Tombrello, Proc. of the 6th Lunar Science Conf., Pergamon Press, 2189 (1975).

9. C. Filleux, T. A. Tombrello and D. S. Burnett, Proc. of the 8th Lunar Science Conf., Pergamon Press, 3755 (1977).

10. C. Filleux, R. Spear, T. A. Tombrello and D. S. Burnett, Proc. of the 9th Lunar Science Conf., Pergamon Press, in press (1978).

V. NUCLEAR TECHNIQUES IN SPUTTERING

When an energetic particle enters a material, some of its energy is lost in collisions with nuclei. Usually, these nuclear recoils have energies that are much lower than that of the primary particle but are much higher than the binding energy in the material (Fig. 1). Because the recoils are comparable in mass to the other atoms of the material, they are very efficient in transferring their energy to other atoms and generate a cascade of recoils in the material. As you can see, this process lies somewhere between the simple two body interaction of the primary with a single nucleus and the level of thermal motion when equilibrium is reached.[1] There are similar processes in several parts of physics; the most familiar to you would probably be the pre-compound nucleus reactions that occur shortly after a high energy proton or pion comes into the nucleus.

Why are people interested in sputtering? The main reason has to do with the use of sputtering in the preparation of thin films, but in the past few years there has been considerable interest from the people working on magnetic confinement fusion reactors. Neutral atoms and neutrons escape the plasma and strike the walls of the confinement vessel, causing sputtering of the walls. This is important for two reasons: the rapid erosion of the thin wall (thin for reasons of thermal cooling and reduced activation) and the build up of higher Z atoms from the wall in the plasma. Since bremsstrahlung losses go as Z^2, these atoms cause large losses in reactor efficiency.

My personal interest arose because of the sputtering of the lunar surface by the solar wind (3×10^8 protons/cm^2/s, 10^7 alpha particles/cm^2/s, . . .). This long-term bombardment of the moon by energetic (1 keV/amu) ions has produced some very strange surface properties that we would like to understand in detail.[2] We have also discovered that solar wind sputtering of the Martian atmosphere has been one of the major loss and fractionation mechanisms for atoms in the atmosphere.[3]

From what I said at first, it's easy to see that the sputtering yield (defined as the number of atoms leaving the surface of the material per incident particle) is going to be approximately proportional to the nuclear component of the stopping power:

$$S \propto \left(\frac{dE}{dx} \right)_{nuc.} \quad .$$

Thus, we would expect that S would tend to be higher at low incident energies and for heavier projectiles. For example, a 10 keV argon beam on a copper target has $S \sim 5$, whereas a 14 MeV neutron on copper has $S \sim 10^{-4}$.

When we got into this business, most people were interested in heavy ion sputtering. The values of S were so high you could measure S by weighing the collected material. There had been a bit of work using neutron activation of sputtered gold, but there was no real interest in achieving very high sensitivity. One of our first experiments was the sputtering of niobium by 12 MeV protons -- a simulation for high energy neutron sputtering, where the few experiments done (with neutrons and protons) tended to disagree.[4]

Figure 2a shows the setup. The niobium foils were activated separately using $^{93}Nb(\alpha,n)^{96}Tc$ ($t_{\frac{1}{2}} = 4.3$ d) with a 17 MeV α beam from our tandem accelerator. The collected material was deposited on the carbon and aluminum foils, then the activity of the niobium and collector foils was measured with a Ge(Li) detector. Figure 2b shows the activity on the niobium target and a carbon collector. The peaks at 778, 812, and 850 keV are the principal peaks from the ^{96}Tc decay. (The ^{60}Co and ^{206}Bi peaks come from activities from (p,n) reactions on ^{56}Fe and ^{206}Pb impurities in the collector foils. Observation of collector foils that were not adjacent to niobium targets showed that the ^{96}Tc had not been produced by $^{96}Mo(p,n)^{96}Tc$ on impurities. We could clearly see the difference between backward sputtered atoms ($S_B = 1.6 \pm 0.1 \times 10^{-4}$) and forward sputtered atoms ($S_F = 4.7 \pm 0.3 \times 10^{-4}$).

Because of our interest in astrophysical and solar wind sputtering processes, we were especially interested in low-energy, light-ion sputtering. Figure 3 shows the apparatus; the key part is the ultra high vacuum system.

Figure 4 shows an angular distribution of material sputtered from a vanadium target by a 90 keV $^{40}Ar^+$ beam. In this case the activation was by $^{51}V(p,n)$-^{51}Cr; the collector foil was segmented and each piece counted with a Ge(Li) detector. To show that we have plenty of sensitivity, Fig. 5 shows the angular distribution for the alpha particle sputtering (90 keV) of a molybdenum target where the sputtering yield is smaller by a factor of 300 than in the case of $^{40}A^+$ on vanadium.[5]

Figure 6 was our first attempt to observe isotopic effects in sputtering; we had produced a range of technetium isotopes in a molybdenum target.[5] As you can see, there was no large effect. (Recently, we have observed isotopic effects

for the sputtering of calcium isotopes; but here we have used a high precision mass spectrometer.)[6]

To show that there are some broad-range techniques available, Fig. 7 shows the spectrum of ^{16}O ions backscattered from an aluminum collector, onto which we had sputtered vanadium and molybdenum.[5] Because the energy of the scattered ions at 180° goes as

$$E_{180^{\circ}} = E_{beam}\left(\frac{M_T - M_{beam}}{M_T + M_{beam}}\right)^2 \quad ,$$

it is clear that using heavy ions greatly improves the mass resolution for higher values of M_T. We have been using backscattering to study the sputtering of amorphous (splat cooled) alloys, where we are especially interested in changes of composition that might affect their superconducting properties.

Though the activation techniques have allowed us an improvement in sensitivity of $\sim 10^3$ over most conventional techniques, we had a few ideas to test where we needed much greater sensitivity. An idea that came to mind was to use ^{235}U as a tracer. We would sputter material that contained ^{235}U; the collector, which was made of mica, could then be put in a nuclear reactor. The high fission cross section of the ^{235}U by thermal neutrons allowed great sensitivity because the tracks of the fission fragments in the mica could be detected with 100% efficiency and very low background.[7] Figure 8 shows tracks in the mica that are exposed by etching the mica in 48% HF. (The mica is viewed under an ordinary optical microscope with a moveable calibrated stage.)

We used this technique to look at the sputtering of uranium metal and compounds by various light ions.[8] However, we got a surprise, because occasionally we saw a small star-shaped pattern of tracks. Since we were using a neutron fluence that corresponded to an efficiency for fissioning ^{235}U of 10^{-6}, this star corresponded to a "chunk" of ^{285}U with $\sim 10^7$ atoms. (Obviously, we checked very carefully to make sure that the collectors had not been contaminated with small amounts of uranium dust.) Some of the "chunks" emitted were quite large, as shown in Fig. 9. (This beauty has $> 10^8$ ^{235}U atoms.)

A few people had thought that they had seen chunks of niobium sputtered by 14 MeV neutrons, but it was a subject of heated argument. Our results showed that chunks were emitted even when uranium was sputtered by 13 keV protons. Our technique even allowed us to measure the distribution of chunk masses.[8]

We still don't understand this process; obviously a single incident particle cannot cause the emission of a chunk, because neither energy nor momentum could be conserved by many orders of magnitude. Our data has, however, provided a clue; the chunk emission yield turns out to be roughly proportional to the atomic sputtering yield. By using beams of ^{40}Ar, ^{4}He and protons we could vary S_{atomic} by over 10^4, and S_{chunk} tracked S_{atomic} over this range. Thus, we see that the chunk emission is somehow related to the "damage" per unit volume produced by the incident beam. There must, however, be some additional collective mechanism involved, but we haven't found it yet. (It's a most spectacular process -- as if you dropped a grain of sand onto a large boulder and the boulder shot into the sky.)

We have been able to use the sensitivity of the ^{235}U detection to learn a bit more about the sputtering process. One other variable that one should measure is the energy spectrum of the sputtered atoms.[9] Figure 10 shows the system we've used. The beam is chopped by parallel electrostatic deflectors so that the beam pulse passes through the slots in a wheel spinning at 30 000 rpm. The sputtered atoms then come back through the cold trap which isolates the motor chamber and the uhv target chamber and are deposited around the rim of the wheel.

For ^{235}U we then segment the wheel, put the pieces between mica sheets, and expose it to thermal neutrons in a reactor. The resulting time-of-arrival spectrum is shown in Fig. 11 for the ^{40}Ar^{+} sputtering of a ^{235}U target. Figure 12 shows how the time-of-arrival spectrum becomes an energy spectrum; in this case for the sputtering of a ^{235}U metal target. The dashed line is a very simple theoretical model; the solid line shows a slight modification of the theory.

We've been curious about how chemical effects can modify the sputtering process; Fig. 13 compares the spectra from uranium metal and UO_2. The spectrum from UO_2 peaks at a lower energy and the overall distribution is somewhat broader.

We have just received some new motors that run at 120 000 rpm. This will allow us to shorten the flight path for heavier atoms (and we gain solid angle as the square of the flight path) or to run much lighter atoms at comparable resolution. It will not be trivial to use the full capability of these motors, however, since if we used the same 0.10 m wheels as now, there are no materials that are strong enough to hold together at that rim speed. (The present rim speed is 579 km/h; the new motors would have 2317 km/h.)

180

Before I close, I'll tell you about one experiment that uses some of the sensitivity of the ^{235}U technique. To believe the results of the previous experiment we need to know that the ^{235}U atoms actually stick to the collector. We've done this by means of a double scattering technique (Fig. 14).

In this way we found that 98% of the uranium atoms stick to the second target and have measured the angular distributions of the 2% that rebound. Figures 15a and b show how the angular distribution of the rebounding atoms changes with the presence of adsorbed gas on the surface of the second target; the more adsorbed material, the flatter the distribution.

We've begun an even harder version in which we are measuring the percent that stick as a function of their energy.

Obviously, we have an astrophysical axe to grind -- we want to find out whether variations in the sticking properties of atoms that strike interstellar grains could be responsible for the depletion of certain elements in the interstellar medium.
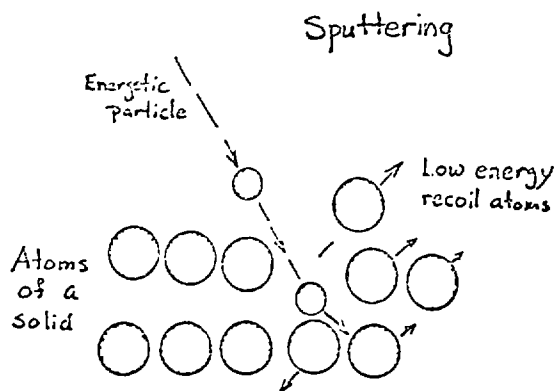
Fig. 1. A schematic diagram of the sputtering cascade.

COMPONENT		MATERIAL	THICKNESS		HOLE DIAM
T'	Aperture	Tantalum	0.5	mm	3 mm
T	Spacer	Tantalum	0.25	mm	13 mm
C	Collector	C foil on	23	$\mu g/cm^2$	
		Al frame	0.5	mm	8 mm
N	Target	Niobium	2.5	μm	—
A'	Shield	Aluminum	6	μm	—
A	Collector	Aluminum	25	μm	—
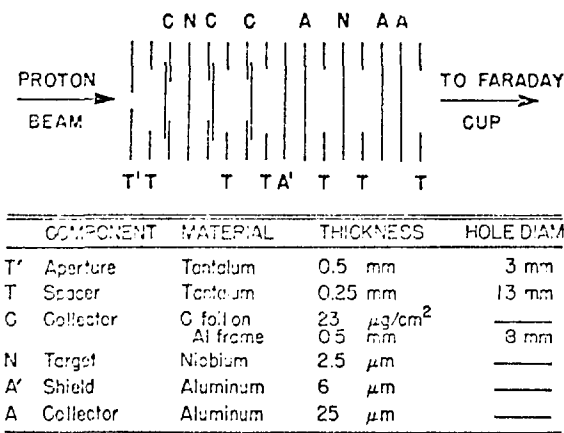
Fig. 2a. Schematic diagram of target arrangement used for the sputtering. The entire stack was clamped together, with a total thickness of about 4mm.
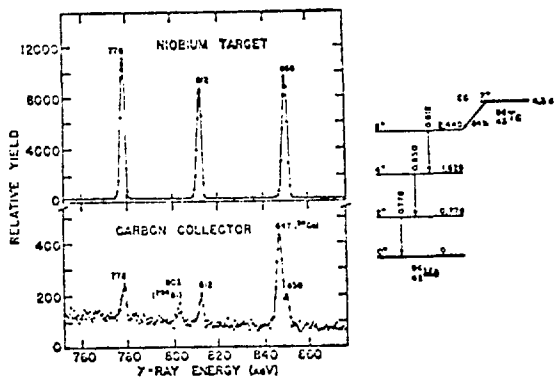
Fig. 2b. Portions of γ-ray energy spectra obtained from a section of activated Nb foil (top) and from the downstream carbon collector foil (bottom).
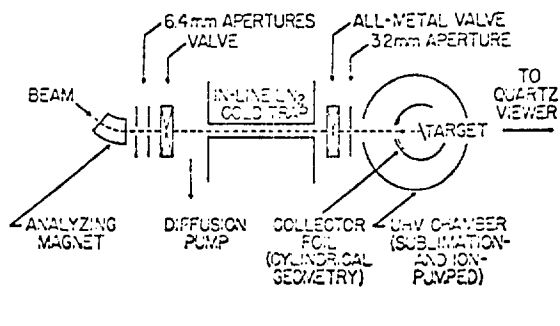
Fig. 3. Schematic diagram of the sputtering apparatus.
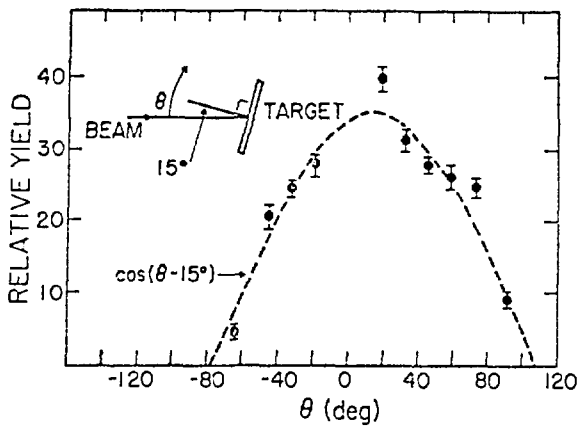
Fig. 4. Angular distribution of material sputtered from a V target by 90-keV $^{40}Ar^+$ ions. The error bars reflect statistical uncertainties only. θ (see inset) is the emission angle of sputtered material from the target relative to the incident beam direction; the target normal was oriented at θ=15°. The solid curve is a cosine function fitted to the data by eye and centered at the target normal.
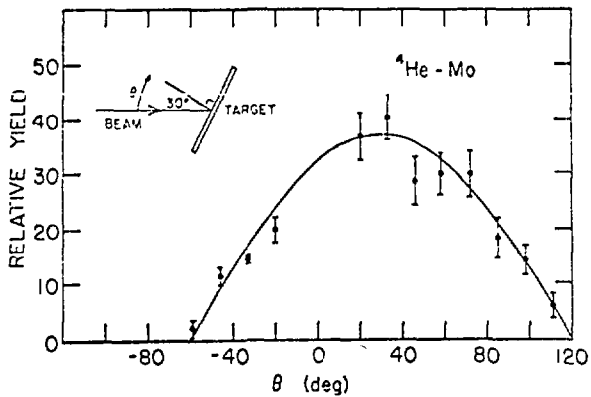
Fig. 5. Activation measurements of the angular distribution of material sputtered from a Mo target by 90-keV $^4He^+$ ions. The target normal was oriented at θ=30°.
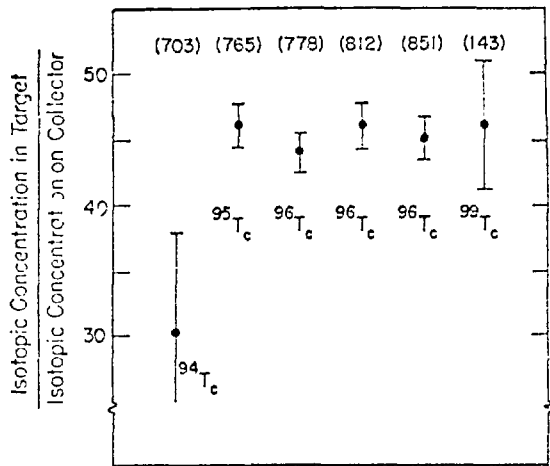
Fig. 6. The ratios of sputtered activity to target activity for several prominent γ rays, from activation of several Mo isotopes. The error bars reflect statistical uncertainties. The γ-ray energies (in keV) are noted above the points.
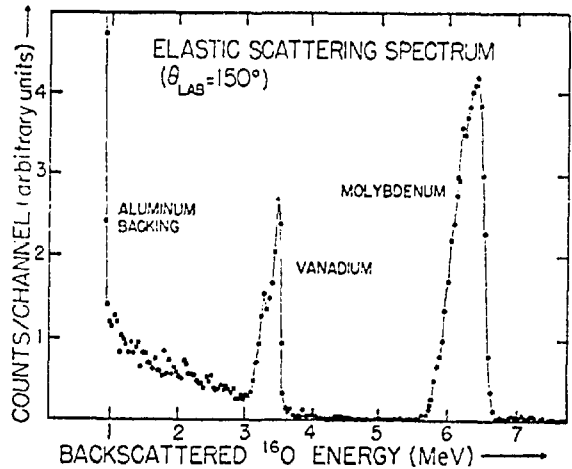
Fig. 7. Energy spectrum of ^{16}O ions elastically backscattered (θ$_{lab}$ = 150°) from a collector foil following 90-keV $^{40}Ar^+$ sputtering of Mo and V targets.

Fig. 8. Fission-fragment tracks in mica after 15-min etch in 48% HF. The photo was made in transmitted light at a magnification of about 450x. The fission star is fairly typical of the many observed in this experiment but is somewhat smaller than average.
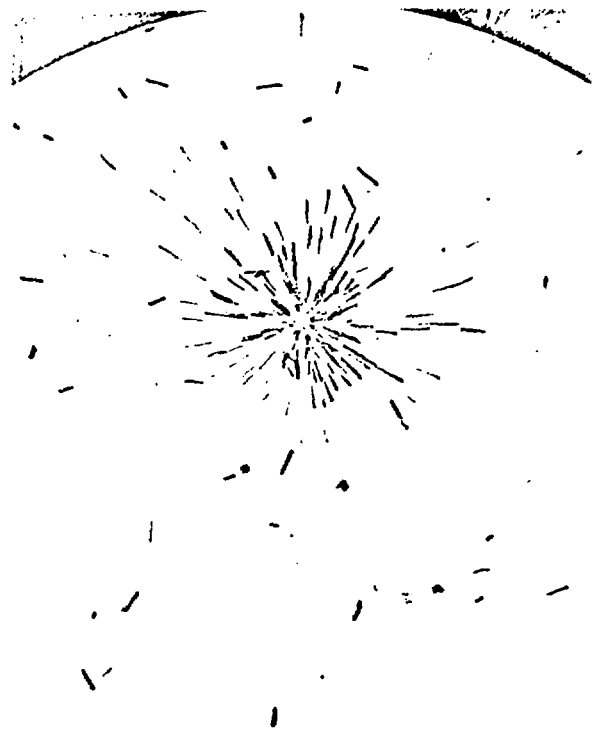

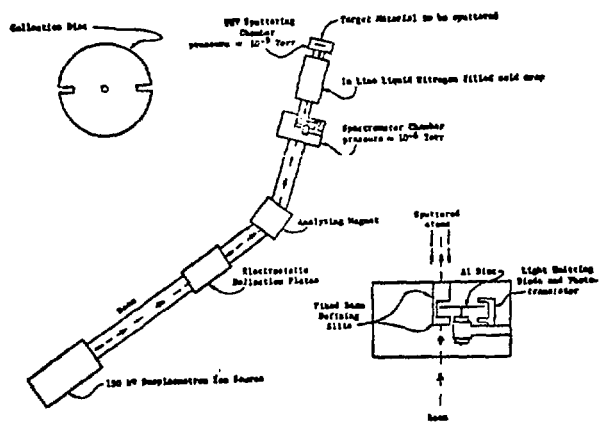Fig. 9. A larger-than-average fission star seen at 450x.

Fig. 10. Schematic diagram of the apparatus described in the text. A collector wheel (upper left) is also shown. The wheel's diameter is 10.16 cm, and the slits in the rim are 0.45 x 1.11 cm.

184
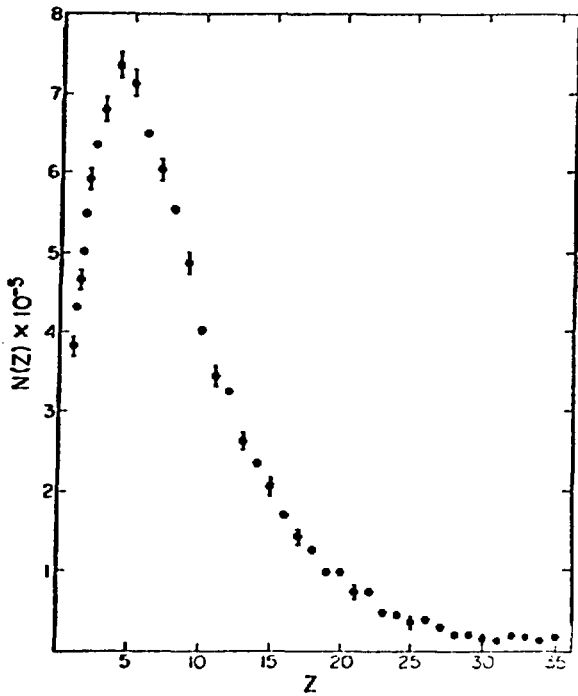
Fig. 11.   The average number of tracks
per area cm^2. N(z)=σφp(z), is
plotted as a function of posi-
tion on the collector, z (mea-
sured in units of the slit
width d=0.447 cm). The rep-
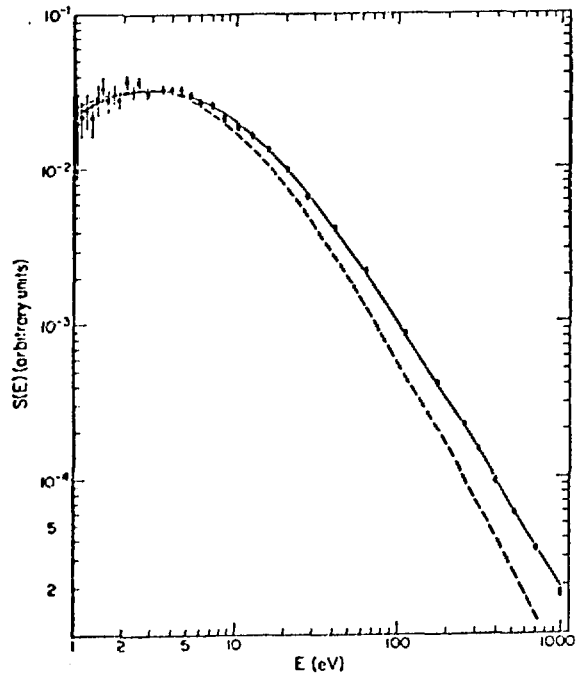resentative error bars shown
are statistical.

Fig. 12.   The energy spectrum, S(E) in
arbitrary units of sputtered
^{235}U inferred from the data
of Fig. 1. Error bars are
statistical. The smooth curve
is an empirical fit to the
data. The dashed curve is
the function 6.5 E/(E+5.4)
(Ref. 6). Note that the ver-
tical scale is arbitrary, and
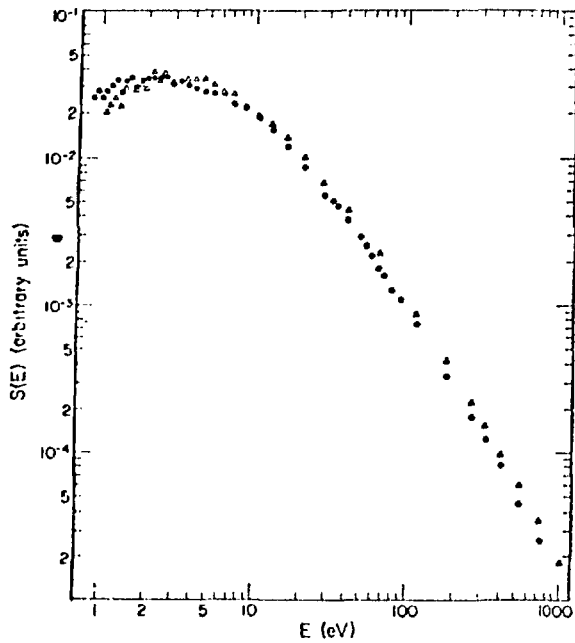the curves have been normal-
ized to agree near the peak.

Fig. 13. The energy spectrum of ^{235}U atoms sputtered from targets of uranium metal (triangles) and UO_2 (dots) by 80 keV $^{40}Ar^+$ ions. The U metal data are well described by $AE/(E+B)^{2.77}$ where $A=3.83$ (normalization constant) and $B=5.4$ eV (the sublimation energy for uranium.
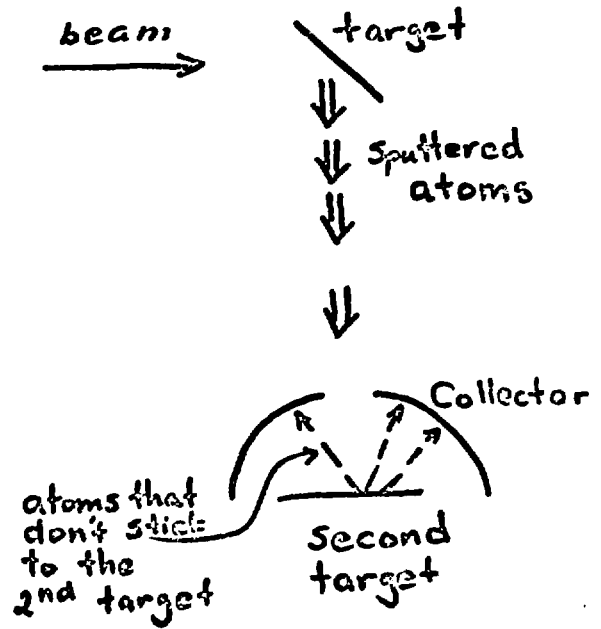
Fig. 14. The experimental arrangement for the sticking factor measurements.

Fig. 15. The angular distributions of sputtered ^{235}U atoms rebounding from Al films at: a) 125°C, b) 23°C.
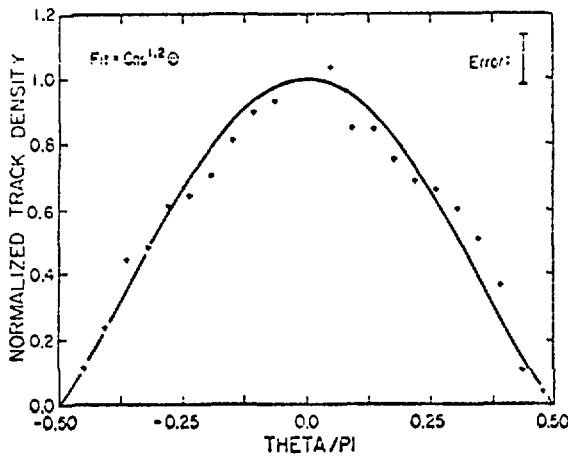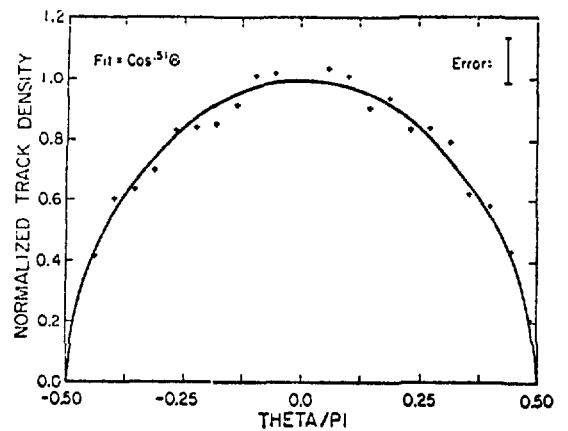

Fig. 15a. Angular distribution $^{235}U \rightarrow Al$ film at 125°C.

Fig. 15b. Angular distribution $^{235}U \rightarrow Al$ film at 23°C.

186

REFERENCES

1. P. Sigmund, Phys. Rev. 184, 383 (1969).

2. Z. E. Switkowski, P. K. Haff, T. A. Tombrello, and D. S. Burnett, J. Geophys. Res. 82, 3797 (1977).

3. P. K. Haff, Z. E. Switkowski, and T. A. Tombrello, Nature 272, 803 (1978).

4. R. W. Ollerhead, F. M. Mann, D. W. Kneff, Z. E. Switkowski, and T. A. Tombrello, Phys. Rev. Lett. 36, 439 (1976).

5. Z. E. Switkowski, F. M. Mann, D. W. Kneff, R. W. Ollerhead, and T. A. Tombrello, Radiation Effects 29, 65 (1976).

6. W. A. Russell, D. A. Papanastassion, T. A. Tombrello, and S. Epstein, Proc. 8th Lunar Science Conf. Pergamon Press, 3791 (1977).

7. R. Gregg, Z. E. Switkowski, and T. A. Tombrello, Nucl. Instr. & Meth. 144, 613 (1977).

8. R. Gregg and T. A. Tombrello, Radiation Effects 35, 243 (1978).

9. R. A. Weller and T. A. Tombrello, Radiation Effects 37, 83 (1978).

HARTREE FOCK CALCULATIONS OF NUCLEAR STRUCTURE--AN INTRODUCTION

by

D.W.L. Sprung
McMaster University, Hamilton, Ontario, Canada

INTRODUCTION

I was asked to give a set of lectures of pedagogic nature describing Hartree Fock calculations of nuclear structure. The audience I had in mind consists of graduate students who have completed courses in quantum mechanics and nuclear physics. I have tried to concentrate on basics, and perhaps have put too much emphasis on how some expressions are derived, rather than on how they are used. Some of the results are presented but very little of the sweat that went into obtaining them. By way of personal bias I have discussed work done at McMaster and Orsay omitting reference to equivalent (or better) work done elsewhere. But this is meant only to be an introduction, not a complete survey which is nowadays impossible. For those who wish to read more I can recommend the articles by Friar and Negele[1] and by Quentin and Flocard.[2] If these lectures serve as a suitable introduction to these reviews my aim would be fulfilled.

I. Basic Premises

In nuclear physics, as a working hypothesis, we generally assume that a reasonably accurate description of the nuclear wave function can be obtained in terms of only the nucleonic degrees of freedom: that is, the role of pions and other virtual bosons is to generate a nuclear force which can be represented by a potential. After that, it was hoped, we can restrict our attention to the nucleons alone. Of course, there is now considerable evidence that this view is incorrect. Even in such a simple process as photo disintegration of the deuteron: $\gamma + d \rightarrow p + n$, or its inverse: radiative capture, $n(p,d)\gamma$ there are believed to be significant "exchange current" contributions to the observed cross sections. Nevertheless, a nuclear wave function which ignores the existence of pions may still be a useful quantity. Some nuclear processes, specifically the bulk properties (energy, size, shape, . . .) may be well described, and for other processes such a wave function may provide a suitable zeroth order approximation.

188

From this point of view we will think of a many body Hamiltonian

$$H = -\sum_i \frac{\hbar^2}{2m} \nabla_i^2 + \frac{1}{2} \sum_{ij} V_{ij} + \frac{1}{6} \sum_{ijk} V_{ijk} + \ldots \qquad (1.1)$$

where $V_{ij} = V(r_i\sigma_i\tau_ip_i; r_j\sigma_j\tau_jp_j \ldots)$ is a two body potential, V_{ijk} is likewise a three body potential, and there is no reason in principle why more complicated N-body interactions cannot exist. The pion theory of the nucleon-nucleon force certainly predicts that a three body force should exist--it corresponds to an interaction between three particles which is additional to just the three pairwise interactions. In a diagrammatic language, one has processes like
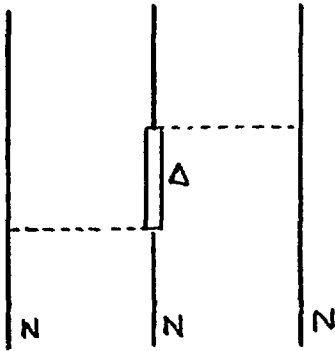
where particle two is excited into a virtual Δ or (3,3) resonance state in between exchanging pions with two neighboring nuclei. This particular process has been studied by a number of groups. The best estimate is that the three-body force might contribute one to two MeV/A to nuclear binding energies. In contrast the two-body force is reckoned to contribute about 35 MeV/A. The reason for the relative unimportance of the three-body force is that the nucleus is a low density system, making it unlikely for three nucleons to be close together at once. Also, the Pauli principle restricts clustering. More than four-body clusters (n and p with spins up and down) are unlikely to be very important.

For these reasons, it is assumed in the first instance that the Hamiltonian can be restricted to two-body forces. In this case, one can study the two-body force by carrying out N-N scattering experiments. If $E_{LAB} < 350$ MeV, the scattering is mainly elastic, so can be analyzed using nonrelativistic quantum mechanics. The measured cross sections, polarizations, depolarizations, etc., are used to determine phase parameters $\delta_{\ell j}(E)$ which characterize the N-N interaction, and these in turn are used to fit two-body potentials. If these potentials were weak enough, one could attempt to solve the many body Schroedinger equation directly, using perturbation theory for example. Since the potentials incorporate both strong attraction and repulsion, more complicated methods have been

developed. The most extensive work in this direction has proceeded along the lines of the Brueckner theory. In one approach, called the Local Density Approximation or LDA, one first tries to solve the problem of infinite nuclear matter, and constructs as a function of the density $\rho = (2/3\pi^2) k_F^3$ a local "effective interaction" which in first order of perturbation theory will reproduce selected nuclear matter properties. Since in the infinite system there is only one parameter, the density, one produces in this way a "density dependent effective interaction."

According to the Local Density Approximation (LDA), introduced by Brueckner, Gammel and Weitzner,[3] a finite nucleus can be thought of as made up of small elements of nuclear matter. In each such region the two body effective interaction is taken to be what it is in infinite nuclear matter at some average value of the local density. We have often used the arithmetic average $[\rho_n(1) + \rho_p(1) + \rho_n(2) + \rho_p(2)]/4$ when a neutron-proton pair at positions $\underset{\sim}{r}_1$ and $\underset{\sim}{r}_2$ interact. The validity of the LDA depends partly upon the short range of the NN interaction, compared to the nuclear radius. But even the heaviest nuclei are more than half surface, where the density is falling rapidly, so it is not obvious that the LDA should hold. This makes the success of the theory all the more interesting.

The effective interaction of Campi and Sprung,[4] called G-0, was written as a sum of Gaussians

$$V(r,k_F) = \sum_i (a_i + b_i k_F^{\lambda}) e^{-(r/\lambda_i)^2} + (W-W_0)A\delta(r) \qquad 1.2$$

$$= v_a(r) + k_F^{\lambda} v_b(r) + v_w.$$

The density dependence is separable $[k_F = (\frac{3\pi^2}{2}\rho)^{1/3}]$. The saturating property of the nuclear force leads to a low power of k_F: $\lambda = 1/2$ for force G-0. That is, at low density the presence of other particles has a rapidly varying effect, but at higher densities the density dependence is small. The effective interaction is designed to be used only in first order. At each density it reproduces the diagonal elements of the G-matrix in infinite nuclear matter.

2. Hartree Fock Method

Given a Hamiltonian containing only one and two body terms, the total energy of the system can be expressed in terms of the one body and two body density

matrices. To see this consider an antisymmetric wave function

$$\psi(1,2,. . .A)$$

depending on the coordinates of A particles, and normalized

$$\int \psi^*(1. . .A)\psi(1. . .A)d\tau_1. . .d\tau_A = 1. \tag{2.1}$$

The expectation value of the kinetic energy is

$$<T> = -\int \psi^*(1. . .A)(\sum_i \frac{\hbar^2}{2m} \nabla_i^2)\psi(1. . .A)d\tau \tag{2.2}$$

$$= - A \cdot \frac{\hbar^2}{2m}\int \psi^*(1. . .A)\nabla_1^2\psi(1. . .A)d\tau \tag{2.3}$$

Since the antisymmetry of ψ makes $\psi^*\psi$ a symmetric function of its coordinates, so each of the terms in the sum contributes equally. By integrating by parts, one of the gradients can be thrown onto ψ^*.

Setting

$$\rho(1,1') = A \int \psi^*(1. . .A)\psi(1'2. . .A)d\tau_2. . .d\tau_A \tag{2.4}$$

we have

$$<T> = \frac{\hbar^2}{2m} \quad [\nabla_1\nabla_1,\rho(1,1')]_{1=1'}d\tau_1 = \frac{\hbar^2}{2m} \int \tau(r)d^3r \quad . \tag{2.5}$$

Here $\rho(1,1')$ is the off diagonal element of the one body density matrix, and $\tau(r)$ is called the kinetic energy density. Similarly

$$<V> = \int \psi^*(1. . .A) (\frac{1}{2} \sum_{ij} V_{ij})\psi(1. . .A)d\tau_1. . .d\tau_A$$

$$= \frac{A(A-1)}{2}\int \psi^*(1. . .A)V_{12}\psi(1. . .A)d\tau_1. . .d\tau_A$$

$$= \frac{1}{2}\int \rho(12,12)V_{12} \, d\tau_1 d\tau_2 \tag{2.6}$$

where

$$\rho(12,1'2') = A(A-1)\int \psi^*(1'2'3. . .A) (123. . .A)d\tau_3. . .d\tau_A \tag{2.7}$$

Here I have assumed that V_{12} is a local force. In principle then, one does not require a full knowledge of the many body wave function but only those simpler objects $\rho(12, 1'2')$. Unfortunately, no one has devised a way to tell whether a given ρ is an allowed density matrix corresponding to an allowed many body wave function; some necessary conditions but no sufficient conditions are known.[5]

It is true that, Mihailović and coworkers[6] have done calculations of ^{20}Ne, ^{28}Si in which the density matrix was treated as a variational quantity, ρ being expressed in an oscillator basis. A number of necessary conditions were imposed on ρ, and apparently sensible results obtained. However, this method is not well developed.

According to the variational principle, the ground state of an A-body system is that completely antisymmetric state $\psi(1. . .A)$ which minimizes $\langle\psi|H|\psi\rangle$ subject to the condition that $\langle\psi|\psi\rangle = 1$. This can be included in the variational problem by introducing a Lagrange multiplier E, and demanding a minimum of

$$\langle\psi|H|\psi\rangle - E(\langle\psi|\psi\rangle - 1) \quad . \tag{2.8}$$

This implies

$$\langle\delta\psi| \; (H-E) \; |\psi\rangle = 0 \text{ for all variations } |\delta\psi\rangle$$
together with $\delta E(\langle\psi|\psi\rangle - 1)$ for arbitrary variations δE. $\qquad(2.9)$

Since $|\delta\psi\rangle$ is arbitrary, we have $(H-E) \; |\psi\rangle = 0$; the variational principle leads to the Schroedinger equation.

The variational method consists of introducing a trial wave function $\phi(a_1 a_2 a_3 . . .)$ depending on a certain number of parameters $(a_1, a_2, a_3 . . .) \equiv \underset{\sim}{a}$. These parameters are varied until

$$\langle\psi|H|\psi\rangle - E(\langle\psi|\psi\rangle - 1) = H(\underset{\sim}{a}) - E[N(\underset{\sim}{a}) - 1] \tag{2.10}$$

is a minimum. Necessary conditions for a stationary value are

$$\frac{\partial H}{\partial a_i} - E \frac{\partial N}{\partial a_i} = 0 \quad ; \quad N(\underset{\sim}{a}) = 1 \quad . \tag{2.11}$$

The Hartree Fock approximation is an application of the variational method, which utilizes a large number of variational parameters. Hartree's idea was to ascribe to each particle a state, or single particle orbital $\phi_i(r_i)$, so the total ψ is a product of these orbitals. Fock introduced antisymmetry by making a Slater determinant rather than a simple product.

$$\psi(1,2,\ldots.A) = \frac{1}{\sqrt{A!}} \det[\phi_i(r_j)] = \frac{1}{\sqrt{A!}} \sum_P (-)^P \phi_1(r_\alpha)\ldots\phi_A(r_\delta) \quad . \quad (2.12)$$

An elementary property of determinants is that they change sign when only two rows (or columns) are interchanged. The symbols $(\alpha\beta\ldots.\delta)$ are a permutation P of the labels 1 2. . .A and $(-1)^P$ is the signature of the permutation. To ensure that $|\psi>$ is normalized, the orbitals $\phi_i(r)$ form an orthonormal set. For such a ψ the density matrix takes a very simple form

$$\rho(1,1') = \frac{A}{A!} \sum_P \sum_Q (-)^{P+Q} \int \phi_1^*(r_\alpha)\ldots\phi_A^*(r_\delta)\phi_1(r_a)\ldots\phi_A(r_d)d^3r_1\ldots d^3r_A \quad .$$

$$(2.13)$$

Suppose that 1 occurs at position k in P, and at position ℓ in Q. A subset of $(A-1)!$ of the permutations P (or Q) allow this. But if we fix P, only a single permutation Q gives a non zero result, due to orthogonality of the ϕ's: it is $Q = P$.

$$\int \phi_1^*(r_a)\phi_1(r_a)d^3r_a \int \phi_k^*(r_b)\phi_2(rb)d^3r_b\ldots = 1.$$

Each of the $(A-1)!$ permutations P gives an identical result. Finally, k can be any one of the 1. . .A, so

$$\rho(1,1') = \sum_{k=1}^{A} \phi_k(r_1)\phi_k^*(r_1') \quad (2.14)$$

is just a projector onto the subspace of occupied orbitals $\phi_k(r)$. Similarly, the kinetic energy density is

$$\frac{\hbar^2}{2m} \tau(1) = \frac{\hbar^2}{2m} \sum_{k=1}^{A} \nabla\phi_k(r_1)\cdot\nabla\phi_k^*(r_1) \quad (2.15)$$

The two body density matrix is calculated similarly.

$$\rho(12,1'2') = \frac{A(A-1)}{A!} \sum_{PQ} (-)^{P+Q}$$

$$\int \phi_1^*(r_\alpha) \ldots \phi_A^*(r_\delta) \phi_1(r_a) \ldots \phi_A(r_d) d^3r_1 \ldots d^3r_A \qquad (2.16)$$

If P places 1 at k and 2 at ℓ, there will be two allowed permutations Q: Q = P or the "exchange" case with 1 at ℓ and 2 at k. Since this permutation differs by a single pair interchange, it has opposite signature. Thus,

$$\rho(12,1'2') = \sum_{k\ell} \phi_k^*(r_1')\phi_\ell^*(r_2')[\phi_k(r_1)\phi_\ell(r_2) - \phi_k(r_2)\phi_\ell(r_1)]$$

$$= \rho(11')\rho(22') - \rho(21')\rho(12') \quad . \qquad (2.17)$$

If ψ were not taken to have the simple Slater determinant form, the two particle density matrix would not be expressible in terms of the one particle density matrix. An additional term would appear, which would correspond to "dynamical correlations" between the two bodies, which are additional to the Pauli correlations contained in the above.

So far, ψ is just a trial wave function. The variational method tells us to vary the orbitals $\phi_i(r)$ until <H> is minimized; this will give the optimum wave function within the restricted part of the Hilbert space spanned by all Slater determinant wave functions. From (2.15), (2.17) we have

$$<\psi|H|\psi> = \int H(r)d^3r \qquad (2.18)$$

with

$$H(r) = \frac{\hbar^2}{2m} \tau(r) + \frac{1}{2} \int \rho(rr',rr')V(r-r')d^3r'$$

$$<\psi|H|\psi> = \int \frac{\hbar^2}{2m} \tau(r)d^3r + \frac{1}{2}\iint [\rho(r)\rho(r') - |\rho(r,r')|^2]V(\underset{\sim}{r}-\underset{\sim}{r}')d^3r'd^3r \qquad (2.19)$$

Since $\phi(r)$ is complex, we can vary its real and imaginary parts independently. Alternatively we can consider $\phi(r)$ and $\phi^*(r)$ as independent variational quantities; this leads to two sets of equations which are hermitian conjugates of each other.

194

We consider varying $\phi_k^*(R)$ at the point $\underset{\sim}{r} = \underset{\sim}{R}$, by an amount $\delta\phi_k^*(R)\delta(\underset{\sim}{r}-\underset{\sim}{R})$. In the potential energy term we will get two equal contributions corresponding to $\underset{\sim}{r} = \underset{\sim}{R}$ and $\underset{\sim}{r}' = \underset{\sim}{R}$, removing the factor 1/2. The result is the Hartree Fock equations:

$$-\frac{\hbar^2}{2m}\nabla^2\phi_k(R) + \phi_k(R)\int\rho(\underset{\sim}{r}')V(\underset{\sim}{R}-\underset{\sim}{r}')d^3r'$$

$$-\int\phi_k(r')\rho(R,r')V(\underset{\sim}{R}-\underset{\sim}{r}')d^3r'$$

$$= \varepsilon_k\phi_k(R) \tag{2.20}$$

In arriving at this result, use is made of the freedom to make a unitary transformation among the set of occupied states $[\phi_k(r)]$ in order that only a single ϕ_k appears on the right hand side (see Appendix A). The Hartree Fock equations are a set of integro-differential equations which determine the set ϕ_k of states which minimize the total energy in the space of Slater determinants. The left hand side of Eq. (2.20) is the Hartree Fock one body Hamiltonian

$$h(\underset{\sim}{r},\underset{\sim}{r}') = [-\frac{\hbar^2}{2m}\nabla^2 + U_D(\underset{\sim}{r})]\delta(\underset{\sim}{r}-\underset{\sim}{r}') + U_E(\underset{\sim}{r},\underset{\sim}{r}')$$

consisting of the kinetic energy, the local "direct" interaction and the non local "exchange" interaction. The direct term is just the potential energy at $\underset{\sim}{r}$ due to the presence of particles at $\underset{\sim}{r}'$ with probability $\rho(r')d^3r'$, summed over all $\underset{\sim}{r}'$:

$$U_D(\underset{\sim}{r}) = \int\rho(\underset{\sim}{r}')V(\underset{\sim}{r}-\underset{\sim}{r}')d^3r' \quad .$$

This contains a "self interaction" since the state $\phi_k(r)$ is included in the sum $\rho(r')$; however, this is seen to be cancelled out by an equal term contained in the exchange field. The exchange field represents the additional energy due to the possibility of the particle in state ϕ_k exchanging position with any of the remaining (A-1) particles. If exchange is ignored, ψ reduces to a simple product wave function and only the direct potential minus the self interaction occurs. This is the Hartree approximation.

The Hartree Fock method is also called the self consistent field method. The one body Hamiltonian determines the orbitals $\phi_k(r)$, but these are required [to construct $\rho(r,r')$] before we know $h(r,r')$. The usual method of solution is to start from a trial set of $\phi_k(r)$, usually oscillator or Woods Saxon wave functions, then construct $h(r,r')$, and finally solve for a new set $\phi_k(r)$. This process is continued until the output set $\phi_k(r)$ are close enough to the input set. At this point the fields constructed from ϕ_k are self consistent in that they reproduce the same set of $\phi_k(r)$. There is no mathematical demonstration that this procedure will converge, but considerable numerical experience gives confidence in it. Except for magic nuclei, problems can arise, where successive iterations oscillate between (say) different configurations. A common remedy in this situation is to average the field $\mu h^{(n)} + (1-\mu)h^{(n+1)} = \bar{h}^{(n+1)}$ between successive iterations.

In Eq. (2.20) we may multiply by $\phi_k^*(R)$, sum over k and integrate over all R: The result is

$$\frac{\hbar^2}{2m}\int \tau(R)d^3R + \iint [\rho(R)\rho(r')-|\rho(R,r')]^2 \, V(\underset{\sim}{R}-\underset{\sim}{r'})d^3Rd^3r' = \sum_k \varepsilon_k \quad . \quad (2.21)$$

This is not the same as $\langle\psi|H|\psi\rangle$ because the potential energy is counted twice. Since the Hartree Fock one body field ultimately is due to the interaction of state k with all other states ℓ, when we sum up the potential energies of all states k we will have counted the k-ℓ interaction twice, once for state k and again for state ℓ.

If we add the total kinetic energy to Eq. (2.21), and divide by 2, we will reproduce

$$\langle\psi|H|\psi\rangle = E_{HF} = \frac{1}{2}[\sum_k \varepsilon_k + \frac{\hbar^2}{2m}\int \tau(r)d^3r] = \frac{1}{2}\sum_k (\varepsilon_k + t_k) \qquad (2.22)$$

where $t_k = -\frac{\hbar^2}{2m}\int \phi_k^*\nabla^2\phi_k \, d^3r$ is the kinetic energy of state k. The Hartree Fock eigenvalues ε_k are approximately equal to the removal energies for a particle in state k, but their sum is not equal to the total energy.

At this point we can see that the Hartree Fock approximation with a static two body force will be in trouble in describing nuclear structure. From experiments such as (e,e'p) or (p,2p) which remove a nucleon from deep inside the

nucleus, we learn that the removal energy for a 1s nucleon is at most of order 50 MeV. From nuclear radii, which are accurately known from electron scattering, the kinetic energy can be estimated. In infinite nuclear matter, the average kinetic energy is $\frac{\hbar^2}{2m} \frac{3}{5} k_F^2 \simeq 23$ MeV per particle. Allowing for the fact that it is slightly less in finite nuclei, we still have an estimated total energy of only -2 to -4 MeV/A according to the Hartree Fock relation (2.22). But real nuclei are bound by -8 MeV/A. This conundrum was emphasized by Kerman about 10 years ago.

The effective interaction theory allows us to find the additional binding energy from the density dependence of the effective interaction implied by the local density approximation. Density dependence means that the Hamiltonian depends on the solution to the Schroedinger equation. In this case the variational principle does not hold, but we can appeal to the principle of maximum self consistency to derive Hartree Fock equations which contain additional "rearrangement terms" arising from

$$\frac{\partial V}{\partial \rho} \frac{\delta \rho}{\delta \phi_k^*(r)} \quad .^\dagger$$

In the simplest case the density dependence is separable and of the form

$$V_b(\underset{\sim}{r}-\underset{\sim}{r}')\{\tfrac{1}{2}[\rho(r) + \rho(r')]\}^\alpha \equiv V_b(\underset{\sim}{r}-\underset{\sim}{r}',\rho) \quad . \tag{2.23}$$

Then the rearrangement term is

$$\phi_k(r) \int \alpha V_b(r-r',\rho) \cdot \{\tfrac{1}{2}[\rho(r)+ (r')]\}^{-1} \cdot \{\rho(r)\rho(r')-[\rho(r,r')]^2\}d^3r \quad . \tag{2.24}$$

There are both direct and exchange parts of the rearrangement field, but both are local fields due to our choice of the form of density dependence.

The presence of these additional fields means that the Hartree Fock relation, Eq. (2.22) will no longer produce the total energy of the nucleus. Rather

---
$\dagger$ In some effective interactions, there is dependence on other local functionals, such as $\tau(r)$, $\nabla^2\rho(r)$ and $\underset{\sim}{\nabla}\rho(r)$. One will then consider variations

$$\frac{\partial}{\partial \tau} \frac{\delta\tau(r)}{\delta\nabla\phi_k^*(r)} \quad , \text{ for example.}$$

$E = E_{HF} + E_{Rear}$ where E_{HF} is still given by Eq. (2.22) and E_{Rear} is constructed from (2.24) above. Exploiting the symmetry between r, r' we write

$$E_{Rear} = - \alpha \iint V_b(r-r',\rho) [\rho(r)\rho(r') - \rho(r,r')|^2] d^3r' d^3r \quad . \tag{2.25}$$

At this point, to make the discussion more concrete I will describe some HF calculations for spherical nuclei done by Campi and myself using a force called G-0 (Eq. 1.2). In addition to the ingredients already listed, this includes two additional elements. One is a zero range two body spin orbit interaction, $V_{LS} = iB\delta(r_{12})(\sigma^1+\sigma^2) \cdot (k' \times k)$, with a strength constant $B = 130$ MeV fm^5. The second is an "energy dependence" which arises from the fact that in a finite nucleus, while the density varies from place to place, the energy of a given state is a global quantity which is fixed. In infinite nuclear matter at a given density, the average energy of occupied states is a function of that density. In the surface of a finite nucleus you have matter at low density but a (relatively) large single particle binding energy. The effective interaction is less attractive when the particles are well bound, and this can be well represented by a term of the form $[W-W_0(k_F)]A^{ST}(k_F)\delta(r_{12})$ where $W_0(k_F)$ is the average single particle energy in nuclear matter at density corresponding to the local Fermi momentum k_F; W is the average single particle energy in the finite nucleus excluding Coulomb effects; $A^{ST}(k_F)$ is a strength parameter determined in nuclear matter calculations and the zero range nature of this force reflects the fact that its matrix elements are constant. The force acts only in S-states and is much stronger in the triplet than in the singlet case:

$$A^{13} = 1.64 \ (1 + 0.486 \ k_F)^{-3}$$
$$A^{31} = 15.60 \ (1 + 0.87 \ k_F)^{-3} \quad .$$

This force contributes an almost constant 0.6 MeV/A to nuclear binding energy.

In Campi and Sprung, spherical Hartree Fock calculations were reported for doubly closed shell nuclei ^{4}He, ^{16}O, ^{40}Ca, ^{48}Ca, ^{90}Zr, and ^{208}Pb. The force G-0 was adjusted so as to give saturation in nuclear matter at $E_s = - 16.5$ MeV, $k_s = 1.35$ fm^{-1}. We then found that nuclear binding energies were reproduced to within 250 keV/A and charge radii within 1%. Some of the relevant results are summarized in Figs. 1 and 2 and Tables I and II from CS.

The force was also tested on the series of isotopes of He and O and gave a reasonably good account of the trend of binding energies and radii, as in Figs. 3, 4, 5 and 6.

3. Skyrme Forces

In place of an effective interaction deduced from nuclear matter calculations in the local density approximation, considerable work has been done using purely phenomenological effective interactions designed to produce saturation in finite nuclei. The first such forces were those of Volkov,[7] and Brink and Boeker,[8] which were purely static forces. Brink and Vautherin[9] first carried out Hartree Fock calculations using the BB force, obtaining good radii for the magic nuclei but binding energies of only 6 MeV/A. These forces consist of a repulsive plus an attractive Gaussian, and a suitable exchange mixture to ensure that most of the attraction comes from even states.

Brink and Vautherin then revived a very simple form of effective interaction, originally suggested by Skyrme, which contains only a small number of adjustable parameters. It is of the form $V_2 + V_3$ where[+]

$$V_2 = t_0(1 + x_0 P_\sigma)\delta(r_{12}) + \frac{t_1}{2}(1 + x_1 P_\sigma)[k'^2\delta(r_{12}) + \delta(r_{12})k^2]$$

$$+ t_2(1 + x_2 P_\sigma)\underset{\sim}{k'} \cdot \delta(r_{12})\underset{\sim}{k} + iW(\underset{\sim}{\sigma}^1 + \underset{\sim}{\sigma}^2) \cdot [\underset{\sim}{k'} \times \delta(r_{12})\underset{\sim}{k}] \qquad (3.1)$$

and V_3 incorporates a suitable density dependence. Originally it was taken to be a contact three body force

$$V_3 = t_3\delta(r_{12})\delta(r_{23}) \qquad (3.2)$$

but subsequently it has been found preferable to consider it a density dependent two body force

$$V_3' = \frac{t_3}{6}(1 + x_3 P_\sigma)\rho_0^\alpha \, \delta(r_{12}) \qquad (3.3)$$

(for $x_3 = 1$, $\alpha = 1$, this force makes the same contribution to the Hartree Fock

---

[+]Note P_σ is the spin exchange operator; $\underset{\sim}{k}$ is the operator $(-i\nabla)$ acting to right; $\underset{\sim}{k'}$ to left.

energy as does V_3. However, if one considers excitations of the system, through RPA vibrations, they are no longer equivalent and the second form leads to better results).

There are several popular sets of Skyrme force parameters which have been fitted to reproduce nuclear properties over a wide region of the N,Z diagram. These have names, S-I, S-II, etc. Some of these are listed in Table III. In most cases the exchange parameters s_1 and s_2 are set to zero, $s_3 = 1$ and $\alpha = 1$ corresponding to the above remarks. This leaves six real parameters, t_0, x_0, t_1, t_2, t_3, and W, the strength of the spin orbit interaction. A value of W = 120 MeV fm^5 gives reasonable spin orbit splittings for the eigenvalues near magic nuclei. The various Skyrme forces can be characterized by the value of t_3, the amount of density dependence. Flocard et al.[14] have found that there is a linear relationship among the Skyrme parameters, so that any number of acceptable sets can be found which give good agreement for nuclear binding energies and radii. These forces differ in how density dependence is traded off against velocity dependence of the effective interaction. S-III is rather similar to force G-0 in that it corresponds to an effective mass of above 0.76 m in the nuclear interior (G-0 corresponds to about 0.66 m in nuclear matter).

The Skyrme forces not only reproduce a large amount of nuclear data from a small number of adjustable parameters; they are exceedingly easy to use. The zero range nature of the force ensures that the Hartree Fock fields are local, and in fact are simple polynomials of local densities. The most time consuming part of a HF calculation with a finite range force is constructing the non-local exchange field; here this is entirely avoided.

In Vautherin and Brink (1972) it is shown that for a Skyrme force, $H(r)$ (Eq. 2.18) can be expressed as an algebraic functional of just three densities $\rho_q(r)$, $\tau_q(r)$, and a vector density $\underset{\sim}{J}_q(r)$. To be realistic I will not introduce spin and isospin degrees of freedom, neglected in the discussion so far. Besides a position $\underset{\sim}{r}$, a particle will have a spin coordinate $\sigma = \pm 1/2$ and a charge coordinate q taking values n,p. We consider an even-even nucleus, and assume that the subspace of occupied orbitals is invariant under time reversal. (For an axially symmetric system this implies that states of $J_z = \pm m$ will have equal occupation.) Since protons and neutrons are distinguishable particles, the density matrix will be diagonal in the coordinate q. If we sum over both spin states we can define the following densities:

$$\rho_q(r) = \sum_{k\sigma} |\phi_k(\underset{\sim}{r},\sigma,q)|^2 \tag{3.4}$$

$$\tau_q(r) = \sum_{k\sigma} |\underset{\sim}{\nabla}\phi_k(\underset{\sim}{r},\sigma,q)|^2 \tag{3.5}$$

$$\underset{\sim q}{J}(r) = -i \sum_{k\sigma\sigma'} \phi_k^*(r\sigma q)[\underset{\sim}{\nabla}\phi_k(r\sigma'q) \times <\sigma|\underset{\sim}{\sigma}|\sigma'>] \tag{3.6}$$

The expression for $H(r)$ is

$$H(r) = \frac{\hbar^2}{2m}\tau(r) + \frac{1}{2}t_0[(1 + \frac{1}{2}x_0)\rho^2 - (x_0 + \frac{1}{2})(\rho_n^2 + \rho_p^2)]$$

$$+ \frac{1}{4}(t_1 + t_2)\rho\tau + \frac{1}{8}(t_2 - t_1)(\rho_n\tau_n + \rho_p\tau_p)$$

$$+ \frac{1}{16}(t_2 - 3t_1)\rho\nabla^2\rho + \frac{1}{32}(3t_1 + t_2)(\rho_n\nabla^2\rho_n + \rho_p\nabla^2\rho_p)$$

$$+ \frac{1}{16}(t_1 - t_2)(\underset{\sim n}{J}^2 + \underset{\sim p}{J}^2) + \frac{1}{4}t_3\rho_n\rho_p\rho$$

$$+ H_c(r) - \frac{1}{2}W_0(\rho \text{ div } J + \rho_n \text{ div } J_n + \rho_p \text{ div } J_p) \tag{3.7}$$

$$H_c(r) = \frac{1}{2}\rho_p(r)V_c(r) - \frac{3}{4}e^2(\frac{3}{\pi})^{1/3}\rho_p(r)^{4/3} \tag{3.8}$$

with

$$V_c(r) = e^2\int\frac{\rho_p(r')}{|\underset{\sim}{r}-\underset{\sim}{r}'|}d^3r' \quad . \tag{3.9}$$

The exchange part of the Coulomb interaction is taken in Slater's approximation (see Bethe and Jackiw[10] for a discussion).

As before, Hartree Fock equations are deduced by minimizing

$$\int\{H(r) - \sum_k \varepsilon_k[|\phi_k(r)]|^2 - 1\}d^3r \tag{3.10}$$

by variations of the orbitals $\phi_k^*(r)$. Since $H(r)$ is algebraic, this is not diffi-cult to do. The only complication is that besides ϕ_k, H depends on derivatives $\underset{\sim}{\nabla}\phi_k$, so that in order to produce an expression proportional to $\delta\phi_k^*(r)$, an integra-tion by parts must be done. This will affect the terms involving t_1, t_2. The result may be expressed as

$$\frac{\partial H}{\partial \phi_k^*} - \nabla \left(\frac{\partial H}{\partial (\nabla \phi_k^*)} \right) + \nabla^2 \left(\frac{\partial H}{\partial (\nabla^2 \phi_k^*)} \right) = \varepsilon_k \phi_k(r) \quad . \tag{3.11}$$

Actually, by means of integration by parts, the $\rho \nabla^2 \rho$ terms can be replaced by $(\nabla \rho)^2$ terms, so the third term in (3.11) is unnecessary. The resulting HF equations are

$$[-\nabla \left(\frac{\hbar^2}{2m_q^*(r)} \nabla \right) + U_q(r) + W_q(r) \, (-i\nabla \times \sigma)] \phi_k(r) = \varepsilon_k \phi_k(r) \tag{3.12}$$

where q is the charge of the particle in state k,

$$\frac{\hbar^2}{2m_q^*(r)} = \frac{\hbar^2}{2m} + \frac{1}{4}(t_1 + t_2)\rho(r) + \frac{1}{8}(t_2 - t_1)\rho_q(r) \tag{3.13}$$

is called the effective mass term, and

$$U_q(r) = t_0[(1 + \frac{1}{2}x_0)\rho - (x_0 + \frac{1}{2})\rho_q] + \frac{1}{4}t_3(\rho^2 - \rho_q^2)$$

$$- \frac{1}{8}(3t_1 - t_2)\nabla^2\rho + \frac{1}{16}(3t_1 + t_2)\nabla^2\rho_q + \frac{1}{4}(t_1 + t_2)\tau$$

$$+ \frac{1}{8}(t_2 - t_1)\tau_q - \frac{1}{2}W_0(\nabla \cdot J + \nabla J_q) + \delta_{qp}(V_c(r) - e^2(\frac{3}{\pi})^{1/3}\rho_p^{1/3})$$

$$W_q = \frac{1}{2}W_0(\nabla\rho + \nabla\rho_q) + \frac{1}{8}(t_1 - t_2)J_q \quad . \tag{3.14}$$

In the first paper by Vautherin and Brink[9] spherical symmetry was also assumed, and calculations were carried out for the doubly closed shell nuclei. In this case the vector density J has only a radial component:

$$J(r) = \hat{r} \, J(r) \quad .$$

The first term in W_q leads then to the familiar Blin-Stoyle[11] form

$$W_q(-i\nabla \times \sigma) = W_0 \frac{1}{r}\frac{d}{dr}(\rho + \rho_q)\frac{1}{2}\sigma \cdot \ell \tag{3.15}$$

202

In the spherical case,

$$\phi_k(r\sigma\tau) = \frac{1}{r} R_\alpha(r) \, Y^{jm}_{\ell 1/2} \cdot \chi_q(\tau) \tag{3.16}$$

so

$$\rho(r) = \frac{1}{4\pi r^2} \sum_\alpha (2j_\alpha+1) R_\alpha^2(r) \tag{3.17}$$

$$\tau(r) = \frac{1}{4\pi} \sum_\alpha (2j_\alpha+1) \left[\left(\frac{dR_\alpha}{dr}\right)^2 + \frac{\ell_\alpha(\ell_\alpha+1)}{r^2} R_\alpha^2(r) \right] \tag{3.18}$$

$$J(r) = \frac{1}{4\pi} \sum_\alpha (2j_\alpha+1) <\underset{\sim}{\sigma}\cdot\underset{\sim}{\ell}>_\alpha R_\alpha^2(r) \qquad <\underset{\sim}{\sigma}\cdot\underset{\sim}{\ell}> = \begin{cases} +\ell \\ -\ell-1 \end{cases} . \tag{3.19}$$

The Hartree Fock equations (3.12) may now be solved in the usual partial wave representation as ordinary second order differential equations. A transformation to remove the first derivative allows the powerful Numerov method to be used.

There are a number of special recipes which have been applied to all Skyrme calculations which we should note. In Eq. (3.14) the term $1/8(t_1-t_2)\underset{\sim}{J}_q$ represents a central-force contribution to the spin orbit splitting. This has invariably been <u>omitted</u>, on aesthetic grounds. Correspondingly, the term $1/16(t_1-t_2)$ $(J_n^2+J_p^2)$ has been dropped from the energy density Eq. (3.7), in order to preserve the variational principle. Secondly the one body part of the center of mass motion has been subtracted from the kinetic energy. The Hamiltonian (1.1) is written in an arbitrary coordinate system, and the calculations have been carried out using all A particle coordinates. This means that the center of mass of the nucleus is not at rest. The center of mass momentum $\underset{\sim}{P} = \sum_i \underset{\sim}{p}_i$ ought to be a constant of motion. To remove the energy of motion of the center of mass from the Hamiltonian one should subtract

$$\frac{1}{2mA} \underset{\sim}{P}^2 = \frac{1}{2mA} \sum_i p_i^2 + \frac{1}{2mA} \sum_{i\neq j} \underset{\sim}{p}_i \cdot \underset{\sim}{p}_j \quad .$$

The first term on the right hand side can be combined easily with the kinetic energy part of (1.1):

$$(1 - \frac{1}{A}) \sum_i \frac{\hbar^2}{2m} \nabla_i^2 = T'$$

merely reducing the value of $\frac{\hbar^2}{2m} \simeq 20.73$ MeV fm^2 by $\frac{1}{A}$. The two body part $(\underset{\sim}{p}_i \cdot \underset{\sim}{p}_j)$ is neglected. For nuclei A>4 this leads to an error comparable to the correction made. However, for Skyrme forces this may be regarded as a prescription which has gone into fitting of the parameters.

To gain some insight into the meaning of the parameters we consider an N=Z nucleus and omit Coulomb effects. Then $\rho_q = \frac{1}{2} \rho$ is the same for both charges:

$$\frac{\hbar^2}{2m^*} = \frac{\hbar^2}{2m} (1 - \frac{1}{A}) + \frac{1}{16} (3t_1 + 5t_2)\rho \tag{3.20}$$

$$U(r) = \frac{3}{4} t_0\rho + \frac{3}{16} t_3\rho^2 + \frac{1}{16} (3t_1 + 5t_2)\tau$$

$$+ \frac{1}{32} (5t_2 - 9t_1)\nabla^2\rho - \frac{3}{2} W_0 \text{ div } J \tag{3.21}$$

$$\underset{\sim}{W} = \frac{3}{4} W_0\nabla\rho + \frac{1}{16} (t_1 - t_2)\underset{\sim}{J} \quad . \tag{3.22}$$

The effective mass has the form postulated by Migdal. The combination $(3t_1 + 5t_2)$ is a measure of "velocity dependence" of the effective interaction. $(9t_1 - 5t_2)$ is related to the surface energy, since it occurs with $\nabla^2\rho$ in U(r) and with $(\nabla\rho)^2$ in H:

$$H(r) = \frac{\hbar^2}{2m} (1 - \frac{1}{A})\tau + \frac{3}{8} t_0\rho^2 + \frac{1}{16} t_3\rho^3$$

$$+ \frac{1}{16} (3t_1 + 5t_2)\rho\tau + \frac{1}{64} (t_1 - t_2)J^2$$

$$+ \frac{1}{64} (9t_1 - 5t_2) (\nabla\rho)^2 - \frac{3}{4} W_0\rho \underset{\sim}{\text{div}} \underset{\sim}{J} \quad . \tag{3.23}$$

In the limit of infinite nuclear matter $(\underset{\sim}{\nabla}\rho = 0, \underset{\sim}{\nabla} \cdot \underset{\sim}{J} = 0, \tau = \frac{3}{4} k_F^2)$

$$\frac{E}{A} = \frac{H}{\rho} = \frac{3}{5} T_F + \frac{3}{8} t_0\rho + \frac{1}{16} t_3\rho^2 + \frac{3}{8} (3t_1 + 5t_2)\rho k_F^2 \quad . \tag{3.24}$$

204

The compressibility modulus

$$K = k_F^2 \frac{\partial^2 (E/A)}{\partial k_F^2} = \frac{6}{5} T_F + \frac{9}{4} t_0 \rho + \frac{15}{8} t_3 \rho^2 + \frac{3}{4} (3t_1 + 5t_2) \rho k_F^2 \qquad (3.25)$$

at the saturation point k_F where

$$\frac{\partial (E/A)}{\partial k_F} = 0 \quad . \quad (T_F = \frac{\hbar^2}{2m} k_F^2)$$

Treating E/A, k_F and K as input quantities one can solve for

$$t_0 \rho = \frac{40}{3} \left(\frac{E}{A}\right) + \frac{4}{9} K - \frac{16}{5} T_F$$

$$\frac{3}{16} t_3 \rho^2 = 15 \frac{E}{A} + K - \frac{9}{5} T_F$$

$$\frac{1}{16} (3t_1 + 5t_2) \rho k_F^2 = 2T_F - 15 \left(\frac{E}{A}\right) - \frac{5}{6} K \quad . \qquad (3.26)$$

It is believed that E/A $\simeq$ -16 MeV, $T_F \simeq$ +38 MeV and K $\simeq$ 200 MeV. All Skyrme forces give K of the least 300 MeV, somewhat greater than other "realistic" effective interactions.

In a second paper Vautherin[12] extended his calculations to axially symmetric deformed nuclei. A basis of deformed oscillator states - essentially the asymptotic basis of the Nilsson model, was used. The matrix elements of the one body hamiltonian have to be calculated between the basis states, then the eigenvalues and eigenvectors of this matrix are found numerically. In practice, the matrix elements are calculated by numerical integration using a Gaussian quadrature rule in the (r,z) plane. There is, then, a shuffling back and forth between real space - where the HF hamiltonian $[\hbar^2/2m^*(r), U_q(r), W_q(r)]$ is easily expressed - and the oscillator space, where the eigenvalue problem for the HF orbitals is conveniently solved. The calculations are well within the capabilities of present computers.

Taking the symmetry axis along OZ, $J_z = \Omega_k$ is a good quantum number. One can take orbitals of the form

$$\phi_k(\underset{\sim}{r},\sigma,q) = [\phi_k^+(r,z) e^{-i\Lambda^-\phi} \chi_+ + \phi_k^-(r,z) e^{i\Lambda^+\phi} \chi_-] \chi_q \qquad (3.27)$$

where $\chi_{\pm}$ are spin up/down states and χ_q denotes the charge state. $\Lambda^{\pm} = \Omega_k \pm \frac{1}{2}$. The distance perpendicular to OZ is r. The expressions for the one body density lead to

$$\rho(r,z) = \sum_k |\phi_k^+(r,z)|^2 + |\phi_k^-(r,z)|^2 \tag{3.28}$$

$$\tau(r,z) = \sum_k \{ |\nabla_r \phi_k^+(r,z)|^2 + |\nabla_z \phi_k^+(r,z)|^2 + \frac{1}{r^2}|\Lambda^-\phi_k^+(r,z)|^2 (+\leftrightarrow -) \} \tag{3.29}$$

where $\nabla_r = \frac{\partial}{\partial r}$, $\nabla_z = \frac{\partial}{\partial z}$, $\nabla_\phi = \frac{1}{r}\frac{\partial}{\partial \phi}$ in cylindrical coordinates. div J has a simi-lar expression.

The time reversal operator is $\hat{T} = -i\sigma_y K_0 = \frac{1}{2}(\sigma_- - \sigma_+)K_0$ where K_0 denotes com-plex conjugation. If it is applied to the state ϕ_k (3.29) it has the effect of replacing $[\phi_k^+, \phi_k^-, \Omega_k] \rightarrow [-\phi_k^-, \phi_k^+, -\Omega_k]$. However, such an interchange of the spinor components leaves the densities ρ, τ, div J invariant. Thus, we are allowed to divide the orbitals ϕ_k into a set with $\Omega_k > 0$ and the set of time reversed states $\phi_{\bar{k}}$ with $\Omega_{\bar{k}} < 0$. These make equal contributions to the densities, so we calculate only the first set and finally double the result. Similarly, the parity operation changes $\underset{\sim}{r} \rightarrow -\underset{\sim}{r}$, or $(r,z,\phi) \rightarrow (r,-z, \phi + \pi)$. The densities are independent of ϕ, depending only on r,z. If we assume that the states (3.27) are reflection symmetric - i.e., are even in z, then so are the densities and the HF equations. These therefore admit reflection symmetric solutions. We need only then consider z > 0 and may confine calculations to the first quadrant of the (r,z) plane.

Pairing Correlations:

As one moves away from a closed shell nucleus, the level occupations have a large effect on the solution of the HF equations. Unless there is a large gap between the energies of occupied and empty orbitals, it is by no means clear that the lowest total energy solution will arise from filling of the lowest energy orbitals, especially since $E \neq \sum_k \varepsilon_k$. The Hartree-Fock Bogolyubov (HFB) formalism is an extension of HF which introduces pairing correlations, and amounts to using a mixture of different configurations in place of a single Slater determinant for ψ.

If one were dealing with a fundamental many-body Hamiltonian, one would pro-ceed to apply the HFB formalism to it. But in dealing with a Skyrme force, or

other effective interaction which has been simplified with the aim of reproducing average or bulk properties of the nucleus, one would have to introduce additional parameters in order to guarantee that sensible pairing matrix elements were obtained. Recognizing this, Vautherin[12] proposed to introduce this additional parameter in a way related to the simple BCS solution.

Each orbital is assigned an occupation

$$n_k = v_k^2 \quad \text{where } u_k^2 + v_k^2 = 1$$
$$u_{\bar{k}} = u_k \tag{3.30}$$
$$v_{\bar{k}} = -v_k,$$

so

$$\rho(\underset{\sim}{r}) = 2 \sum_k{}' n_k |\phi_k(r)|^2 , \text{ etc.} \tag{3.31}$$

(The primed sum implies only $\Omega_k > 0$ states to be summed, as discussed above.) To the total energy of the system is added a pairing energy

$$E_p = -G \left(\sum_k{}' u_k v_k \right)^2 \tag{3.32}$$

Following BCS, we might say that only a band of states within (say) 10 MeV of the Fermi level takes part in the pairing interaction, then outside this band $u_k v_k = 0$. The energy E is now a function of both the orbitals ϕ_k and the occupations n_k. These are additional constraints

$$\lambda_q \left(\sum_k \delta_{q_k,q} n_k - N_q \right) \tag{3.33}$$

ensuring that on average the system contains the correct N,Z. Treating all of these as variational parameters leads to two sets of equations. First is the same HF equations (3.12 to 3.14) as before, except that now the densities involve partially occupied levels. Next there are BCS equations

$$2(\epsilon_k - \lambda_{q_k}) u_k v_k - \Delta_q (u_k^2 - v_k^2) = 0 \tag{3.34}$$

with

$$\Delta_q = G \sum_k{}' u_k v_k \tag{3.35}$$

whose solution is

$$n_k = \frac{1}{2}\left[1 - \left\{\frac{\varepsilon_k - \lambda_{q_k}}{[(\varepsilon_k - \lambda_{q_k})^2 + \Delta_q^2]^{1/2}}\right\}\right] .$$ (3.36)

λ_n, λ_p are determined so the particle numbers are correct.

At each iteration of the HF calculation the occupations are determined using the HF eigenvalues ε_k. These occupations are used in constructing the HF fields for the succeeding iteration. This procedure was also used by Campi, Sprung and Martorell[13] in their study of the tin nuclei. A suitable value for the pairing force constant is

$$G_q \simeq 18/(11 + N_q) \text{ MeV.}$$ (3.37)

This is about 25% greater than in Nilsson model calculations, because the level density obtained in HF calculations is too low compared to experiment, in the vicinity of the Fermi surface.

Vautherin astutely proposed a variation on the BCS method, which treats the pairing gap Δ as the fundamental quantity rather than the pairing force strength. Since Δ is known experimentally from even-odd mass differences, this may be regarded as removing one parameter from the work.

If the pairing energy

$$E_p = - \Delta(\sum_k' u_k v_k)$$ (3.38)

is added to the total energy, one would not get the same HF-BCS equations as before (treating now Δ as fixed). This is because the variation $\frac{\partial}{\partial v_k}$ previously brought down a factor 2 in Eq. (3.32). The remedy is simply to include $2E_p$ in the quantity to be minimized; this restores the desired equations. However, in computing the energy of the system, E_p is counted only once. In this method, only the Fermi energy λ_q needs to be determined since Δ_q is fixed, so the BCS equations are even easier to solve. Also, the pairing force may be allowed to act between all the states included in the HF calculation.

The paper by Beiner, Flocard, Van Giai and Quentin[14] reports a systematic study of the applicability of Skyrme forces. Some 120 nuclei along the valley of β-stability were included in their calculations, and several sets of Skyrme

208

parameters were fitted. Among them, S-III has come to be a preferred choice. All these calculations were done in a spherical basis. In between closed shells there are discrepancies of up to 20 MeV (for the nucleus) between calculated and experimental binding energies; this allows for the nucleus to gain energy by deformation. Some of these results are summarized in the Figs. 7 to 10 and Tables IV and V.

In a sequel, Flocard and Quentin[15] did deformed calculations of the (s,d) shell even-even nuclei and found that S-III and S-IV gave a good account of their properties. Campi, Flocard, Kerman and Koonin[16] studied the sodium isotopes and showed that a shape transition setting in at A=32 could explain an anomaly in the measured masses. These results are illustrated in the Figs. 11 and 12.

In deformed code calculations some care has to be put into optimizing the basis. The deformed oscillator is characterized by two frequencies $\omega_\perp$, ω_z or equivalently

$$b = \sqrt{\frac{m\omega_0}{\hbar}} \,, \quad \omega_0^3 = \omega_\perp^2 \omega_z \quad \text{and} \quad q = \omega_\perp/\omega_z \quad .$$

Also the basis is cut off after N_0 major shells, where $N_0 = 6$ or 8 is adequate for light nuclei but 10 or 12 is necessary for the rare earths and actinides. This was discussed by Flocard, Quentin and Vautherin.[17]

Potential energy surfaces (binding energy versus quadrupole moment Q and/or hexadecupole moment h) can be mapped out by constrained Hartree Fock or HF-BCS calculations in which a quadratic constraint[32] $\frac{C}{2}(Q-Q_0)^2$ is added to the preceding Hamiltonian. When the minimum is reached one has $\frac{dE}{dQ} = -C(Q-Q_0)$ with $Q = <Q>$ being the self consistent moment. Q_0 is a specified "target" value. To see how Q varies with Q_0 we have

$$\frac{dQ_0}{dQ} = 1 + \frac{1}{C}\frac{d^2E}{dQ^2} \quad .$$

This means that a large enough

$$C > |\frac{d^2E}{dQ^2}|$$

will ensure that $\frac{dQ_0}{dQ}$ is monotonic, so by varying Q_0 one can map out the entire range of Q values. If a simple linear constraint were employed this would not

be possible. Further, some fundamental objections to calculations using the linear constraint have been raised by Fonte and Schiffrer;[18] see also Bassichis et al.[19] (These apply to unbounded operators.)

4. Density Matrix Expansion

The relationship between the successful Skyrme interaction and the finite range "realistic" effective interactions was elucidated by the Density Matrix Expansion of Negele and Vautherin.[20] A major reason for the simplicity of Skyrme calculations is that the exchange field is local; this is due to the $\delta(r_{12})$ function in the force. A pair of nucleons interacts only when they touch. For a short range interaction it is interesting to expand the off-diagonal $\rho(\underset{\sim}{r},\underset{\sim}{r}')$ in powers of the internucleon separation $\underset{\sim}{s}$: $\underset{\sim}{r} = \underset{\sim}{R} + \underset{\sim}{s}/2$, $\underset{\sim}{r}' = \underset{\sim}{R} - \underset{\sim}{s}/2$. Formally

$$\rho(\underset{\sim}{R} + \frac{\underset{\sim}{s}}{2}, \underset{\sim}{R} - \frac{\underset{\sim}{s}}{2}) = \sum_{\alpha} \left[e^{\underset{\sim}{s} \cdot (\underset{\sim}{\nabla}_1 - \underset{\sim}{\nabla}_2)/2} \phi_\alpha^*(\underset{\sim}{R}_1) \phi_\alpha(\underset{\sim}{R}_2) \right]_{\underset{\sim}{R}_1 = \underset{\sim}{R}_2 = \underset{\sim}{R}} . \tag{4.1}$$

Thinking of a short range interaction suggests that an average over the angles between s and R may be a good approximation; this gives

$$\hat{\rho}(\underset{\sim}{R} + \frac{\underset{\sim}{s}}{2}, \underset{\sim}{R} - \frac{\underset{\sim}{s}}{2}) = \left[\frac{\sinh[\frac{1}{2} \underset{\sim}{s} \cdot (\underset{\sim}{\nabla}_1 - \underset{\sim}{\nabla}_2)]}{\frac{1}{2} \underset{\sim}{s} \cdot (\underset{\sim}{\nabla}_1 - \underset{\sim}{\nabla}_2)} \rho(\underset{\sim}{R}_1, \underset{\sim}{R}_2) \right]_{\underset{\sim}{R}} . \tag{4.2}$$

In any case one can argue that for a time reversed invariant system, there is no term linear in $\underset{\sim}{s}$, so the approximation begins only in order s^2.

Rather than simply expanding this in powers of s^2, Negele and Vautherin looked for a reordering of the terms such that the leading term is the correct result for a uniform system (nuclear matter). The desired result is

$$\hat{\rho}\left(\underset{\sim}{R} + \frac{\underset{\sim}{s}}{2}, \underset{\sim}{R} - \frac{\underset{\sim}{s}}{2}\right) = \frac{1}{sk} \sum_{n=0}^{\infty} (4n+3) j_{2n+1}(sk) Q_n\left[\left(\frac{\underset{\sim}{\nabla}_1 - \underset{\sim}{\nabla}_2}{2k}\right)^2\right] \rho(\underset{\sim}{R}_1 \underset{\sim}{R}_2)_{\underset{\sim}{R}} \tag{4.3}$$

where k is arbitrary, $j_\ell(x)$ is the spherical Bessel function and

$$Q_n(z^2) \equiv \frac{(-)^n}{iz} P_{2n+1}(iz) \text{ is a Legendre polynomial. We will denote}$$

$$(2\ell+1)!! j_\ell(x)/x^\ell = \hat{j}_\ell(x) \approx 1 - \frac{x^2}{2(2\ell+3)} \cdots \tag{4.4}$$

210

The two leading terms of the expansion are then

$$\hat{\rho}(\underset{\sim}{r},\underset{\sim}{r}') \simeq \hat{j}_1(sk)\rho(R) + \frac{1}{6}s^2\,\hat{j}_3(sk)\left[\frac{1}{4}\nabla^2\rho - \tau + \frac{3}{5}k^2\rho\right]_R + \dots \qquad (4.5)$$

In the nuclear matter limit, $\nabla^2\rho$ vanishes and $\tau(R) = \frac{3}{5}k_F^2\rho(R)$ so only the leading term survives, and is the well known Slater approximation to the density matrix. In this case we see that k ought to be chosen as

$$k_F = \left(\frac{3\pi^2}{2}\rho\right)^{1/3}$$

evaluated at the center of mass of the interacting pair. This prescription can be carried over to finite nuclei, though Campi and Bouyssy[21] have recently made a more astute suggestion.

The approximate form for $\rho(\underset{\sim}{r},\underset{\sim}{r}')$, Eq. (4.5) can be substituted into Eq. (2.19) for the expectation value of the total potential energy. In so doing it is consistent to omit the square of the second term because other terms of order s^4 are already neglected. Taking account of spin and isospin degrees of freedom, the like particle and unlike particle components of the effective interaction are formed: these are functions of $r_{12} = s$ and of density:

Direct:
$$V_D^\ell = \frac{1}{4}V^{SE} + \frac{3}{4}V^{TO}$$

$$V_D^u = \frac{3}{8}V^{TE} + \frac{1}{8}V^{SO} + \frac{1}{8}V^{SE} + \frac{3}{8}V^{TO} \qquad (4.6)$$

Exchange:
$$V_E^\ell = \frac{1}{4}V^{SE} - \frac{3}{4}V^{TO}$$

$$V_E^u = \frac{3}{8}V^{TE} - \frac{1}{8}V^{SO} + \frac{1}{8}V^{SE} - \frac{3}{8}V^{TO} \qquad (4.7)$$

Then

$$\langle\psi|V|\psi\rangle = \frac{1}{2}\int d^3r\,d^3r'\,\Big\{[\rho_p(r)\rho_p(r') + \rho_n(r)\rho_n(r')]V_D^\ell(s)$$

$$+ 2\rho_p(r)\rho_n(r')V_D^u(s)$$

$$+ [\hat{\rho}_p^2(R,s) + \hat{\rho}_n^2(R,s)]V_E^\ell(s)$$

$$+ 2\hat{\rho}_p(R,s)\hat{\rho}_n(R,s)V_E^u(s)\Big\} \qquad (4.8)$$

211

In the last two terms I emphasize that $\hat{\rho}$ is a function of the variables $\underset{\sim}{R},\underset{\sim}{s}$. Using (4.5) we expand these two terms as follows

$$
\begin{aligned}
\langle\psi|V|\psi\rangle_{Ex} \simeq \frac{1}{2}\int d^3R\,d^2s\,\Big|\; & \rho_p^2(R)\,\hat{j}_1^2(k_p s)\,v_E^\ell(s) \\
& + \rho_p(R)\rho_n(R)\,\hat{j}_1(k_p s)\,\hat{j}_1(k_n s)\,v_E^u(s) \\
& + \frac{2}{6}\rho_p(r)\,[\tfrac{1}{4}\nabla^2\rho_p(R)-\tau_p(R)+\tfrac{3}{5}k_p^2\rho_p(R)]\,\hat{j}_3(k_p s)\,\hat{j}_1(k_p s)\,s^2 v_E^\ell(s,k_p) \\
& + \frac{2}{6}\rho_p(R)\,[\tfrac{1}{4}\nabla^2\rho_n(R)-\tau_n(R)+\tfrac{3}{5}k_n^2\rho_n(R)]\,\hat{j}_3(k_n s)\,\hat{j}_1(k_p s)\,s^2 v_E^u(s,k_F) \\
& + (p\leftrightarrow n)\;\Big|
\end{aligned}
\tag{4.9}
$$

In these terms we have introduced Fermi momenta for neutrons and protons:

$$
k_q = [3\pi^2\rho_q(R)]^{1/3}
\tag{4.10}
$$

as well as

$$
k_F = \{\tfrac{3\pi^2}{2}[\rho_n(R)+\rho_p(R)]\}^{1/3}
\tag{4.11}
$$

The point is that in Eq. (4.9) the integral over s may be performed first, defining certain functionals of the neutron and proton densities $\rho_p(R)$, $\rho_n(R)$:

$$
\begin{aligned}
\langle\psi|V|\psi\rangle_{Ex} = \frac{1}{2}\int d^3R\,\Big\{ & v_E^{NM}(\rho_n,\rho_p) \\
& + 2[\rho_p(R)G_{LE}(\rho_p)+\rho_n(R)G_{UE}(\rho_n,\rho_p)](\tfrac{1}{4}\nabla^2\rho_p-\tau_p+\tfrac{3}{5}k_p^2\rho_p) \\
& + 2[\rho_n(R)G_{LE}(\rho_n)+\rho_p(R)G_{UE}(\rho_p,\rho_n)](\tfrac{1}{4}\nabla^2\rho_n-\tau_n+\tfrac{3}{5}k_n^2\rho_n)\Big\}
\end{aligned}
\tag{4.12}
$$

where

$$
G_{LE}(\rho_\alpha) = \frac{1}{6}\int d^3s\, s^2\hat{j}_1(k_\alpha s)\,\hat{j}_3(k_\alpha s)\,v_E^\ell(s,k_\alpha)
$$

$$
G_{UE}(\rho_\alpha,\rho_\beta) = \frac{1}{6}\int d^3s\, s^2\hat{j}_1(k_\alpha s)\,\hat{j}_3(k_\beta s)\,v_E^u(s,k_F)
\tag{4.13}
$$

These functions may be calculated once and for all, for a given effective force, and tabulated on a grid $\rho_\alpha = [0.0(0.01)0.17]fm^{-3}$, and values interpolated as required. This form of the energy density is essentially that obtained when using a Skyrme interaction, except that the constants $t_0 t_1 t_2 t_3$, x_0 are replaced by functions of the density which are known numerically. In particular, when we vary $<\psi|V|\psi>_{Ex}$, in the form (4.12) to derive HF equations, a local HF potential will result, plus an effective mass just as obtained for Skyrme interactions. The direct terms in Eq. (4.8) already produce a local Hartree or direct potential, so the DME allows one to avoid the time consuming construction of the non-local Fock potential. Calculations carried out in this way are called DMEX calculations, because the DME has been applied to the exchange field. It has been shown by Negele and Vautherin, and Vallieres et al.[22] that the DMEX is an accurate substitute for a full finite-range HF calculation. The computer codes written originally for use with Skyrme forces have been adapted for DMEX calculations by adding in the calculation of the direct terms.

A further approximation can be made, which makes a similar approximation to the direct part of the potential energy, the initial two terms of Eq. (4.8). The angle average of $\rho_\alpha(r_1)\rho_\beta(r_2)$ is expressed as

$$\frac{1}{4\pi} \int d\Omega_s \; \rho_\alpha(R + \frac{s}{2})\rho_\beta(R - \frac{s}{2}) = \rho_\alpha(R)\rho_\beta(R)$$

$$+ \frac{s^2}{6} \hat{j}_3(sk_F)\left[\frac{1}{4}\nabla^2\rho_\alpha \cdot \rho_\beta + \frac{1}{4}\rho_\alpha\nabla^2\rho_\beta - \frac{1}{2}\nabla\rho_\alpha \cdot \nabla\rho_\beta\right] + \ldots \qquad (4.14)$$

This allows the direct potential energy to be similarly expressed in terms of (numerical) functions of ρ_n, ρ_p. Combining with the exchange terms one has finally for the energy density

$$H(r) = \left[\frac{\hbar^2}{2m} + B(\rho_p, \rho_n)\right]\tau_p + \left[\frac{\hbar^2}{2m} + B(\rho_n, \rho_p)\right]\tau_n$$

$$+ A(\rho_p, \rho_n) + C(\rho_n, \rho_p)|\nabla\rho_n|^2 + C(\rho_p, \rho_n)|\nabla\rho_p|^2$$

$$+ D(\rho_n, \rho_p)\nabla\rho_n \cdot \nabla\rho_p \quad . \qquad (4.15)$$

From this form, HF equations can be deduced that are only very slightly more complex than those of the Skyrme interaction. The same zero range two body spin

213

orbit force may be used as with the finite range effective interaction.

Comparing Eq. (4.15) with (3.7) we can identify the following correspondences

$$A(\rho_n \rho_p) = \frac{1}{2} t_0 \left[(1 + \frac{x_0}{2})\rho^2 - (x_0 + \frac{1}{2}) (\rho_n^2 + \rho_p^2) \right] + \frac{1}{4} t_3 \rho_n \rho_p \rho$$

$$B(\rho_n \rho_p) = \frac{1}{4} (t_1 + t_2)\rho + \frac{1}{8} (t_2 - t_1)\rho_n$$

$$C(\rho_n \rho_p) = \frac{3}{32} (T_1 - t_2)$$

$$D(\rho_n \rho_p) = - \frac{1}{8} (T_2 - 3t_1)$$

The question arises as to what extent the simple density dependence postulated by the Skyrme force can reproduce that of the functions A,B,C,D calculated from a "realistic" effective interaction. Negele and Vautherin made such a comparison for Negele's force,[23] in the neighborhood of the nuclear matter situation $\rho_n = \rho_p = \frac{1}{2} \rho$. In this case

$$A + B\tau + \frac{1}{2} (C + \frac{1}{2} D)|\nabla\rho|^2$$

$$= \frac{3}{8} t_0 \rho^2 + \frac{1}{16} t_3 \rho^3 + \frac{1}{16} (3t_1 + 5t_2)\rho\tau + \frac{1}{64} (9t_1 - 5t_2)|\nabla\rho|^2 \quad .$$

Also, looking at an expansion of A in powers of $\delta\rho = \rho_n - \rho_p$,

$$A[\frac{1}{2}(\rho + \delta\rho), \frac{1}{2}(\rho - \delta\rho)] = A - \frac{1}{4} t_0 (x_0 + \frac{1}{2}) (\delta\rho)^2 - \frac{1}{16} t_3 \rho(\delta\rho)^2$$

allows one to identify x_0. First of all, we see that

$$3t_1 + 5t_2 = 16 \, B/\rho$$

$$9t_1 - 5t_2 = 32C + 16D$$

To identify t_0, t_3 and x_0 we form

$$\Delta = \frac{\partial A}{\partial \rho_n} - \frac{\partial A}{\partial \rho_p} = t_0 (x_0 + \frac{1}{2})\delta\rho + \frac{1}{4} t_3 \, \delta\rho$$

$$\Sigma = \frac{1}{2} \left(\frac{\partial A}{\partial \rho_n} + \frac{\partial A}{\partial \rho_p} \right) = t_0 \cdot \frac{3}{4} \rho + \frac{t_3}{16} [3\rho^2 - (\delta\rho)^2]$$

$$A - \frac{1}{4} \Delta\delta\rho \equiv a = \frac{3}{8} t_0 \rho + \frac{1}{16} t_3 \rho\delta\rho \quad .$$

Solving the last two gives

$$t_3 = \frac{16}{\rho^3} \frac{(\rho\Sigma - 2a)}{\left[1 - (\frac{\delta\rho}{\rho})^2 \right]}$$

$$t_0 = \frac{8}{3\rho^2} \frac{\left[3 - (\frac{\delta\rho}{\rho})^2 \right] - \rho\Sigma}{1 - (\frac{\delta\rho}{\rho})^2}$$

At the symmetry point $\delta\rho = 0$,

$$t_3 \rightarrow \frac{16}{\rho^3} (\rho\Sigma - 2A)$$

$$t_0 \rightarrow \frac{8}{3\rho^2} (3A - \rho\Sigma)$$

$$(\frac{1}{2} + x_0) = \frac{1}{t_0} (\frac{\Delta}{\delta\rho} - \frac{1}{4} t_3) .$$

At $\rho_n = \rho_p = 0.08 \text{ fm}^{-3}$, these formulae give

	t_0	t_1	t_2	t_3	x_0
N-V	-1248.	381.1	15.1	14 542	0.50
S-III	-1128.75	395.0	-95.0	14 000	0.45

which compare rather well with the S-III parameters. Over the range of densities $0.05 < \rho < 0.15$, t_0, t_3 and x_0 vary by about 30%, suggesting suitably chosen constant values of these parameters might work rather well.

Why does the DME method work? The complete DME approximation is only qualitatively correct, but it does provide a justification for the Skyrme-like parameterization of the force. It also shows how more parameters could usefully be added to the Skyrme form. Treiner and Krivine[24] for example, made a simple parameterization of the A, B, C, D functions issuing from the force G-0.

At the next level of complexity, the DMEX approximation seems to be accurate to a few percent for most bulk quantities. This success is ascribed to the short range nature of the effective interaction, which allows the exchange energy density to be parameterized in terms of the local quantities $\rho(R)$, $\underset{\sim}{\nabla}\rho$, $\nabla^2\rho$ and $\tau(R)$. The exact treatment of the direct terms lends stability to the calculation. Many applications of DMEX calculations have been made at Los Alamos by Negele and Rinker.[25]

Recently Campi and Bouyssy[21] have proposed a further simplification of the DME method. Noting that in Eq. (4.5) the parameter k is arbitrary (except for its nuclear matter limit) they propose to choose k so that the second term is always zero:

$$\hat{k}^2 = \frac{5}{3\rho(r)} [\tau(r) - \frac{1}{4} \nabla^2\rho(R)] \quad .$$

Then

$$\hat{\rho}(\underset{\sim}{r},\underset{\sim}{r}') = \hat{j}_1(s\hat{k})\rho(R)$$

has the simple form of the Slater approximation. The parameter $\hat{k}^2$ is called the Local Fermi Momentum. At a given point in a finite nucleus, one wishes to make the infinite nuclear matter density matrix fit as well as possible to the actual $\rho(r,r')$; this is achieved by the choice $\hat{k}$. Suppose for example, returning to Eq. (4.5), we wish to calculate the (approximate) local kinetic energy density. One finds using (2.5) that

$$\hat{\tau}(r) = [\frac{3}{5} k^2\rho(R) + \frac{1}{4} \nabla^2\rho] - [\frac{1}{4} \nabla^2\rho - \tau(R) + \frac{3}{5} k^2\rho(R)]$$

coming from the first and second terms of Eq. (4.5). In the usual DME, $k^2 = k_F^2$, so the role of the correction term in $\hat{j}_3$ is to restore the correct value of the local kinetic energy density. In the Campi Bouyssy approximation the first term is arranged to already equal $\tau(R)$, by virtue of the choice $k \to \hat{k}$, so no correction is required. Rather than a local density approximation, the LFMA treats both $\rho(R)$ and $\tau(R)$ as quantities characterizing the system. This suggests that rather than interpreting the effective interaction $V(r_{12},k_F)$ as a <u>density</u> dependent interaction, one should interpret $k_F \to \hat{k}$ in a finite nucleus, making it an LMF-dependent interaction.

Since $\hat{k}^2$ is a function of ϕ_k, $\nabla\phi_k$ and $\nabla^2\phi_k$, the variational principle will lead to terms of the three types included in (3.11). Hence the Hartree Fock equations deduced will involve an effective mass in the form

$$\frac{1}{4}\left[\frac{\hbar^2}{2m^*}\nabla^2 + 2\nabla\left(\frac{\hbar^2}{2m^*}\nabla \right) + \nabla^2 \frac{\hbar^2}{2m^*} \right] \phi_k(r) \quad .$$

Most of the rearrangement terms end up in this effective mass. Work on such calculations is now in progress. It seems likely that significant differences can arise from previous LDA calculations.

CONCLUSION

I have tried to survey the basic elements of Hartree Fock calculations applied to nuclear structure. The subject has been developing in many directions. Hoodbhoy and Negele[26] have shown how to carry out deformed HF calculations entirely in coordinate space without the necessity of introducing an oscillator basis. With a remarkably coarse grid they have obtained good convergence. This method promises to make more extensive calculations, and large deformations, much easier. Some authors have sought to reduce computing time by giving prescriptions for good starting fields. Sometimes these are based on Thomas Fermi theory. One of the most recent references is Brack;[27] he refers to earlier work. The hope is that a single HF iteration, or a very few, will give an accurate solution. A large amount of work has been done on Time Dependent Hartree Fock calculations, after the pioneering work of Bonche, Koonin and Negele.[28] These promise to give insight into nuclear reactions. As a means of gaining insight into nuclear collective motions, the adiabatic Time Dependent Hartree Fock theory has been devised, principally by Baranger and Veneroni,[29] and by Villars.[30] There is also an interesting development of sum rules related to energy weighted moments of transition operators on the HF ground state. The paper by Goeke, Lane and Martorell[31] gives an introduction to this work. Perhaps this is enough by way of some guideposts for further reading.

To impose the A^2 conditions of orthonormality on the orbitals $\phi_k(r)$ we introduce A^2 Lagrange multipliers $\varepsilon_{k\ell}$, and minimize

$$\langle\psi|H|\psi\rangle - \sum_{k\ell} \varepsilon_{k\ell} (\langle\phi_k|\phi_\ell\rangle - \delta_{k\ell}) \quad .$$

We take $\varepsilon_{k\ell} = \varepsilon_{\ell k}^*$ so the sum is real. The variation $\delta\phi_k^*(R)$ adds to $\langle\delta\psi|H|\psi\rangle$ a sum

$$- \sum_\ell \varepsilon_{k\ell} \phi_\ell(R)$$

which can be transferred to the right hand side. We now argue that the equations may be simplified by taking linear combinations

$$\sum_s U_{ts}\phi_s(r) \equiv \tilde{\phi}_t(r) \quad .$$

If U is unitary, the new states $\tilde{\phi}$ remain orthonormal

$$\phi_s(r) = \sum_t (U^\dagger)_{st}\tilde{\phi}_t(r) \quad .$$

Also

$$\rho(r,r') = \sum_k \phi_k(r)\phi_k^*(r')$$

$$= \sum_{kts} [U_{kt}^\dagger \tilde{\phi}_t(r)][\phi_s^*(r)U_{sk}]$$

$$= \sum_t \tilde{\phi}_t(r)\tilde{\phi}_t^*(r)$$

is invariant. Thus we have, applying U_{sk} to Eq. (2.20)

$$\int h(r,r')\tilde{\phi}_s(r')d^3r' = \sum_{k\ell t} U_{sk} \varepsilon_{k\ell} U_{\ell t}^\dagger \tilde{\phi}_t(r) \quad .$$

The unitary transformation U, so far arbitrary, may be selected to diagonalize the hermitian matrix $\varepsilon_{k\ell}$: $(U\varepsilon U^\dagger)_{st} = \varepsilon_s\delta_{st}$. Then on the right we have just $\varepsilon_s\tilde{\phi}_s(r)$ as stated. We can remove the tilde and call these states the new set $\phi_k(r)$.

ACKNOWLEDGEMENTS

TABLE I

PROPERTIES OF ^{16}O, ^{40}Ca, ^{90}Zr AND ^{208}Pb OBTAINED WITH THE

ORIGINAL (a) AND RENORMALIZED FORCE (b) G-0

	^{16}O		^{40}Ca		^{90}Zr		^{208}Pb	
	a	b	a	b	a	b	a	b
E_{HF}/A	-1.57	-3.71	-1.75	-3.96	-1.39	-3.59	-0.51	-2.61
E_K/A	-1.92	-3.76	-2.52	-4.56	-3.13	-5.27	-3.44	-5.58
E_V/A	-0.70	-0.99	-0.68	-0.95	-0.57	-0.86	-0.44	-0.73
E_{VR}/A	0.34	0.30	0.39	0.31	0.43	0.30	0.45	0.32
E_T/A	-3.62	-7.68	-4.02	-8.33	-4.16	-8.63	-3.50	-7.87
r_a	2.75	2.67	3.39	3.38	4.19	4.28	5.41	5.60
r_p	2.79	2.69	3.46	3.43	4.14	4.21	5.23	5.39
s_p	7.9	12.7	5.5	9.9	3.5	8.4	3.3	9.2
s_n	10.9	15.8	12.0	16.7	9.8	13.2	6.2	8.0

TABLE II

SPHERICAL NUCLEI

PROPERTIES OF CLOSED-SHELL NUCLEI COMPARED TO EXPERIMENT

	^{16}O	^{40}Ca	^{48}Ca	^{90}Zr	^{208}Pb
E_T/A	-7.68	-8.33	-8.40	-8.63	-7.87
$-B_{exp}$	-7.98	-8.55	-8.67	-8.71	-7.87
E/A	-7.07	-8.13	-8.22	-8.55	-7.85
$E_{c.m.}/A$	-0.61	-0.20	-0.18	-0.08	-0.02
r_a	2.67	3.38	3.63	4.28	5.60
r_p	2.69	3.43	3.45	4.21	5.39
r_{ch}	2.75	3.49	3.51	4.27	5.45
$r_{ch\ exp}$	2.73	3.49–3.50	3.48–3.49	4.23–4.30	5.50–5.52
s_p	12.7	9.9	16.0	8.4	9.2
$s_{p\ exp}$	12.1	8.3	15.3	8.4	8.0
s_n	15.8	16.7	10.5	13.2	8.0
$s_{n\ exp}$	15.7	15.6	9.9	12.0	7.4

TABLE III

PARAMETERS OF THE SKYRME INTERACTIONS SII TO SVI

	t_0 (MeV·fm^3)	t_1 (MeV·fm^5)	t_2 (MeV·fm^5)	t_3 (MeV·fm^6)	x_0	W (MeV·fm^5)
SII	-1169.9	586.6	-27.1	9331.1	0.34	105.0
SIII	-1128.75	395.0	95.0	14000.0	0.45	120.0
SIV	-1205.6	765.0	35.0	5000.0	0.05	150.0
SV	-1248.29	970.56	107.22	0.0	-0.17	150.0
SVI	-1101.81	271.67	-138.33	17000.0	0.583	115.0

TABLE IV

DIFFERENCES ΔB_0 BETWEEN SPHERICAL HF AND EXPERIMENTAL

TOTAL BINDING ENERGIES OF MAGIC NUCLEI

	B_{exp} (MeV)	ΔB_0 (MeV)				
		SVI	SIII	SII	SIV	SV
^{16}O	127.62	0.30	0.59	-1.44	0.90	0.45
^{40}Ca	342.06	-1.04	-0.18	-5.60	-0.29	0.93
^{48}Ca	416.01	2.76	2.20	-13.43	3.13	2.25
^{56}Ni	484.01	1.75	-0.37		-4.54	-11.3
^{90}Zr	783.92	-1.33	-1.26	-25.2	-1.83	-3.22
^{140}Ce	1172.70		-0.30		0.60	1.57
^{208}Pb	1636.49	0.62	0.12	-68.6	0.08	0.55

The experimental binding energies are also shown in the first column.
The interactions have been ordered according to the decreasing values
of the parameter t_3.

TABLE V

BINDING ENERGY PER PARTICLE E/A, FERMI MOMENTUM k_F,

INCOMPRESSIBILITY COEFFICIENT K, EFFECTIVE MASS RATIO m^*/m AND

SYMMETRY COEFFICIENTS ε_1 AND ε_2 IN NUCLEAR MATTER CALCULATED

WITH THE INTERACTIONS SII TO SVI

	E/A (MeV)	k_F (fm^{-1})	K (MeV)	m^*/m	ε_1 (MeV)	ε_2 (MeV)
SVI	-15.77	1.29	364	0.95	26.89	0.67
SIII	-15.87	1.29	356	0.76	28.16	0.83
SII	-16.00	1.30	342	0.58	34.2	1.10
SIV	-15.98	1.31	325	0.47	31.22	1.37
SV	-16.06	1.32	306	0.38	32.72	1.70

The interactions have been ordered according to the decreasing
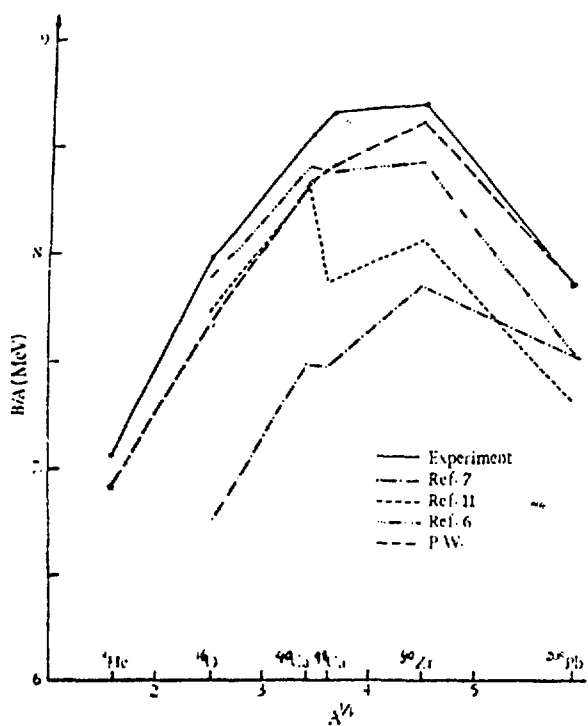values of the parameter t_3.

220

Fig. 1. Energy per particle for dif-
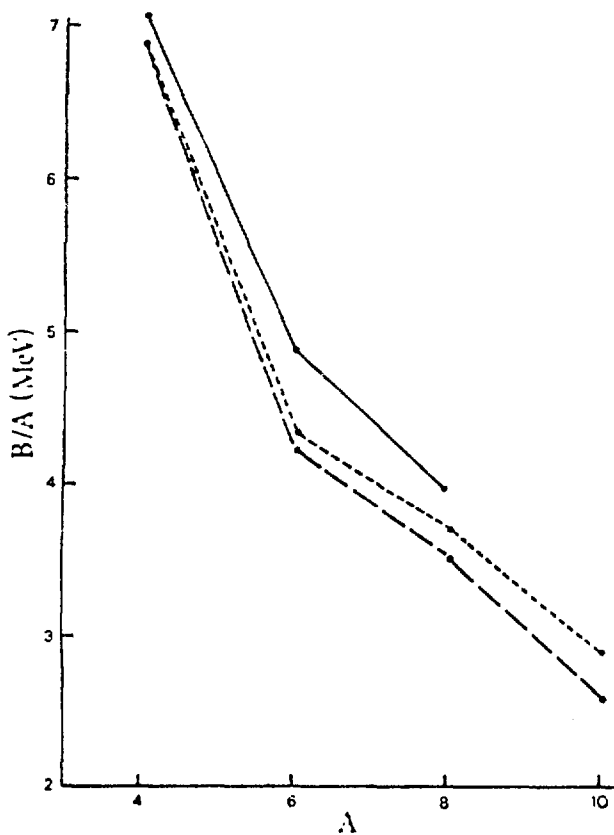ferent calculations using den-
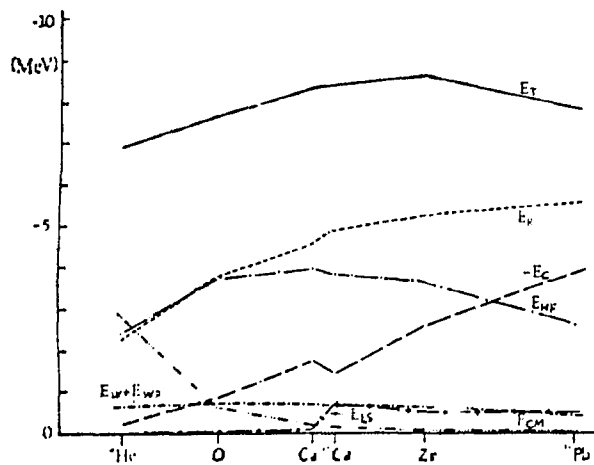sity-dependent forces.

Fig. 2. Contributions to the total
energy per particle as a func-
tion of mass number.

Fig. 3. Binding energy per particle
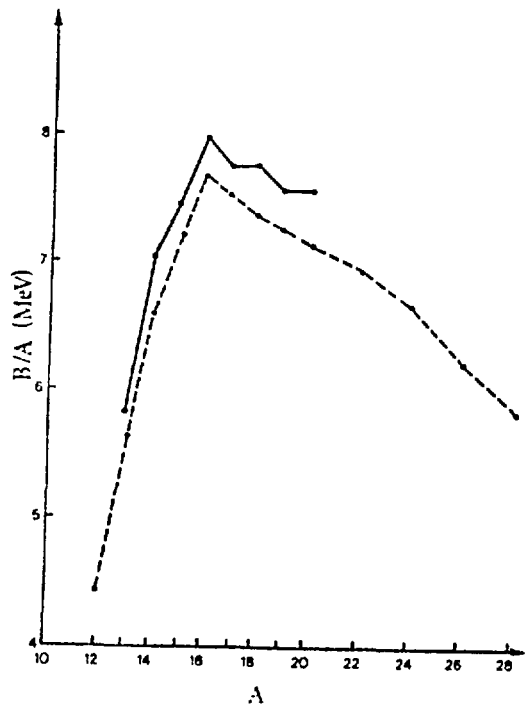for the neutron-rich isotopes
of helium

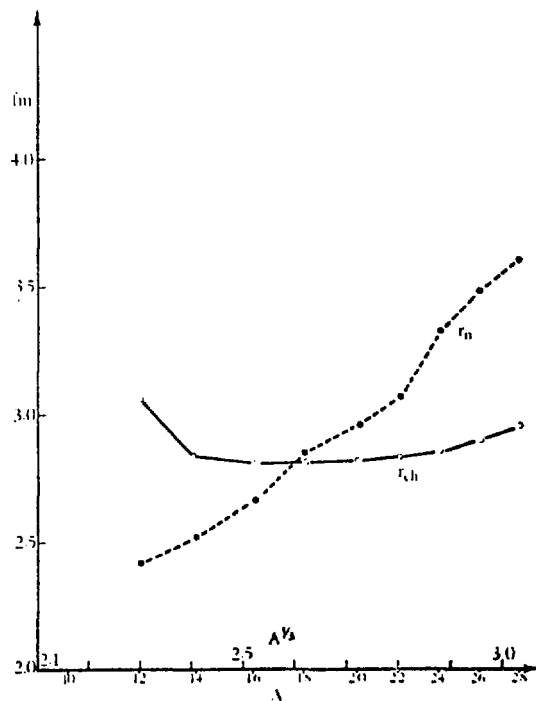Fig. 4. Binding energy per particle for the oxygen isotopes.

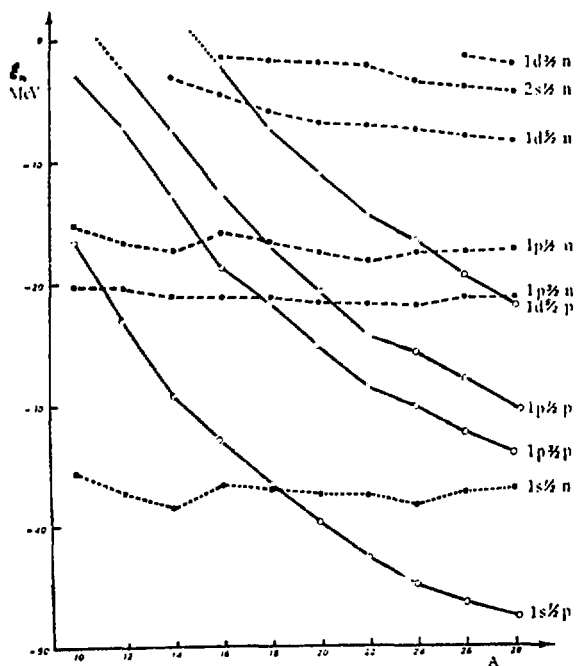

Fig. 6. Neutron and charge radii in the oxygen isotopes.

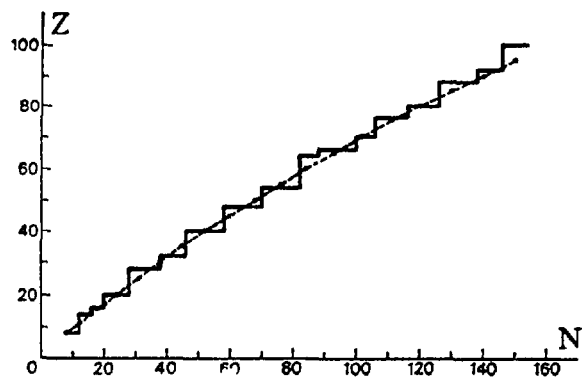Fig. 5. Positions of the single particle levels in the oxygen isotopes.

Fig. 7. Distribution of the calculated nuclei in the (Z,N) plane.
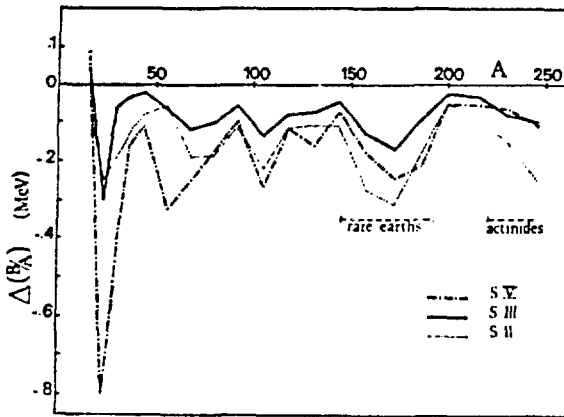
Fig. 8. Differences $\Delta(B/A)$ between spherical HF and experimental binding energies per particle.
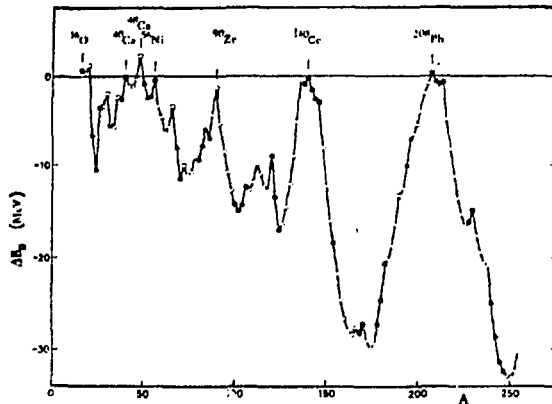
Fig. 9. Differences ΔB_0 between spherical HF (calculated with the force SIII) and experimental total binding energies. The squares indicate doubly closed shell (or subshell) nuclei. Black (white) circles or squares correspond to isotone (isotope) series.
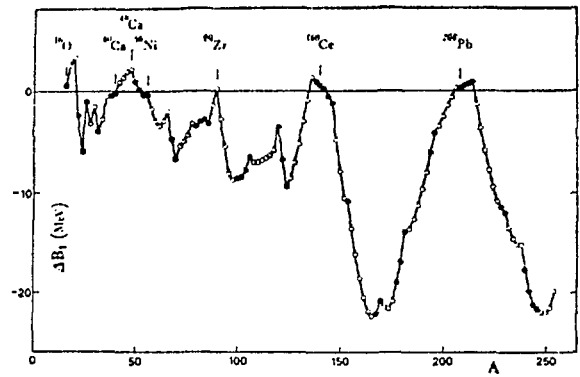
Fig. 10. Differences ΔB_1 between spherical HF+BCS and experimental total binding energies. Series of black and white circles correspond respectively to successive isotones and isotopes. The calculated values correspond to interaction SIII.
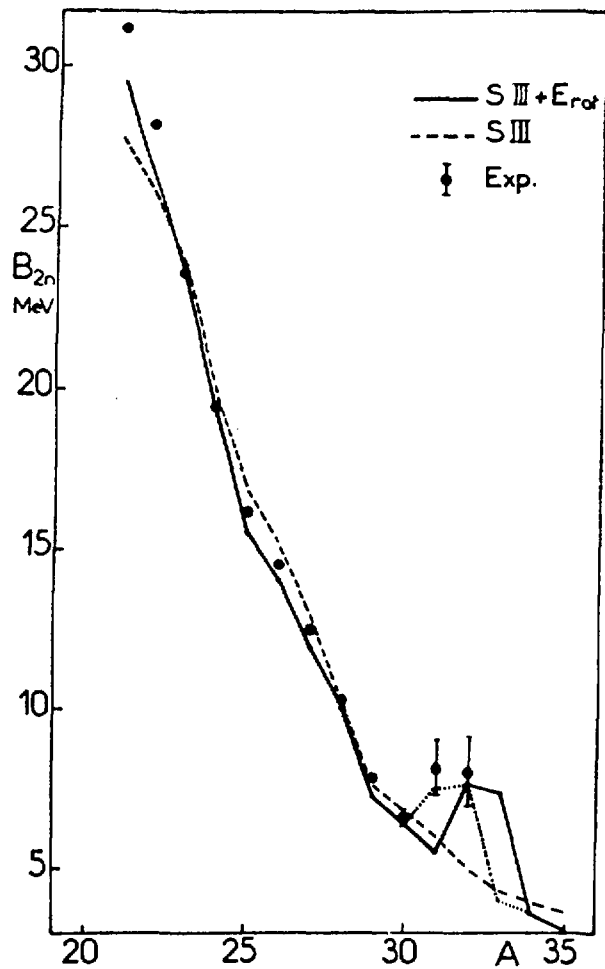
Fig. 11. Experimental and calculated
values of the separation ener-
gies of the last pair of neu-
trons
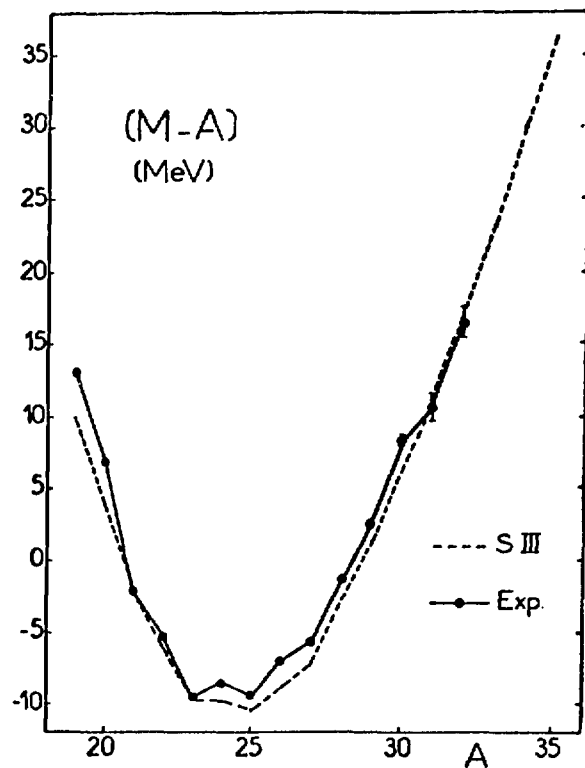
Fig. 12. Experimental and calculated
mass excesses.

REFERENCES

1. J. L. Friar and J. W. Negele, Advances in Nucl. Phys. $\underline{8}$, 219-376 (1975).

2. P. Quentin and H. Flocard, preprint LA-UR-78-1046.

3. K. A. Brueckner, J. L. Gammel and H. Weitzner, Phys. Rev. $\underline{110}$, 431 (1958).

4. X. Campi and D. W. L. Sprung, Nucl. Phys. $\underline{A194}$, 401-442 (1972).

   X. Campi, thèse d'Etat, Univ. de Paris-Sud, Orsay (1973).

5. A. J. Coleman, Revs. Mod. Phys. $\underline{35}$, 668 (1963).

6. M. V. Mihailovic and M. Rosina, Nucl. Phys. $\underline{A237}$, 221-228, 229-234 (1975).
   C. Garrod, M. V. Mihailovic and M. Rosina, J. Math. Phys. (1976).

7. A. B. Volkov, Nucl. Phys. $\underline{74}$, 33 (1965).

8. D. M. Brink and E. Boeker, Nucl. Phys. $\underline{91}$, 1 (1961).

9. D. Vautherin and D. M. Brink, Phys. Rev. $\underline{C5}$, 626-647 (1972).

10. H. A. Bethe and R. Jackiw, "Intermediate Quantum Mechanics," second edition, W. A. Benjamin, New York, Ch. 4 (1968).

11. R. J. Blin-Stoyle, Phil. Mag. $\underline{46}$, 973 (1955).

12. D. Vautherin, Phys. Rev. $\underline{C7}$, 296-316 (1973).

13. X. Campi, D. W. L. Sprung and J. Martorell, Nucl. Phys. $\underline{A223}$, 541-562 (1974).

14. M. Beiner, H. Flocard, N. Van Giai, P. Quentin, Nucl. Phys. $\underline{A238}$, 29-39 (1975).

15. H. Flocard and P. Quentin (1975), reported in thesis of H. Flocard.

16. X. Campi, H. Flocard, A. K. Kerman and S. Koonin, Nucl. Phys. $\underline{A251}$, 193-205 (1975).

17. H. Flocard, P. Quentin and D. Vautherin, Phys. Lett. $\underline{46B}$, 304-308 (1973).

18. G. Fonte and G. Schiffrer, Nucl. Phys. $\underline{A259}$, 20-28 (1976).

19. W. H. Bassichis, M. R. Strayer, and M. T. Vaughan, Nucl. Phys. $\underline{A263}$, 378-389 (1976).

20. J. W. Negele and D. Vautherin, Phys. Rev. $\underline{C5}$, 1472-1493 (1972).

21. X. Campi and A. Bouyssy, Phys. Lett. $\underline{73B}$, 263-267 (1978).

22. D. W. L. Sprung, M. Vallieres, X. Campi and C. M. Ko, Nucl. Phys. $\underline{A253}$, 1-14 (1975).

225

23. J. W. Negele, Phys. Rev. $\underline{C1}$, 1260-1320 (1970).

24. J. Treiner and H. Krivine, J. Phys. G. (Nucl. Phys.) $\underline{2}$, 285-307 (1976).

25. J. W. Negele and G. Rinker, Phys. Rev. $\underline{C15}$, 1499-1514 (1977).

26. P. Hoodbhoy and J. W. Negele, Nucl. Phys. $\underline{A298}$, 23-44 (1977).

27. M. Brack, Phys. Lett. $\underline{71B}$, 239-242 (1977).

28. P. Bonche, S. Koonin and J. W. Negele, Phys. Rev. $\underline{C13}$, 1226-1258 (1976).

29. M. Baranger and M. Veneroni, submitted to Annals of Physics.

30. F. M. H. Villars, Nucl. Phys. $\underline{A285}$, 269-296 (1977).

31. K. Goeke, A. M. Lane and J. Martorell, Nucl. Phys. $\underline{A296}$, 109-133 (1978).

32. H. Flocard, P. Quentin, A. K. Kerman and D. Vautherin, Nucl. Phys. $\underline{A203}$, 433-472 (1973).

GIANT MULTIPOLE RESONANCES FROM HADRON AND HEAVY-ION INELASTIC SCATTERING[*]

by

D. H. Youngblood

Texas A&M University
College Station, TX

INTRODUCTION

In this talk I will first describe the multipole resonances, then give a brief summary of the state of experimental knowledge (primarily of the quadrupole state) 1 to 2 years ago; there is a review article available[1] which describes this. I will present several specific results regarding the quadrupole which seem interesting, and discuss recent experimental work on the low energy octupole resonance. Next I shall present recent convincing evidence for the breathing mode state in several nuclei and the implications for the nuclear compressibility. I will conclude with existing evidence for excitation of these modes in heavy-ion inelastic scattering.

It is useful to describe the basic oscillations of the nucleus which result in the various giant multipole resonances. These modes of oscillation[2] are illustrated from the view of the hydrodynamic model in Fig. 1 for electric resonances. The monopole mode is a spherically symmetric oscillation of the nuclear density; it is the only mode that is primarily a volume oscillation of the nucleus. Its energy is directly related to the nuclear compressibility, and its existence has been conclusively established only very recently. The isovector dipole mode is an oscillation of the proton and neutron distributions against one another, and has been studied most extensively of all the modes. The quadrupole and higher modes are shape oscillations; there have been extensive studies of the isoscalar quadrupole mode in the last several years, and some interesting features of the isoscalar octupole mode have been revealed. There is little evidence for multipole resonances of still higher order.

These resonances in the simplest shell model picture are coherent 1p-1h excitations and are illustrated in Fig. 2. The monopole is a $2\hbar\omega$ excitation, while the dipole is a $1\hbar\omega$ excitation. A quadrupole can be both $0\hbar\omega$ (within a shell and responsible for low lying 2^+ states) and $2\hbar\omega$. The octupole strength is split between $1\hbar\omega$ and $3\hbar\omega$ excitations. Except for the dipole mode, both isoscalar (neutrons and protons in phase) and isovector (neutrons and protons out of phase) modes can occur; the isoscalar modes will be somewhat below and the isovector modes somewhat above the nominal energy due to the nature of the residual interaction.

The experimental problem in studying these modes is illustrated in Fig. 3 where the positions of these low-order modes are schematically illustrated. The E0 and E2 isoscalar modes occur in the vicinity of the E1 mode; all have large natural widths and overlap so that experiments must be chosen carefully to select the components of interest. The $1\hbar\omega$ E3 strength lies in a region of high level density (close to the particle threshold in many nuclei) while the $3\hbar\omega$ E3 strength and isovector E0 and E2 strength lie further in the continuum and consequently would be much broader and more difficult to isolate.

Several different reactions are available to study these modes. Photonuclear reactions (and their inverse) have detailed the giant dipole resonance (GDR) thoroughly, but E1 excitation dominates all other multipolarities, restricting their usefulness when studying other modes. Inelastic electron scattering can be used to study the lower multipolarities nicely, and has the advantage that the interaction is known, but the disadvantage that isoscalar and isovector modes are excited with comparable strengths, preventing isolation of certain modes. Inelastic proton and ^{3}He scattering may also excite both $\Delta T = 0$ and $\Delta T = 1$ modes, although experimental evidence indicates that the $\Delta T = 1$ mode is excited at most very weakly. Inelastic deuteron and alpha scattering excite to first order $\Delta T = 0$ modes only, making them very useful tools for studying these modes. Of the existing hadron data, inelastic alpha scattering has the most easily defined background and the best peak to continuum ratios. Also DWBA calculations seem less model dependent and hence more useful for L assignments and strength determinations than for other projectiles.

Inelastic scattering strengths are characterized by the surface deformation parameter β, obtained by comparing the experimental cross-sections with DWBA calculations using a deformed optical potential for the form factor. β can be directly related to B(EL) values and if $\beta_m R_m = \beta_z R_z$ (m refers to the matter

228

distribution and z refers to the charge distribution) the B(EL) values obtained by inelastic α scattering are directly comparable to electromagnetic values. Strengths are then generally expressed in terms of the fraction of the energy weighted sum rule (EWSR) which for $L \geq 2$ is given by

$$S(EL) = \Sigma(E_n - E_0) \, B(EL) = \ell(\ell + 1) \, \frac{h^2}{2mR^2} \, \frac{4 \, z^2}{3A^2}$$

The techniques for doing calculations for giant resonances have been covered by Satchler,[3] while the relationships between inelastic scattering and electromagnetic B(EL) values is discussed thoroughly be Bernstein.[4]

THE GIANT QUADRUPOLE RESONANCE

The giant dipole resonance has been extensively studied in the 30 years since its discovery, primarily by photonuclear reactions, and I shall not discuss it. Since the discovery of what has since been proven to be the giant quadrupole resonance (GQR) in 1971 by inelastic electron scattering[5] and inelastic proton scattering[6] its properties in many nuclei have been obtained. In addition to these works the GQR has been studied with inelastic deuteron, ^{3}He and (very extensively) α particle scattering.[1] Figure 4 shows inelastic α particle spectra obtained[7] at Texas A&M on 27 nuclei from ^{14}N to ^{208}Pb. The arrow marks the position where the GQR would be expected[8] to occur, and for all nuclei studied with $A \geq 36$ a prominent broad peak is apparent residing on the continuum. Angular distributions obtained are generally best described if the peak is assumed to be primarily E2 in character. Plots of excitation energy and EWSR strength are shown in Fig. 5 and it is readily apparent that a large portion of the isoscalar E2 sum rule strength is located near $E_x \sim 63/A^{1/3}$ MeV for the heavier nuclei. The strength decreases for the lighter nuclei and no definite E2 strength was identified in the Texas A&M work below $A \simeq 36$, however subsequent inelastic α scattering experiments at higher bombarding energies have identified the GQR in many light nuclei. The reason the GQR was not seen in the Texas A&M work (done at E_α = 96 MeV) is apparent in the spectra shown in Fig. 6 obtained at Jülich[9] at 106, 145, and 173 MeV. At the lower energy broad α groups from break-up of ^{5}Li and ^{5}He formed in the (α, ^{5}Li) and (α, ^{5}He) reactions are immediately adjacent to the GQR, obscuring the peak. Additionally, although the continuum cross-sections are nearly the same at both energies, the GQR cross-section increases

rapidly as the bombarding energy increases, making it much more apparent. This is illustrated in Fig. 7 where DWBA calculations[10] for the cross-section at the second maximum in the angular distribution of the GQR and the 1.37 MeV 2^+ state in ^{24}Mg are shown as a function of bombarding energy. The cross-section for the GQR more than doubles going from 100 to 150 MeV due to the large angular momentum mismatch, whereas that for the 1.37 MeV state increases only $\sim 20\%$. Thus it is apparent that higher bombarding energies are desirable for studying the GQR.

Several interesting features of the GQR are apparent. In the heavier nuclei ($A \gtrsim 60$) it appears to be highly collective with most of the EWSR concentrated in one state, whereas in the light nuclei the GQR contains considerable structure. In Fig. 8 the behavior of the GQR as one goes from ^{90}Zr to ^{24}Mg is illustrated.[10] When viewed with about 150 keV energy resolution the GQR in ^{90}Zr appears as a single Gaussian or lorentzian-like peak with a width of about 4.5 MeV; in ^{40}Ca there are components at $\sim$ 18 MeV ($\Gamma \sim 3.5$ MeV, S $\approx$ 43%) and $\sim$ 14 MeV ($\Gamma \sim 2$ MeV, S $\approx$ 9%); in ^{28}Si and ^{24}Mg it appears as a grouping of discrete almost resolved states. Spectra obtained at Jülich for nitrogen and oxygen isotopes are shown in Fig. 9. A concentration of E2 strength is apparent in each of the nuclei, although the relatively poor energy resolution hides much of the structure. I will now consider several light nuclei for which particularly interesting results are apparent.

^{16}O

The GQR in ^{16}O has been studied primarily by two groups. At Groningen[11] 104 MeV alpha scattering with 100 keV resolution has defined the structure and identified 45% of the E2 EWSR in discrete states between 15 to 26 MeV. In Jülich-Heidelberg collaborations[12] the gross-structure was obtained (Fig. 9) with 300 to 500 keV resolution and the alpha and proton decay of the GQR were measured[13] in coincidence experiments, both performed at $E_\alpha = 155$ MeV. This fractionation into many states spread over many MeV has been qualitatively explained by Dehesa et al.[14] as follows. The ^{16}O GQR would have 1p-1h configurations involving primarily tne $f_{7/2}$, $f_{5/2}$, $p_{3/2}$, and $p_{1/2}$ single particle levels. These levels are well into the continuum, however, and the theoretical widths for the $f_{5/2}$, $p_{3/2}$, and $p_{1/2}$ resonances are very large; hence they would contribute only to the broad background. The narrow part of the GQR would mainly be the $(f_{7/2} \, p_{3/2}^{-1})$ configuration and the observed broadening and structure would be due to the fragmentation of the $f_{7/2}$ resonance.

230

This explanation is supported by the ^{16}O GQR decay studies,[13] where decay α particles and protons were detected in coincidence with inelastically scattered α particles. Figure 10 shows inelastic α spectra obtained in coincidence with decay α's and protons. Essentially no proton decay is observed. The $p_{1/2}$ ^{15}N ground state could be reached only by decay of the $(f_{5/2} \ p_{1/2}^{-1})$ configuration, while the penetrability severely inhibits f wave proton decay to the 6 MeV $p_{3/2}$ state in ^{15}N. It is apparent that there is substantial α decay of the GQR and the well established 18.4 MeV L = 2 state is quite apparent. However, this pair of angles is near the peak for quasifree scattering of incoming α particles off of α clusters in ^{16}O and this process can also contribute broad peaking in the region corresponding to 15 to 40 MeV excitation in ^{16}O. The angular correlation for decay α particles is shown in Fig. 11 and is in agreement with plane wave L = 2 predictions. The angular correlation for the GQR decay should have a similar peak 180° from the one observed, but there the quasifree component will be absent so that the amount of quasifree scattering present can be determined by completing the correlation. Nevertheless the observed decay to the ^{12}C ground state is in rough agreement with the observed ^{12}C (α, γ) E2 strength both as to shape and magnitude, suggesting that inelastic α scattering and (α, γ) are in agreement for the ^{16}O GQR. The large α decay is consistent with the predictions of Kurath and Towner[15] who show that a 1p-1h excitation of the ground state does not alter the α cluster structure of the state. As the ^{16}O$_{g.s}$ is well known to have a significant overlap with ^{12}C$_{g.s}$ the 1p-1h GQR would also be expected to have a large overlap with ^{12}C$_{g.s}$ + α, as is observed.

^{24}Mg

The GQR in ^{24}Mg has been investigated by α scattering at Jülich,[9] Texas A&M[10] and Groningen[16] and as is apparent in Fig. 8, the strength is quite fragmented. Some interesting results are obtained by the Groningen group by a comparison of the ^{24}Mg (α, α') and ^{20}Ne (α, γ) ^{24}Mg[17] leading to 2^+ states. The results of both reactions for the GR region are shown in Fig. 12. While it is clear that all the states seen in the (α, γ) are also seen in (α, α'), the inverse is not true. There is considerable E2 strength observed in (α, α') that is not apparent in the capture work. The EWSR fractions obtained from the inelastic scattering and capture reaction are approximately equal for both the 12.8 and 13.1 MeV 2^+ states, suggesting that $\Gamma_{\alpha_0}/\Gamma_{total}$ for these states is close to unity. Comparing the capture and

inelastic scattering yields for the other 2^+ states, however shows that $\Gamma_{\alpha_0}/\Gamma_{total}$ varies from 0.15 to 0.5 for states observed in both experiments. It is clear that one cannot assume that the decay is purely statistical, which predicts at most 0.1 for this ratio. Essentially all of the isoscalar E2 strength is now known in ^{24}Mg; below 15 MeV about 45% of the E2 EWSR is known in discrete states, and between 15 to 25 MeV Groningen finds $(60 \pm 15\%)$ of the $\Delta T = 0$ E2 EWSR.

The Groningen group also compared the ^{24}Mg (α, α') to ^{24}Mg (p,p') data taken at Oak Ridge.[1] As can be seen in Fig. 12 all of the structure seen in the GR region by (p,p') is also seen by (α, α'), implying that it is isoscalar structure. Similar results were obtained for ^{28}Si,[18] although for both cases calculations indicate that the GDR should contribute significantly in this region, suggesting that the existing estimates for GDR excitation by inelastic proton scattering are too large.

^{40}Ca

An inelastic α spectrum of the GR region of ^{40}Ca is shown in Fig. 13 after subtraction of the continuum. The angular distributions for the 14 and 18 MeV groups are also shown and are fit well by DWBA calculations for L = 2 transfer. The 18 MeV group exhausts about 43% of the $\Delta T = 0$ E2 EWSR whereas the 14 MeV group contains only about 9% of the EWSR strength. Structure is apparent in both components, and a comparison of peak shapes at different angles suggests some other multipoles also contribute to the 14 MeV group. The 18 MeV group appears to consist of 2 or 3 broad components while the 14 MeV group has several narrow components.

The α particle and proton decay of the ^{40}Ca GQR after excitation by inelastic alpha scattering has been studied[19] and the results are intriguing. The 14 MeV and 18 MeV groups have very different decay properties as is illustrated in Fig. 14. The 14 MeV group is apparent in coincidence with decay α particles, but the 18 MeV group is very weak, if present at all. There is a strong proton decay of the 18 MeV group, however, with only weak proton decay of the 14 MeV group apparent. Angular correlations for proton decay of the 18 MeV group to the ground and first excited states of ^{39}K are shown in Fig. 15, along with DWBA predictions for the different partial waves expected to contribute. The correlations for decay to both states are quite consistent with the expected dominant configurations of the GQR [$(g_{7/2}\ d_{3/2}^{-1})$ for the ground state and $(d_{5/2}\ s_{1/2}^{-1})$ for the

first excited state]. The proton branching to higher levels in [39]K is consider-
ably stronger than might be expected from the relatively simple GQR wave function,
suggesting that the GQR frequently decays into more complicated configurations
before particle emission. The angular correlation for the ground state α decay
of the 14 MeV group is also shown in Fig. 16 and is fit excellently by an L = 2
DWBA calculation, further confirming the 2^+ character of the group. The large
ground state α decay ($\Gamma_{\alpha_0}/\Gamma_{total}$ = 0.9 ± 0.2) suggests its character must be
quite different from the major part of the GQR; this is not at all understood as
far as I know.

[208]Pb

The GR region in [208]Pb has been studied extensively by inelastic electron,[20]
proton,[1] and alpha[7,21,22] scattering. It is of particular interest because of
the large amount of structure present. Additionally Halbert et al.[23] have pre-
dicted considerable contribution from multipolarities other than E2 in the
region of the GQR. The GR peak is now known to consist of at least two broad
components, one centered at about 11 MeV containing predominantly quadrupole
strength, and one centered at about 13.7 MeV containing predominantly monopole
strength (I shall discuss this component extensively later). In addition, as is
illustrated in Fig. 16, a broad group at 8.9 MeV and fine structure superimposed
on the 11 MeV group is seen in (e,e') data which has variously been interpreted
as either isoscalar or isovector E2 strength. Also shown is a [208]Pb (α,α')
spectrum taken at 7°, where the E2 and E0 groups are quite weak. Considerable
structure is apparent in this data also and a detailed comparison with (e,e')
suggests that much of the same structure is being observed. (α,α') angular dis-
tributions for two of these states are shown in Fig. 17, where it is readily
apparent that they must be negative parity states (either 1^- or 3^-). This is
consistent with the relative strength of the fine structure and the underlying
GQR, as the fine structure is becoming stronger where the GQR is at a minimum.
Thus it is unlikely that the structure seen in (α,α') is L = 2; good statistics
data for the small angles where one could easily distinguish L = 1 from L = 3 is
not yet available, however. Thus we have a conflict between inelastic α and
electron scattering at the moment.

The RPA calculations of Speth et al.[24] have suggested the existence of con-
siderable 4^+ strength in the vicinity of the [208]Pb GQR. DWBA calculations

utilizing inelastic scattering form factors generated from the RPA wave functions have predicted that only about half the (α,α') strength in the region is 2^+ with the remainder primarily 0^+ and 4^+. Figure 18 shows two analyses of the 11 MeV group in ^{208}Pb with somewhat different background criteria. Superimposed are DWBA predictions for L = 2 + L = 4; it is apparent that the observed distribution is consistent with a small amount of E4 contribution in the region, although uncertainties in subtraction of the continuum prevent a definitive determination of the amount.

THE DEFORMED NUCLEI

A comparison[7] of GR peaks for the ^{144,148,154}Sm isotopes is shown in Fig. 19 and it is immediately apparent that the width increases as one goes from the spherical ^{144}Sm to soft ^{148}Sm and then to deformed ^{154}Sm. Accounting for the recently discovered monopole resonance which is unresolved from the GQR, the width of the GQR increases from $\Gamma \approx 2.6$ MeV in ^{144}Sm to $\Gamma \approx 4.5$ MeV in ^{154}Sm. This is significantly less than the 4 MeV splitting observed for the GDR and the total 6 MeV splitting between the K = 0 and 2 components obtained from a simple estimate[25] utilizing the usual QQ interaction. However, a rigorous application of self-consistency to the coupling of the quadrupole mode leads to a modified QQ interaction which reduces the splitting to about 2 MeV between the K = 0 and 2 components consistent with the observed broadening. G. Kyrchev et al.[26] have performed microscopic calculations considering isoscalar and isovector 2^+ strength simultaneously for many even-even deformed nuclei from ^{150}Nd to ^{246}Cm. The width and position they obtain for the GQR in ^{154}Sm (Γ = 4.5 MeV, E_x = 12.3 MeV) are in excellent agreement with our experimental values ($\Gamma \approx 4.5$ MeV, E_x = 12.2 MeV). Zawischa and Speth[27] have performed RPA calculations for several deformed nuclei (although not for ^{154}Sm) and also obtain widths generally around 4 to 6 MeV.

In the other region of deformed nuclei (the sd shell) there is evidence of splitting of the GQR due to the deformation. In the inelastic α scattering experiments of Knöpfle et al.[28] the E2 strength in ^{20}Ne (Fig. 20) was observed to be split into two distinct components, one centered at $E_x \sim 22$ MeV containing $\sim 35\%$ of the EWSR and the other at $E_x \sim 14.5$ MeV containing about 20% of the EWSR. W. Knüpfer et al.[29] using an excited core model have obtained predictions in agreement with experiment (Fig. 10). The GR excitations of a ^{16}O core were

coupled with excitations of valence nucleons. Similar results were obtained studying the effects of coupled monopole, β and γ quadrupole vibrations within the GCM by Abgrall et al.[30]

THE LOW ENERGY OCTUPOLE RESONANCE (LEOR)

In inelastic α spectra taken at Texas A&M while studying the GQR, a prominent group of states was observed[31] at an excitation energy considerably below the GQR which was out of phase with it. This is illustrated for many nuclei in Fig. 21. This structure is centered at $E_x \sim 32/A^{1/3}$ MeV and the angular distributions are fit nicely by L = 3 calculations (Fig. 22) exhausting 6 to 23% of the $\Delta T = 0$ E3 EWSR. This collection of strength is notably absent in ^{40}Ca and ^{208}Pb, and is observed to be quite weak in several other nuclei. The observed properties of the LEOR are summarized in Table I.

TABLE I

PROPERTIES OF LEOR FROM INELASTIC ALPHA

SCATTERING AT TEXAS A&M

Nucleus	E_x (MeV)	G_3 (SPU)	S %EWSR
^{66}Zn	6.6	10	16
^{75}As	$\sim$6.5	$\sim$ 9	$\sim$14
^{89}Y	7.1	$\sim$13	$\sim$20
^{90}Zr	7.2	14	20
^{92}Mo	6.7	16	22
^{96}Mo	6.2	$\sim$ 6	$\sim$ 8
^{100}Mo	6.1	$\sim$ 5	$\sim$ 6
^{Nat}Ag	6.4		$\sim$20
^{116}Sn	6.5	17	23
^{118}Sn	6.9	$\sim$14	$\sim$20
^{124}Sn	6.2	13	20
^{142}Nd	6.2	17	22
^{144}Sm	6.5	17	21
^{154}Sm	3.7	9.9	8.1
	5.7	3.2	3.8
^{197}Au	4.1	22	19

In the harmonic oscillator-based schematic model of giant resonances the octupole EWSR strength is divided into two parts, roughly corresponding to $3\hbar\omega$ and $1\hbar\omega$ strength. The LEOR is in good accord with the expected properties of the $1\hbar\omega$ giant resonance and exhausts roughly 2/3 of its expected strength (30 to 40% of the total EWSR in the schematic model). The absence of a strong LEOR in ^{208}Pb and ^{40}Ca cannot be understood in terms of such a simple model, however. Indeed the presence of two strong collective 3^- states (the first 3^- and the LEOR) in the region between ^{66}Zn and ^{154}Sm requires a more sophisticated theory. In Fig. 23 we compare RPA calculations of Liu and Brown[32] to the present data for 3^- strength in ^{40}Ca, ^{90}Zr, and ^{208}Pb. The calculations employed a residual interaction of the Skyrme type. The agreement for ^{90}Zr is excellent; the theory

correctly predicts both the location and strength of the LEOR. The excitation energy of the lowest 3^- state is, however, only half of the experimental value. In ^{40}Ca and ^{208}Pb a rather weak LEOR is indicated theoretically which is very suggestive of the experimentally observed absence of a strong resonance. In these two nuclei the exceptionally strong low-lying 3^- state already exhausts a large part of the $1\hbar\omega$ octupole strength.

To see whether the RPA can correctly account for the gross properties of the LEOR and low-lying 3^- states in other nuclei, we have performed calculations for ^{40}Ca, ^{58}Ni, ^{66}Zn, ^{116}Sn, ^{142}Nd, ^{197}Au, and ^{208}Pb. The code, written by T. Kishimoto, employs a Nilsson-type harmonic oscillator potential and an octupole-octupole residual interaction. The strength of the interaction was chosen by requiring the calculation to correctly reproduce the excitation energy of the first 3^- state in each nucleus. Figure 24 shows the results of the calculations compared to the LEOR data. The marked decrease in strength of the LEOR in ^{208}Pb and ^{58}Ni is extremely well reproduced.

The balance of EWSR strength between the LEOR and the low-lying 3^- state can vary substantially over a small change in A, but the total $1\hbar\omega$ strength remains rather constant. The partitioning of the octupole strength, correctly predicted by the RPA, is the result of spin-orbit splitting of the unperturbed octupole response function. The balance between these two solutions of the RPA equation depends largely on the initial strength associated with the low-energy configurations. If the low-energy configurations contain much initial strength, as is the case in ^{40}Ca and ^{208}Pb where both protons and neutrons can contribute, the low-lying 3^- is favored. In the mass region between A = 66 and A = 148 there is typically either a low-energy neutron (near Z = 50) or proton configuration (near N = 50 or 82) but not both.

The effect of quadrupole deformation on the LEOR in the samarium isotopes is large and reminiscent of the behavior of the GDR. In ^{144}Sm and ^{148}Sm the LEOR strength is contained in one peak (with fine structure in the case of ^{144}Sm) at $E_x \sim 6.5$ MeV. In deformed ^{154}Sm two octupole peaks are seen at $E_x = 5.7$ MeV and 3.7 MeV. The lower of these states has a width $\Gamma \sim 2$ MeV compared to $\Gamma \sim 1$ MeV for the upper state. This suggests that the lower peak may contain at least two of the four expected components of an octupole vibration of an axially symmetric quadrupole deformed nucleus (with angular momentum projections K = 0^- through 3^-).

Two theoretical models have been advanced to explain the structure of the LEOR in deformed nuclei. One, due to Malov et al.,[33] is based on a continuum RPA treatment. The other, by Kishimoto,[34] is an extension of the work of Ref. 25 to the octupole case. A central feature of the latter model is a renormalization of the 0-0 residual interaction which arises from the requirement that the interaction be self consistent. The data is presently sufficiently poor that no choice between them can be made.

The nuclei ^{75}As, ^{96}Mo, and ^{100}Mo also exhibit a weakening of the LEOR which is likely due to an octupole-quadrupole coupling effect. The peak cross section for the molybdenum isotopes 92, 96, and 100 are respectively 20 mb/sr, 7 mb/sr, and 6 mb/sr. The magnitude of the continuum in ^{96}Mo and ^{100}Mo prevents one from drawing any firm conclusion about the quantitative nature of this process; the resonance may be weaker or merely broader than in ^{92}Mo. Our RPA calculations for these three isotopes using a residual interaction derived from the first 3$^-$ in ^{92}Mo indicate that the observed weakening is not primarily a simple shell model effect.

THE ISOSCALAR BREATHING MODE STATE

The possible existence of an isoscalar breathing mode state in nuclei has been the subject of considerable experimental interest in recent years. The isoscalar giant resonance (GR) observed by inelastic scattering at an excitation energy of $\sim$60/$A^{1/3}$ MeV in many nuclei was a possible candidate but has been considered to be predominantly quadrupole.[1] A high resolution study[35] of ^{208}Pb (p,p') and (^{3}He,^{3}He') has located a peak at 9.11 MeV in ^{208}Pb which depletes 7% of the E0 T = 0 EWSR; the rest of the strength was not identified.

The Sendai group has presented an interpretation of their electron-scattering data[36] on ^{90}Zr and ^{208}Pb which suggests that the breathing mode state may be located at an energy very close to the GDR, however, this interpretation is critically dependent upon the model chosen for excitation of the GDR, whose contribution must be subtracted from the data. Marty et al.[37] have suggested that differences in their inelastic deuteron data and our inelastic alpha spectra might be due to a breathing-mode state located just above the GQR in ^{40}Ca, the dashed line in Fig. 27. For ^{208}Pb considerable fine structure was apparent on the GR peaks and fits consisting of four narrow Gaussian components plus two broad Gaussian components generally were necessary. For ^{90}Zr and ^{144}Sm no fine

structure was apparent so fits were restricted to two broad components. Excerpts from ^{144}Sm spectra after subtraction of the continuum are shown in Fig. 29 with sample two-peak fits. The angular distribution obtained for the broad components for both ^{144}Sm and ^{208}Pb at E_α = 96 MeV are also shown in Fig. 29. The predictions for a monopole state, the isovector dipole state and a quadrupole state are shown superimposed on the data. It is readily seen that the lower excitation component is relatively well fit by the quadrupole calculation, while the higher excitation component is fit adequately by the monopole calculation. In particular, the predicted signature of a monopole state, a sharp minimum around 4°, is very apparent in the data for the higher excitation component for both nuclei, while no such dip exists in the data for the lower excitation component. The prediction for the GDR is out of phase with the observed data. Excerpts from ^{90}Zr spectra are shown along with angular distributions for the two components in Fig. 30. Again the lower excitation component is well described as E2 while the upper component appears to be E0. The parameters obtained for the monopole peaks are summarized in Table II.

TABLE II

PARAMETERS OF MONOPOLE PEAKS OBTAINED IN DIFFERENT REACTIONS

Nucleus	E_x (MeV)	Γ (MeV)	%EWSR	K_N (MeV)	Reference
^{90}Zr	17	∿1.8	34 ± 17	183	Texas A&M
	17.5				37
	17	4	(108)		36
^{144}Sm	15.1 ± 0.5	2.9 ± 0.5	100 ± 50	197	22
	14.8 ± 0.2	2.4 ± 0.15	20 ± 10		38
	∿15		60 - 100		1*
^{208}Pb	13.7 ± 0.4	3.0 ± 0.5	105 ± 50	208	22
	13.5				37
	13.5		97^{+27}_{-14}	10^{+20}_{-9}	36
	13.9 ± 0.3	2.5 ± 0.6	110 ± 22		21
	14.3 ± 0.15	3.3 ± 0.1	∿50		38
	∿14		50 - 75		1*

*Reanalyzed.

238

For ^{208}Pb and ^{90}Zr these results are in rough agreement with those from Sendai[36] and the peak parameters obtained are consistent with those from Groningen.[21] Also we have performed a graphical reanalysis of (p,p') data on ^{208}Pb and ^{90}Zr and ^{208}Pb.

In our alpha scattering studies[7] the GR peak was observed to be asymmetric in many heavy nuclei. An analysis separating the GR peak into two components was performed for ^{142}Nd and ^{144,148,154}Sm. The angular distributions for both components were the same within the uncertainties over the angular range $13^\circ \leq \theta_L \leq 25^\circ$, hence the entire asymmetric peak was attributed to the GQR. In recent work[21] at Groningen utilizing inelastic alpha scattering at 120 MeV, a shoulder on the higher excitation side of the GR has been observed in ^{206,208}Pb, ^{197}Au and ^{209}Bi (Fig. 25). The angular distributions obtained from $12^\circ \leq \theta_L \leq 21^\circ$ for this shoulder are consistent with L = 0, 2 or 4 transfer.

Inelastic alpha scattering at angles small enough to observe the first minimum in the angular distribution has been established as a reliable technique for obtaining L transfer. DWBA calculations for ^{144}Sm (α,α') with L = 0, 2 and 4 transfer are shown in Fig. 26 using optical parameters from Ref. 7. The breathing mode form factor of Satchler[3] (Version I) was used for the L = 0 calculation. The form factors used for the other modes were standard collective form factors. The magnitudes of the DWBA predictions changed somewhat with differing optical potentials, form factors (both Satchler's Version I and II were tried for the monopole), and differing Coulomb excitation parameters, however, the shapes of the angular distributions remained unchanged. In particular, the deep minimum around 4° was present exclusively for L = 0 transfer in all calculations.

Inelastic alpha scattering measurements were performed at Texas A&M[22] using an 86-cm-long resistive wire proportional counter backed by a scintillator in the Enge split-pole spectrograph. By blocking the elastics from the counter and blocking events above the excitation regions of interest, spectra of the giant resonance region can be obtained with good statistics in times ranging from 5 hours at $\theta_L = 3^\circ$ to less than an hour for $\theta_L \geq 6^\circ$.

Data were taken with E_α = 96 MeV on ^{90}Zr, ^{144}Sm and ^{208}Pb at 3°, $3\text{-}1/2^\circ$, 4°, $4\text{-}1/2^\circ$, 5°, 6°, 7°, and 8° with good statistics to ascertain the shape behavior of the GR peaks over these small angles. ^{208}Pb spectra taken at 3°, 4°, and 6° with E_α = 96 MeV are shown in Fig. 27. The broad bumps from the (α,^{5}He) reaction are apparent; a dashed line indicates the background chosen for analysis of

the GR peaks. Although the GR to continuum yield improves at higher bombarding energies, the angular distribution features which distinguish among the even (odd) multipoles move to smaller angles as the energy is raised resulting in increased problems with slit scattering and beam tuning.

The angular distributions obtained for the ^{208}Pb 2.61 MeV $J^{\pi} = 3^-$ and 3.20 MeV $J^{\pi} = 5^-$ states are shown in Fig. 28. The DWBA fits are quite good over the angular range $3^{\circ} \leq \theta_L \leq 20^{\circ}$ and the deformation parameters obtained are in agreement with those obtained previously.

Analysis of the GR peaks was accomplished by fitting a multicomponent peak to the observed peak after subtraction of a nuclear continuum as indicated by ^{144}Sm published by the Oak Ridge group. The spectra they obtained are shown in Fig. 31 with graphical fits using two peaks with the parameters from Ref. 22. This provides a good representation of the data (within the statistical errors). If the lower excitation peak is assumed to exhaust most of the E2 EWSR, and relative E2/E1/E0 cross sections are taken from the calculations of Satchler,[3] excitation of the GDR would account for less than half of the observed strength of the higher excitation component. If the remainder is assumed to be E0 about 50% of the EWSR strength is indicated. Additionally there is evidence (mentioned earlier) from (p,p') in light nuclei that excitation of the GDR is overestimated in the calculations of Satchler, hence an even larger portion of the second peak may be E0.

These results are in agreement with those from Orsay[37] and with the Sendai[36] results using the Goldhaber-Teller model for analysis of the E1. Recent Darmstadt[38] electron scattering results on ^{208}Pb at low momentum transfers where the E1 excitation strength is essentially model independent also obtain E0 (or E2) strength at this energy. Microscopic calculations by Speth[39] yield a form factor for (e,e') to the GDR in ^{208}Pb much like the GT form factor, further confirming that the GT model is preferred.

An energy of 13.7 MeV for the breathing mode in ^{208}Pb is in excellent agreement with the estimates of Krewald et al.[40] and Speth et al.[41] Utilizing the liquid drop model, the breathing mode energy E_0 is related to the nuclear matter compressibility K by:

$$E_0 = \frac{\pi}{3R} \sqrt{\frac{\hbar^2 K}{m}}$$

where R is the nuclear radius and m is the nucleon mass. The values of K obtained for ^{90}Zr, ^{144}Sm and ^{208}Pb are 183, 197 and 208 MeV, respectively. Microscopic RPA calculations were performed by Blaizot et al.[42] for five interactions which were particularly successful in Hartree-Fock calculations. Keeping in mind that their $K_A = (\pi^2/15)K$, the Skyrme interactions (S IV and SIII) gave K = 310 and 340 MeV respectively, for ^{208}Pb and similar values for ^{90}Zr, much higher than the experimental values. The interaction BI of Brink and Boecker[43] gave K $\approx$ 170 MeV while DI of Gogny[44] gave K $\approx$ 222 MeV, somewhat closer to the measured value.

EXCITATION OF GIANT RESONANCES BY HEAVY IONS

Groups at Michigan State University[45] and Karlsruhe[46] have utilized inelastic scattering of ^{6}Li ions to observe the GQR. In the MSU work performed on ^{90}Zr at $E_{^6Li}$ = 74 MeV, a weak broad structure was seen at E_x = 13.8 MeV which is likely the GQR, although the angular distribution obtained was featureless. The work at Karlsruhe utilized 156 MeV ^{6}Li ions on ^{208}Pb and the resulting spectrum is shown in Fig. 32. The GQR appears very prominently on a rather small continuum background. The angular distribution obtained is featureless, but is fit reasonably well in both shape and magnitude by DWBA calculations. The higher beam energy seems necessary to produce a reasonable cross section for the GQR, as in alpha scattering. These results suggest inelastic ^{6}Li scattering at energies around 150 MeV may be very useful in determining at least the shape and position of the GQR in nuclei.

The only other reported excitation of the GQR by heavy-ions of which I am aware is by a group at Yale[47] who utilized ^{27}Al(^{12}C,^{12}C*)^{27}Al. A spectrum from their work is shown in Fig. 33. They have drawn a suggested background, implying that the yield above this is due to excitation of the GQR (and possibly the LEOR). When the yield above the suggested background is compared to the known ^{27}Al GQR (seen in alpha scattering, Fig. 8), there are some similarities, however, the known GQR is considerably narrower. The ^{12}C angular distribution obtained is featureless and not in particularly good agreement with DWBA predictions. In this case no clear prescription for drawing the background is apparent in the spectra, and I must admit to being skeptical of the chosen background. The separation of the GQR, from the continuum, indeed even the presence of the GQR is

---

not obvious from the data. A similar experiment on ^{40}Ca, where the GQR is quite narrow and should be immediately apparent would be quite interesting.

CONCLUSION

The large amount of inelastic scattering data now available has elucidated many properties of the giant multipole resonances. Many more intriguing questions have now been revealed. The structure observed in the GQR in light nuclei and the differences between different excitation modes suggest that decay measurements to better define the wave functions of these fairly simple configurations would be very interesting. Many predictions are now available regarding the behavior of both the GQR and the LEOR in deformed nuclei, and more thorough studies of these in deformed nuclei would be valuable. The structure in the region of the ^{208}Pb GQR is very poorly understood and requires more work. The properties of the LEOR are just beginning to be defined; little is known about its fine structure and many nuclei have not been investigated at all. The breathing mode state has just been definitively identified very recently, and its location in lighter nuclei as well as its general properties remain to be established. The field of heavy-ion excitation of giant resonances is wide open; there have been suggestions that the deep inelastic processes proceeds through giant resonance, but there is little evidence of their direct excitation with projectiles heavier than lithium. Finally the superb peak to continuum ratio for the GQR obtained with 156 MeV ^{6}Li ions indicates the possibility of obtaining the properties of the GQR much more accurately than with lighter projectiles.

242

REFERENCES

1. F. E. Bertrand, Ann. Rev. Nucl. Sci., 26. 457 (1976).

2. H. Überall, Electron Scattering from Complex Nuclei, Academic Press, N.Y., 1971, Ch. 6.

3. G. R. Satchler, Nucl. Phys., A195, 1 (1974); Comm. Nucl. Part. Phys., 5, 145 (1972); Part. and Nucl., 5, 105 (1973).

4. A. M. Bernstein, Adv. Nucl. Phys., 3, 325 (1969).

5. R. Pitthan and T. Walcher, Phys. Lett., 36B, 563 (1971).

6. M. B. Lewis and F. E. Bertrand, Nucl. Phys., A196, 337 (1972).

7. D. H. Youngblood, J. M. Moss, C. M. Rozsa, J. D. Bronson, A. D. Bacher, and D. R. Brown, Phys. Rev. C, 13, 994 (1976).

8. A. Bohr and B. R. Mottelson, Neutron Capture Gamma-Ray Spectroscopy, IAEA, Vienna, 1969; B. R. Mottelson, in Proc. of the 15th Solvay Conf. in Physics, 1970, Editions Stoops, Brussels, 1970.

9. A. Kiss, C. Mayer-Böricke, M. Rogge, P. Turek, and S. Wiktor, Phys. Rev. Lett., 37, 1188 (1976).

10. D. H. Youngblood, C. M. Rozsa, J. M. Moss, D. R. Brown and J. D. Bronson, Phys. Rev. C, 15, 1644 (1977).

11. M. N. Harakeh, A. R. Arends, M. J. A. DeVoigt, A. G. Drentje, S. Y. Van der Werf, and A. Van der Woude, Nucl. Phys., A265, 189 (1976).

12. K. T. Knöpfle, G. J. Wagner, H. Breuer, M. Rogge, and C. Mayer-Böricke, Phys. Rev. Lett., 35, 779 (1975).

13. H. Breuer, K. T. Knöpfle, P. Paul, G. J. Wagner, C. Mayer-Böricke, M. Rogge and P. Turek in Proc. of Intern. Conf. on Nuclear Structure, Tokyo, 1977, p. 179.

14. J. S. Dehesa, S. Krewald, J. Speth, and A. Faessler, Phys. Rev. C., 15, 1858 (1977).

15. D. Kurath and I. S. Towner, Nucl. Phys. A222, 1 (1974).

16. F. E. Bertrand, K. Van der Borg, A. G. Brenjte, M. N. Harakeh, J. Van der Plicht and A. Van der Woude (to be published).

17. E. Kuhlmann, E. Ventura, J. R. Calarco, D. G. Mavis, and S. S. Hanna, Phys. Rev. C., 11, 1525 (1975).

18. K. Van der Borg, M. N. Harakeh, S. Y. Van der Werf, A. Van der Woude, and F. E. Bertrand, Phys. Lett. 67B, 405 (1977).

19. D. H. Youngblood, A. D. Bacher, D. R. Brown, J. D. Bronson, J. M. Moss, and C. M. Rozsa, Phys. Rev. C., 15, 246 (1977).

20. R. Pitthan and F. R. Buskirk, Phys. Rev. C., 16, 983 (1977).

21. M. N. Harakeh, K. Van der Borg, T. Ishimatsu, H. P. Morsch, A. Van der Woude, and F. Bertrand, Phys. Rev. Lett., 13, 676 (1977).

22. D. H. Youngblood, C. M. Rozsa, J. M. Moss, D. R. Brown and J. D. Bronson, Phys. Rev. Lett., 39, 1188 (1977).

23. E. C. Halbert, J. B. McGrory, G. R. Satchler, and J. Speth, Nucl. Phys. A245 189 (1975).

24. P. Ring and J. Speth, Nucl. Phys. A, 235, 315 (1974).

25. T. Kishimoto, J. M. Moss, D. H. Youngblood, J. D. Bronson, C. M. Rozsa, D. R. Brown, and A. D. Bacher, Phys, Rev. Lett., 35, 552 (1975).

26. G. Kyrchev, L. A. Malov, V. O. Nesterenko, V. G. Soloviev, JINR, E4-9962, Dubna, 1976.

27. D. Zawischa and J. Speth, Phys. Rev. Lett. 36, 843 (1976).

28. K. T. Knöpfle, G. J. Wagner, A. Kiss, M. Rogge and C. Mayer-Böricke, Phys. Lett., 64B, 263 (1976).

29. W. Knüpfer, K. Knauss, and M. G. Huber, Phys. Lett., 66B, 305 (1977).

30. Y. Abgrall, B. Morond, E. Caurier, and B. Grammaticos, Proc. of the Intern. Conf. on Nuclear Structure, Tokyo, 1977, p. 199.

31. J. M. Moss, D. H. Youngblood, C. M. Rozsa, D. R. Brown, and J. D. Bronson, Phys. Rev. Lett., 37, 816 (1976).

32. K. F. Liu and G. E. Brown, Nucl. Phys. A265, 385 (1976)

33. L. A. Malov, V. O. Nesterenko and V. G. Soloviev, J. of Phys. G, Nucl. Phys., 3, L219 (1977).

34. T. Kishimoto (to be published).

35. H. P. Morsch, P. Decowski and W. Benenson, Phys. Rev. Lett., 37, 263 (1976).

36. S. Fukuda and Y. Torizuka, Phys. Lett., 62B, 146 (1976); M. Sasao and Y. Torizuka, Phys. Rev. C, 15, 217 (1977).

37. N. Marty, M. Morlet, A. Willis, V. Comporat and R. Frascaria, Proc. of the Intern. Symposium on Highly Excited States in Nuclei, Jülich, 1975 p. 17; IPNO-PhN-76-03, Inst. de Physique Nucleaire, Orsay, France.

38. A. Richter, Proc. of the Intern. Conf. on Electro- and Photoexcitation, Sendai, Japan, 1977.

39. J. Speth, Proc. of the Intern. Conf. on Nuclear Structure, Tokyo, 1977.

40. S. Krewald, R. Rosenfelder, J. E. Galonska, and A. Faessler, Nucl. Phys. A269, 112 (1976).

41. J. Speth, L. Zamick and P. Ring, Nucl. Phys., A232, 1 (1974).

42. J. P. Blaizot, D. Gogny, and B. Grammaticos, Nucl. Phys., A265, 315 (1976).

43. D. M. Brink and E. Boeker, Nucl. Phys. A91, 1 (1967).

44. D. Gogny, Nuclear Self Consistent Fields, ed. G. Ripka and M. Porneauf, North-Holland, Amsterdam, 1975, p. 333.

45. R. Pardo, R. G. Markham, W. Benenson, A. I. Galonsky and E. Kashy (to be published).

46. H. J. Gils, H. Rebel, J. Buschmann, and H. Klewe-Nebenius, Phys. Lett., 68B, 427 (1977).

47. R. R. Betts, S. B. DiCenzo, M. H. Mortensen, and R. L. White, Phys. Rev. Lett., 39, 1183 (1977).
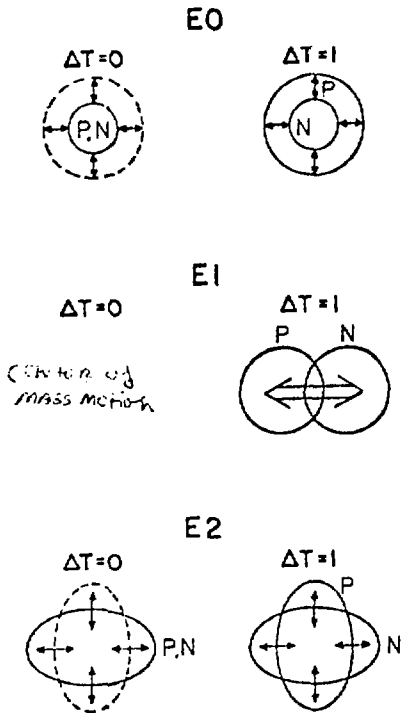
Fig. 1. Monopole, dipole and quadrupole oscillations of the nucleus are illustrated from the hydrodynamic model viewpoint.
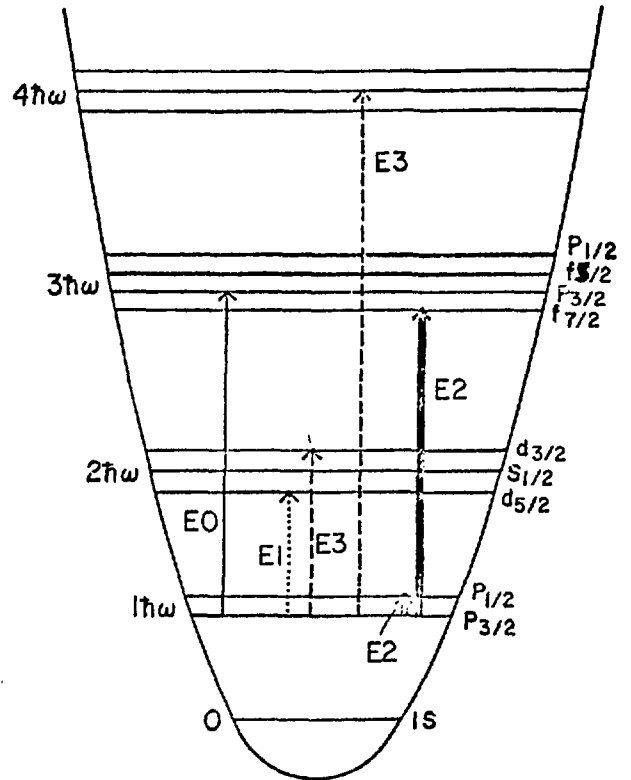
Fig. 2. Particle-hole excitations responsible for the multipole oscillations are illustrated with a harmonic oscillator potential.
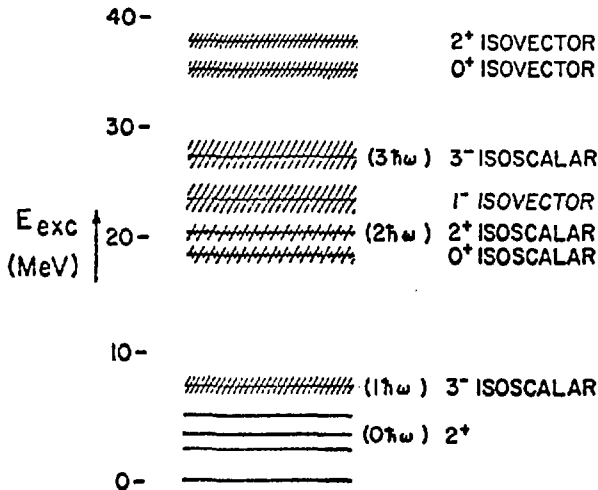
Fig. 3. The location of giant multipole resonance strength in a nucleus of mass about 40 is indicated schematically.

246
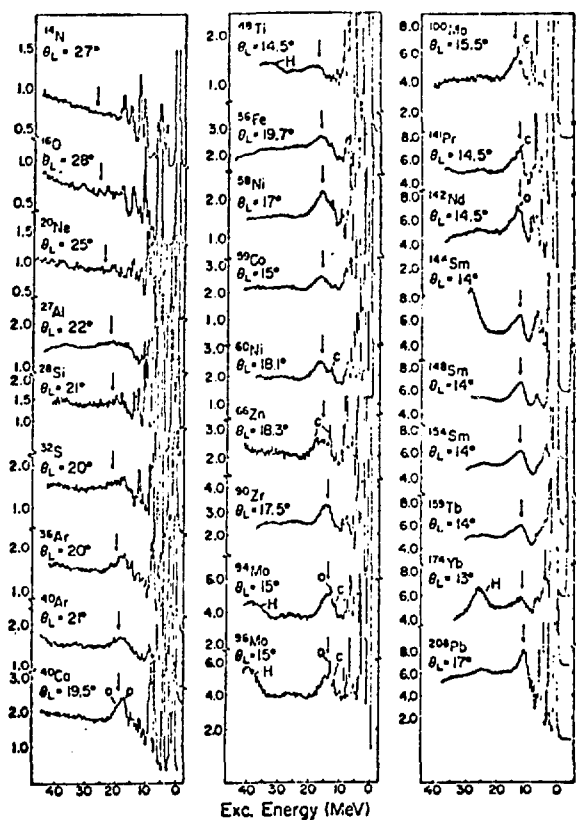
Fig. 4. Inelastic α scattering spectra taken at Texas A&M. The bombarding energy was 96 MeV for all targets with A≤ 56 and for ^{90}Zr. All others were taken at E_α = 115 MeV.
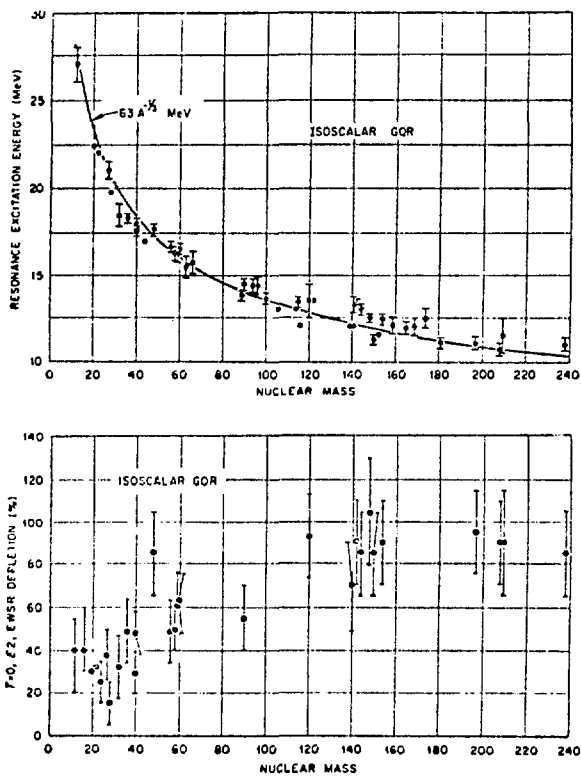
Fig. 5. The excitation energy and EWSR fraction obtained in many works for the GQR are shown.
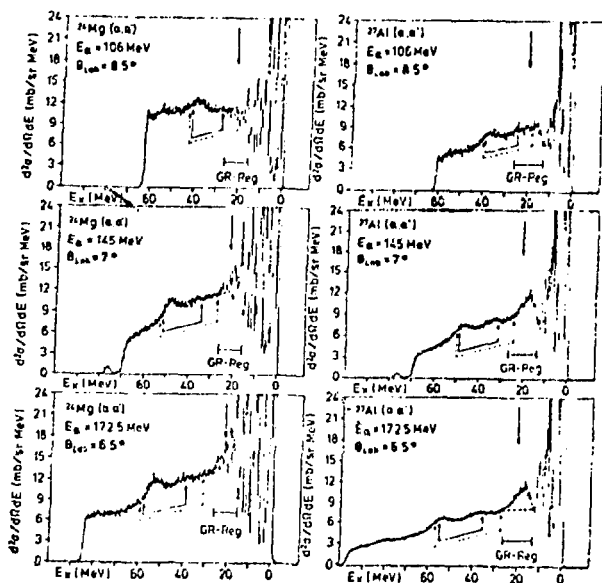
Fig. 6. Inelastic α scattering spectra
taken at Julich at E_α = 106,
145, and 172.5 MeV. The kine-
matic limits for ^{5}He and ^{5}Li
break up contributions are
indicated by solid and dashed
arrows.
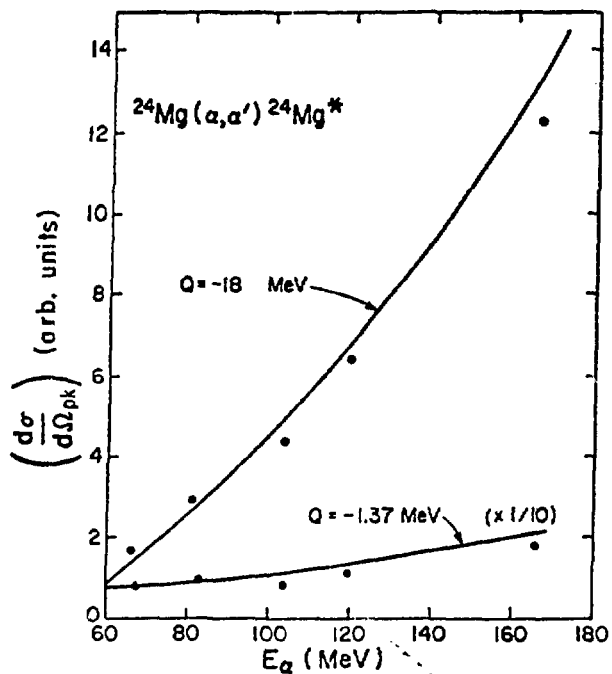
Fig. 7. The solid lines are DWBA cross
sections at the second maximum
in the L=2 angular distribu-
tions using a fixed set of
optical parameters. The cir-
cles were calculated using op-
tical potentials appropriate
to the bombarding energy.

248
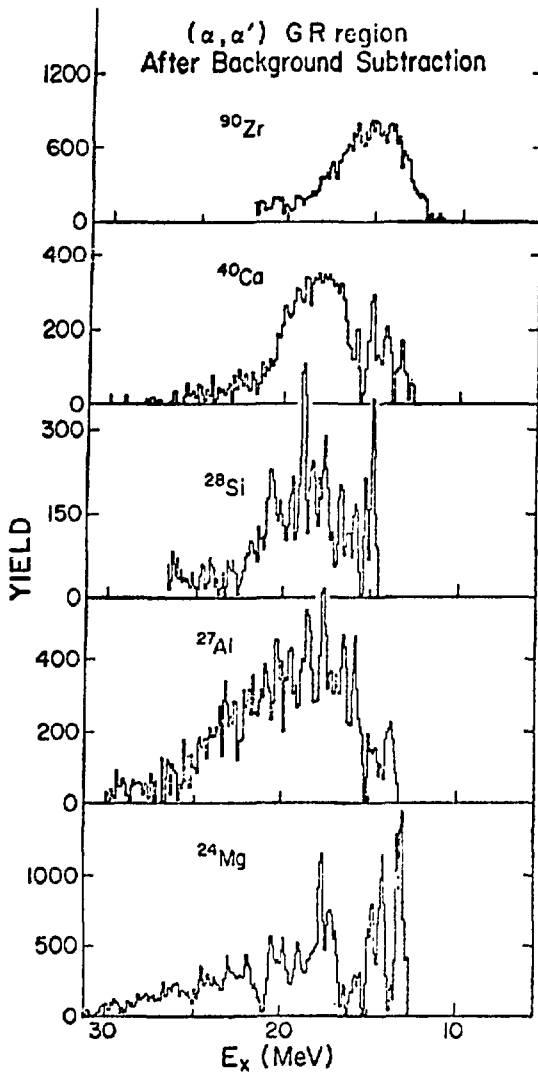
Fig. 8. (α,α') spectra in the giant resonance region after subtraction of the continuum.
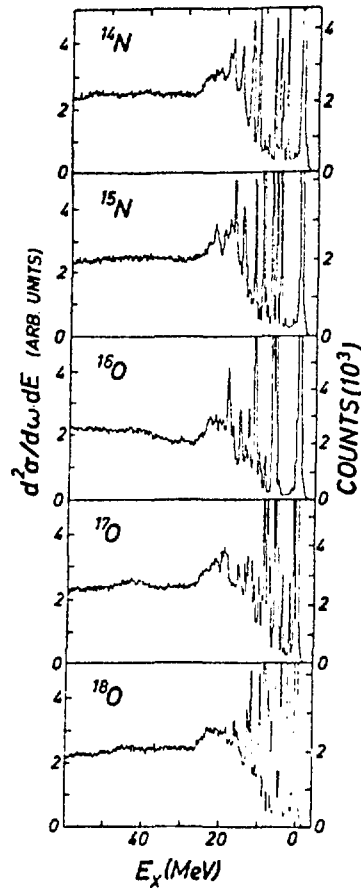
Fig. 9. Inelastic α spectra taken at $E_\alpha = 155$ MeV in a Jülich-Heidelberg collaboration.
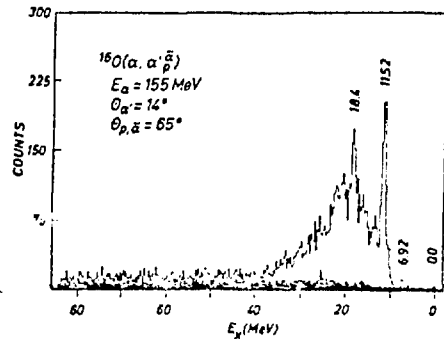
Fig. 10. Spectra of α particles inelastically scattered from ^{16}O in coincidence with decay protons (dark region) and decay α particles (line) from Ref. 13.

249
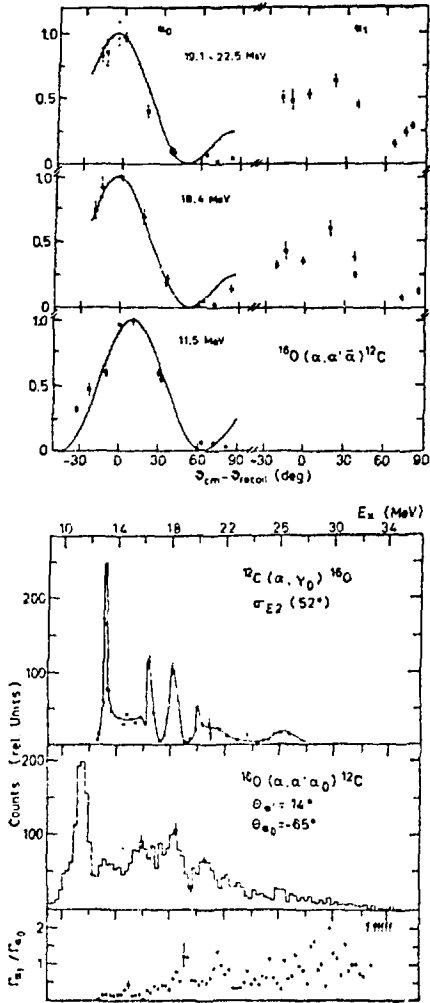
Fig. 11. Angular correlations for α_0 and α_1 decay of ^{16}O are shown at the top. The curves are plane wave predictions. ^{16}O $(\alpha\alpha'\alpha_0)$ and $^{12}C(\alpha,\gamma)$ E2 are compared in the bottom spectra.
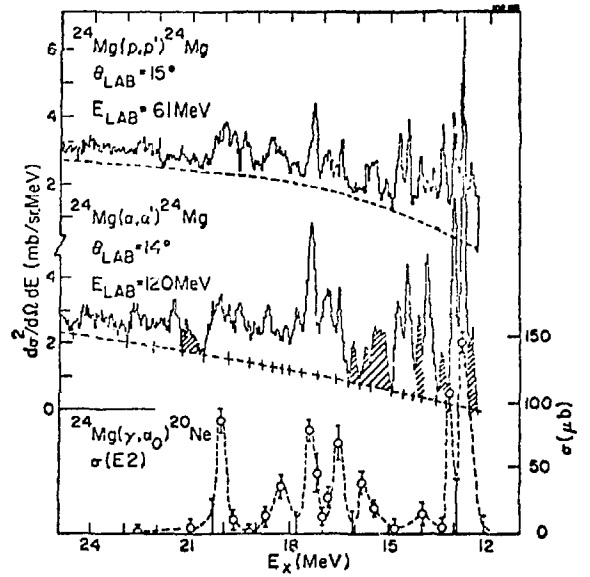
Fig. 12. Spectra of ^{24}Mg (α,α') and (p,p') are compared with an E2(γ,α_0) excitation function. Shaded regions possibly contain other than L=2 multipolarity.
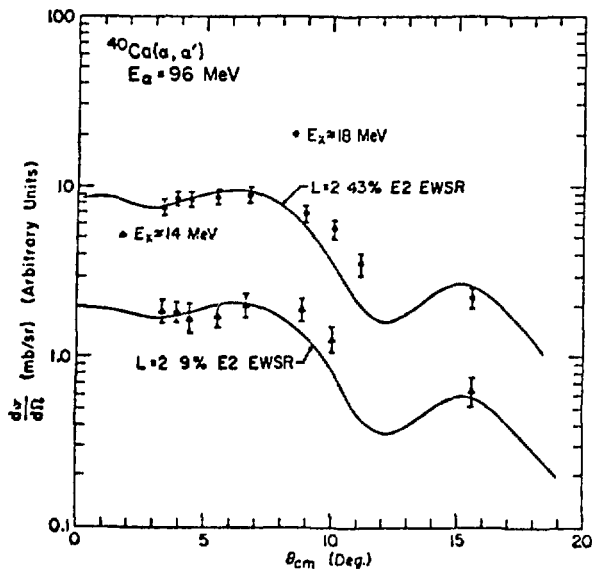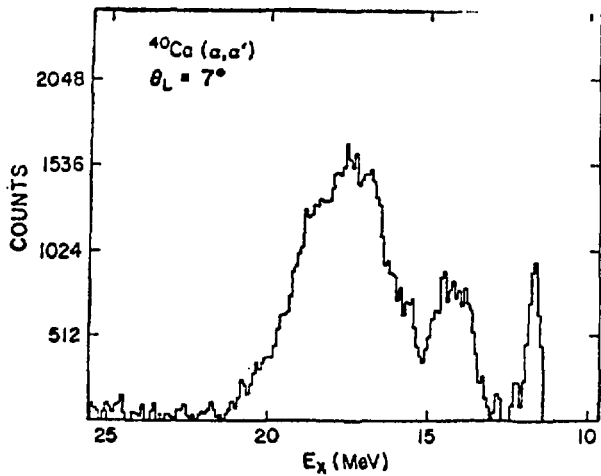
Fig. 13. A portion of the ^{40}Ca(α,α') spectrum taken at $\theta_L = 7^\circ$ is shown after continuum subtraction. Angular distributions for the 18 MeV and 14 MeV groups are also shown along with L = 2 DWBA calculations.
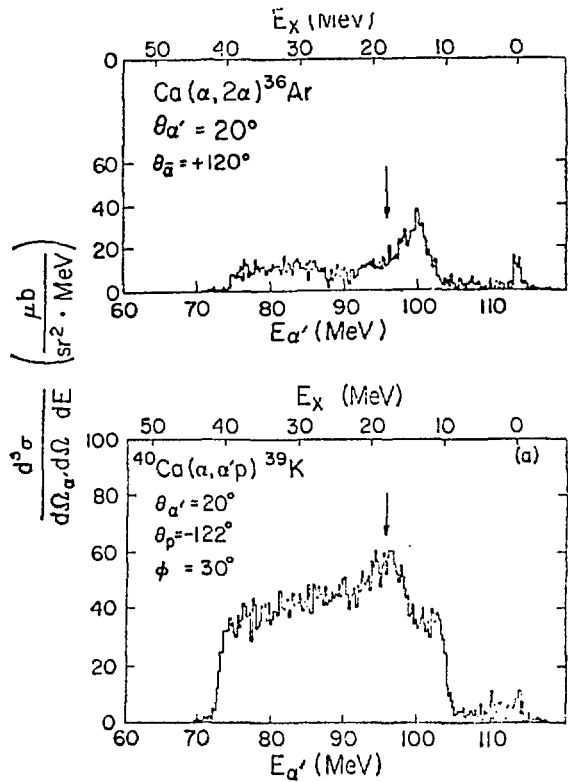
Fig. 14. Spectra of alpha particles inelastically scattered from ^{40}Ca in coincidence with decay protons (bottom) and decay alpha particles (top).
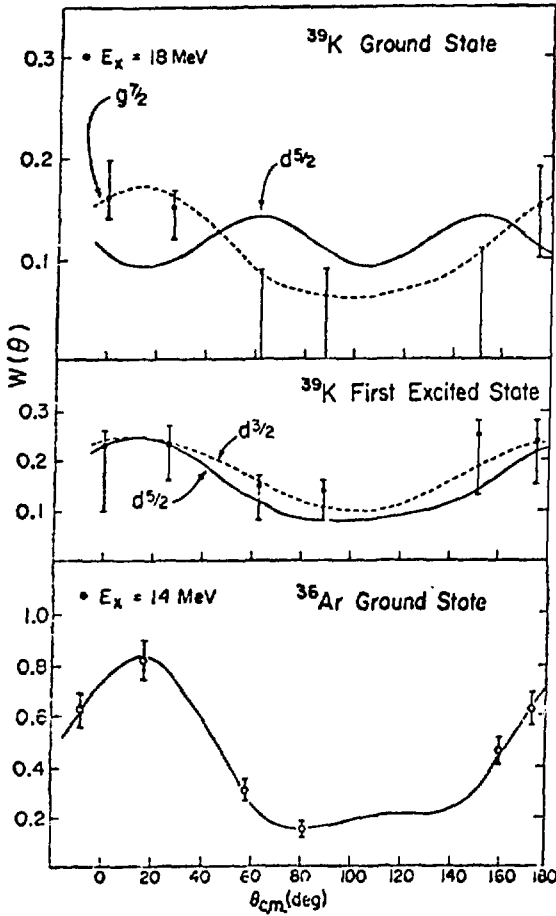
Fig. 15. Angular correlations obtained for p decay of the 18 MeV group and for α_0 decay of the 14 MeV group. The lines represent DWBA predictions for the partial waves indicated.
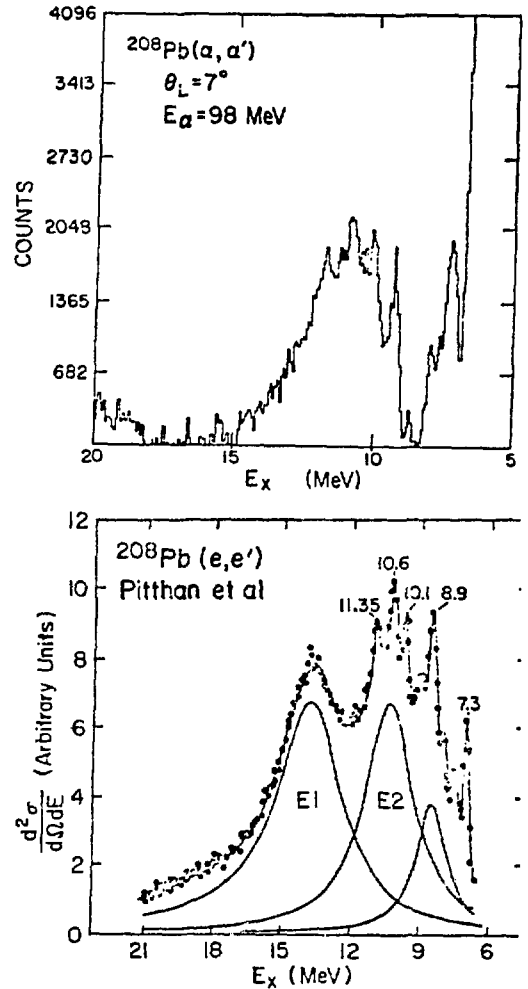
Fig. 16. A ^{208}Pb (α,α') spectrum after continuum subtraction taken at an angle where the structure is enhanced (from Texas A&M). A ^{208}Pb (e,e') spectrum from Ref. 20 for comparison.
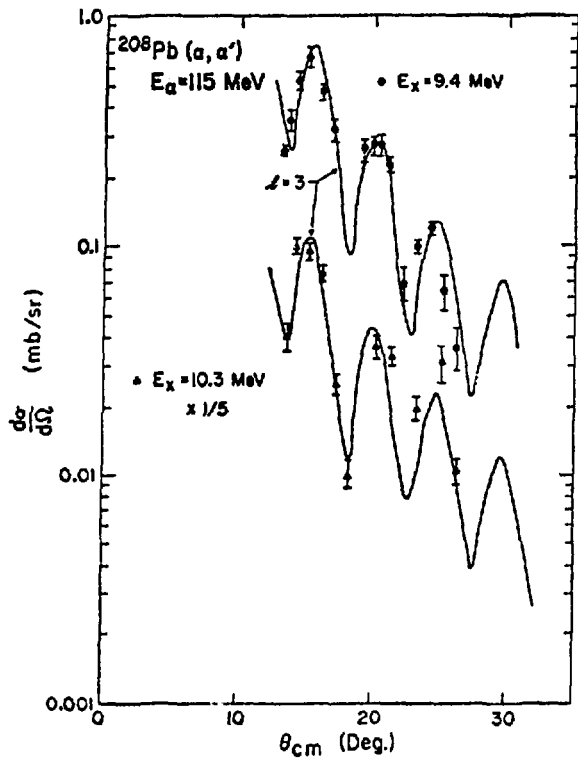
Fig. 17. Inelastic α scattering angular distributions for the narrow 9.4 and 10.3 MeV states in ^{208}Pb. The curves are DWBA predictions for L=3 transfer.
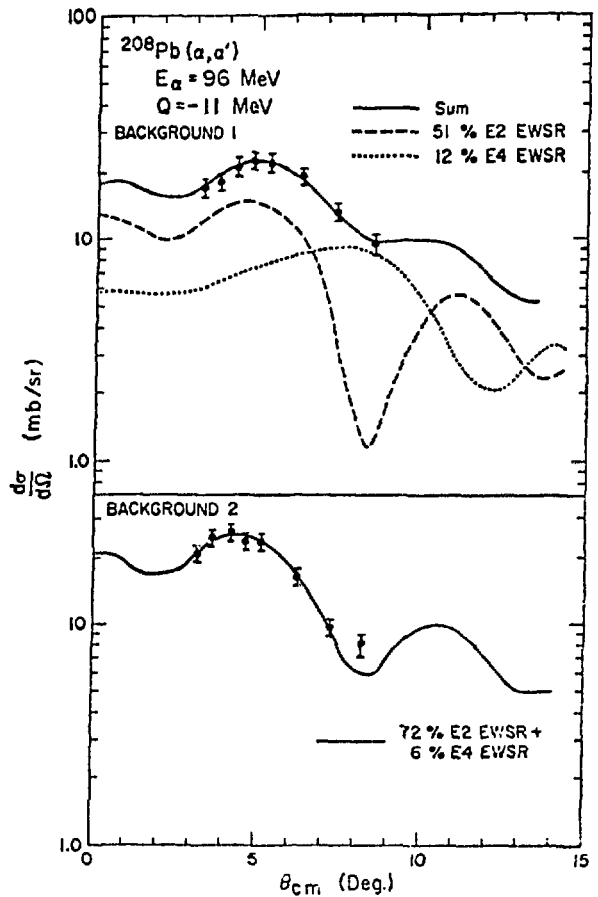
Fig. 18. (α,α') angular distributions obtained for the 11-MeV group in ^{208}Pb are shown for two analyses. E2 and E4 DWBA calculations are shown, and the combinations required to fit the data are indicated.
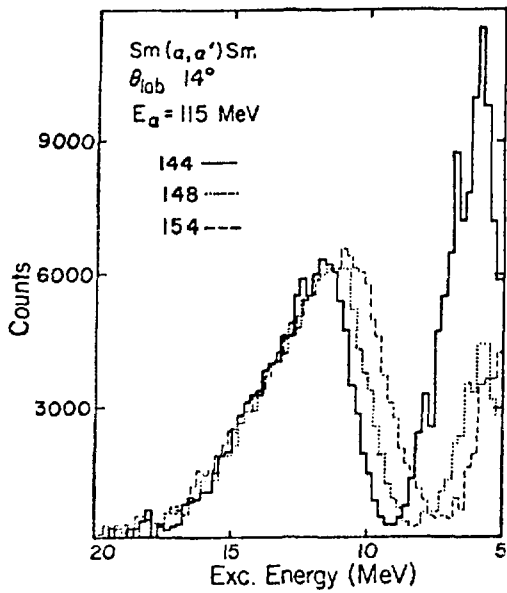
Fig. 19. ^{144,148,154}Sm GR peaks are shown superimposed after continuum subtraction.
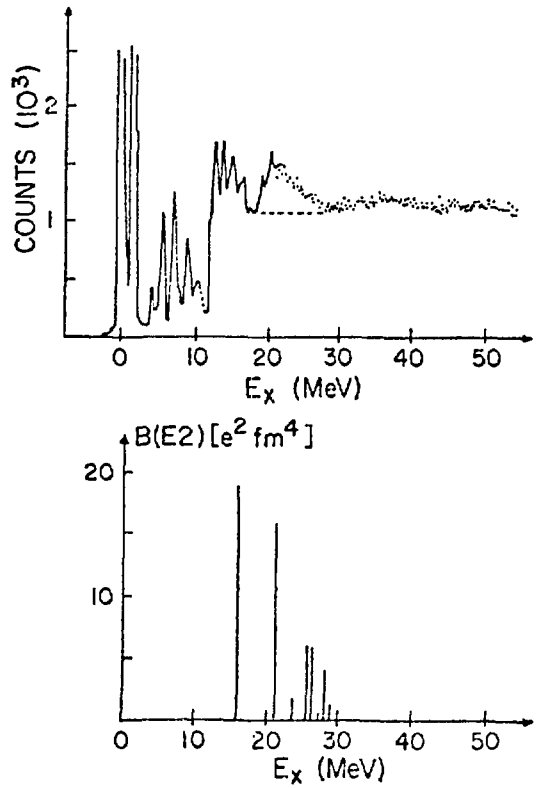
Fig. 20. A ^{20}Ne(α,α') spectrum is shown along with theoretical predictions for location of E2 strength.
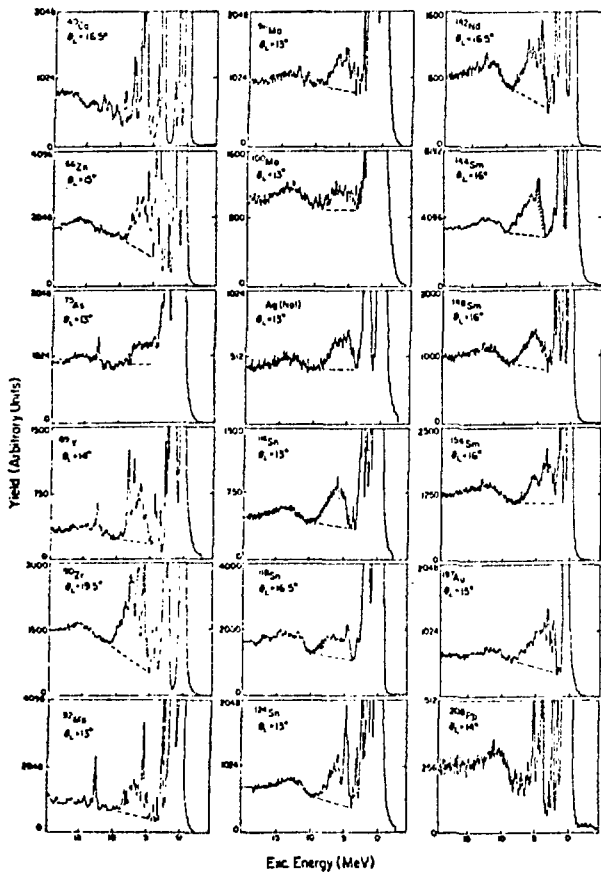
Fig. 21. (α,α') spectra taken at a peak in the E3 cross section are shown. The background chosen for analysis of the LEOR is indicated.
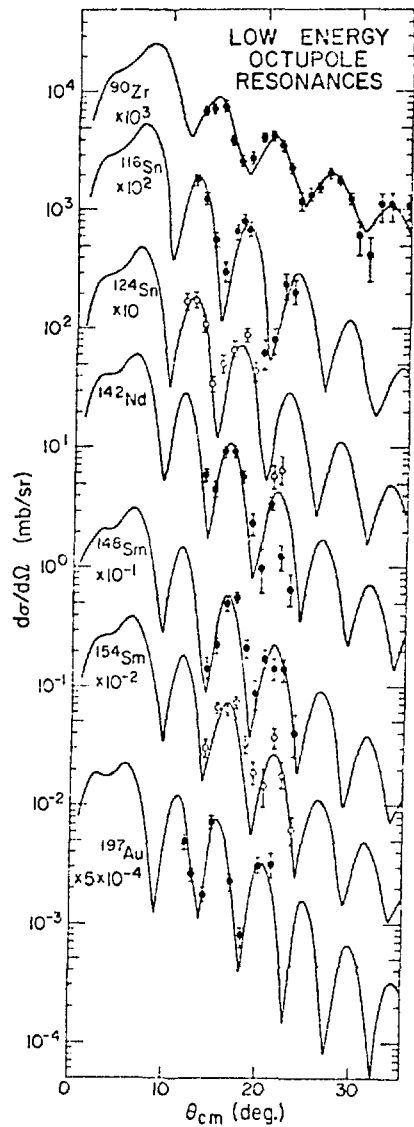
Fig. 22. (α,α') angular distributions obtained for LEOR in several nuclei are shown with L=3 DWBA predictions.

255
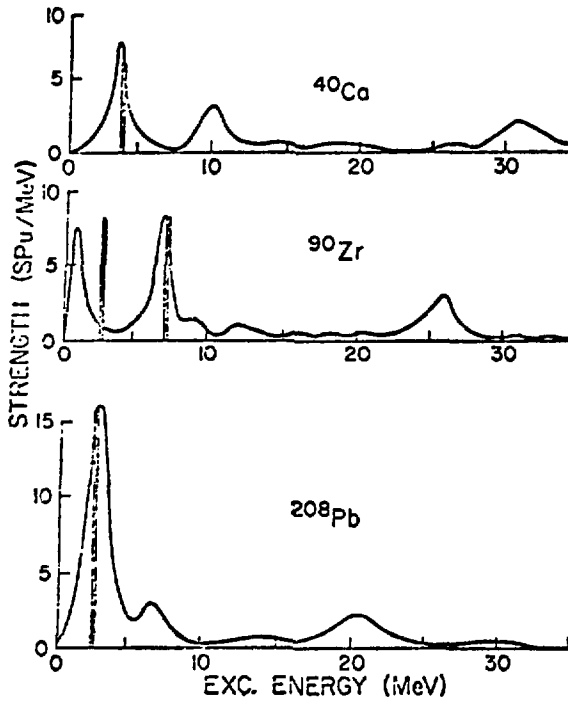
Fig. 23. The RPA calculations of Ref. 32 are shown with observed 3⁻ strength indicated by the vertical bars.

Fig. 25. Inelastic α scattering spectra obtained at Groningen on ^{206}Pb. Two peak fits are shown for two background choices (Ref. 21).
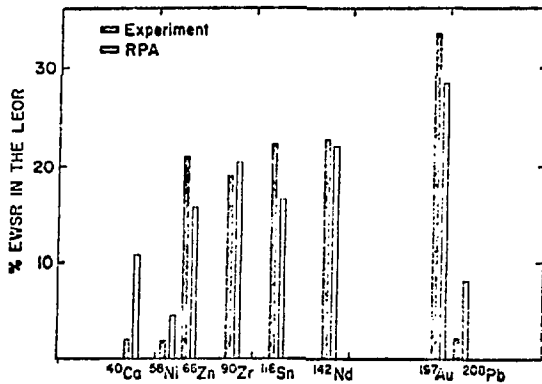
Fig. 24. The 3⁻ strength observed in the vicinity of the LEOR is compared with RPA calculations for several nuclei.
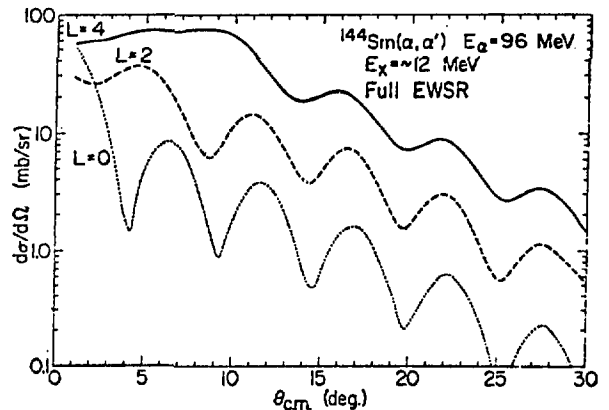
Fig. 26. DWBA calculations normalized to the full EWSR for inelastic alpha scattering on ^{144}Sm are shown for L = 0, 2, 4 transfer.

256
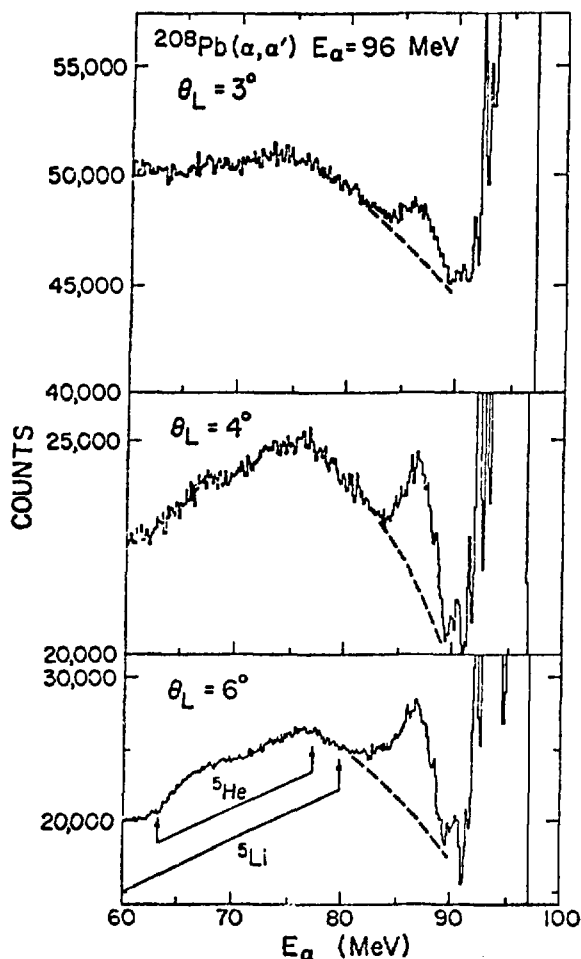
Fig. 27. ^{208}Pb spectra taken at 3°, 4° and 6°. Note the suppressed zero. One background chosen for analysis is indicated.
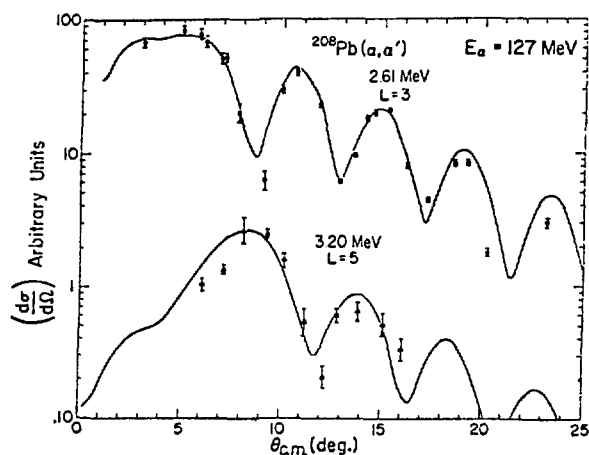

Fig. 28. ^{208}Pb (α,α') angular distributions with DWBA calculations for low-lying 3$^-$ and 5$^-$ states.
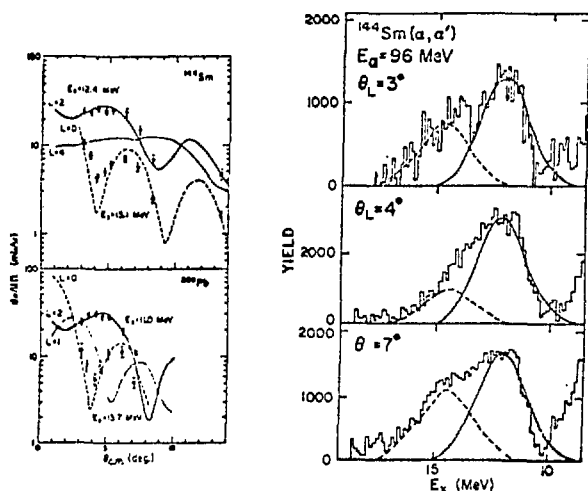

Fig. 29. Excerpts from ^{144}Sm (α,α') spectra after continuum subtraction are shown for 3 angles. Two peak fits are indicated. Also shown are ^{144}Sm and ^{208}Pb angular distributions for both broad components of the GR. L = 0, 1, 2, 4 DWBA calculations are shown.
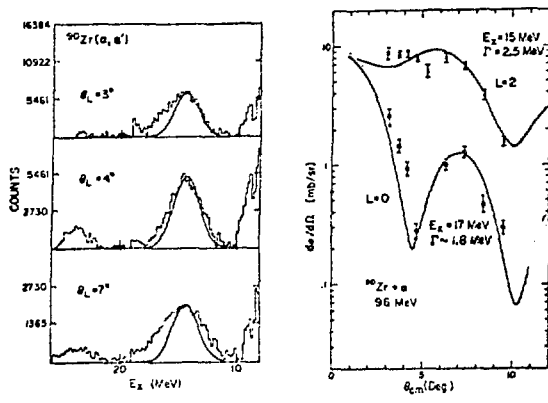
Fig. 30. Excerpts from ^{90}Zr(α,α') spectra after continuum subtraction are shown for 3 angles. A gaussian of constant width and position is shown for each angle. The angular distributions obtained for upper and lower portions of the GR are shown together with L = 0 and 2 DWBA predictions.
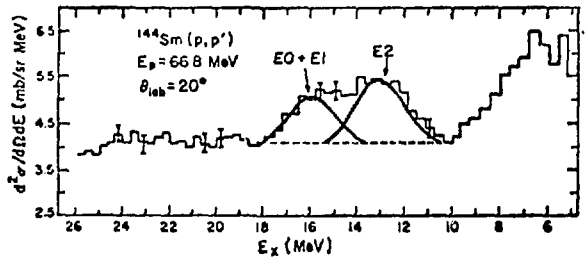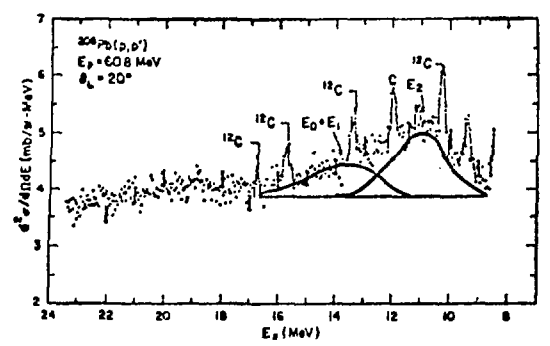

Fig. 31. Inelastic proton scattering spectra from Ref. 1 are shown for ^{144}Sm and ^{208}Pb. Peaks with E_x and Γ corresponding to those from α scattering are shown. The background is that given by the original authors.
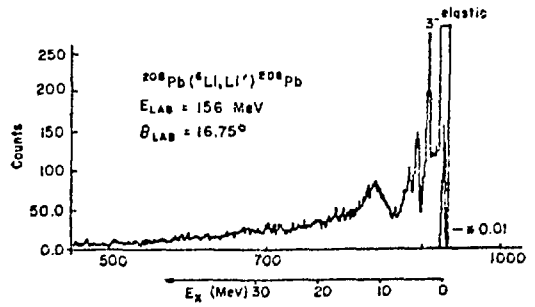

Fig. 32. A ^{208}Pb (^{6}Li,^{6}Li') spectrum taken at Karlsruhe (Ref. 46).
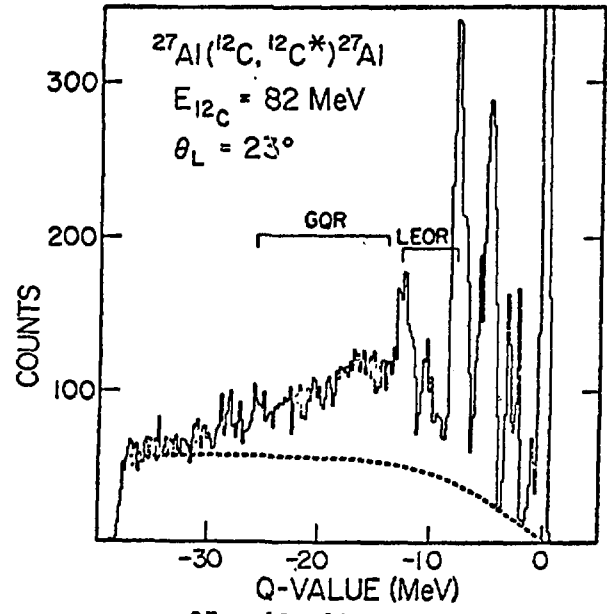
Fig. 33. A ^{27}Al(^{12}C,^{12}C*)^{27}Al spectrum from Yale (Ref. 47).

PARTICIPANTS

Adelberger, Eric	Univ. of Washington	Henning, Walter	Argonne Nat. Lab.
Aniol, Konrad	Univ. of Washington	Hertzog, David	William and Mary
Antonuk, Larry	Alberta, Canada	Hoehn, Martha	P-2, LASL
Barlett, Martin	Univ. of Texas	Hoffman, Cyrus	MP-4, LASL
Bassalleck, Bernd	Univ. of Brit. Col.	Hopkins, Lucy	Univ. of S. Car.
Becker, Jeffrey	Univ. of Illinois	Howe, Steve	P-9, LASL
Bowman, David	MP-4, LASL	Hudson, Jerry	Q-2, LASL
Boyer, Kenneth	Univ. of Texas	Jackson, Harold	Argonne Nat. Lab.
Briscoe, William	Catholic Univ.	Jeppesen, Randy	Univ. of Montana
Chaky, Rebecca	Univ. of Kansas	Johnson, Mikkel	MP-DO, LASL
Chapuran, Thomas	Univ. of Illinois	Johnson, William	CNC-11, LASL
Chakravarti, Soumya	Argonne Nat. Lab.	Joseph, Richard	Univ. of Texas
Colella, Nick	Carnegie-Mellon U.	Kapusta, Joseph	LBL
Cooper, Edward	Univ. of Alberta	Kary, Timothy	MP-4, LASL
Cooper, Martin	MP-4, LASL	Kim, Jungwoo	Virginia Poly. Inst.
Correll, David	P-7, LASL	Kyle, Gary	Univ. of Minnesota
Cottingame, William	Univ. of Texas	Lisowski, Paul	P-3, LASL
Cverna, Frank	MP-4, LASL	Lissanti, Jerry	MP-4, LASL
Dam, Steven	Univ. of S. Car.	Lynch, William	Univ. of Washington
Daneshvar, Kasra	Argonne Nat. Lab.	Marlow, Daniel	Carnegie-Mellon U.
Dowell, David	Univ. of Illinois	Mathie, Edward L.	Univ. of Brit. Col.
Duong-Van, Minh	MP-4, LASL	McGill, John	Univ. of Texas
Essick, John	UCLA	Meyer, Robert	Univ. of Mass.
Faucett, John	Univ. of Oregon	Mischke, Richard	MP-4, LASL
Frank, James	MP-4, LASL	Moore, C. Fred	Univ. of Texas
Friar, James	T-5, LASL	Pepin, Greg	Rice Univ.
Giebink, David	T-5, LASL	Peterson, Bruce	Univ. of Wyoming
Giovanetti, Kevin	William and Mary	Peterson, Dale	Univ. of Michigan
Greene, Steven	Univ. of Texas	Pillai, C.	Oregon State Univ.
Gupta, O. P.	Virginia Poly. Inst.	Preedom, Barry	Univ. of S. Car.
Haji-Saeid, M.	UCLA	Pauletta, Gianni	UCLA
Hamm, Marianne	MP-4, LASL	Ransome, Ronald	Univ. of Texas
Hanson, Kenneth	MP-3, LASL	Redwine, Robert	MP-4, LASL
Harvey, Carol	Univ. of Texas	Reed, Coke	TD-2, LASL

Renner, Timothy	Argonne Nat. Lab.	Tsang, Betty	Univ. of Washington
Roeder, Dennis	WX-1, LASL	Tuggle, Dale	WX-5, LASL
Rundberg, Robert	CNC-11, LASL	Turpin, Steve	Rice Univ.
Scarbrough, Edward	MP-7, LASL	Ullmann, John	UC, Davis
Schiffer, John	Argonne Nat. Lab.	Vieira, David	CNC-11, LASL
Sheers, Bill	Univ. of New Mexico	Vrba, Joseph	ORNL
Shera, E. Brooks	P-2, LASL	Walecka, John	Stanford Univ.
Shor, Asher	Columbia Univ.	Wang, Angel	UCLA
Smith, Greg	Univ. of Colorado	Wapstra, Aaldert	IKO, Netherlands
Smith, Lester	Univ. of Texas	Ward, Herb	Univ. of Texas
Sprung, Donald	McMaster Univ.	Williams, Alton	Univ. of Mass.
Starr, Richard	Univ. of Illinois	Williamson, Steven	Univ. of Illinois
Stephenson, Gerry	T-5, LASL	Wissink, Scott	Stanford Univ.
Stricker, Karen	Michigan State Univ.	Wriekat, Abdl	UCLA
Szyjewicz, Adam	Alberta, Canada	Wright, Neil A.	TRIUMF
Tinsley, James	Univ. of Oregon	Yates-Williams, M.	MP-4, LASL
Tippens, Brad	Texas A&M Univ.	Youngblood, David	Texas A&M Univ.
Tombrello, Tom	Cal. Inst. of Tech.	Yuan, Vincent	MP-4, LASL